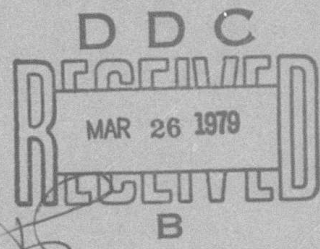


ADA066298

AFAL-TR-78-96

②
NW

LEVEL II



ADVANCED ARCHIVAL MEMORY

C.G. Kirkpatrick G.E. Possin
H.G. Parks R.C. Raymond
K.G. Vosburgh

Corporate Research and Development
General Electric Company
Schenectady, New York 12301

JULY 1978

DDC FILE COPY

Interim Report

June 1, 1977-December 31, 1977



Approved for public release; distribution unlimited.

AIR FORCE AVIONICS LABORATORY
AIR FORCE WRIGHT AERONAUTICAL LABORATORIES
AIR FORCE SYSTEMS COMMAND
WRIGHT-PATTERSON AIR FORCE BASE, OHIO 45433

79 03 16 055

NOTICE

When Government drawings, specifications, or other data are used for any purpose other than in connection with a definitely related Government procurement operation, the United States Government thereby incurs no responsibility nor any obligation whatsoever; and the fact that the government may have formulated, furnished, or in any way supplied the said drawings, specifications, or other data, is not to be regarded by implication or otherwise as in any manner licensing the holder or any other person or corporation, or conveying any rights or permission to manufacture, use, or sell any patented invention that may in any way be related thereto.

This report has been reviewed by the Information Office (OI) and is releasable to the National Technical Information Service (NTIS). At NTIS, it will be available to the general public, including foreign nations.

This technical report has been reviewed and is approved for publication.

B. Millard G. Mier
MILLARD G. MIER
Project Engineer

FOR THE COMMANDER

Robert J. Almassy
ROBERT J. ALMASSY, Maj, USAF
Dep Chief, Electronic Research Branch
Electronic Technology Division

"If your address has changed, if you wish to be removed from our mailing list, or if the addressee is no longer employed by your organization please notify AFAL/DHR, W-PAFB, OH 45433 to help us maintain a current mailing list".

Copies of this report should not be returned unless return is required by security considerations, contractual obligations, or notice on a specific document.

UNCLASSIFIED

SECURITY CLASSIFICATION OF THIS PAGE (When Data Entered)

19 REPORT DOCUMENTATION PAGE		READ INSTRUCTIONS BEFORE COMPLETING FORM
1. REPORT NUMBER AFAL TR-78-96	2. GOVT ACCESSION NO.	3. RECIPIENT'S CATALOG NUMBER
4. TITLE (and Subtitle) 6 ADVANCED ARCHIVAL MEMORY		5. TYPE OF REPORT & PERIOD COVERED Technical-Interim June 1, 1977-Dec. 31, 1977
7. AUTHOR(s) 10 C. G. Kirkpatrick, H. G. Parks, G. E. Possin, R. C. Raymond K. G. Vosburgh		6. PERFORMING ORG. REPORT NUMBER SRD-78-041
8. CONTRACT OR GRANT NUMBER(s) F33615-76-C-1322		9. PERFORMANCE ORGANIZATION NAME AND ADDRESS Corporate Research and Development General Electric Company Schenectady, New York 12301
11. CONTROLLING OFFICE NAME AND ADDRESS Air Force Avionics Laboratory (AFAL/DHR) Wright Patterson Air Force Base, Ohio 45433		10. PROGRAM ELEMENT, PROJECT, TASK AREA & WORK UNIT NUMBERS 31940101 ARPA Order No. 3194-5
14. MONITORING AGENCY NAME & ADDRESS (if different from Controlling Office) 9 Interim Technical rept. 1 Jun - 31 Dec 77		12. REPORT DATE July 1978
		13. NUMBER OF PAGES 314
		15. SECURITY CLASS. (if this report) Unclassified
		15a. DECLASSIFICATION/DOWNGRADING SCHEDULE 12 329P.
16. DISTRIBUTION STATEMENT (of this Report) Approved for public release, distribution unlimited. 16 3294 17 02		
17. DISTRIBUTION STATEMENT (of the abstract entered in Block 20, if different from Report)		
18. SUPPLEMENTARY NOTES *Prepared for Advanced Research Project Agency under ARPA Order No. 3194.		
19. KEY WORDS (Continue on reverse side if necessary and identify by block number) Computer Ion Implantation Memory Systems Alloy Junction Electron Optics Ion Optics		
20. ABSTRACT (Continue on reverse side if necessary and identify by block number) During this six-month period, work on the Advanced Archival Memory System has been concentrated on an ion-implantation based storage concept. Beam and target systems have been developed in parallel. Also, alternative data storage approaches have continued to be explored, and overall systems applications have been studied to provide guidance regarding the important technical parameters. The high current ion writing station appears feasible, and detailed		

406 617 79 03 16 055

20. ABSTRACT (cont.)

design and construction were begun. However, the ion implant target bit packing density appears to be limited to 0.25 microns under best conditions, and to about 0.40 microns with presently available ion sources. The system applications study indicated that, if the technical goals of the program are met, this system should have superior price/performance features to all identified competitors.

ACCESSION for		
NTIS	White Section <input checked="" type="checkbox"/>	
DDC	Buff Section <input type="checkbox"/>	
UNANNOUNCED	<input type="checkbox"/>	
JUSTIFICATION _____		
BY _____		
DISTRIBUTION/AVAILABILITY CODES		
Distr.	AVAIL.	and/or SPECIAL
A		

UNCLASSIFIED

PREFACE

The objective of this basic research program is to demonstrate the feasibility of an advanced archival memory system capable of permanent storage of data on solid planar media with 0.1 micron bit spacing and 10 MHz read and write rates. The eventual goal of this program is the construction of low-cost memory systems of 10^{15} - 10^{16} bit size with megabit per second data rates and fast access times. The data will be stored on semiconductor target plates by permanently altering the electrical conduction properties of a small region (bit site). This will be accomplished by striking the target with a high-current focused electron or ion probe. The bit pattern is read by injecting charge into the target using a focused electron probe, and the resultant current is amplified by a diode field structure integral to the target. The modulation of the current through this diode as the electron beam moves from one bit site to another provides the read signal.

This report covers the effort for the last seven months of 1977. It is the first report in Phase II of this program. Phase I was covered in Reports AFAL-TR-76-213, AFAL-TR-77-35, AFAL-TR-77-157, and AFAL-TR-77-202. In this reporting period effort on the program has been concentrated on an ion-implantation-based storage concept. Beam and target systems have been developed in parallel. Also, alternative data storage approaches have continued to be explored, and overall systems applications have been studied to

provide guidance regarding the important technical parameters.

The high current writing station appears feasible, and detailed design and construction were begun. However, the ion implant target bit packing density appears to be limited to 0.25 microns under best conditions, and to about 0.40 microns with presently available ion sources. The system applications study indicated that, if the technical goals of the program are met, this system should have superior price/performance features to all identified competitors.

TABLE OF CONTENTS

<u>Section</u>		<u>Page</u>
I	INTRODUCTION AND SUMMARY	1
	Ion Implant Target	2
	Ion Implant Column	12
	System Applications Study.	14
II	DEFECT TAILING IN ION IMPLANT TARGETS	17
	Model Predictions.	45
	Experimental Results	53
III	ION IMPLANT TARGET DESIGN AND PROCESSING.	73
IV	HIGH RESOLUTION WRITING INVESTIGATIONS.	83
V	ION IMPLANT TARGET - FOUR-POINT PROBE MEASUREMENTS.	113
	Determination of Damage Depth.	132
VI	OPTICAL DESIGN CONSIDERATIONS FOR THE ION WRITER.	137
	Background and General Optics Considerations .	137
	Investigation of Lens Properties	145
	60 kV Xe ⁺ , Ion Column Design	171
	30 kV Ar ⁺ , Ion Column Design	192
	Ion Beam Deflection Considerations	197
VII	SYSTEM APPLICATIONS STUDY	209
	Typical Configurations, Costs and Service Times.	246
APPENDIX A	263
APPENDIX B	273
APPENDIX C	293
REFERENCES.	313

LIST OF ILLUSTRATIONS

<u>Figure</u>		<u>Page</u>
1	Definition of Isolated Bit Gain Plot for the Determination of the Minimum Bit Spacing.	3
2	Normalized Gain for Isolated Bar and Dot Patterns vs Pattern Size	5
3	Normalized Gain vs Pattern Size for Isolated Dot Patterns.	6
4	Normalized Gain vs Pattern Size for Isolated Dot Patterns from Figure 2 Compared to Two-Dimensional Model	8
5	Normalized Damage Profiles Used for Model Calculations in Figures 6, 7, and 8.	9
6	Multiple Fluence Large Area Ion Writing Experiment Compared to One-dimensional Model	10
7	Comparison of Old and New Two-dimensional Model Calculations for the Normalized Gain vs Pattern Size for Isolated Unwritten and Written Dot Patterns.	11
8	Projected Bit Packing Density Using the Isolated Bit Gain Plot for Light ($5 \times 10^{11} \text{ cm}^{-2}$) and Heavy Writing (10^{13} cm^{-2}) Writing Conditions at Low Ion Energy (30 keV Ar ⁺)	13
9	Normalized Damage Density vs Normalized Depth from Brice Model ¹ Compared to the Gaussian Approximation Used in This Work.	20
10	Normalization Parameter E_D/R_p of Figure 9 vs Atomic Number of Projectile Ion in Si for Ion Energies of 10 keV and 100 keV.	21
11	Idealized Doping Profile of Flat Profile Targets Used for Defect Tailing Measurements.	23
12	Doping Profile of Sample P18A	24
13	Schematic Diagrams of Defect Tailing Measurement Principle Showing: (a) Cross-section of Flat Profile Diode Target and Carriers Generated by Incident Electron Beam of Energy E_B and (b) Typical Recombination Distribution Showing Definition of Threshold Recombination at Damage Depth T_D	26

LIST OF ILLUSTRATIONS (cont'd)

<u>Figure</u>		<u>Page</u>
14	Geometry for Solution of 1-dimensional Carrier Diffusion Equation for Damaged Layer of Depth T_D	27
15	Measured Collection Efficiency vs Beam Energy for Flat Profile Sample Set 107-5(1), -15(2, 4), -17(1) Written with 30 keV Ar ⁺ at Fluences as Indicated Compared to Abrupt Dead Layer Model (Figure 14)	29
16	Normalized Damage Profile (F_e/F) vs Depth (T_D) Derived from Figure 15.	31
17	Definition of Parameters Used to Describe Idealized Damage Profile with Defect Tailing.	33
18	Fit of Data from Figure 15 to Complete 1-dimensional Model ($T_N = 0.9$ micron) Using Defect Damage Distribution Corresponding to Solid Line in Figure 6 ($R_T = 0.5$, $B_5 = 3.7 \times 10^5$ cm ⁻¹ , $R_p = 0.03$ micron.	34
19	Comparison of 1-dimensional Model Calculations ($T_N = 0.9$ micron) of Collection Efficiency vs Beam Energy for Two Similar Damage Distributions with (—) $R_T = 1.0$ and (---) $R_T = 0.25$ Both with $B_5 = 3.7 \times 10^5$ cm ⁻¹ and $R_p = 0.03$ micron.	36
20	Normalized Damage Distribution vs Depth Measured, Using Flat Profile Targets 109-8 for 60 keV Xe ⁺	37
21	Normalized Damage Distribution vs Depth Measured Using Flat Profile Targets 110-14 for 110 keV Kr ⁺	38
22	Normalized Damage Distribution vs Depth Measured Using Flat Profile Targets 110-5 for 60 keV Ar ⁺	39
23	Fit to Complete 1-dimensional Model Using Damage Distribution Shown in Figure 11 Compared to Experimental Data on Writing Series 110-14 Written with 110 keV Kr ⁺ at Indicated Fluences.	40
24	Complete One-dimensional Model ($T_N = 0.9$ micron) Using Damage Distribution Shown in Figure 22 ($R_T = 1.0$, $B_5 = 3$	41
25	Schematic of Doping Profile for a Double n ⁺ np Target.	43

LIST OF ILLUSTRATIONS (cont'd)

<u>Figure</u>		<u>Page</u>
26	Idealized Doping Profile of a Typical n ⁺ np Target Fabricated by 100 keV As ⁺ Implantation at 10 ¹⁴ #/cm ² through 800 Å of Thermal SiO ₂ into a Flat Profile Target Previously Fabricated P ⁺ 9 Implantation and Diffusion.	44
27	Complete One-dimensional Model Calculation of Collection Efficiency vs Beam Energy with Maximum Recombination τ_p as a Parameter	46
28	Complete One-dimensional Model Calculation of Collection Efficiency vs Beam Energy with Maximum Recombination τ_p as a Parameter	47
29	Complete One-dimensional Model Calculation of Collection Efficiency vs Beam Energy with Maximum Recombination τ_p as a Parameter	48
30	Model Approximations to Heavy Damage Writing to a Depth T _D in the Limit of Very High Built-in Electric Fields (Model A) and No Fields (Model B)	49
31	Collection Efficiency vs Beam Energy for Model A (Figure 30)	50
32	Collection Efficiency vs Beam Energy for Model B (Figure 30) for a Junction Depth T _N = 0.8 Micron. .	51
33	Comparison of Model Calculation to Experimental Data.	55
34	Comparison of Model Calculation to Experimental Data.	56
35	Comparison of Model Calculation to Experimental Data.	57
36	Comparison of Model Calculation to Experimental Data.	59
37	Comparison of Two Best Fit Damage Profiles for 40 KeV Ar ⁺ Writing in Target Series 105-10	60
38	Comparison of Model Calculation to Experimental Data.	61

LIST OF ILLUSTRATIONS (cont'd)

<u>Figure</u>		<u>Page</u>
39	Doping Profile for Double As ⁺ Implantation and Low Temperature Anneal (900°C) Based on the Sum of a Measured Profile for 100 keV a As ⁺ at 10 ¹⁴ cm ⁻² (Figure 4 of 3rd quarter Phase I report)	64
40	Doping Profile for Double B ⁺ Implant (50 keV at 10 ¹⁵ cm ⁻² and 100 keV at 10 ¹⁴ cm ⁻²) Based on Crowder (*)	65
41	Comparison of Complete One-dimensional Model to Experimental Data from Target Series 109-23 (3,4) and 109-27(1) Written with 30 keV Ar ⁺ at Indicated Fluences	67
42	Comparison of Complete One-dimensional Model to Experimental Data from Target Series B2-9 Written with 30 keV Ar ⁺ at Indicated Fluences	68
43	Doping Profiles for Typical Planar Diodes -- n ⁺ p (dotted) and n ⁺ -n-p (solid)	74
44	Cross Section of Planar Diode Device as Processed with New Mask Set Z	76
45	Plot of C&W SEM Emission Current as a Function of Time Showing Beam Stability	85
46	Test Pattern Used to Produce Isolated Written and Unwritten Lines	86
47	Definition of Isolated Bit Gain Plot for the Determination of the Minimum Bit Spacing	94
48	Cross Section of an Ion Written Archival Target for the Case of (a) An Isolated Unwritten Area and (b) An Isolated Written Area	95
49	Calculated Collection Probability vs Depth for Typical Doping and Damage Profiles Shown in the Upper Part of the Figures for N ⁺ P Diode	97
50	Normalized Gain Versus Pattern Size Based on the Two-dimensional Resolution Model	99
51	Normalized Readout Gain at 1.5 and 2 keV for N ⁺ NP Sample 109-23(3) Written with Ar ⁺ at 30 keV and 3 x 10 ¹¹ cm ⁻²	100

LIST OF ILLUSTRATIONS (cont'd)

LIST OF ILLUSTRATIONS (cont'd)

<u>Figure</u>		<u>Page</u>
65	Conductivity vs Fluence Measurements for 40 kV Ar ⁺ Written n ⁺ p Targets Formed by 100 kV 5×10^{14} As ⁺ /cm ² Through 800 Å Oxide.	123
66	Conductivity vs Fluence Measurements for 30 kV Ar ⁺ and 50 kV Kr ⁺ Targets Formed by 80 kV 10^{12} p ⁺ /cm ² Through 1000 Å Oxide with Long High Temperature Drive [Targets 107-17(4), 107-5(4), 107-5(1), 107-5(2)].	124
67	Carrier Removal Rate vs Doping Density for the Sample Series of the Preceding Four Figures.	125
68	Conductivity vs Fluence Measurements for 40 kV and 60 kV Ar ⁺ Written nn ⁺ p Structures Formed by 100 kV 2×10^{14} As ⁺ /cm ² Through 800 Å Oxide, with the Diode Formed by 80 kV 10^{12} p ⁺ /cm Through 1000 Å with a Long High Temperature Drive.	126
69	Conductivity vs Fluence Measurements on 50 kV Kr ⁺ Written n ⁺ p Targets Formed by 100 kV 5×10^{14} As ⁺ /cm ² Through 800 Å Oxide.	127
70	Conductivity vs Fluence Measurements for 110 kV Kr ⁺ Written Targets Formed by 80 kV 10^{12} p ⁺ /cm ² Through 1000 Å Oxide with Long High Temperature Drive.	129
71	Conductivity vs Fluence Measurements for 60 kV Ar ⁺ Written n ⁺ p Targets Formed by 80 kV p ⁺ /cm Through 1000 Å Oxide with Long High Temperature Drive [Targets 110-5(3), 110-5(2), 110-5(1)]	130
72	Conductivity vs Fluence Measurements for 110 kV Kr ⁺ Written Targets Formed by 80 kV 10^{12} p ⁺ /cm ² Through 1000 Å Oxide with Long High Temperature Drive.	131
73	Idealized Two-layer Damage Model	133
74	Sheet Conductance vs Ion Fluence for Idealized Two-layer Model.	133
75	Phase I Ion Optics Column.	138
76	Gas Field Ionization Source Cross Section.	140
77	Cross Sections of Various Aperture and Cylinder Electrostatic Lenses	142

LIST OF ILLUSTRATIONS (cont'd)

<u>Figure</u>		<u>Page</u>
78	Parameter Definitions for the First Lens and Source.	146
79	Three Cylinder Einzel Lens.	147
80	Normalized Working Distance vs Lens Voltage Ratio for Three Cylinder Einzel Lens Cases.	151
81	Normalized Spherical Aberration Coefficient vs Lens Voltage Ratio for Three Cylinder Einzel Lens Cases.	152
82	Normalized Chromatic Aberration Coefficient vs Lens Voltage Ratio for Three Cylinder Einzel Lens Cases	153
83	Spherical Aberration Coefficient vs Lens Working Distance for Symmetrical and Asymmetrical Einzel Lenses.	158
84	Chromatic Aberration Coefficient vs Lens Working Distance for Symmetrical and Asymmetrical Einzel Lenses.	159
85	Three Cylinder Tripotential Lens.	161
86	Normalized Working Distance vs Lens Voltage Ratio for Three Cylinder Tripotential Lens Cases.	163
87	Normalized Spherical Aberration Coefficient vs Lens Voltage Ratio for Three Cylinder Tripotential Lenses.	164
88	Normalized Chromatic Aberration Coefficient vs Lens Voltage Ratio for Three Cylinder Tripotential Lenses.	165
89	Two Cylinder Immersion Lens	167
90	Normalized Working Distance vs Lens Voltage Ratio for Two Tube Immersion Lenses	168
91	Normalized Chromatic Aberration Coefficient vs Lens Voltage Ratio for Two Tube Immersion Lenses. .	169
92	Normalized Spherical Aberration Coefficient vs Lens Voltage Ratio for Two Tube Immersion Lenses. .	170
93	Typical Beam Current vs Spot Size Curve Showing Regions of Various Aberration Limits for a Two Lens Field Ion Source Column	177

LIST OF ILLUSTRATIONS (cont'd)

<u>Figure</u>		<u>Page</u>
94	Beam Current vs Spot Size for Xe^+ 60 kV Column with Various First and Final Lens Combinations	185
95	Three Aperture Einzel Lens.	187
96	Beam Current vs Spot Size for Xe^+ , 60 kV Ion Column with Three Aperture Final Lenses	190
97	Cross-sectional Diagram of Xe^+ 60 kV Ion Optics Design.	191
98	Beam Current vs Spot Size Curves for Various First and Final Lens Combinations, for an Ar^+ , 30 kV Design.	196
99	Cross-sectional Diagram of Ar^+ 30 kV Ion Optics Design.	198
100	Cross-sectional Diagram of Double Deflector Optics.	201
101	Uniform Field Model for Double Deflector.	202
102	Pre-lens Deflection of a Collimated Beam.	205
103	Two-level File System	210
104	Small plate AAM Plate	212
105	One Small-plate AAM Data Block.	214
106	Layout of Data Fields Within Small Plate AAM Block.	215
107	Line Format for Small-plate AAM	216
108	Small Plate AAM System Schematic.	217
109	Large-plate AAM Plate	220
110	One View on Large AAM Plate	222
111	Large-plate AAM Block Format.	223
112	Large-plate AAM Line Formats.	224
113	Large-plate AAM System Schematic.	225
114	Elements of the Tape-cartridge System	228
115	Partial Radial Section of Optical Disk Medium . . .	230

LIST OF ILLUSTRATIONS (cont'd)

<u>Figure</u>		<u>Page</u>
116	Schematic Diagram of Optical Disk Read/Write Assembly	232
117	Very Large Optical Disk File System	233
118	Optical Disk Read/Write Station	235
119	Library Application at Constant I/O Rate.	249
120	Library Application - Economy of Scale.	250
121	Library Application - Economy of Scale.	251
122	Library Application - Total File Size 2.002×10^{14} Bits.	253
123	Imagery Application - Constant I/O Rates.	254
124	Imagery Application - Economy of Scale.	255
125	Imagery Application - Economy of Scale.	256
126	Imagery Application - Total File Size 1.922×10^{14} Bits.	258
127	Time-sharing Application - Constant I/O Rates . . .	259
128	Time-sharing Application - Economy of Scale . . .	260
129	Time-sharing Application - Economy of Scale . . .	261
130	Time-sharing Application - Total File Size 1.939×10^{13} Bits	262
131	Layout of Target Segments on a Whole Si Wafer Is Shown	294
132	Diagram Indicates the Width of the Various Bands at the Target Edge.	295
133	Indicates the Area to Be Opened in the Thick Oxide for Boron Implant of the Channel Stopper.	296
134	Indicates the Area to Be Opened in the Thick Oxide for the n-Field Implant	297
135	Is Used to Clear the Oxide in the Field Through Which the Heavier Dose Field Implant Is Performed .	298

LIST OF ILLUSTRATIONS (cont'd)

<u>Figure</u>		<u>Page</u>
136	Is Used to Open Up the Field and Scribe Lanes. . .	299
137	Is Used to Pattern the Front Aluminum to Provide a Contact Pad.	300
138	Quadrant 3 Test Structure Layout Is Shown Indicating Bar Patterns for Writing Experiments. .	301
139	Is Used to Open Up Areas in the Resist for Ion Writing Experiments.	302
140	Is Used to Open Up Areas in the Resist for Ion Writing Experiments.	303
141	Is Used to Open Up Areas in the Resist for Ion Writing Experiments.	304
142	Is Used to Open Up Areas in the Resist for Ion Writing Experiments.	305
143	Indicates Written Areas of a Completed Writing Experiment	306
144	Is Used to Open Up a Resist Area for Ion Implant Writing Experiments.	307
145	Is Used to Open Up a Resist Area for Ion Implant Writing Experiments.	308
146	Is Used to Open Up a Resist Area for Ion Implant Writing Experiments.	309
147	Is Used to Open Up a Resist Area for Ion Implant Writing Experiments.	310
148	Test Pattern P2 Appears on Masks Z2 and Z3 to Open Up the Oxide for the Field Implants of Van der Pauw Patterns.	311
149	Test Pattern P2 on Mask Z4 Is Used to Pattern the Metallization for Contact Pads for Van der Pauw Patterns	312

LIST OF TABLES

<u>Table</u>		<u>Page</u>
1	BAR (n^+np) Process for Archival Planar Diode Substrates	78
2	NAR (N^+NP) Process for Archival Planar Diode Substrate	79
3	PAR (p^+pn) Process for Archival Planar Diode Substrates Produced Using New "Z" Mask Set.	81
4	Processing Archival Substrates for E-Beam Exposure and Ion Writing	89
5	Carrier Removal Rates for Ion Species and Energies Selected to Place Ion Distribution Peaks at Same Depths from Four Point Probe Data Based on Data in Figure 60 with $v = 200 \text{ cm/V-sec}$	128
6	Three Cylinder Einzel Lens Dimensions Normalized to Lens Radius D for Cases Studied.	149
7	Optical Properties for Best Lenses of Table 1	155
8	Normalized Optical Properties Three Cylinder Tripotential and Einzel Properties.	172
9	Normalized Optical Properties Two Cylinder Immersion Lens.	172
10	Properties of First Lens Candidates in cm	176
11	Optimum Magnification and Optimum Radius (cm) for a Symmetrical Three Cylinder Einzel Lens with First Lenses of Table 10.	183
12	Second Lens Dimensions on Optical Properties for Operation with First Lenses of Table 10	183
13	Normalized Lens Dimension for 3 Aperture Einzel Second Lens	188
14	Optical Properties for 3 Aperture Einzel Final Lenses for Operation with an Immersion First Lens S/D = 1.0	189
15	Normalized Optical Properties - Three Cylinder Tripotential Lenses for Ar^+ 30 kV First Lenses.	194
16	Normalized Optical Properties - Two Cylinder Immersion Lenses.	194

LIST OF TABLES

<u>Table</u>		<u>Page</u>
17	Properties of First Lens Candidates (in cm) Ar ⁺ , 30 kV Design.	194
18	Second Lens Radius and Optical Properties for Operation with First Lenses of Table 17	197
19	Major Features of the Applications Considered in This Study	239

SECTION I
INTRODUCTION AND SUMMARY

The results of the first seven months of Phase II of the Advanced Archival Memory Program being conducted by General Electric Corporate Research and Development are reported here. The objective of this phase of the program is the demonstration of an archival memory system capable of permanent storage of data on solid planar media with 0.1 micron bit spacing and 10 megabit write and read rates. The eventual goal of this program is the construction of low cost memory systems of 10^{15} - 10^{16} bit size with megabit/second data rates and fast access times.

The data are stored on semiconductor target plates by permanently altering the electrical conduction process of a small (bit size) region. This is accomplished by striking the target with a high-current focused electron or ion probe. The bit pattern is read by injecting charge into the target using a focused electron probe, and the resultant current is amplified by a diode field structure integral to the target. The modulation of the current through this diode as the electron beam moves from one bit site to another provides the read signal.

In this reporting period, work has primarily been directed to demonstrate an ion-implantation based system. This system was chosen at the end of Phase I as being the most promising, since it appeared capable of the required resolution and was the most highly developed of the methods considered. Parallel studies were conducted of the ion implant target and of the ion write column. In

addition, a study was made of the parametric characteristics of possible memory system applications. These three topics are discussed in this report. Also, studies have been continuing at a low level on systems which would use an electron beam for both reading and writing. The results of that work will be presented in subsequent reports.

ION IMPLANT TARGET

At the end of Phase I the status of the ion implant target development was: (i) Diode readout had been demonstrated from 0.1 micron isolated features. (ii) 0.25 micron bit spacing was projected with improvements down to 0.1 micron considered likely. (iii) The demonstration conditions for the high resolution writing were high ion fluence (10^{13} cm^{-2}) and high ion energy (145 keV Xe^+). From the data now available for gas ionization sources and ion column design parameters, these ion fluence and energy demonstration conditions are not obtainable for 10 Mbit/sec writing rates.

Figure 1 shows the format for both the theoretical and experimental studies. Two types of bit patterns are studied: The isolated written and unwritten areas. Each of these patterns can be described by a single feature or pattern size parameter W. In the case of focused ion beam writing, W is identified with the bit spacing. This identification is exact if the ion beam spot size and the bit spacing are each equal to W. For the Cr pattern experiments, W is the size of the hole in the Cr film or the size of the island of Cr. From the readout gain measurements, isolated bit gain plots are determined as indicated in Figure 1. The crossing point of these two curves serves as a good estimate of the

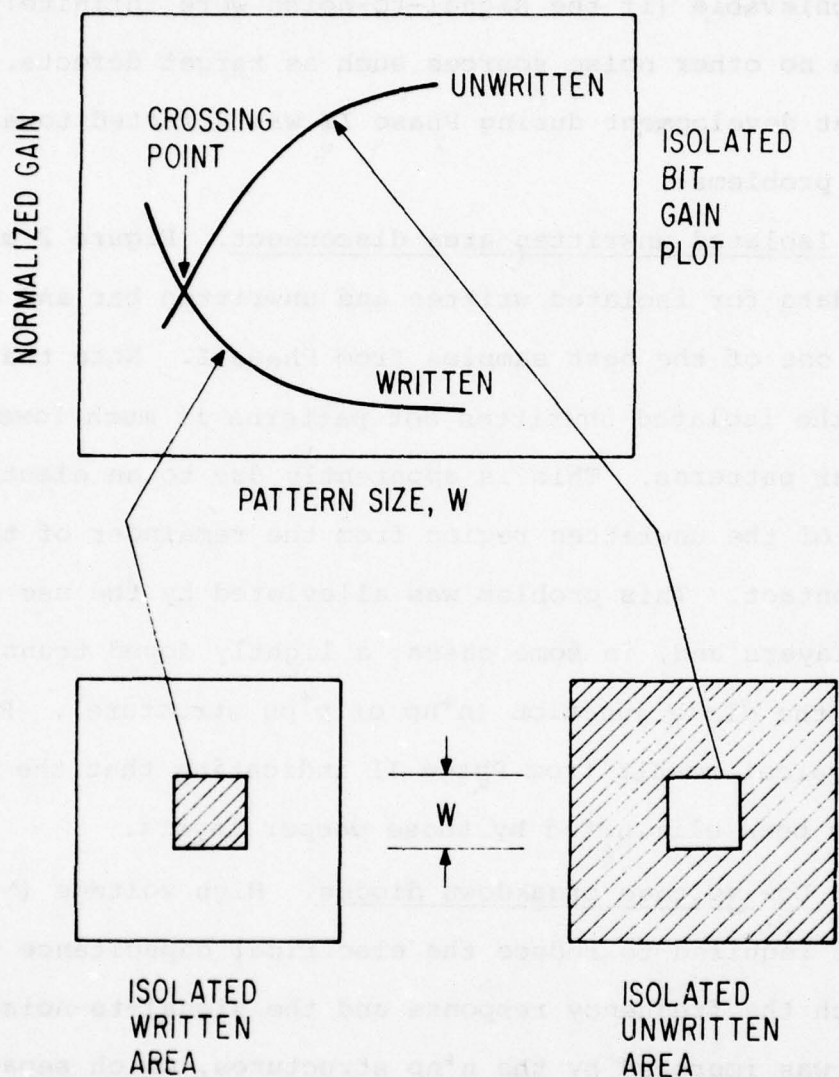


Figure 1. Definition of Isolated Bit Gain Plot for the Determination of the Minimum Bit Spacing

minimum achievable bit spacing. This can be seen from the following argument. If a simple level detection data recovery method were utilized, then the crossing point represents the minimum bit spacing achievable (if the signal-to-noise were infinite), and there were no other noise sources such as target defects.

Target development during Phase II was directed towards three principal problems:

(i) Isolated unwritten area disconnect. Figure 2 shows the measured data for isolated written and unwritten bar and dot patterns for one of the best samples from Phase I. Note that the gain for the isolated unwritten dot patterns is much lower than for the bar patterns. This is apparently due to an electrical isolation of the unwritten region from the remainder of the diode and the contact. This problem was alleviated by the use of deeper n⁺ or p⁺ layers and, in some cases, a lightly doped transition region to the diode junction (n⁺np or p⁺pn structure). Figure 3 shows a typical result from Phase II indicating that the disconnect effect has been eliminated by these deeper layers.

(ii) Low voltage breakdown diodes. High voltage (~100 V) diodes are required to reduce the electrical capacitance which degrades both the frequency response and the signal-to-noise. This situation was improved by the n⁺np structures, which separate the diode junction from the heavily damaged ion implanted region of the n⁺ or p⁺ layer. Diodes with breakdown voltages out to 100 volts have been achieved by this method.

(iii) Disagreement between theory and measurements. At the end of Phase I, the predicted target performance showed discrepancies

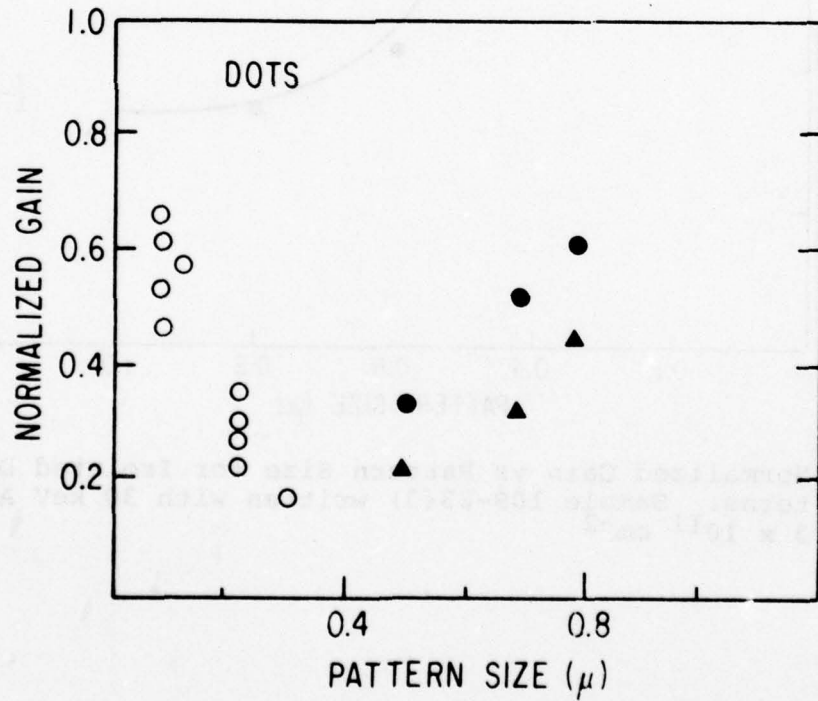
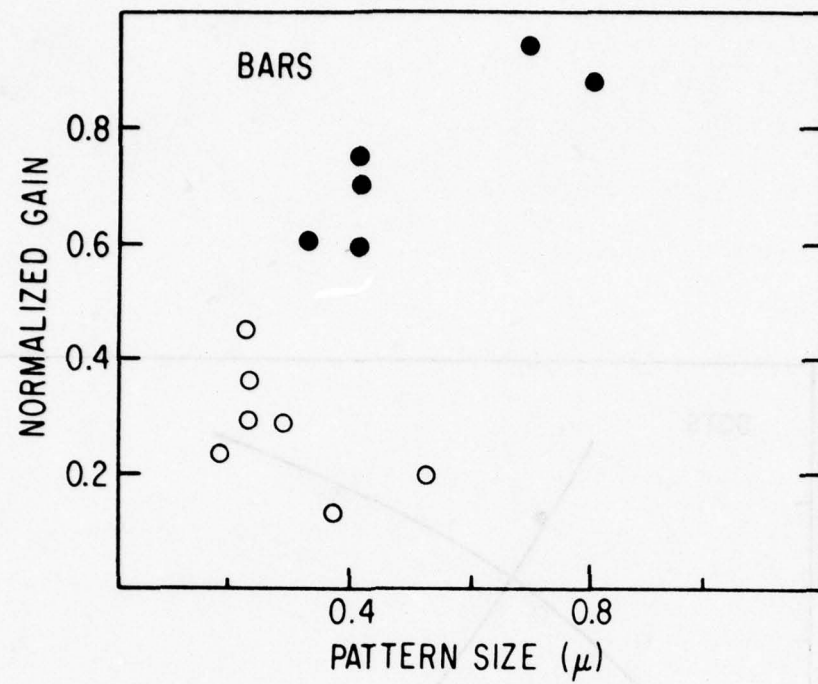


Figure 2. Normalized Gain for Isolated Bar and Dot Patterns vs Pattern Size. Target B13D written with 145 keV Xe^+ at 10^{13} cm^{-2} . Solid points are isolated unwritten and open points isolated written areas.

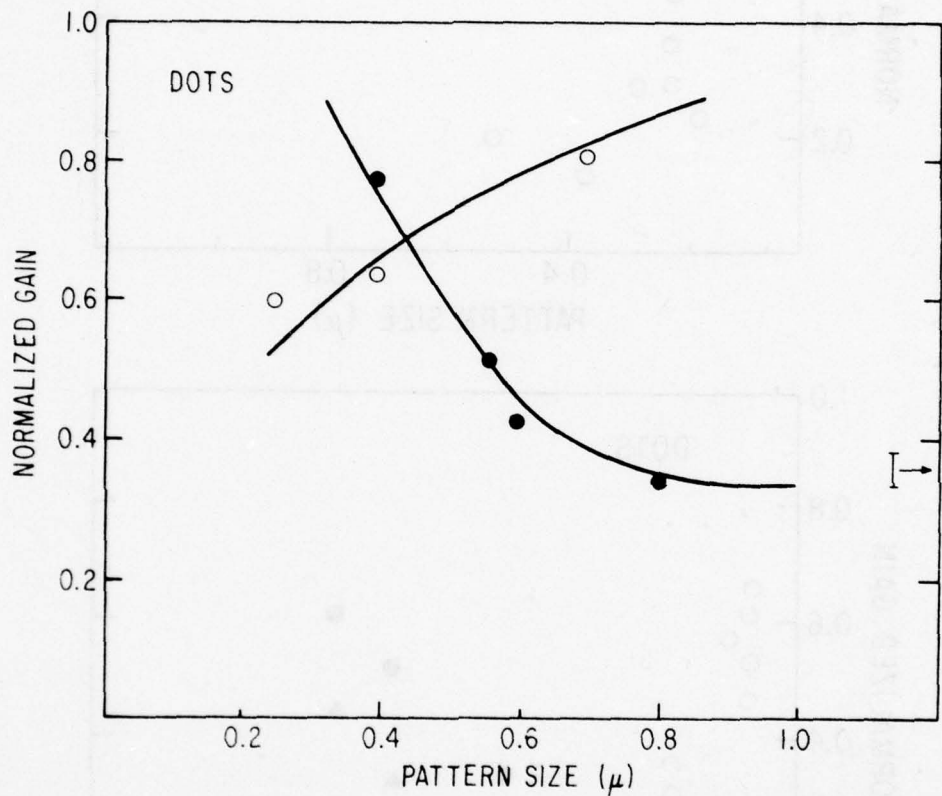


Figure 3. Normalized Gain vs Pattern Size for Isolated Dot Patterns. Sample 109-23(3) written with 30 keV Ar⁺ at $3 \times 10^{11} \text{ cm}^{-2}$

with the measured data for both isolated written and isolated unwritten areas (Figure 4). Because of the disconnection effect, the agreement between theory and measured results for the isolated unwritten areas was poor. When the disconnection effect was eliminated (as discussed above), however, a significant disagreement still remained.

The residual disagreement for the unwritten areas was shown to be due to defect tailing. Figure 5 shows three possible damage profiles due to the writing ion beam. For 40 keV Ar⁺, a gaussian profile as indicated by the dotted curve would be expected, based on the calculations of Brice. Brice calculated only the generation profile of the defects. Extensive experiments during Phase II demonstrated that this profile could not be used to explain the ion-writing behavior of the targets. Figure 6 shows three model fits of the 1-dimensional gain model developed during Phase I to a set of experimental writing data using the three damaged profiles shown in Figure 5. Only the solid curve labeled "best fit" provides a reasonable fit to the data. This type of damage profile may arise from the generation of defects according to the Brice calculation and subsequent diffusion of these defects from the damage tail. The effect of this "defect tailing" is to reduce the isolated unwritten gain as shown in Figure 7.

As is shown in Figure 4, the predicted normalized gain for isolated written areas is somewhat lower than the experimental data. The discrepancy may be due to anomalously large skirts on the spot probe of the SEM; the discrepancy could not be caused by defect tailing. These studies will be continued, since they are relevant to all electron-beam readout techniques.

The behavior has nothing to do with between-cell differences and thus reflects noise sources due to sensors. (For example, sensor noise is not related to distance between the two microphones and therefore cannot be removed by averaging.)

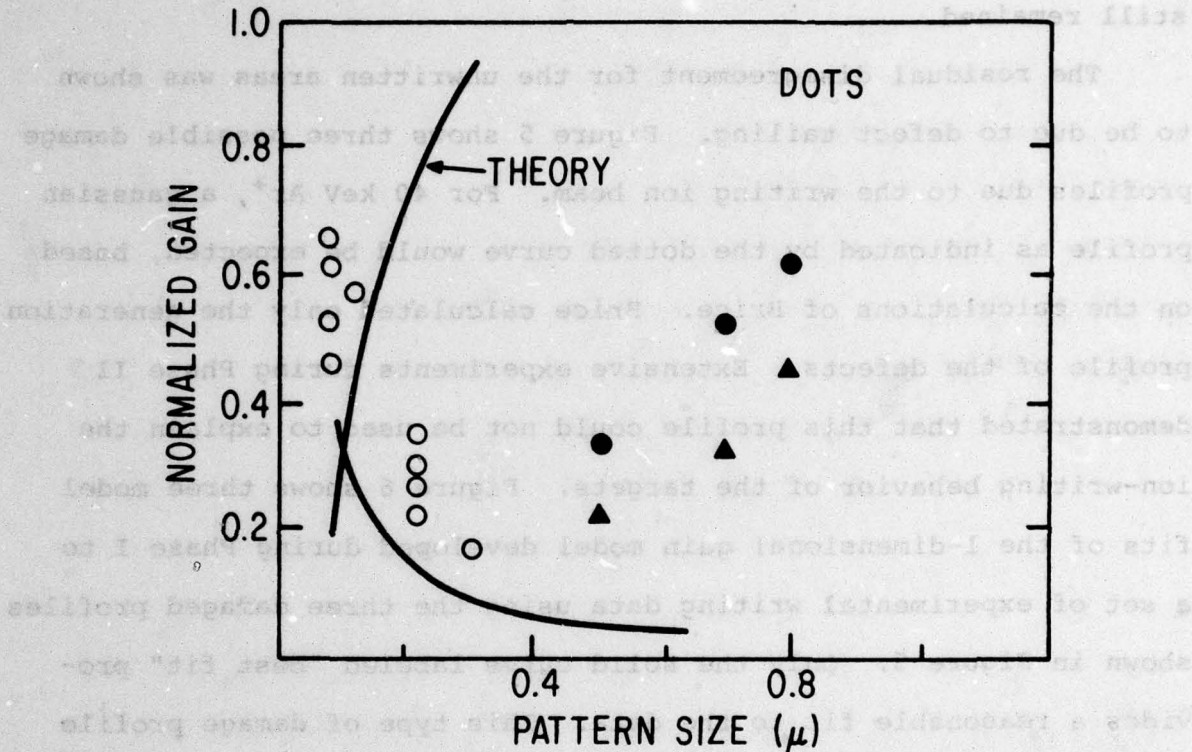


Figure 4. Normalized Gain vs Pattern Size for Isolated Dot Patterns from Figure 2 Compared to Two-dimensional Model.

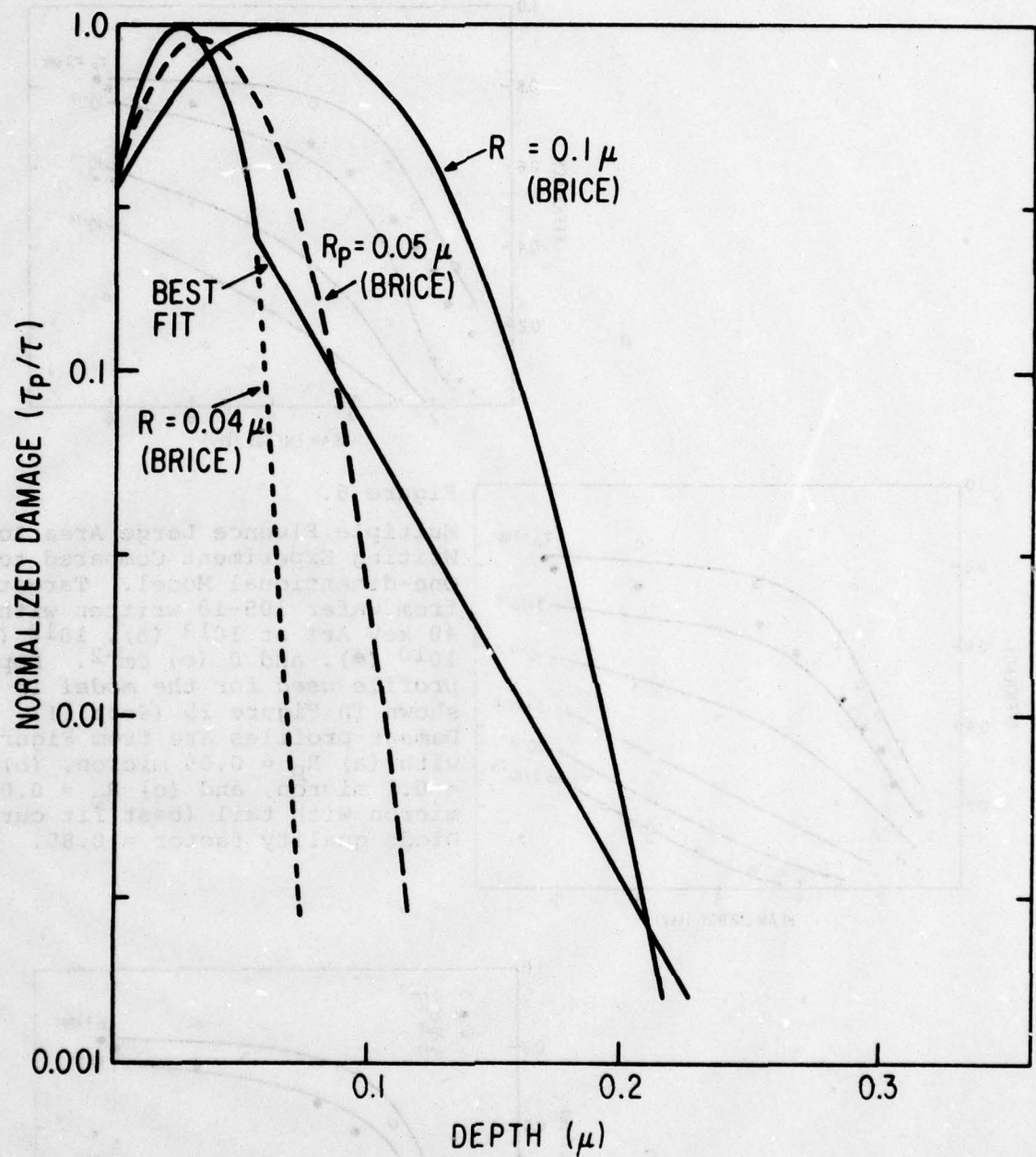


Figure 5. Normalized Damage Profiles Used for Model Calculations in Figures 6, 7, and 8. Solid curve labeled best fit is the measured damage tailing for 40 keV Ar^+ .

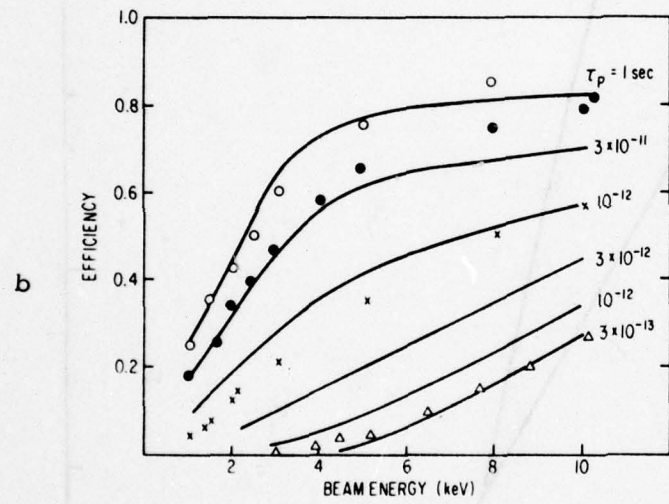
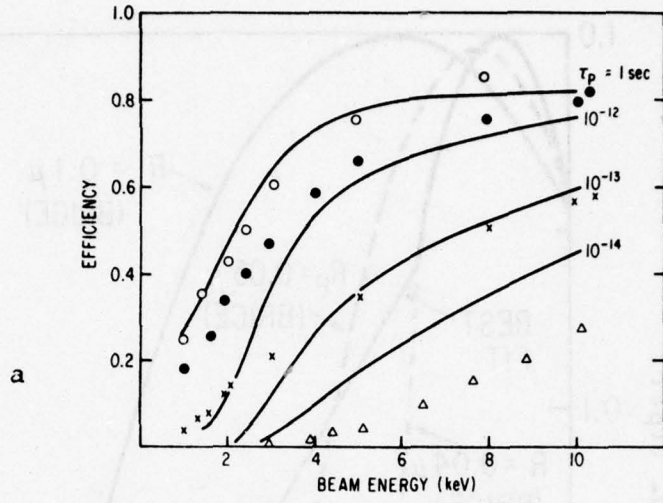
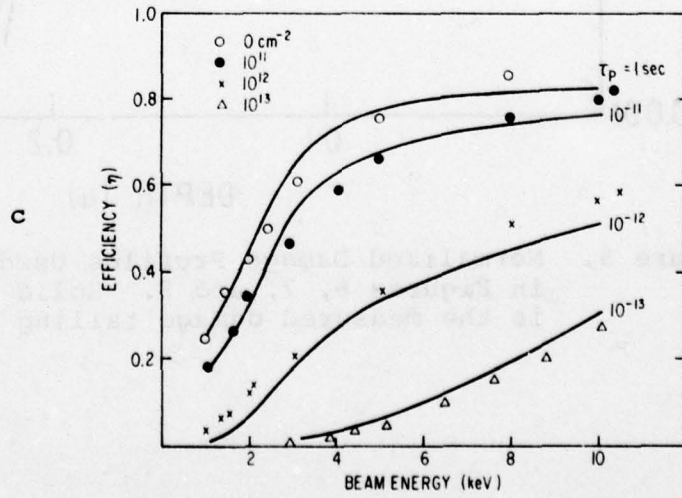


Figure 6.

Multiple Fluence Large Area Ion Writing Experiment Compared to One-dimensional Model. Targets from wafer 105-10 written with 40 keV Ar $^+$ at 10^{13} (Δ), 10^{12} (X), 10^{11} (\bullet), and 0 (\circ) cm $^{-2}$. Doping profile used for the model is as shown in Figure 25 (Sect II). Damage profiles are from Figure 5 with (a) $R_p = 0.05$ micron, (b) $R_p = 0.1$ micron, and (c) $R_p = 0.04$ micron with tail (best fit curve). Diode quality factor = 0.85.



not yet to yield accurate and reliable fits to such data sets. A standard fit gives a maximum fit factor (ratio of theory to data) which is less than unity, indicating that the theory does not fit the data well.

The new theory, however, provides a much better fit to the data.

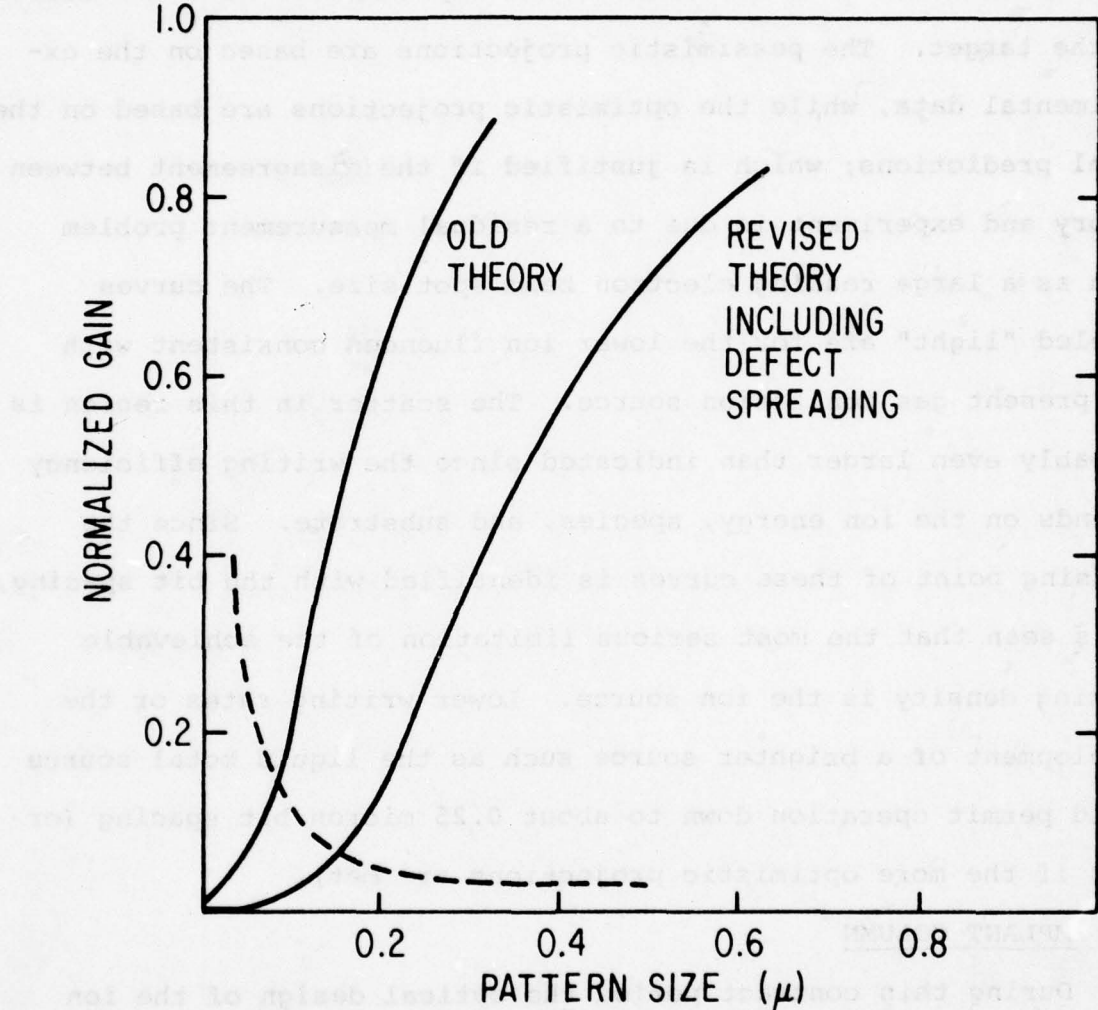


Figure 7. Comparison of Old and New Two-dimensional Model Calculations for the Normalized Gain vs Pattern Size for Isolated Unwritten and Written Dot Patterns. Revised theory includes the effect of defect tailing in depth and laterally under moderate writing conditions (~ 30 keV Ar^+ , $\sim 10^{13} \text{ cm}^{-2}$).

The status of the expected bit packing density for the ion written archival target is summarized in Figure 8, which is a plot of the isolated written and unwritten readout gain versus pattern size based on the most recent experimental data and modeling of the target. The pessimistic projections are based on the experimental data, while the optimistic projections are based on the model predictions; which is justified if the disagreement between theory and experiment is due to a residual measurement problem such as a large reading electron beam spot size. The curves labeled "light" are for the lower ion fluences consistent with the present gas ionization source. The scatter in this region is probably even larger than indicated since the writing efficiency depends on the ion energy, species, and substrate. Since the crossing point of these curves is identified with the bit spacing, it is seen that the most serious limitation of the achievable packing density is the ion source. Lower writing rates or the development of a brighter source such as the liquid metal source would permit operation down to about 0.25 micron bit spacing (or less if the more optimistic projections are met).

ION IMPLANT COLUMN

During this contract period the optical design of the ion writer has been completed using new ion gun parameters and target requirements. A method of comparing lenses and effectively optimizing lens and gun parameters for a maximum current density ion probe was developed. Applications of these techniques have resulted in two possible column designs. One is an Xe^+ ion column with 60 kV landing potential and capable of a 10 megabit writing

units not far off at radio end. However 4.0×10^{-3} to convert
pattern size per bit to average one bit length pattern vs bit size.
Simpler 1.0×10^{-3} to convert

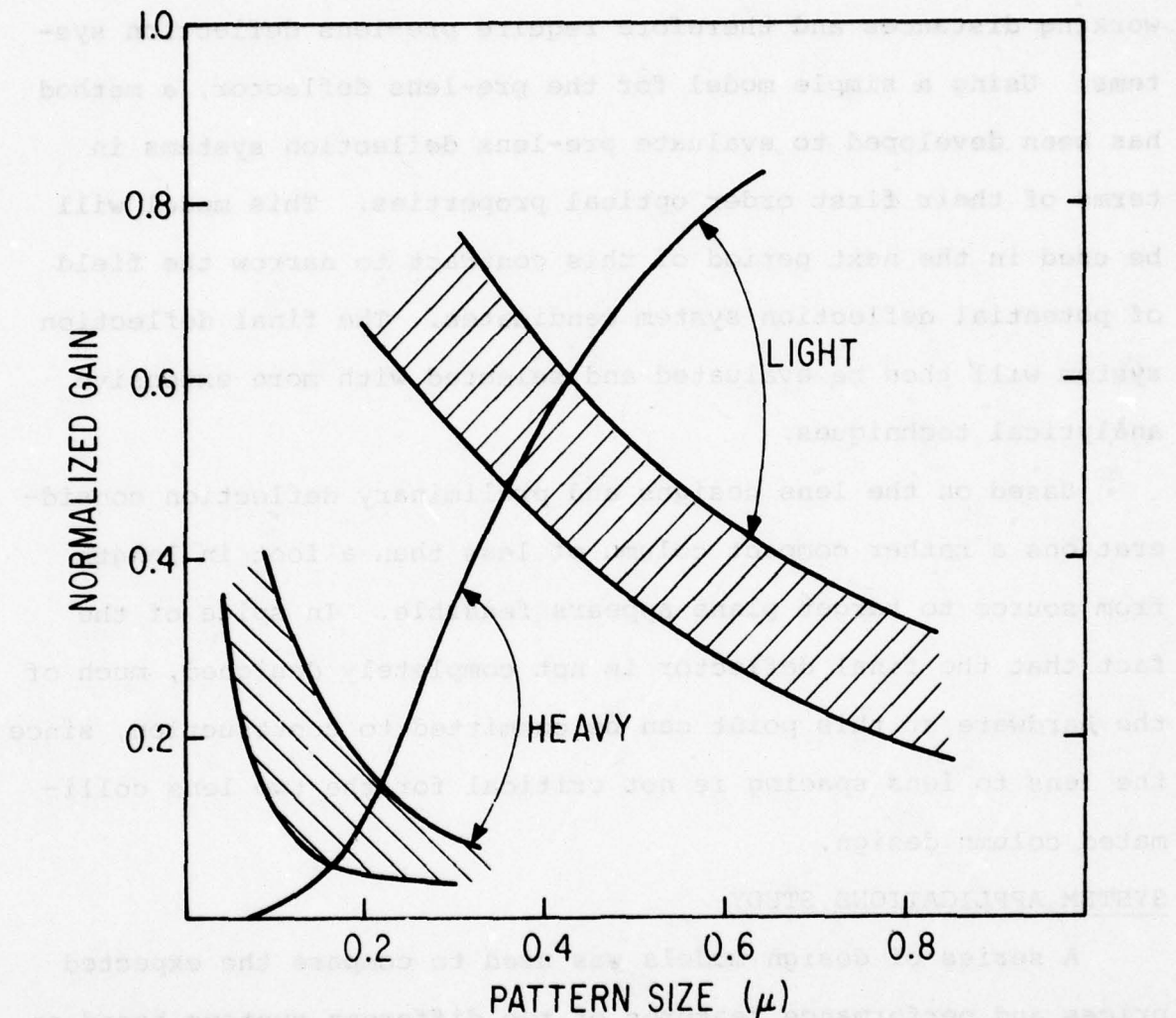


Figure 8. Projected Bit Packing Density Using the Isolated Bit Gain Plot for Light ($5 \times 10^{11} \text{ cm}^{-2}$) and Heavy Writing (10^{13} cm^{-2}) Writing Conditions at Low Ion Energy (30 keV Ar⁺)

fluence of 6.34×10^{11} ions/cm². The other is an Ar⁺ ion column with 30 kV landing potential and capable of a 10 megabit writing fluence of 3.73×10^{11} ions/cm².

Both column designs result in extremely short final lens working distances and therefore require pre-lens deflection systems. Using a simple model for the pre-lens deflector, a method has been developed to evaluate pre-lens deflection systems in terms of their first order optical properties. This model will be used in the next period of this contract to narrow the field of potential deflection system candidates. The final deflection system will then be evaluated and selected with more extensive analytical techniques.

Based on the lens designs and preliminary deflection considerations a rather compact column of less than a foot in length from source to target plane appears feasible. In spite of the fact that the final deflector is not completely designed, much of the hardware at this point can be committed to construction, since the lens to lens spacing is not critical for the two lens collimated column design.

SYSTEM APPLICATIONS STUDY

A series of design models was used to compare the expected prices and performance features of two different systems based on the GE Advanced Archival Memory (AAM) technology with a system based on optical disk media and a system based on magnetic tape cartridge media, as they might appear in 1985. The AAM models are not dependent on the physical mechanism for bit writing, i.e., they apply for either ion or electron writing methods.

Three models of application demands were postulated: (1) Image storage and processing; (2) time-sharing system with high access rate, and (3) library retrieval system. The results of the comparisons are dependent on the number of usable bits stored on the media plates. AAM systems with small (7×10^{10} bit) plates showed better price/performance features than tape-cartridge systems, and price/performance features comparable to those of optical disk systems for file sizes above about 10^{13} bits in all cases. AAM systems using the "large" (1.5×10^{12} -bit) media plates showed better price/performance features than all other systems for all applications at file sizes above 10^{13} bits.

In the report which follows, Sections II-V discuss the experimental and theoretical analysis of the bit density of the ion implant targets. Section VI presents the design of the ion write column optics, and Section VII gives the results of the applications study. Finally, three appendices give the details of the targets and their fabrication processes.

SECTION II

DEFECT TAILING IN ION IMPLANT TARGETS

Defect tailing was discovered during the first part of Phase II. Two different experimental techniques show that the defects generated by the writing ion beam in silicon diffuse about 0.1 microns in depth (and probably laterally) during or shortly after the writing process. Since these defects are responsible for the readout modulation of the target, this phenomenon affects the bit packing density limit of ion beam written archival targets. New target structures have been designed to achieve optimum performance in the presence of defect diffusion. These structures have been fabricated and evaluation of their performance is in progress. It is now estimated that defect diffusion will limit the bit spacing to 0.2 micron or 2.5×10^9 bits/cm².

A. Calculation of the Damage Depth Profile

We consider first the depth profile of the ion beam generated defects. When a high energy ion is stopped by a substrate, energy is lost through two processes: nuclear scattering and electronic scattering. Only nuclear scattering produces damage (defects) through the displacement of the substrate atoms. In the present analysis, it is assumed that the distribution of generated defects is equivalent to the distribution of the energy lost to nuclear scattering events. This is a simplification for several reasons. First, the types of nuclear scattering events that occur near the surface are different from those that occur deeper inside the sample, since the average ion energy is larger near the surface. Hence different types of defects and a different production rate

might be expected near the surface. Second, materials-related effects, such as the interaction of the defects with the sample surface and with chemical impurities or defects, may vary as a function of depth. At higher ion fluences, interactions with other defects will also be important.

The distribution of incident ion energy into nuclear scattering events as a function of depth has been calculated by Brice [1]. The distribution of the incident ions as a function of depth and energy is first constructed. This is then integrated to give energy loss distributions. For low ion energies, this model may be improved by including the effects of recoil silicon atoms, which produce damage at some distance from their point of generation. At low incident ion energies the range of these secondary ions is a significant fraction of the range of the incident ion. For example, for Sb ions incident on silicon at 100 keV, the projected range R_p of the Sb is 450 Å, while the average projected range of the recoil Si ions generated near the surface is 180 Å. Brice includes this recoil correction by incorporating average moments of the silicon recoil damage in the integrals for the damage distribution.

Using this method Brice has calculated the damage density Q_b for the common dopant ions in silicon (B, P, Sb, and As) [1]. For atomic numbers in the range of 15 to 51 and energies in the range 10 to 100 keV these results can be well approximated by a gaussian:

$$\exp \left[-\left(\frac{z-d_p}{\sigma_p} \right)^2 \right] \quad d_p = 0.65 R_p \quad (1)$$
$$\sigma_p = 0.6 R_p$$

Figure 9 compares this gaussian to several results from Brice. The fit is quite good in the regions of present interest, although at higher energies, especially for the low-Z ions, the damage density is far from gaussian. In Figure 10, the normalized damage density $Q_0 R_p/E_0$ is plotted against the normalization constant (E_D/R_p) , where E_D is the total energy deposited into damage). E_D/R_p is approximately independent of ion energy over wide ranges for any incident ion. Figure 10 shows the dependence of E_D/R_p on incident ion atomic number (Z) for a silicon substrate for several ion energies, which may be used for comparing the expected defect generation rates for different writing ions and energies. Because designs for ion written archival target use fixed damage writing depths, it is more relevant to plot E_D/R_p for constant R_p . Since the energy dependence is small these curves are very similar to Figure 10. Such a plot is shown in Figure 62 of Section V.

B. Measurement of Defect Tailing in Flat Profile Targets

The writing ion beam produces defects over its entire path. The maximum damage rate will occur at a depth $\sim 0.6 R_p$ where R_p is the mean writing ion range, as discussed in detail below. The modulation of the readout signal from the target depends on the increased carrier recombination caused by these generated defects. If the defects move or diffuse after their production, then the region of high recombination rate will be larger than expected. While this effect was first observed with archival target structures, the interpretation and analysis is simpler for some later experiments done on flat profile diodes. Hence these experiments will be discussed first.

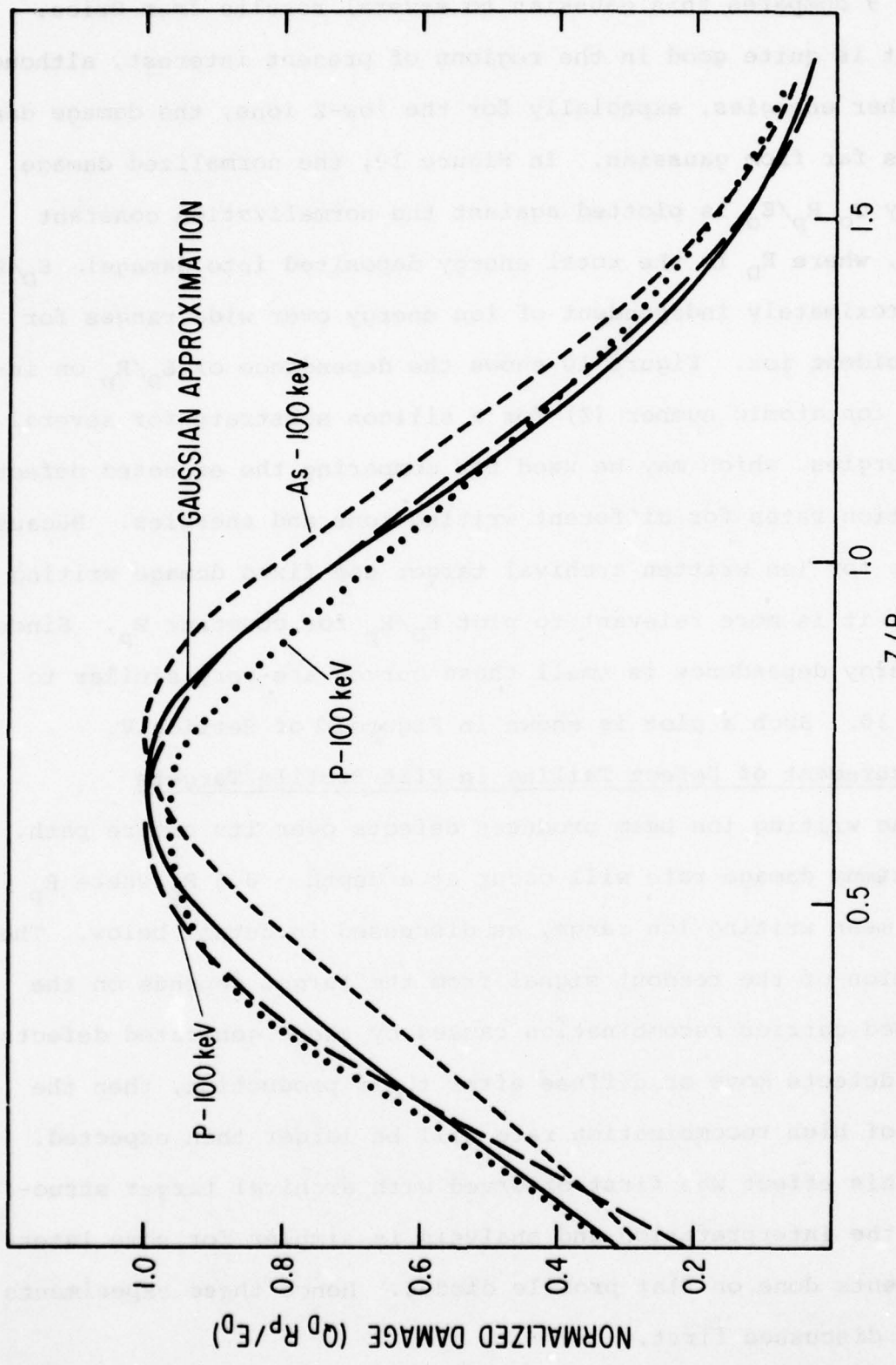


Figure 9. Normalized Damage Density vs Normalized Depth from Brice Model¹ Compared to the Gaussian Approximation Used in this Work

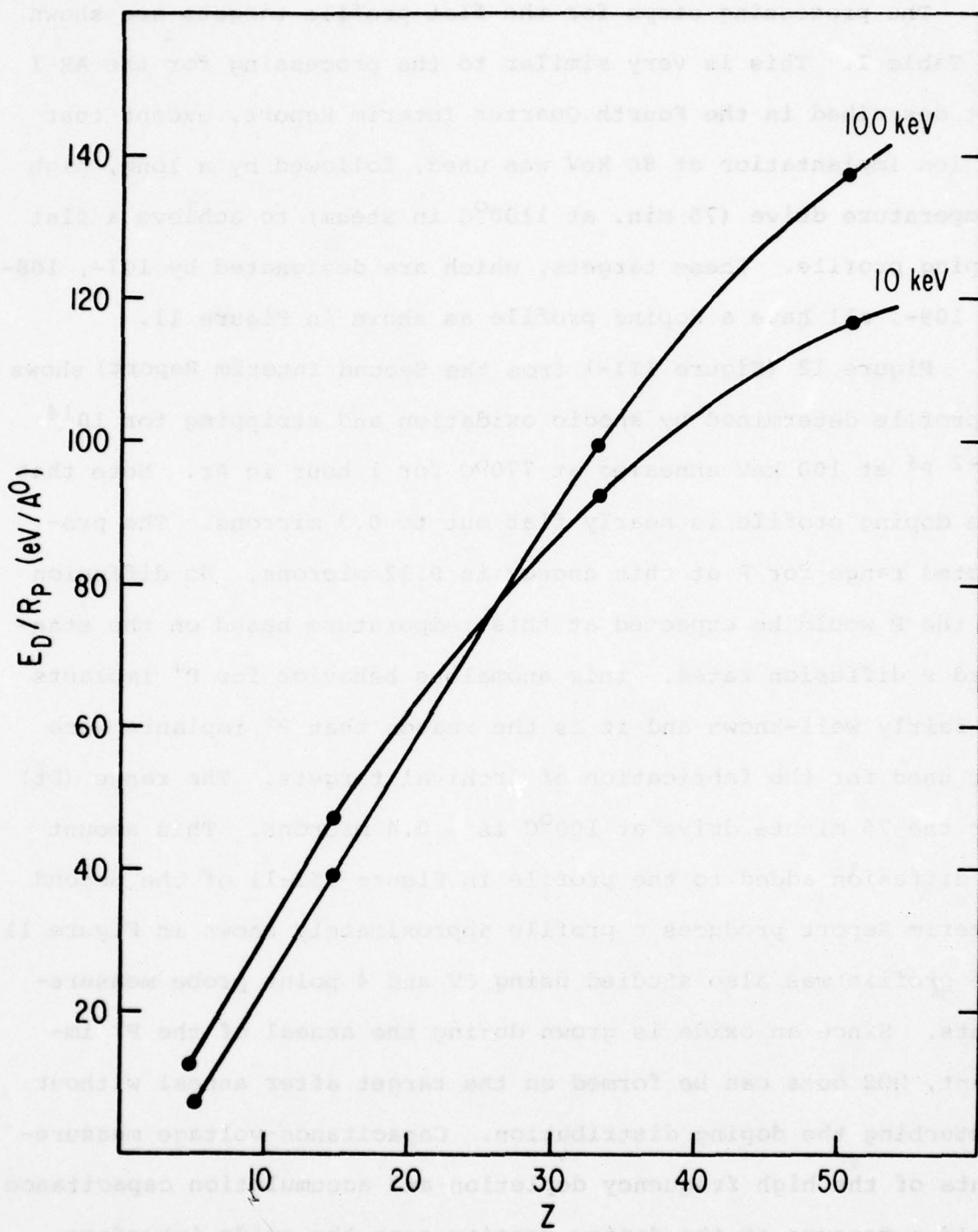


Figure 10. Normalization Parameter E_D/R_P of Figure 9 vs Atomic Number of Projectile Ion in Si for Ion Energies of 10 keV and 100 keV

The processing steps for the flat profile targets are shown in Table I. This is very similar to the processing for the AR-1 lot described in the Fourth Quarter Interim Report, except that P^+ ion implantation at 80 keV was used, followed by a long, high temperature drive (75 min. at $1100^\circ C$ in steam) to achieve a flat doping profile. These targets, which are designated by 107-, 108-, or 109-, all have a doping profile as shown in Figure 11.

Figure 12 (Figure III-1 from the Second Interim Report) shows a profile determined by anodic oxidation and stripping for $10^{14} \text{ cm}^{-2} P^+$ at 100 keV annealed at $770^\circ C$ for 1 hour in Ar. Note that the doping profile is nearly flat out to 0.3 microns. The projected range for P at this energy is 0.12 microns. No diffusion of the P would be expected at this temperature based on the standard P diffusion rates. This anomalous behavior for P^+ implants is fairly well-known and it is the reason that P^+ implants were not used for the fabrication of Archival targets. The range (D_t) for the 75 minute drive at $100^\circ C$ is ~ 0.4 microns. This amount of diffusion added to the profile in Figure III-11 of the Second Interim Report produces a profile approximately shown in Figure 11. The profile was also studied using CV and 4 point probe measurements. Since an oxide is grown during the anneal of the P^+ implant, MOS dots can be formed on the target after anneal without disturbing the doping distribution. Capacitance-voltage measurements of the high frequency depletion and accumulation capacitance yield a measure of the doping density near the oxide interface. Measurements of this type give doping densities near the surface

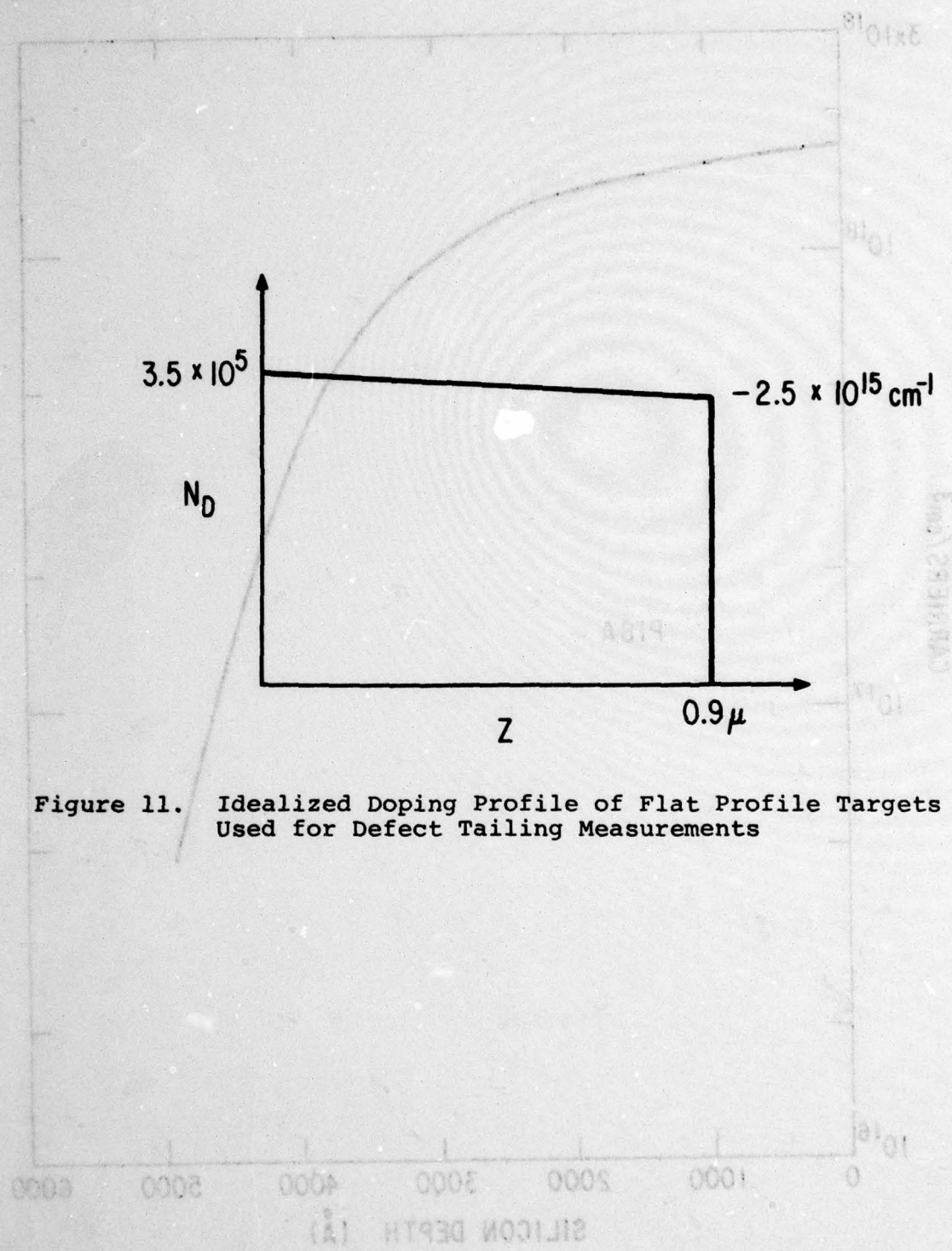


Figure 11. Idealized Doping Profile of Flat Profile Targets Used for Defect Tailing Measurements

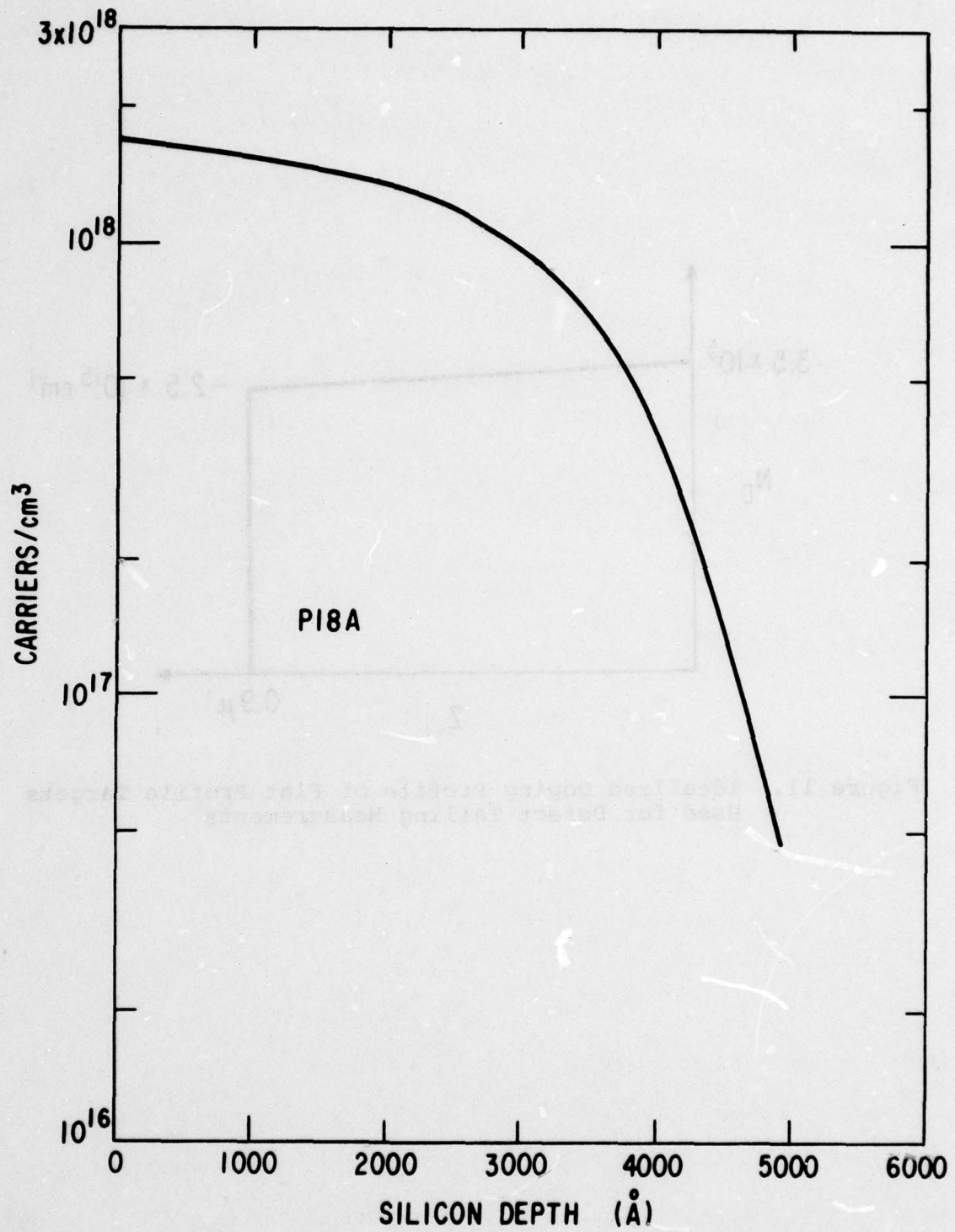


Figure 12. Doping Profile of Sample P18A. $<111>$ 400 Ω cm Si wafer implanted with 100 KeV p⁺ at 10^{14} cm^{-2} and annealed for 1 hour at 770 °C for 1 hour.

for these targets of $3.5 \times 10^{15} \text{ cm}^3$. Four point probe measurements of the sheet resistance of the entire P layer yield $22,200 \Omega/\square$. These data can be fit by an approximately rectangular doping distribution of $3 \times 10^{15} \text{ cm}^{-3}$ 0.8 microns deep in agreement with Figure 11.

Electron beam measurements of the junction depth, as described later in this section, yield a junction depth of 0.9 microns, again in good agreement with Figure 11.

A cross section of a flat profile target after ion beam writing is shown in Figure 13. Since the doping profile in the n-layer is nearly flat, the modeling of the motion of the electron-beam-generated carriers is less complex than for archival type targets. A schematic damage distribution due to the writing ion beam is shown in the lower part of the figure. Damage is represented by $1/\tau$, where τ is the local lifetime in the material. In the simplest model τ_{al}/N_T where N_T is the defect density. The actual $1/\tau$ distribution can be approximated by the box distribution shown in Figure 13 where T_D is the depth $\tau = \tau_T$. τ_T is a threshold recombination which is the recombination level that has a significant effect on the output gain from the target. As discussed in a later section $\tau_T \approx T_D^2/2.5D$. The effect of the recombination distribution shown by the dotted line on the target gain can be calculated using the model shown in Figure 14. Here the region for $z > T_D$ is completely dead, i.e. all carriers generated in this region recombine and are lost to the diode signal. An interface at $z = T_D$ is inserted with a recombination velocity $S_v = 0.75 \times 10^7 \text{ cm/sec}$ which is the maximum rate at which carriers can be

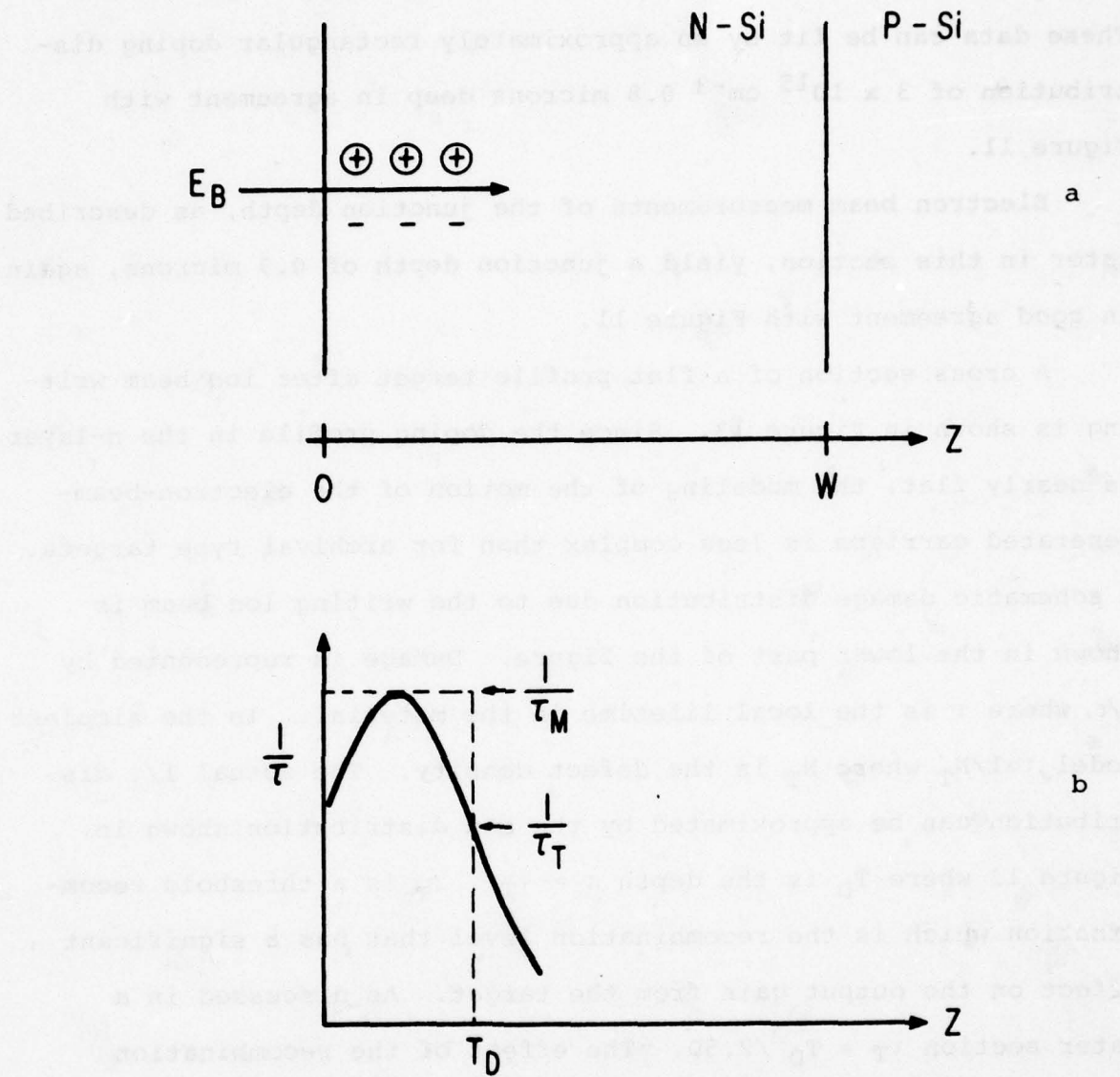


Figure 13. Schematic Diagrams of Defect Tailing Measurement Principle Showing: (a) Cross-section of Flat Profile Diode Target and Carriers Generated by Incident Electron Beam of Energy E_B and (b) Typical Recombination Distribution Showing Definition of Threshold Recombination at Damage Depth T_D

(1) $\frac{d^2V}{dx^2} = 0$ $\Rightarrow V = C_1x + C_2$
 $V = C_1x + C_2$ $\Rightarrow C_1 = 0$ $\Rightarrow V = C_2$

$$(2) \quad \frac{(C_1 - C_2)}{W} \cdot \frac{V^2}{D} + 1 = (C_1 - C_2) \cdot \frac{V^2}{D} + 1$$

$$\frac{W - 1}{W} = (C_1 - C_2) \cdot \frac{V^2}{D}$$

$$W - 1 = (C_1 - C_2) \cdot \frac{V^2}{D}$$

$$W - 1 = (0.8) \cdot \frac{V^2}{D}$$

$$W - 1 = (0.8) \cdot \frac{V^2}{0.0001}$$

$$W - 1 = 8V^2$$

$$W = 1 + 8V^2$$

$$W = 1 + 8(0.75 \times 10^7)^2$$

$$W = 1 + 8(5.625 \times 10^{14})$$

$$W = 1 + 45 \times 10^{14}$$

$$W = 1 + 4.5 \times 10^{15}$$

$$W = 4.5 \times 10^{15} \text{ cm}$$

Depois de se obter o resultado da equação (2), é necessário determinar a constante de integração C_2 .

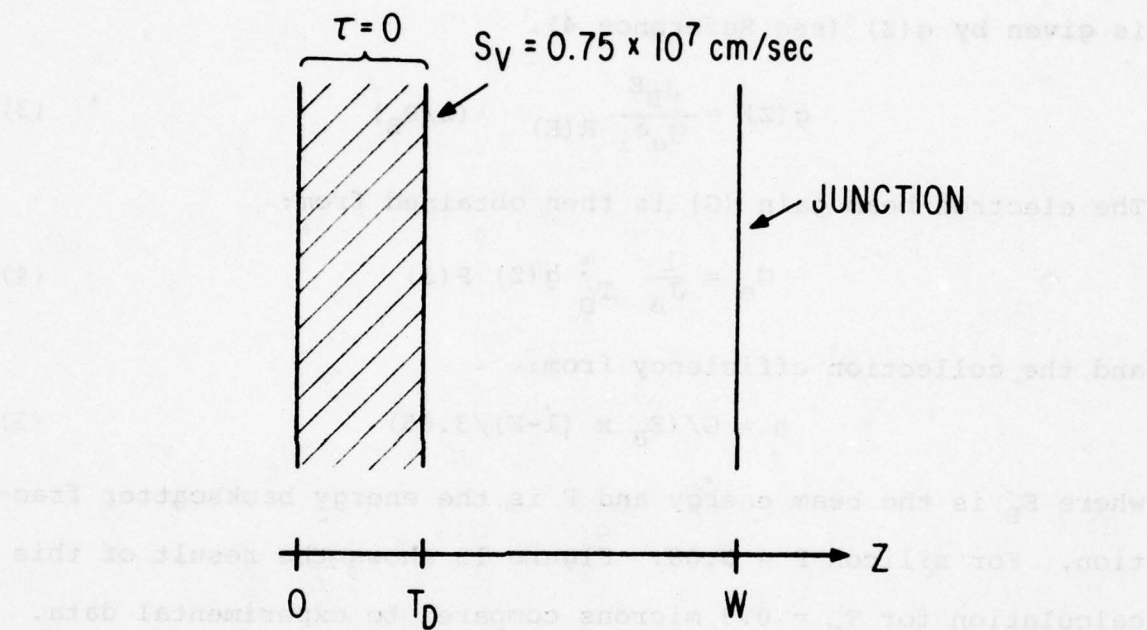


Figure 14. Geometry for Solution of 1-dimensional Carrier Diffusion Equation for Damaged Layer of Depth T_D

collected by a carrier sink such as the high recombination region.[3]

The diffusion equation for the motion of excess minority carriers can be solved. The collection probability $P(z_0)$ is given by:

$$P(z_0) = \frac{1 + \frac{S_v}{D} (z_0 - T_D)}{1 + \frac{S_v}{D} (W - T_D)} \quad T_D < z < W \quad P(z_0) = 0 \quad z < T_D \quad P(z_0) = 1 \quad z > W \quad (2)$$

The distribution of electron beam generated carriers in the target is given by $g(z)$ (see Reference 4).

$$g(z) = \frac{J_B E}{q_e e_i R(E)} \lambda(z/R_E) \quad (3)$$

The electron beam gain (G) is then obtained from:

$$G_e = \frac{1}{J_B} \int_{T_D}^{\infty} g(z) P(z) \quad (4)$$

and the collection efficiency from:

$$\eta = G / (E_B \times (1-F)/3.65) \quad (5)$$

where E_B is the beam energy and F is the energy backscatter fraction. For silicon $F = 0.08$. Figure 15 shows the result of this calculation for $T_N = 0.9$ microns compared to experimental data. The sets of points correspond to different 30 keV Ar^+ ion writing fluences on flat profile targets from group 107. Note that the fit is good despite the approximations made in the recombination distribution. From this comparison to the model, T_D can be determined for each writing ion fluence. Assuming that the shape of the recombination distribution does not change with ion fluence (F_s), i.e.

$$1/\tau = f(z) F_I, \quad (6)$$

$$\tau_M f(T_{D1}) = F_{II}^{-1} \quad (7)$$

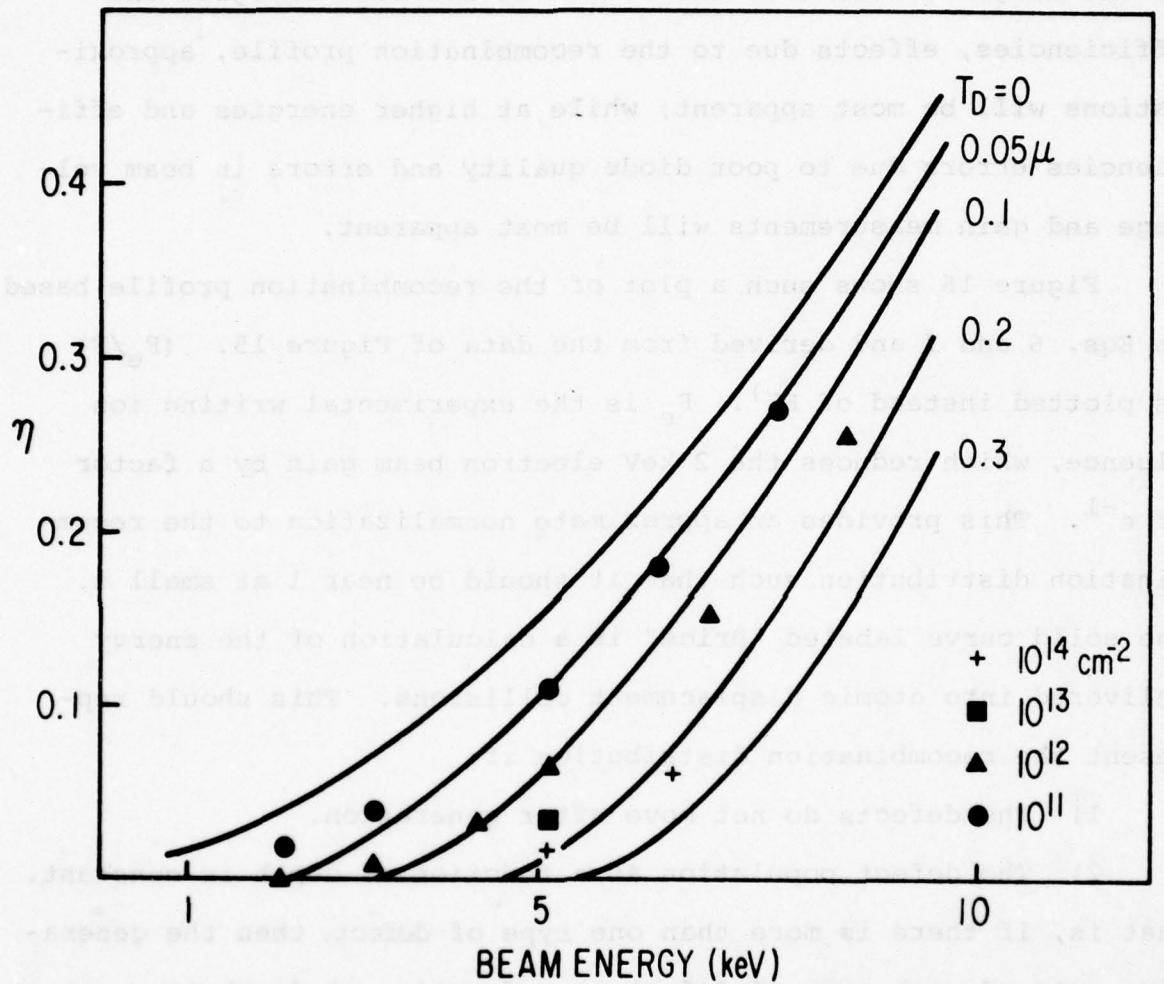


Figure 15. Measured Collection Efficiency vs Beam Energy for Flat Profile Sample Set 107-5(1), -15(2, 4), -17(1) Written with 30 keV Ar⁺ at Fluences as Indicated Compared to Abrupt Dead Layer Model (Figure 14)

where T_{D1} is the best-fit dead layer thickness for writing ion fluence F_{I1} from a plot such as Figure 15. Generally the best results should be obtained if T_D is determined for efficiencies in the range between 0.05 and 0.15. At low beam energies and efficiencies, effects due to the recombination profile, approximations will be most apparent; while at higher energies and efficiencies errors due to poor diode quality and errors in beam voltage and gain measurements will be most apparent.

Figure 16 shows such a plot of the recombination profile based on Eqs. 6 and 7 and derived from the data of Figure 15. (F_e/F) is plotted instead of F^{-1} . F_e is the experimental writing ion fluence, which reduces the 2 keV electron beam gain by a factor of e^{-1} . This provides an approximate normalization to the recombination distribution such that it should be near 1 at small z . The solid curve labeled "Brice" is a calculation of the energy delivered into atomic displacement collisions. This should represent the recombination distribution if:

- 1) The defects do not move after generation.
- 2) The defect population as a function of depth is constant.

That is, if there is more than one type of defect, then the generation rate of each type of defect as a function of depth is constant.

- 3) There are no saturation effects (e.g. change in the Fermi level due to carrier trapping at some defects) which would invalidate the approximation $1/\tau_d \propto$ defect density.

The relative normalization of the Brice model and the measured recombination profile is somewhat arbitrary, although Figure 16 should be approximately correct. The result of Figure 16 is modeled

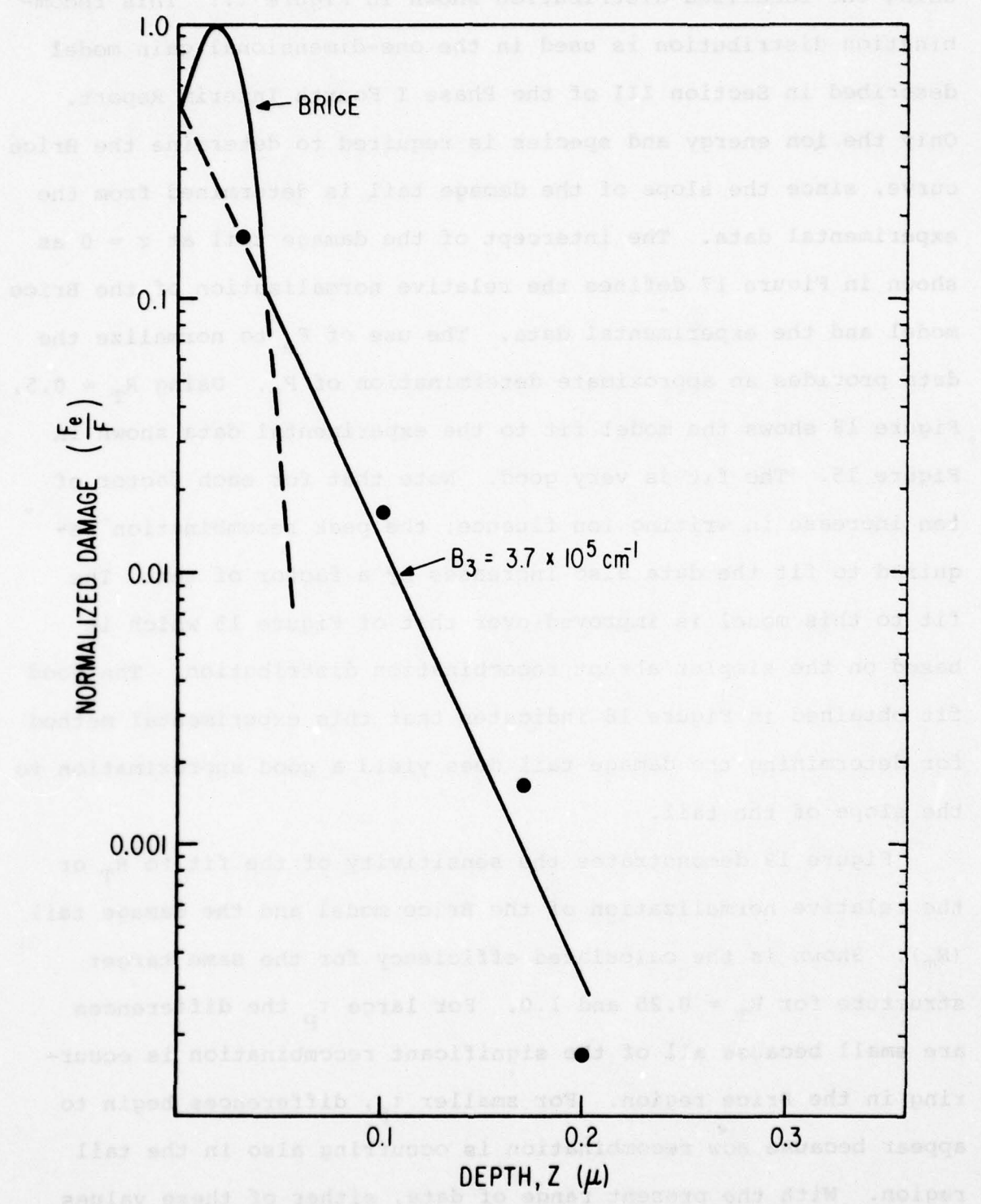


Figure 16. Normalized Damage Profile (F_e/F) vs Depth (T_D)
Derived from Figure 15. $F_e = 1.7 \times 10^{10} \text{ cm}^{-2}$

using the idealized distribution shown in Figure 17. This recombination distribution is used in the one-dimensional gain model described in Section III of the Phase I Fourth Interim Report. Only the ion energy and species is required to determine the Brice curve, since the slope of the damage tail is determined from the experimental data. The intercept of the damage tail at $z = 0$ as shown in Figure 17 defines the relative normalization of the Brice model and the experimental data. The use of F_e to normalize the data provides an approximate determination of R_T . Using $R_T = 0.5$, Figure 18 shows the model fit to the experimental data shown in Figure 15. The fit is very good. Note that for each factor of ten increase in writing ion fluence, the peak recombination required to fit the data also increases by a factor of ten. The fit to this model is improved over that of Figure 15 which is based on the simpler abrupt recombination distribution. The good fit obtained in Figure 18 indicates that this experimental method for determining the damage tail does yield a good approximation to the slope of the tail.

Figure 19 demonstrates the sensitivity of the fit to R_T or the relative normalization of the Brice model and the damage tail (R_T). Shown is the calculated efficiency for the same target structure for $R_T = 0.25$ and 1.0 . For large τ_p the differences are small because all of the significant recombination is occurring in the Brice region. For smaller τ_p , differences begin to appear because now recombination is occurring also in the tail region. With the present range of data, either of these values of R_T fit equally well. Hence the value of R_T should be considered

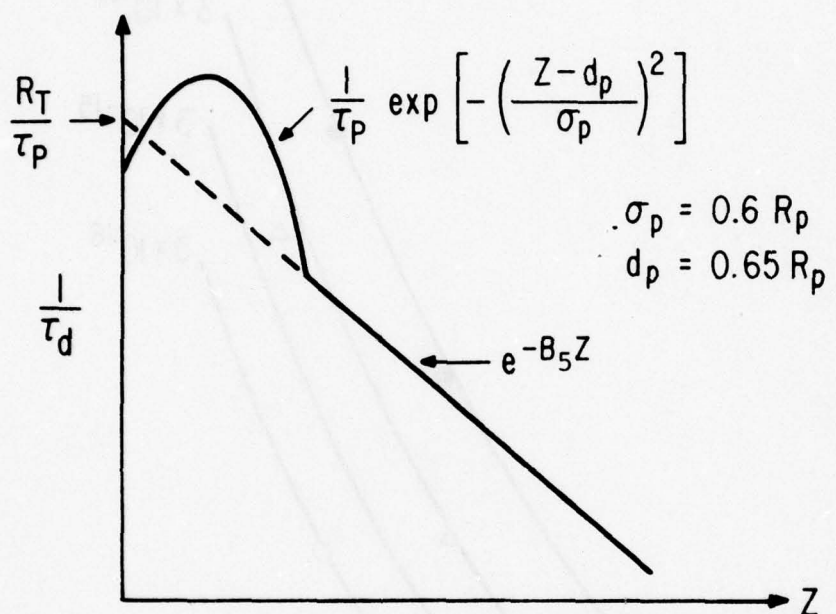


Figure 17. Definition of Parameters Used to Describe Idealized Damage Profile with Defect Tailing

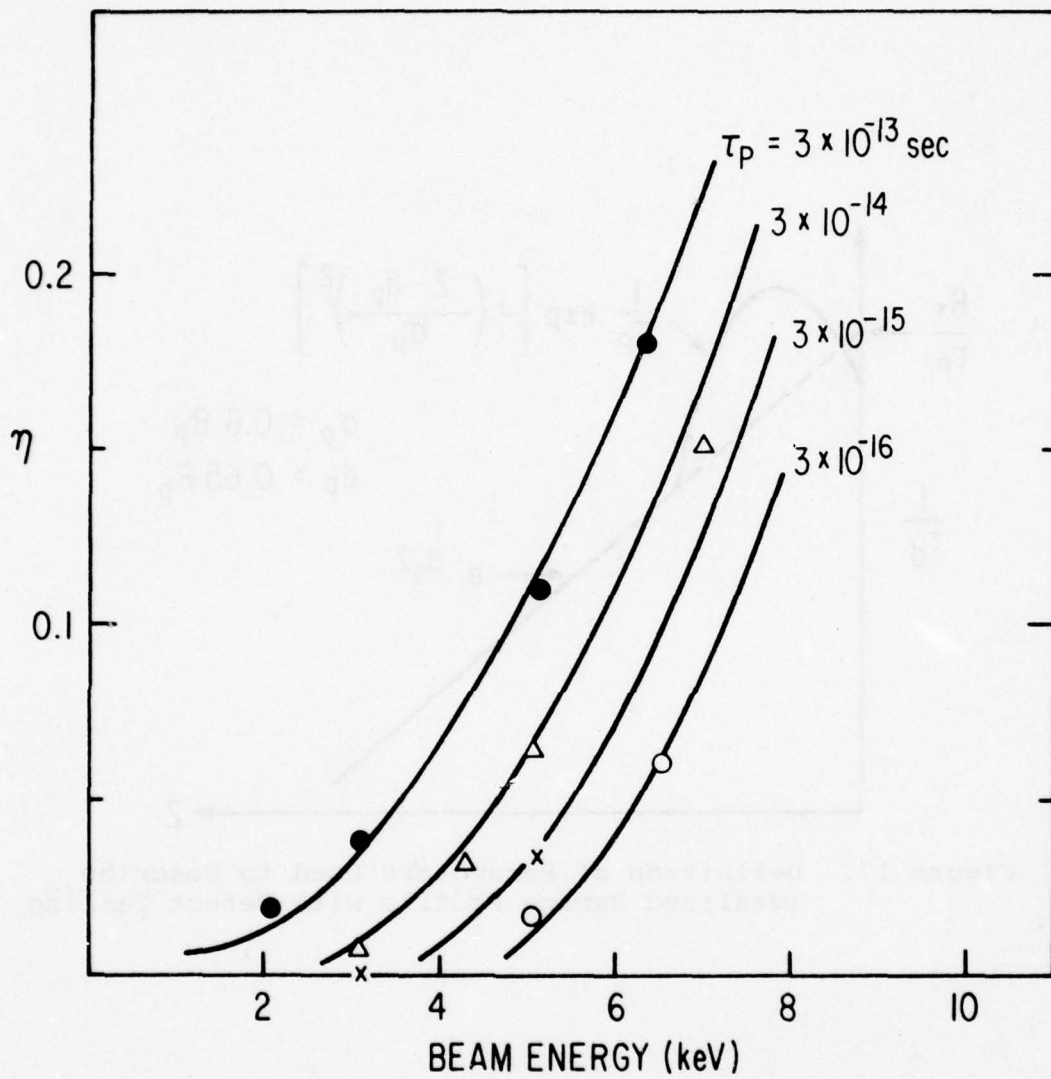


Figure 18. Fit of Data From Figure 15 to Complete 1-dimensional Model ($T_N=0.9$ micron) Using Defect Damage Distribution Corresponding to Solid Line in Figure 6 ($R_T = 0.5$, $B_5 = 3.7 \times 10^5 \text{ cm}^{-1}$, $R_p = 0.03$ micron)

uncertain within about a factor of 5. It is difficult to determine R_T precisely by the method just described because in the low fluence range, the gain or efficiency is strongly surface recombination velocity sensitive. Thus effects due to subtle changes in R_T would be masked. This problem does not apply in the high fluence region since the damage near the surface is so great that the effect of the surface recombination is eliminated.

Figures 20 through 22 show similarly determined recombination tails for other energies and ion species. The relative normalization of the Brice model and the experimental points are done by the same F_e method and should be considered only an approximation. The Brice model is included in these figures primarily to compare the shape of the defect generation curve profile to the measured recombination profile.

There is a great degree of similarity between the four measured damage tails. The damage tailing is greater for higher ion energies. The projected ion range appears to be the controlling factor. Both Ar^+ at 30 keV and Xe^+ at 60 keV have the same projected range of 0.03 microns and both have the same damage tail. Kr^+ at 110 keV and Ar^+ at 60 keV have the same projected range of 0.06 microns and the same amount of damage tailing.

Figures 23 and 24 show fits to the experimental data using the damage tailing determined i.e. from Figures 21 and 22 respectively. For both cases the model uses a uniform n-layer of depth 0.8 microns $B_5 = 2.2 \times 10^5 \text{ cm}^{-1}$ and $R_T = 0.5$. Again the fit is good with the peak recombination decreasing inversely as the writing fluence.

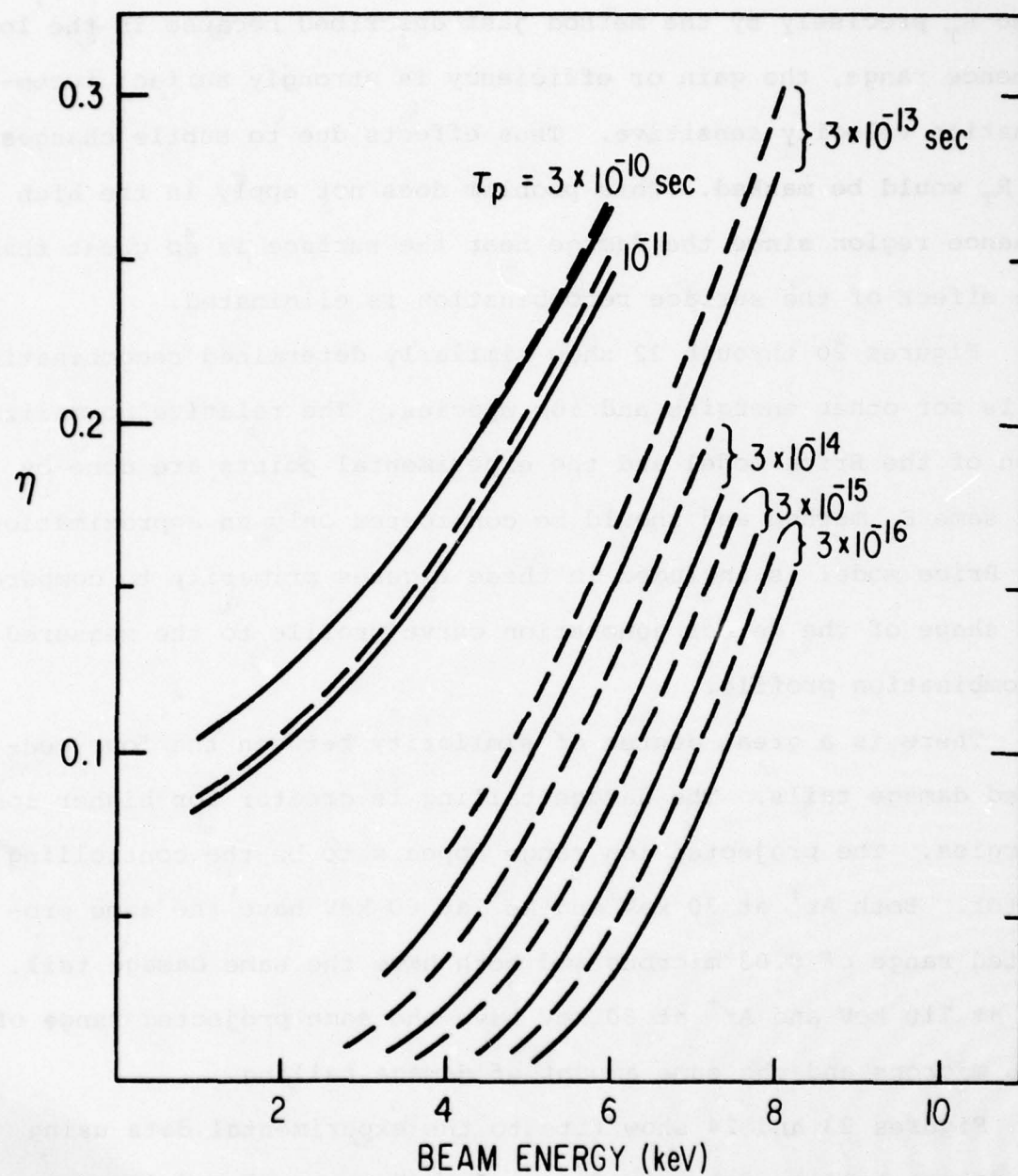


Figure 19. Comparison of 1-dimensional Model Calculations ($T_N = 0.9$ micron) of Collection Efficiency vs Beam Energy for Two Similar Damage Distributions With (—) $R_T = 1.0$ and (---) $R_T = 0.25$ Both With $B_5 = 3.7 \times 10^5$ cm⁻¹ and $R_p = 0.03$ micron

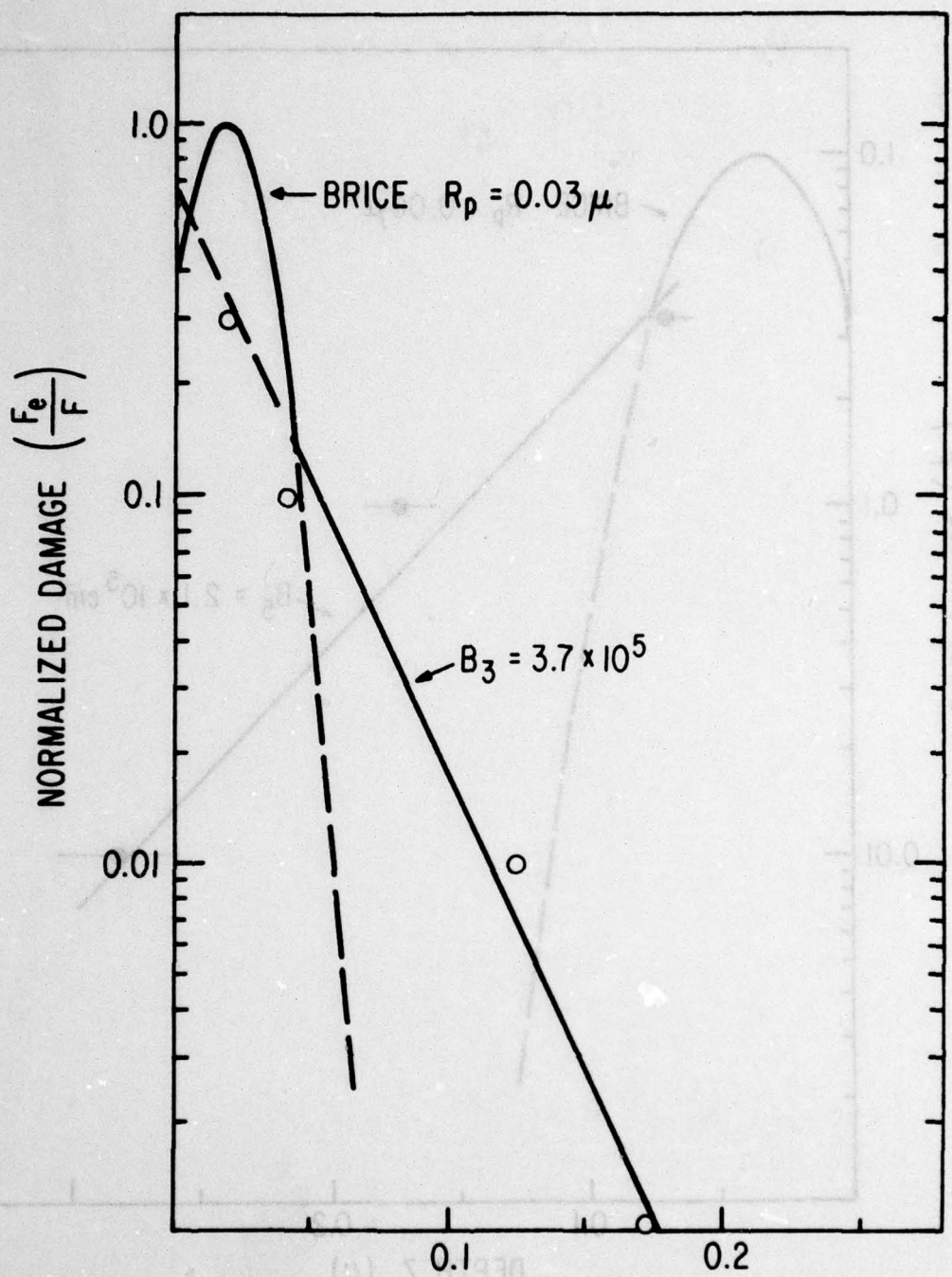


Figure 20. Normalized Damage Distribution vs Depth Measured, Using Flat Profile Targets 109-8 for 60 keV Xe^+ .
 $F_e = 10^{10} \text{ cm}^{-2}$.

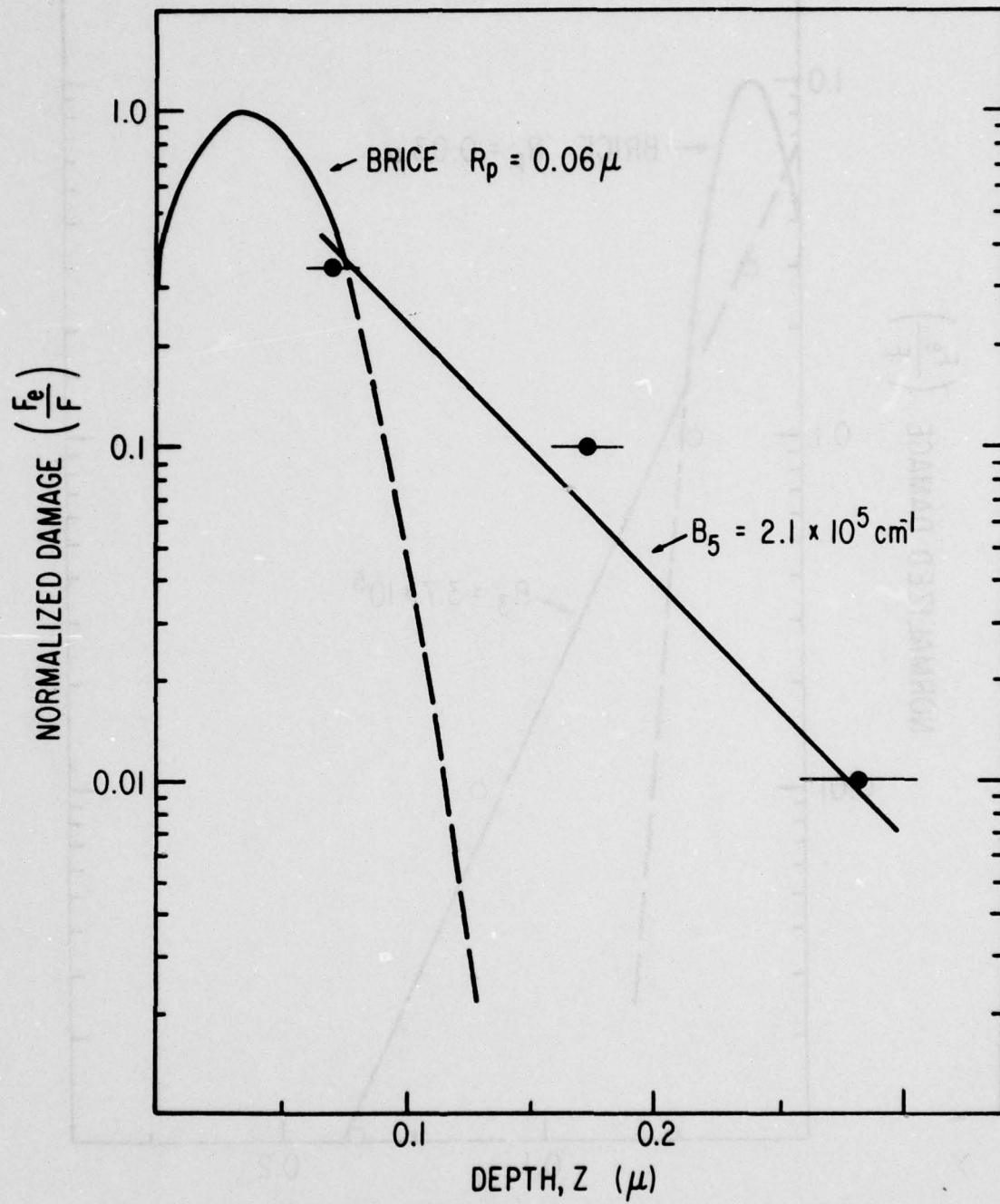


Figure 21. Normalized Damage Distribution vs Depth Measured Using Flat Profile Targets 110-14 for 110 keV Kr⁺.
 $F_e = 10^{10} \text{ cm}^{-2}$.

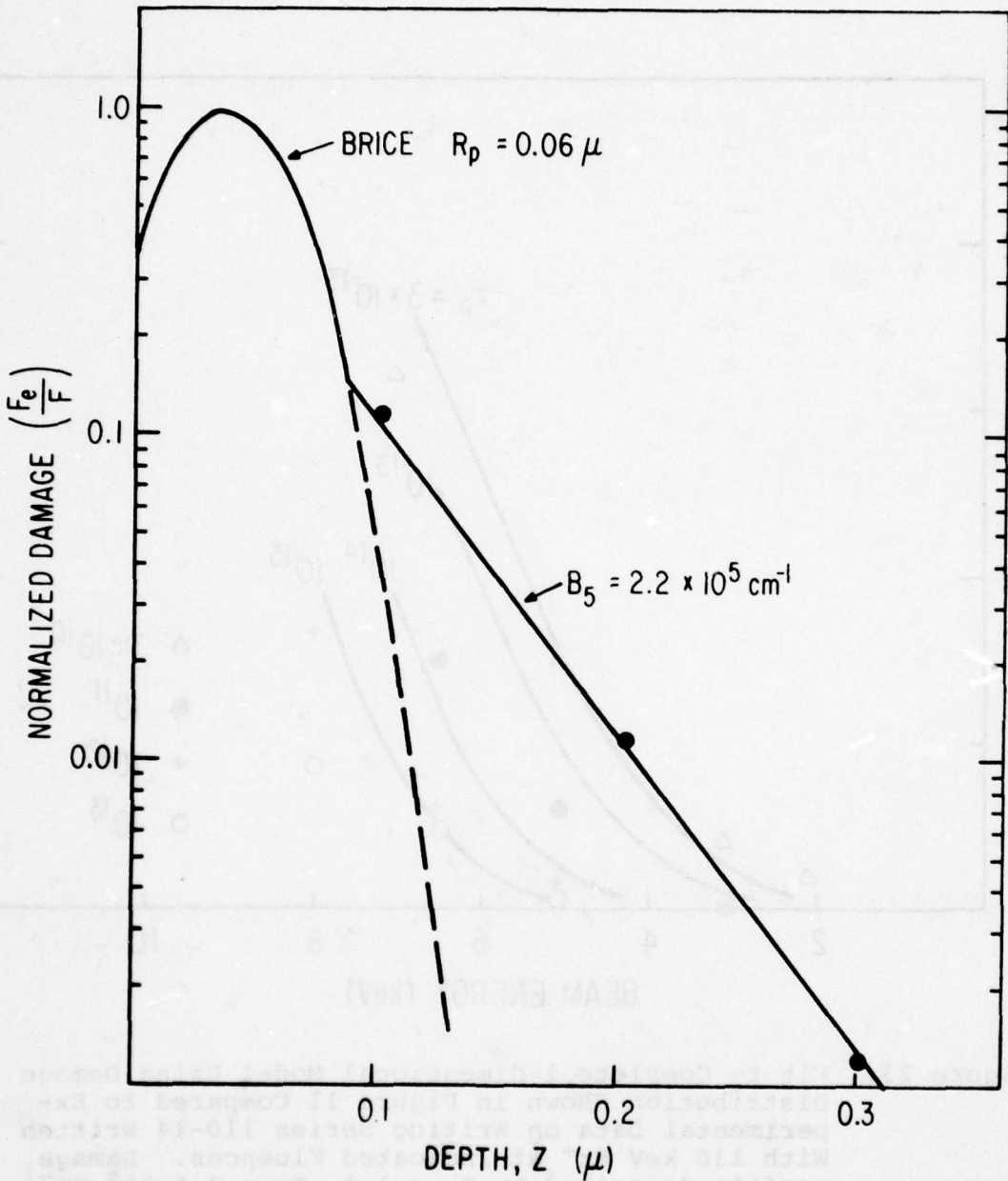


Figure 22. Normalized Damage Distribution vs Depth Measured Using Flat Profile Targets 110-5 for 60 keV Ar⁺.
 $F_e = 1.2 \times 10^{10} \text{ cm}^{-2}$.

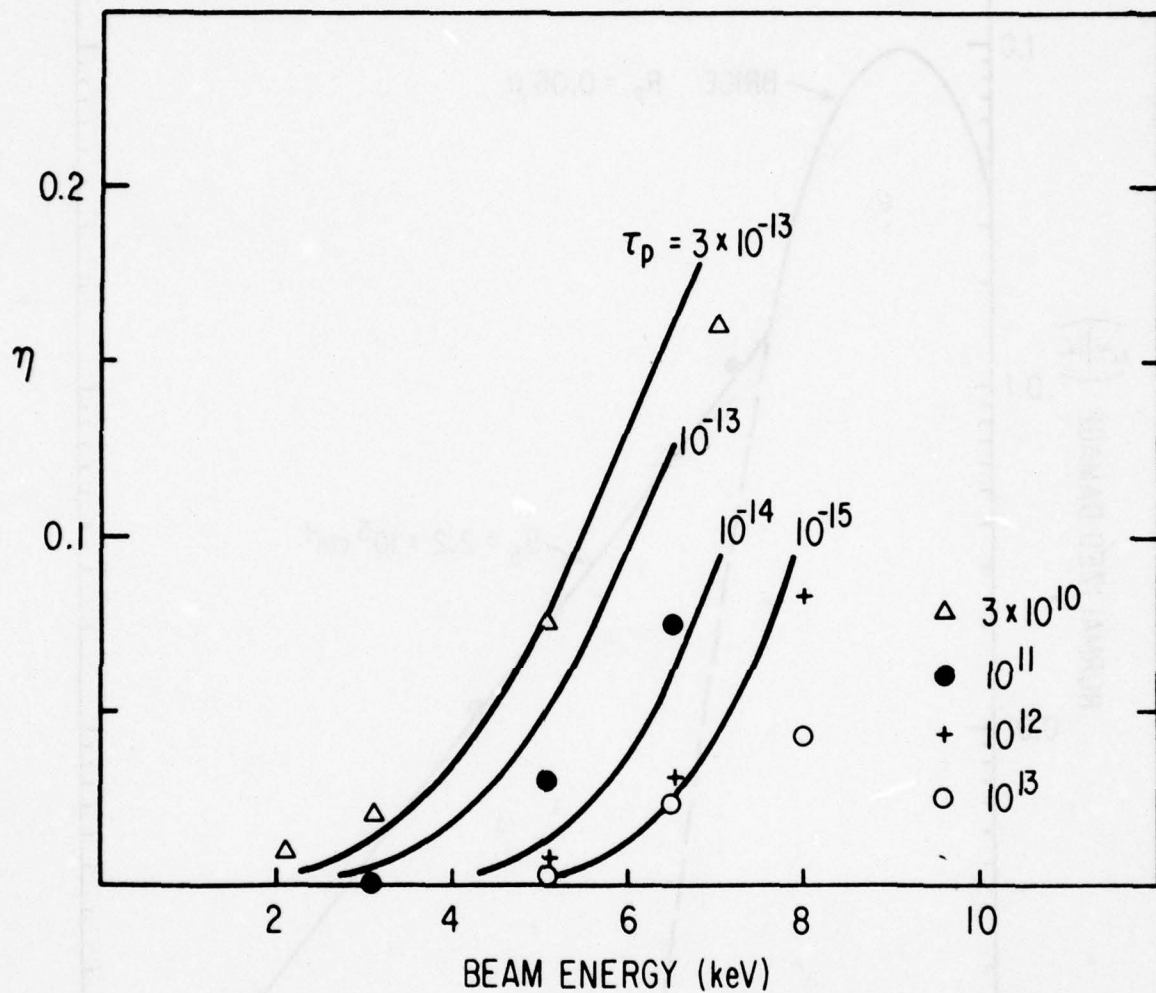


Figure 23. Fit to Complete 1-dimensional Model Using Damage Distribution Shown in Figure 11 Compared to Experimental Data on Writing Series 110-14 Written With 110 keV Kr⁺ at Indicated Fluences. Damage profile described by $R_T = 1.0$, $B_5 = 2.1 \times 10^5 \text{ cm}^{-1}$ and $R_p = 0.06 \text{ micron}$.

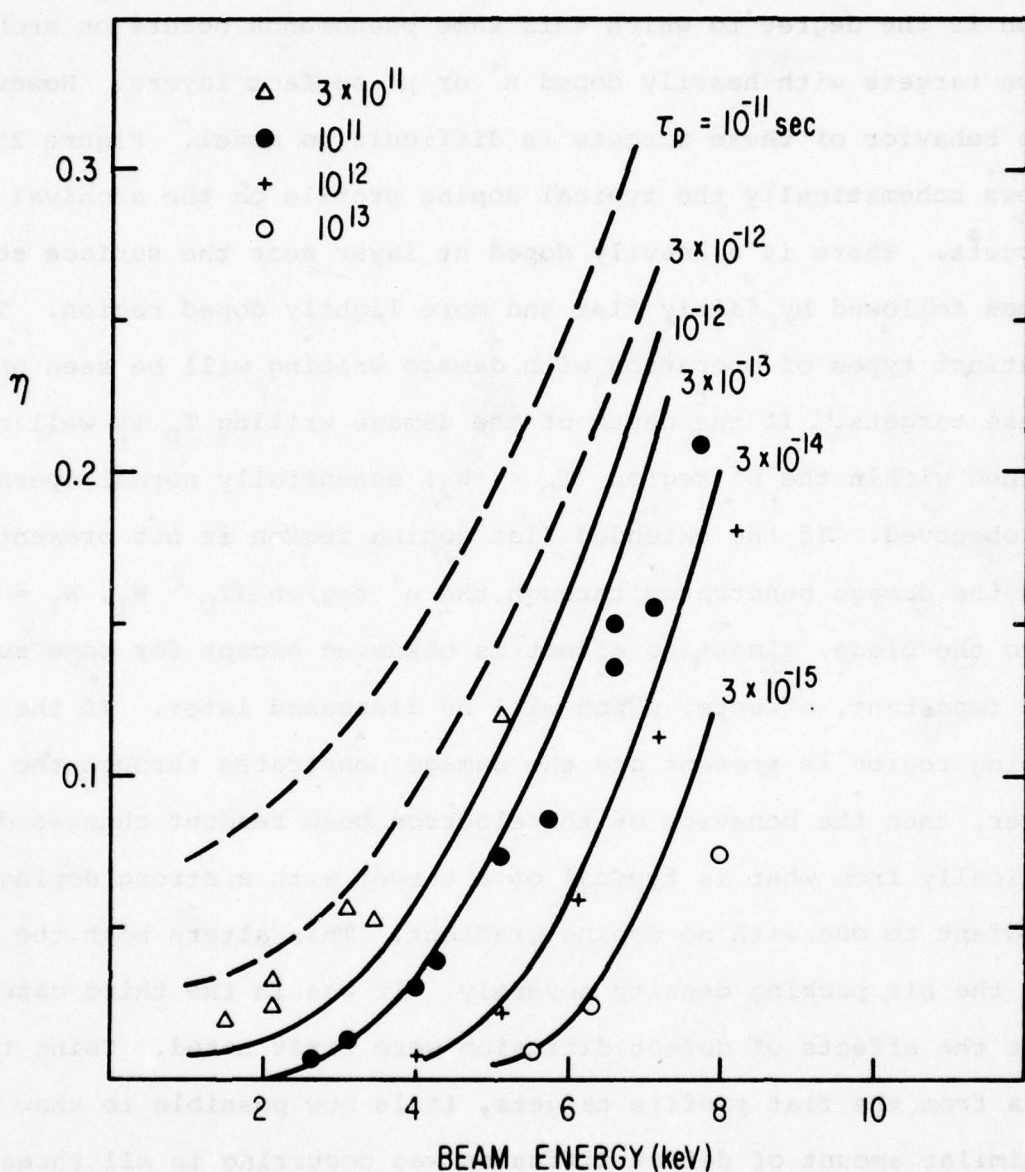


Figure 24. Complete One-dimensional Model ($T_N = 0.9$ micron) Using Damage Distribution Shown in Figure 22 ($R_T = 1.0$, $B_5 = 2.2 \times 10^5$ cm $^{-1}$ and $R_p = 0.06$ micron) Compared to Experimental Data from Writing Series 110-5 Written with 60 keV Ar $^+$ at Indicated Fluences

All of the measurements described up to this point have been on flat profile targets with low doping levels. An important question is the degree to which this same phenomenon occurs on archival type targets with heavily doped n^+ or p^+ surface layers. However, the behavior of these targets is difficult to model. Figure 25 shows schematically the typical doping profile on the archival targets. There is a heavily doped nt layer near the surface sometimes followed by fairly flat and more lightly doped region. Three distinct types of operation with damage writing will be seen on these targets. If the depth of the damage writing T_D is well contained within the n^+ region ($T_D \ll W_2$) essentially normal operation is observed. If the extended flat doping region is not present, and the damage penetrates through the n^+ region ($T_D > W_1$, $W_1 \approx W_2$) into the diode, almost no effect is observed except for some subtle, but important, effects, which will be discussed later. If the flat doping region is present and the damage penetrates through the n^+ layer, then the behavior of the electron beam readout changes dramatically from what is typical of a target with a strong doping gradient to one with no doping gradient. This alters both the gain and the bit packing density severely. It was in the third case that the effects of defect diffusion were first noted. Using the data from the flat profile targets, it is now possible to show that a similar amount of defect diffusion was occurring in all three target structures. This will be illustrated by both model experimental data in this section.

C. Observation of Defect Tailing in N^+NP Targets

Experiments were conducted on n^+np targets with doping profiles as shown in Figure 26. The n^+ part of the profile is

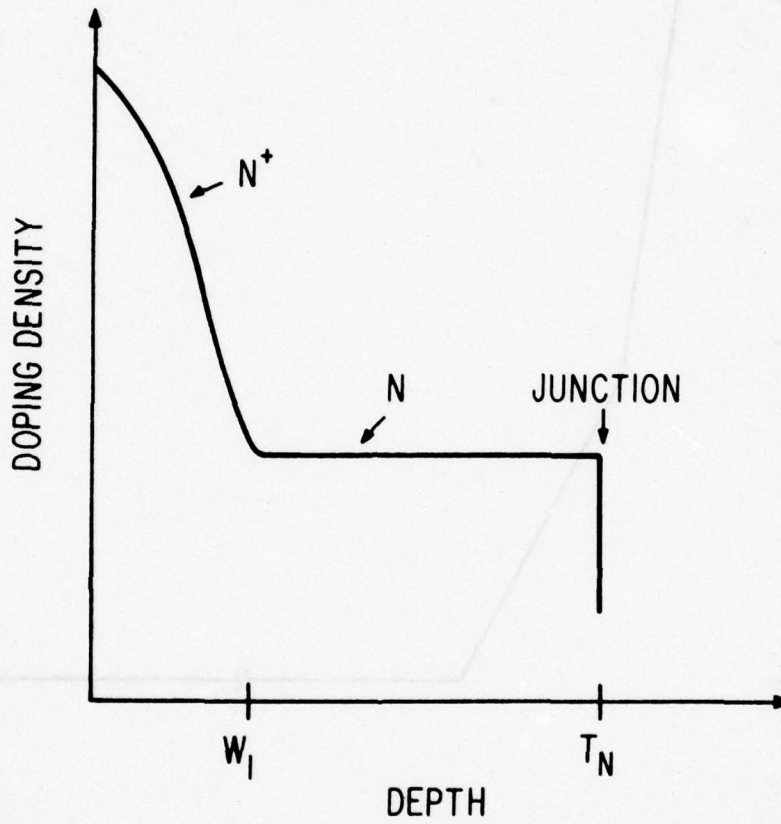


Figure 25. Schematic of Doping Profile for a Double n^+np Target

target an is used to effect paired diffusion of impurities in a multilayered wafer consisting of a p -type layer 1000 Å thick, a n^+ layer 100 Å thick, and a n -type layer 1000 Å thick. The n^+ layer is formed by diffusion of phosphorus into the p -type layer. The n -type layer is formed by diffusion of arsenic into the n^+ layer. The p -type layer is formed by diffusion of boron into the n -type layer.

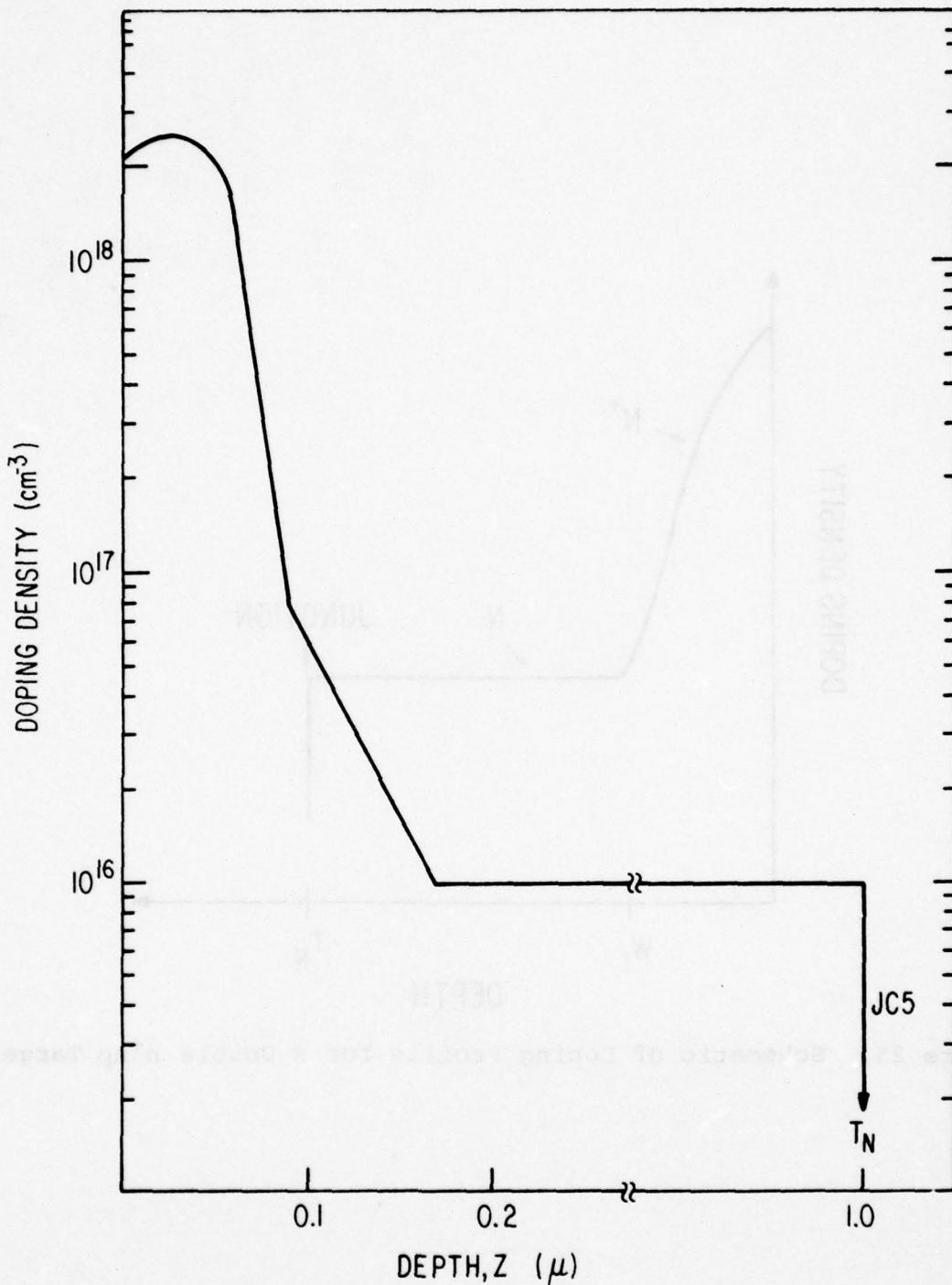


Figure 26. Idealized Doping Profile of a Typical n^+np Target Fabricated by 100 keV As^+ Implantation at $10^{14} \text{ #}/\text{cm}^2$ through 800 Å of Thermal SiO_2 into a Flat Profile Target Previously Fabricated P^+ 9 Implantation and Diffusion. As^+ profile based on anodic oxidation profile in Figure 15 of Fourth Quarter Phase I Report.

fabricated by 100 keV As⁺ implantation through 800Å of oxide into previously processed P⁺ implanted flat profile targets.

MODEL PREDICTIONS

Figures 27 and 28 show the one-dimensional model prediction of the writing behavior of a target with the doping profile shown in Figure 26. The damage profile used is a gaussian with σ_p and d_p as defined in Figure 17. Figure 27 shows the predicted efficiency versus electron beam energy for $R_p = 0.025$ microns. This is contrasted with Figures 28 and 29 for $R_p = 0.05$ microns. In all cases there is no tail on the damage profile. The large difference in the collection efficiency is due to the penetration of the damage into or near the flat profile region. This penetration provides a clear signature of writing which passes into the flat profile region. Other model simulations show that, for the doping profiles used here, the maximum damage depth T_D must be at least 0.05 microns less than the flat profile region (W_1) to give the type of behavior shown in Figure 27.

To place these results in perspective it is useful to discuss two simple limiting case models, as shown schematically in Figure 30. For model A, the built-in electric field is so strong that carriers generated beyond the damaged or written region (cross-hatched region) have unity collection probability. Model B is the one used above to analyze the flat profile targets; (see Section II, e.g. [1]) it corresponds to no built-in electric field. Figures 31 and 32 show the calculated collection efficiency versus beam energy for these two models. Model A (Figure 31) is independent

achi obizo ho 1000 deuchi noisomogni fai vod 001 ud hessolind
recepas sifosz daff hanolmi "i hessocq visoiverd

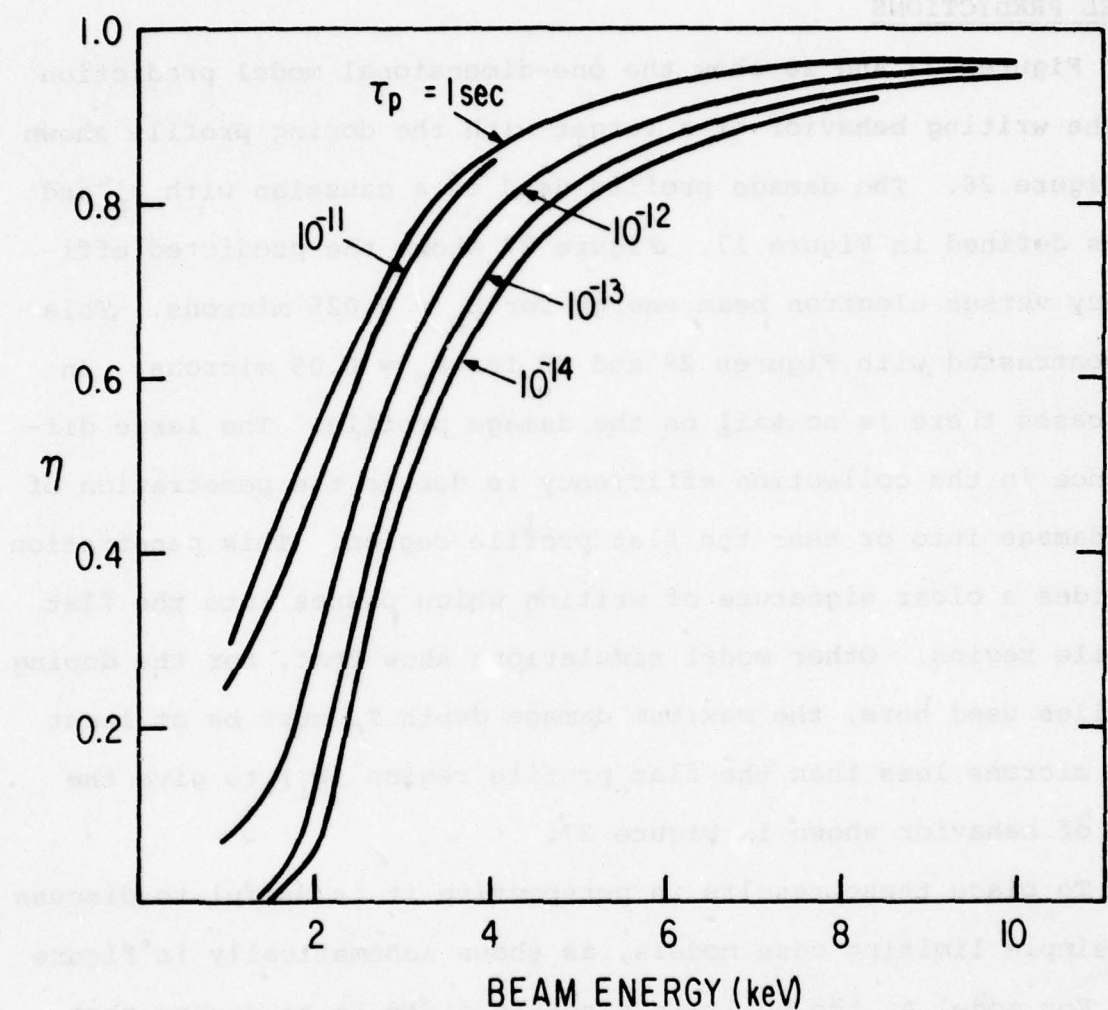


Figure 27. Complete One-dimensional Model Calculation of Collection Efficiency vs Beam Energy with Maximum Recombination τ_p as a Parameter. Doping profile as shown in Figure 16 with $T_N = 1.0 \mu$ and $S_V = 10^6 \text{ cm/sec}$. Gaussian damage profile based on Brice as shown in Figure 17 with $R_p = 0.025$ micron and no tail.

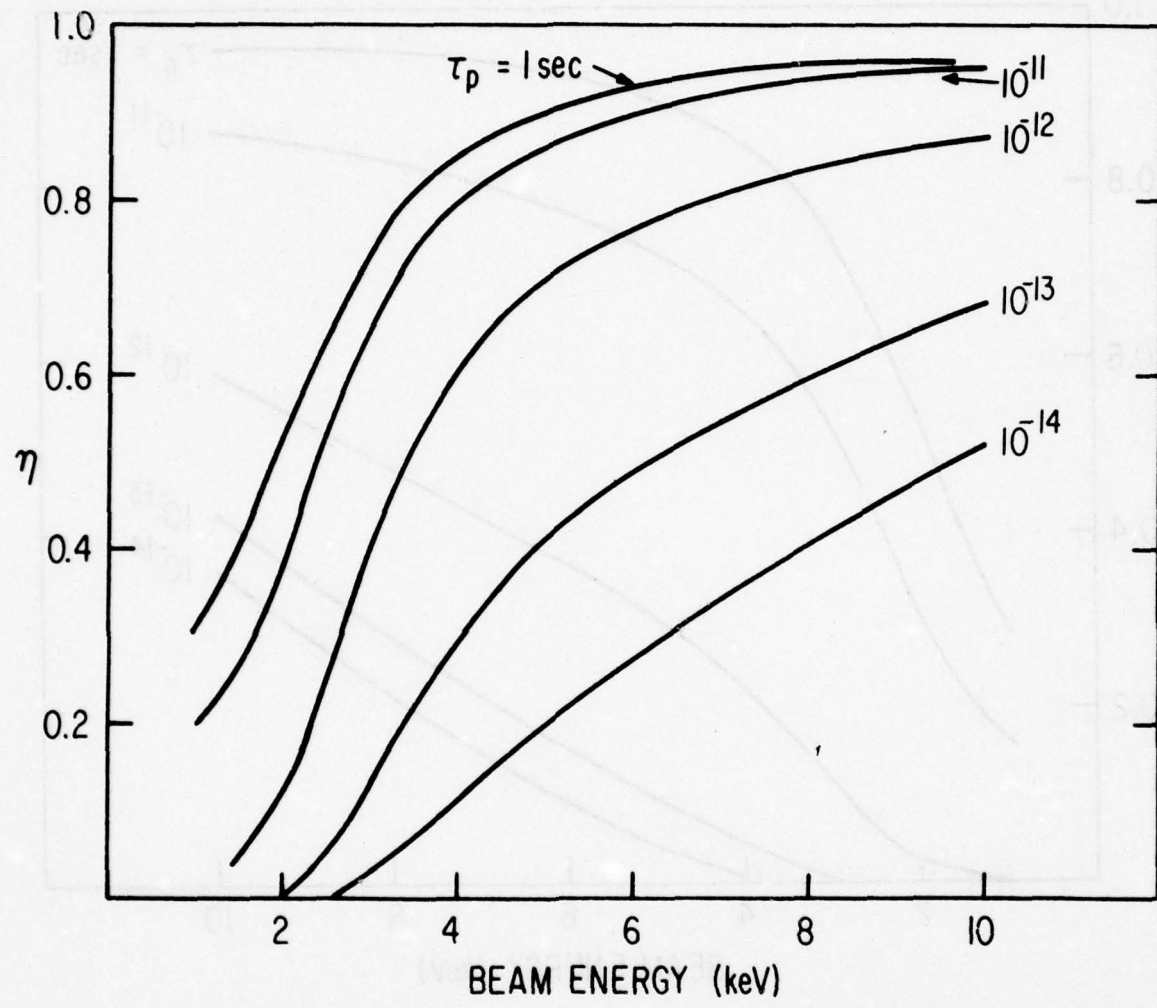


Figure 28. Complete One-dimensional Model Calculation of Collection Efficiency vs Beam Energy with Maximum Recombination τ_p as a Parameter. Doping profile as shown in Figure 16 with $T_N = 1.0 \mu$ and $S_v = 10^6 \text{ cm/sec}$. Gaussian damage profile based on Brice as shown in Figure 17 with $R_p = 0.05$ micron and no tail.

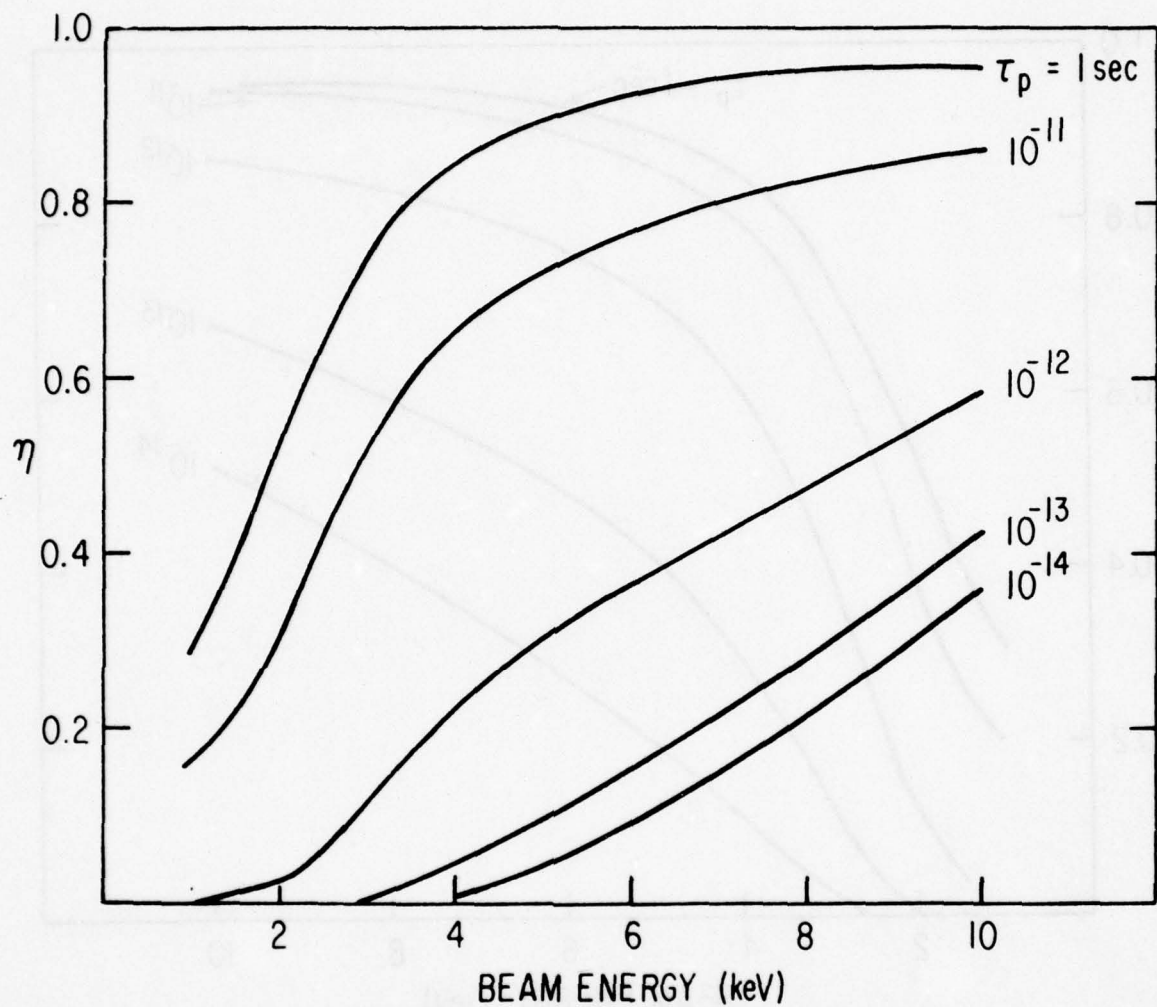
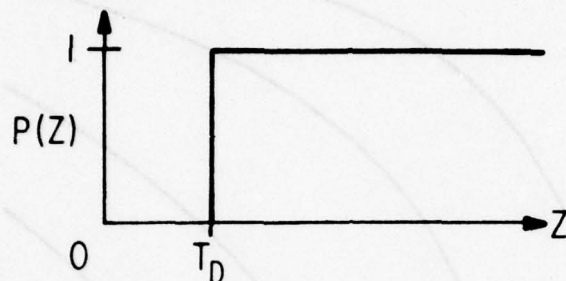


Figure 29. Complete One-dimensional Model Calculation of Collection Efficiency vs Beam Energy with Maximum Recombination τ_p as a Parameter. Doping profile as shown in Figure 16 with $T_N = 1.0\mu$ and $S_V = 10^6 \text{ cm/sec}$. Gaussian damage profile based on Brice as shown in Figure 17 with $R_p = 0.075$ micron and no tail.

$S_V = 0$



MODEL A



$S_V \approx 10^7 \text{ cm/sec}$



MODEL B

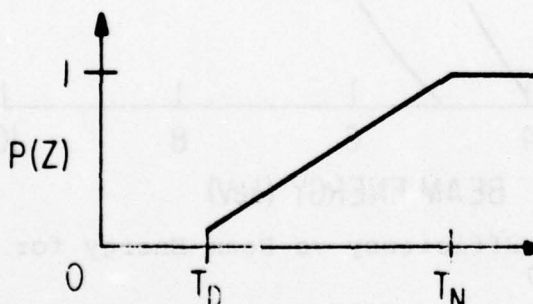


Figure 30. Model Approximations to Heavy Damage Writing to a Depth T_D in the Limit of Very High Built-in Electric Fields (Model A) and No Fields (Model B)

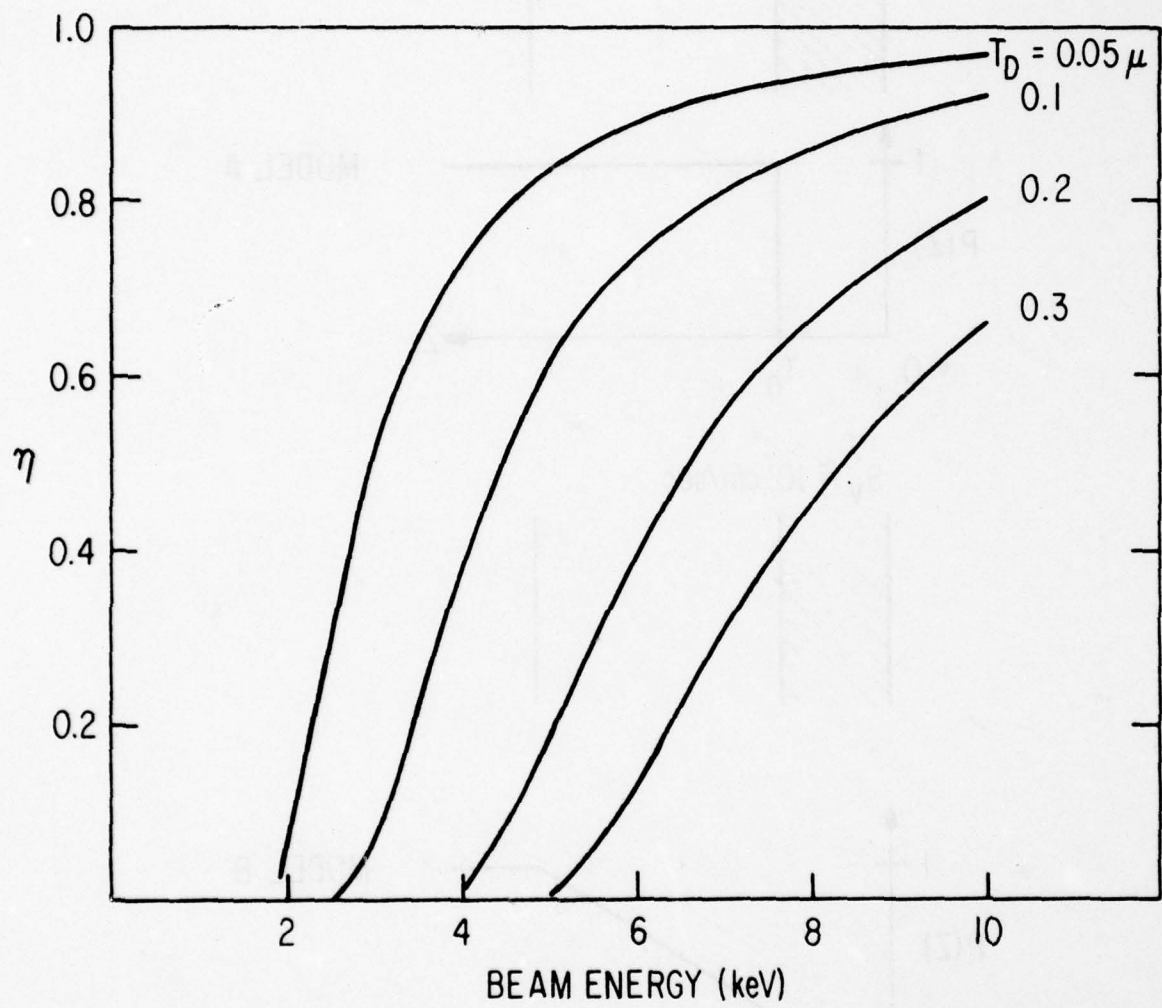


Figure 31. Collection Efficiency vs Beam Energy for Model A
(Figure 30)

bottoming a mawine nwoe at n. IashoN . dgeis nofennig elcib edt zo
alzog zell oit to from to Japoyt at doldw anocob 8.0 = W hqeb
nolwered ent neowte nnozotiffo epriL edt etoh . heifoue stonel
et or sub el S-lebon tot vonebilis rsoni edT .d bne A lebon to

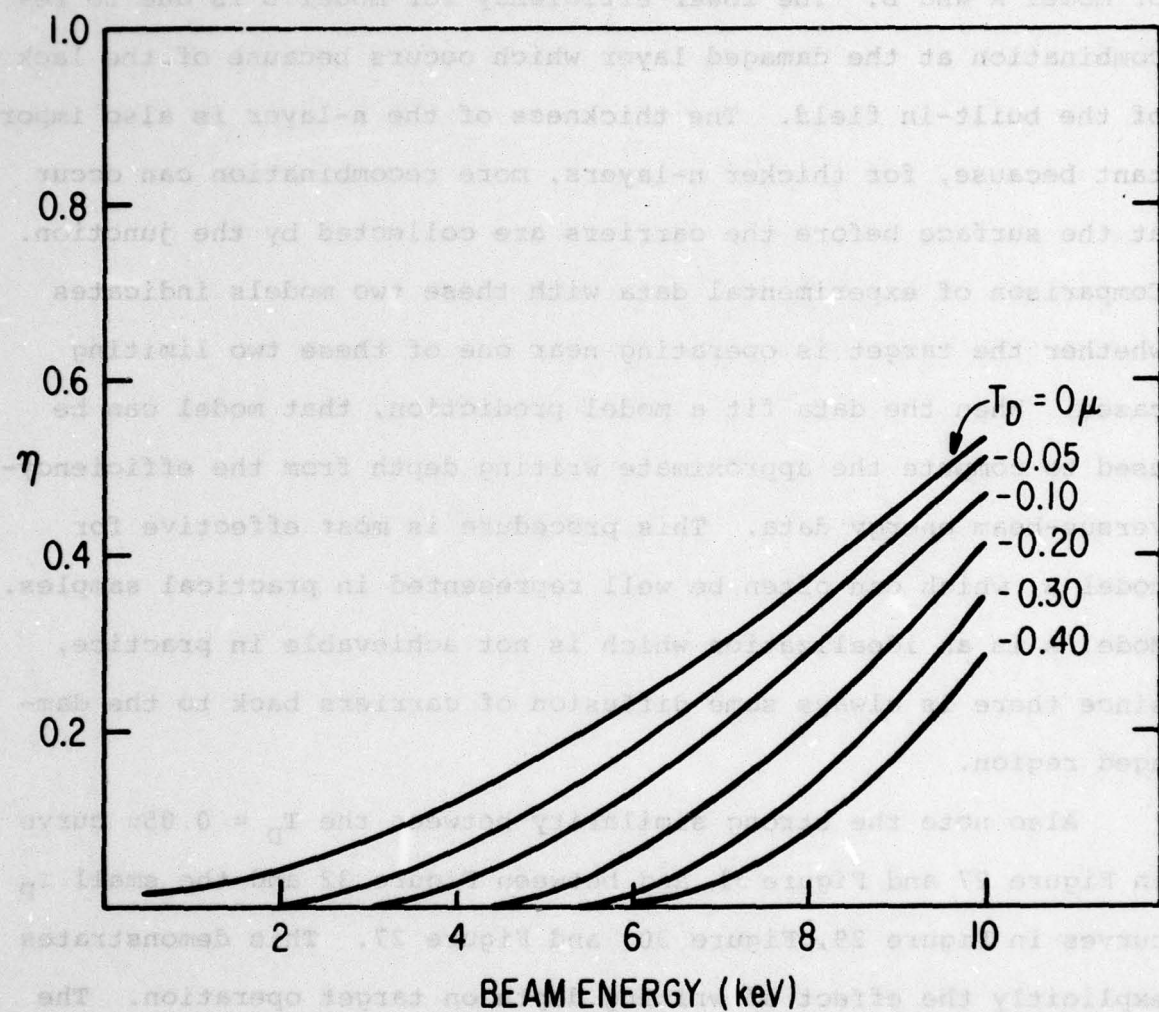


Figure 32. Collection Efficiency vs Beam Energy for Model B (Figure 30) for a Junction Depth $T_N = 0.8$ Micron

of the diode junction depth. Model B is shown only for a junction depth $W = 0.8$ microns which is typical of most of the flat profile targets studied. Note the large differences between the behavior of model A and B. The lower efficiency for model B is due to recombination at the damaged layer which occurs because of the lack of the built-in field. The thickness of the n-layer is also important because, for thicker n-layers, more recombination can occur at the surface before the carriers are collected by the junction. Comparison of experimental data with these two models indicates whether the target is operating near one of these two limiting cases. When the data fit a model prediction, that model can be used to compute the approximate writing depth from the efficiency-versus-beam energy data. This procedure is most effective for model B, which can often be well represented in practical samples. Model A is an idealization which is not achievable in practice, since there is always some diffusion of carriers back to the damaged region.

Also note the strong similarity between the $T_D = 0.05\mu$ curve in Figure 27 and Figure 31, and between Figure 32 and the small τ_p curves in Figure 29, Figure 30, and Figure 27. This demonstrates explicitly the effect of writing depth on target operation. The maximum writing depth using the Brice model is about $2.0 R_p$, so that in Figure 27 the maximum writing depth is about 0.05 microns, which is well within the n^+ region. For Figure 29 the maximum writing depth of 0.15 micron just reaches the flat profile region, so that model B (Figure 22) is well approximated. In Figure 28

for the higher values of peak recombination ($\tau_p \sim 10^{-11}$ sec), the written target behaves like model A with the damage well contained within the n^+ region. At smaller τ_p , the target behaves like model B.

Figure 29 shows this transition more clearly. For $\tau_p = 10^{-12}$ sec, two break points in the efficiency curve can be distinguished. The low gain below 2 keV is due to the heavy damage for depths < 0.05 microns. (The Grün electron range at 2 keV is 0.07 microns.) The behavior between 2 and 4 keV is due to a moderate level of damage in the n^+ region near the flat profile region but still within the n^+ region. This rapidly increasing efficiency versus beam energy is characteristic of model A. (The electron range at 4 keV is 0.2 microns.) Finally, above 4 keV, most of the carriers are being generated in the flat profile region and there is enough damage in the n^+ region within 0.05 microns of the h region to approximate the behavior of model B (i.e. a slowly rising efficiency curve). Some of the experimental data to be discussed below will demonstrate this general behavior. However, in view of the damage tailing results discussed earlier in this section, Figure 27, 28, or 29 would not be expected to fit the experimental data since these simulations have assumed a damage profile without tailing.

EXPERIMENTAL RESULTS

The n^+np targets were fabricated by As^+ implantation at 100 keV through SiO_2 into flat profile targets. Processing of this type of target is discussed in Section III. The typical doping profile is as shown in Figure 26. The n-layer doping level and junction depth vary somewhat among various lots as indicated in each case.

Figure 33 shows the first attempt to fit the collection efficiency data with the model using the doping profile in Figure 26 and the damage profile including defect tailing as shown in Figures 16 and 19-22. In this experiment the Ar^+ writing ion energy was 40 keV, the slope of the damage tail was chosen as $3 \times 10^5 \text{ cm}^{-1}$, which is intermediate between the slope observed at 30 and 60 keV for Ar^+ and Xe^+ . The definition of the damage profile parameters is shown in Figure 17. In general, the fit is encouraging but far from perfect. The principle discrepancy is for the unwritten target, which falls below the model by about 10%. This behavior is frequently observed on archival targets. It is believed to be due to recombination in the diode, which attenuates the readout current under all conditions. Unwritten target gain data agreed within 2% for all four targets studied. A second possible explanation is that the lifetime in the n-layer is low. Figure 34 shows the effect of introducing in the model a uniform bulk lifetime ($\tau_0 = 4 \text{ nsec}$) throughout the n^+ and n regions. This improves the fit, but note that the peak lifetime τ_p required to fit the data does not increase in decade amounts for their writing fluences. The best fits are for about 3×10^{-12} seconds for the 10^{11} cm^{-2} writing fluence and 5×10^{-13} seconds and $\sim 10^{-14}$ seconds for the two higher fluences. Also, for 10^{-12} seconds and 10^{-13} seconds respectively, the fit for the 10^{12} cm^{-2} fluence is poor. Figure 35 shows the effect of assuming some recombination in the collecting diode. The best fit for the unwritten areas is obtained for a 15% carrier loss in the collecting diode. This gives a better fit than the assumption of bulk recombination in the n-layer, but the fit for the 10^{12} and 10^{13} cm^{-2}

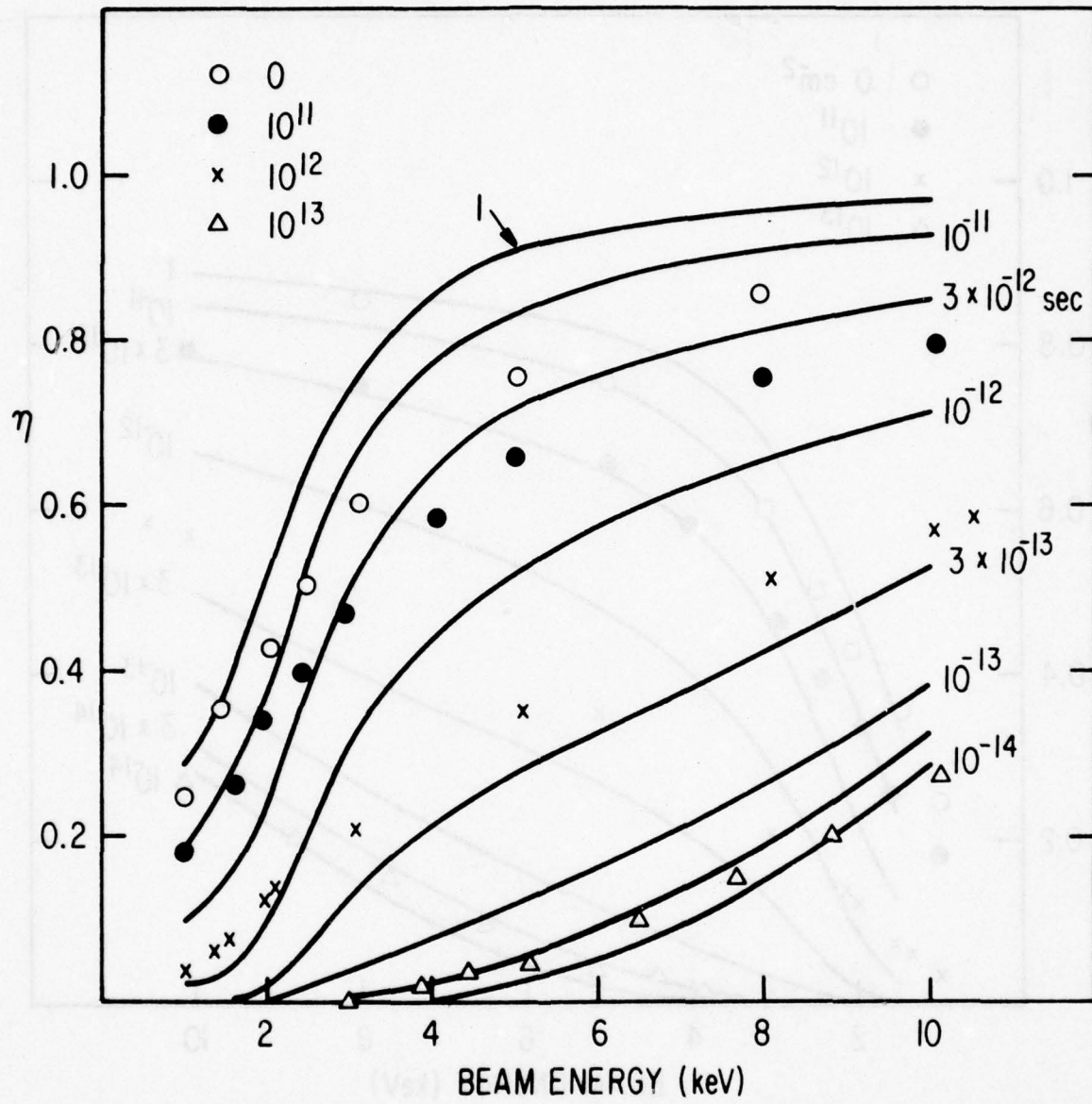


Figure 33. Comparison of Model Calculation to Experimental Data. Target series 105-10 written with 40 keV Ar^+ at fluences indicated. Model calculation uses doping profile in Figure 26 and a damage profile described by $R_p = 0.04$ micron, $B_5 = 3 \times 10^5 \text{ cm}^{-1}$, $R_T = 0.5$, and τ_p as indicated.

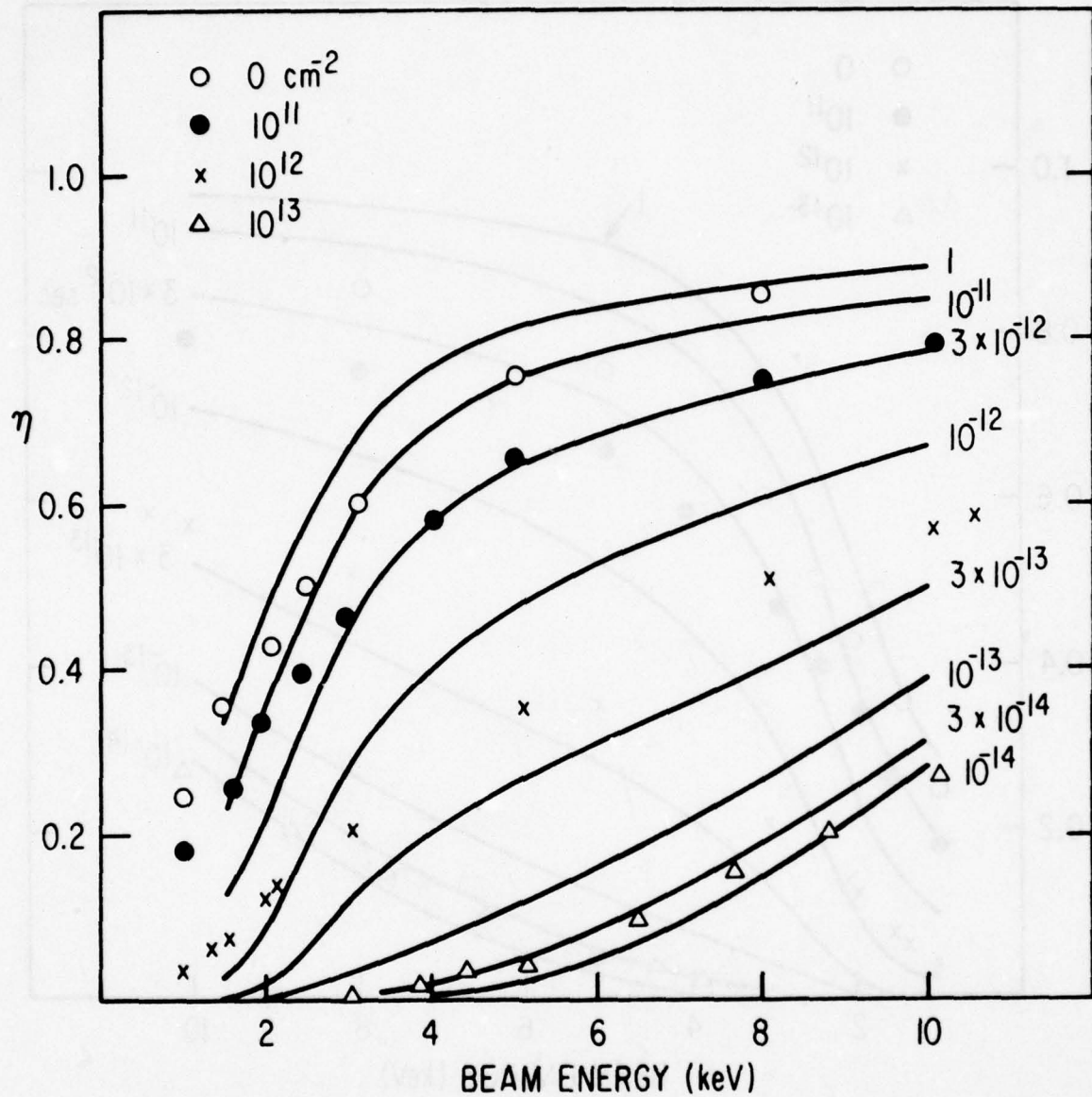


Figure 34. Comparison of Model Calculation to Experimental Data. Target series 105-10 written with 40 keV Ar^+ at indicated fluences. Model calculation based on doping profile in Figure 16 and a damage profile described by $R_p = 0.04$ micron, $R_T = 0.7$, $B_5 = 3 \times 10^5 \text{ cm}^{-1}$, $\tau_0 = 4 \times 10^{-9}$ sec, and τ_p as indicated in seconds.

and the effect of varying the beam voltage on the collection efficiency is shown. The number of atoms in either neutralized or ionized form is plotted to determine which species is present at various beam voltages and the influence of beam voltage on the collection efficiency.

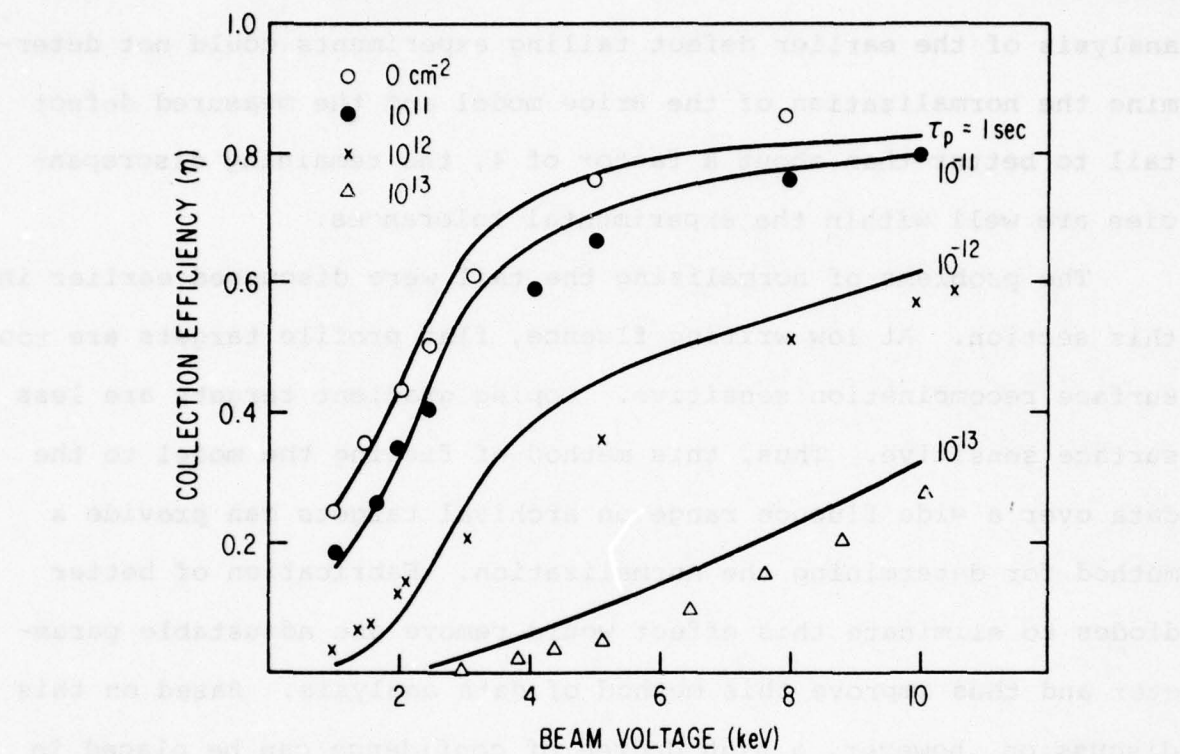


Figure 35. Comparison of Model Calculation to Experimental Data. Target series 105-10 written with 40 keV Ar⁺ at indicated fluences. Model calculation based on doping profile in Figure 26 and a damage profile described by $R_p = 0.04$ micron, $R_T = 0.7$, $B_5 = 3 \times 10^5$ cm⁻¹, and a diode quality factor of 0.85.

fluence samples could still be improved. Figure 36 shows the effect of altering the recombination profile as shown in Figure 37. The dotted tail was assumed for Figures 33 through 35. For Figure 36 the increased amount of defect tailing corresponding to the solid line was used. The fit is improved considerably. Since the data analysis of the earlier defect tailing experiments could not determine the normalization of the Brice model and the measured defect tail to better than about a factor of 4, the remaining discrepancies are well within the experimental tolerances.

The problems of normalizing the tail were discussed earlier in this section. At low writing fluence, flat profile targets are too surface recombination sensitive. Doping gradient targets are less surface sensitive. Thus, this method of fitting the model to the data over a wide fluence range on archival targets can provide a method for determining the normalization. Fabrication of better diodes to eliminate this effect would remove one adjustable parameter and thus improve this method of data analysis. Based on this discussion, however, a high degree of confidence can be placed in the normalized damage depth profile shown in Figure 37 for 40 keV Ar⁺. For reference, Figure 38 shows the fit assuming an increased amount of damage tailing identical to Figure 36 but using a 4 nsec bulk lifetime in the n-layer to account for the low gain. This fit is almost as good, except for the highest fluence case which is insensitive to the bulk lifetime, because the defect tailing has reduced the lifetime below the bulk level out to ~ 0.4 microns. The better fit in Figure 36 substantiates the conclusion that the low gain is due to carrier recombination in the collection diode rather than bulk recombination in the n-layer.

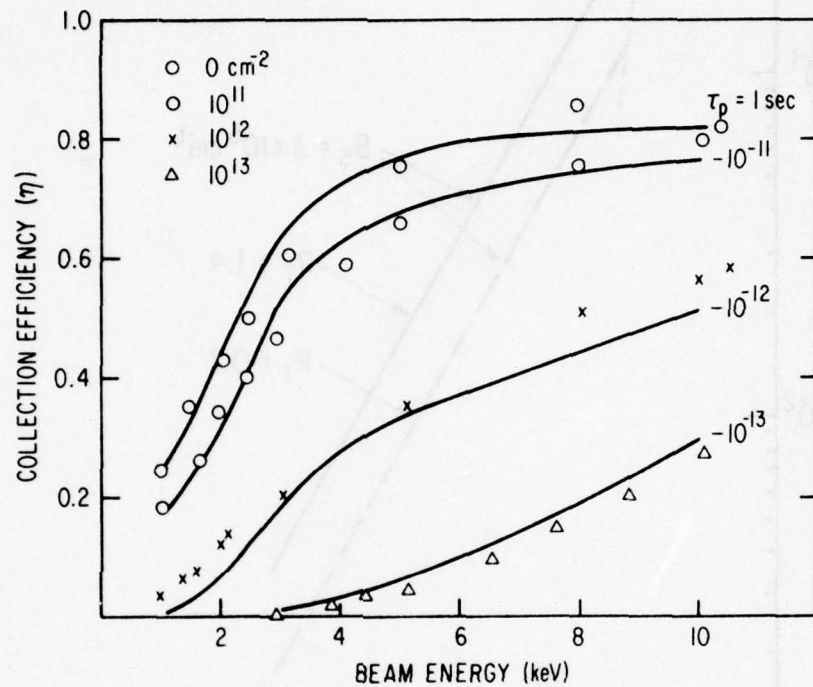


Figure 36. Comparison of Model Calculation to Experimental Data. Target series 105-10 written with 40 keV Ar⁺ at indicated fluences. Model calculations based on doping profile in Figure 26 and a damage profile described by $R_p = 0.04$ microns, $R_T = 1.4$, $B_5 = 3 \times 10^5 \text{ cm}^{-1}$, and a diode quality factor = 0.85.

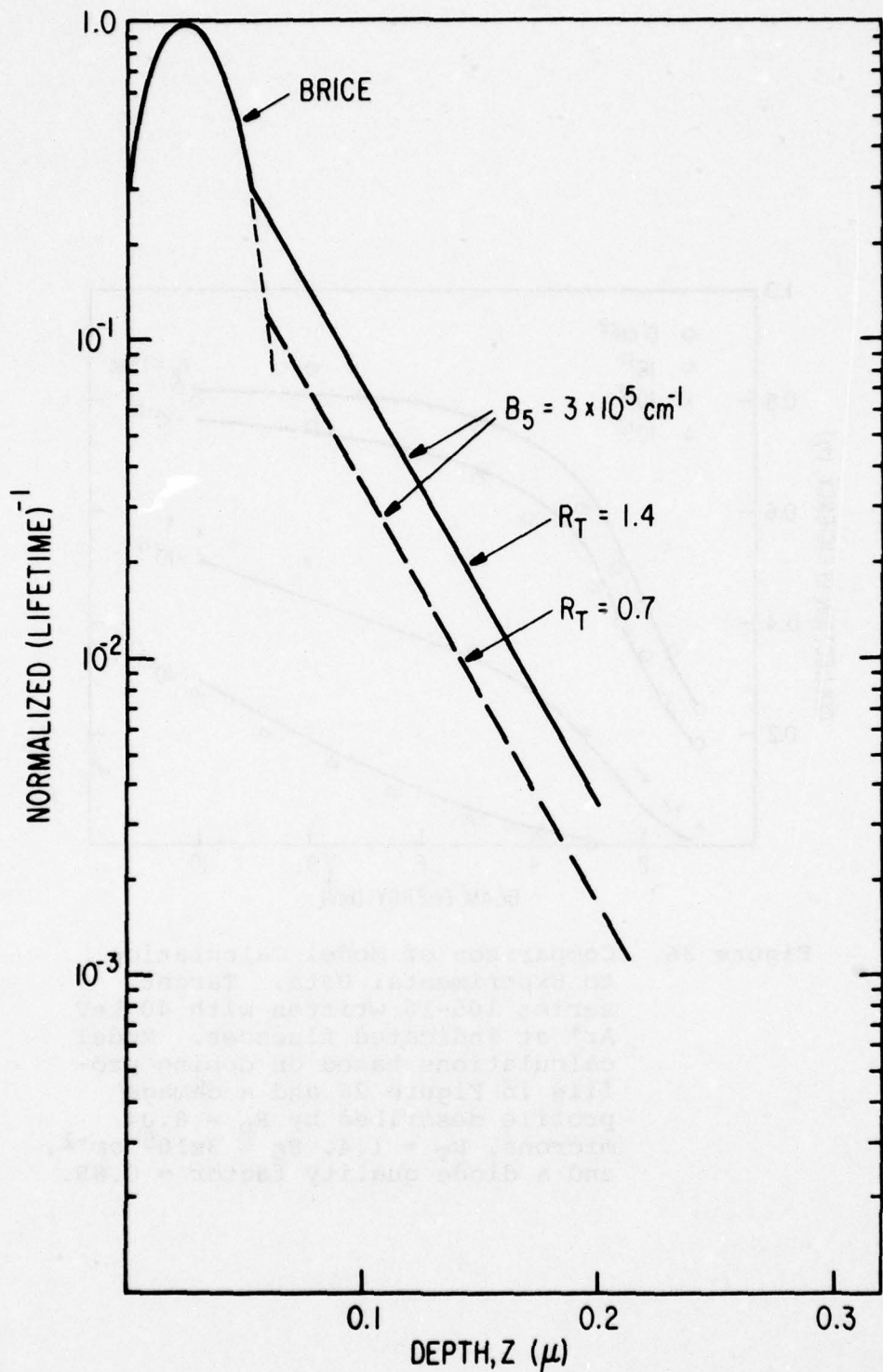


Figure 37. Comparison of Two Best Fit Damage Profiles for 40 keV Ar⁺ Writing in Target Series 105-10. Solid curve with $R_T = 1.4$ (see Figure 36) gives the best fit.

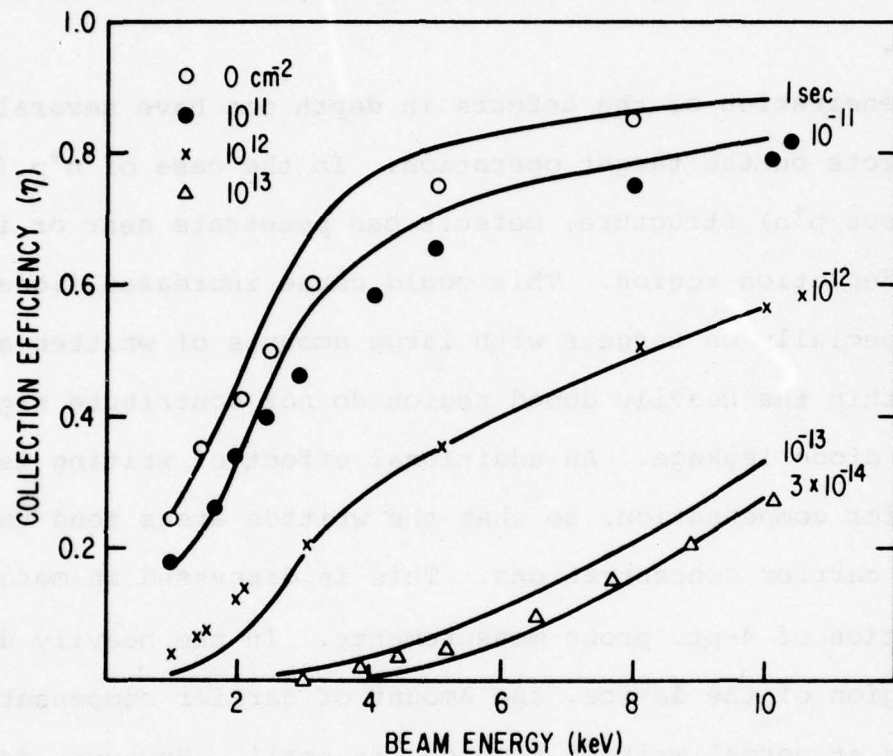


Figure 38. Comparison of Model Calculation to Experimental Data. Target series 105-10 written with 40 keV Ar^+ at indicated fluences. Model calculation based on doping profile in Figure 26 and a damage profile described by $R_p = 0.04 \text{ micron}$, $R_T = 1.4$, $B_5 = 3 \times 10^5 \text{ cm}^{-1}$, $\tau_0 = -x10^{-9} \text{ sec}$, and τ_p as indicated.

D. Design of Improved Target Structures

The anomalous defect diffusion can have several effects on archival target operation. Most significant, the observation of defect diffusion normal to the surface indicates that defects are also spreading laterally a similar amount. This has the direct consequence of degrading bit packing density, as discussed in Section IV.

The penetration of the defects in depth can have several secondary effects on the target operation. In the case of n^+p (or the analogous p^+n) structure, defects can penetrate near or into the diode depletion region. This could cause increased diode leakage especially on targets with large amounts of written areas. Defects within the heavily doped region do not contribute significantly to diode leakage. An additional effect of writing is to cause carrier compensation, so that the written areas tend to have lower carrier concentrations. This is discussed in more detail in the section of 4-pt. probe measurements. In the heavily doped surface region of the device, the amount of carrier compensation that occurs at normal writing fluences is small. However, defect tailing raises the possibility that carrier compensation could occur deeper in the device. Note that the slope of the defect distribution and the doping profiles are both in the range of 10^5 to 10^6 cm^{-1} so that it is possible for defect profile to out-run the doping profile. Also, the defects generated by writing will tend to degrade the mobility in the written areas. The net effect of these mechanisms can be to electrically disconnect isolated unwritten areas from the remainder of the diode and diode contact.

This disconnection effect was observed in Phase I and discussed at some length in the Fourth Report. The present observations on defect diffusion explain why it was observed before when it was not expected. The depths of the n⁺ and p⁺ layers had been designed to contain all of the generated defects based on the Brice type of defect generation model. To avoid these types of effects, slightly thicker n^t or p^t layers are required.

The effect of defect diffusion on n⁺np targets is more severe. If defects tail into or near the n region, the entire mode of target operation changes. The written target changes from model A to model B type of behavior (Figure 30). This type of behavior was observed in the data of Figures 33 through 38. In fact, it was this data that first clearly demonstrated the importance of defect tailing in archival targets.

To eliminate these defect penetration effects, targets with deeper n⁺ or p⁺ layers may be designed. A number of processing schedules were investigated for this purpose; they are summarized in Section III. Double implants were one of the most promising methods. Figure 39 shows the profile that can be obtained by double As⁺ implants at 30 and 100 keV with no surface oxide. The 100 keV implant profile is taken from the anodic oxidation measurements of the Phase I and the 30 keV profile is obtained by scaling this profile proportional to the energy ratio. This is felt to be a more realistic procedure than using the LSS profiles which differ significantly from the measured profile because of incomplete activation at the 900 °C annealing temperature, anomalous diffusion, and tailing. Figure 40 shows a double implant boron

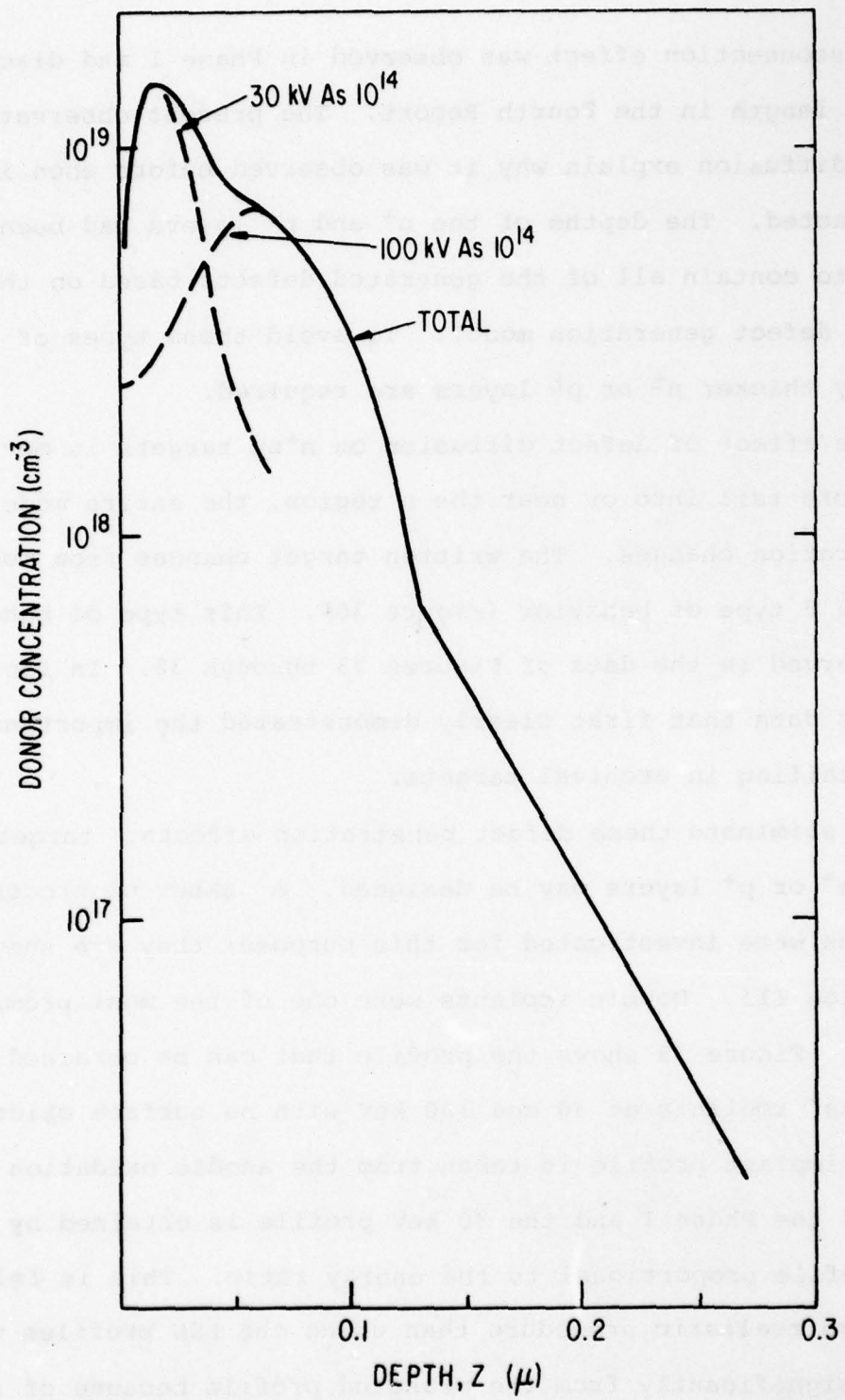


Figure 39. Doping Profile for Double As^+ Implantation and Low Temperature Anneal (900°C) Based on the Sum of a Measured Profile for 100 keV As^+ at 10^{14} cm^{-2} (Figure 4 of 3rd quarter Phase I report) and a Profile for 30 keV Scaled from 1 wekV

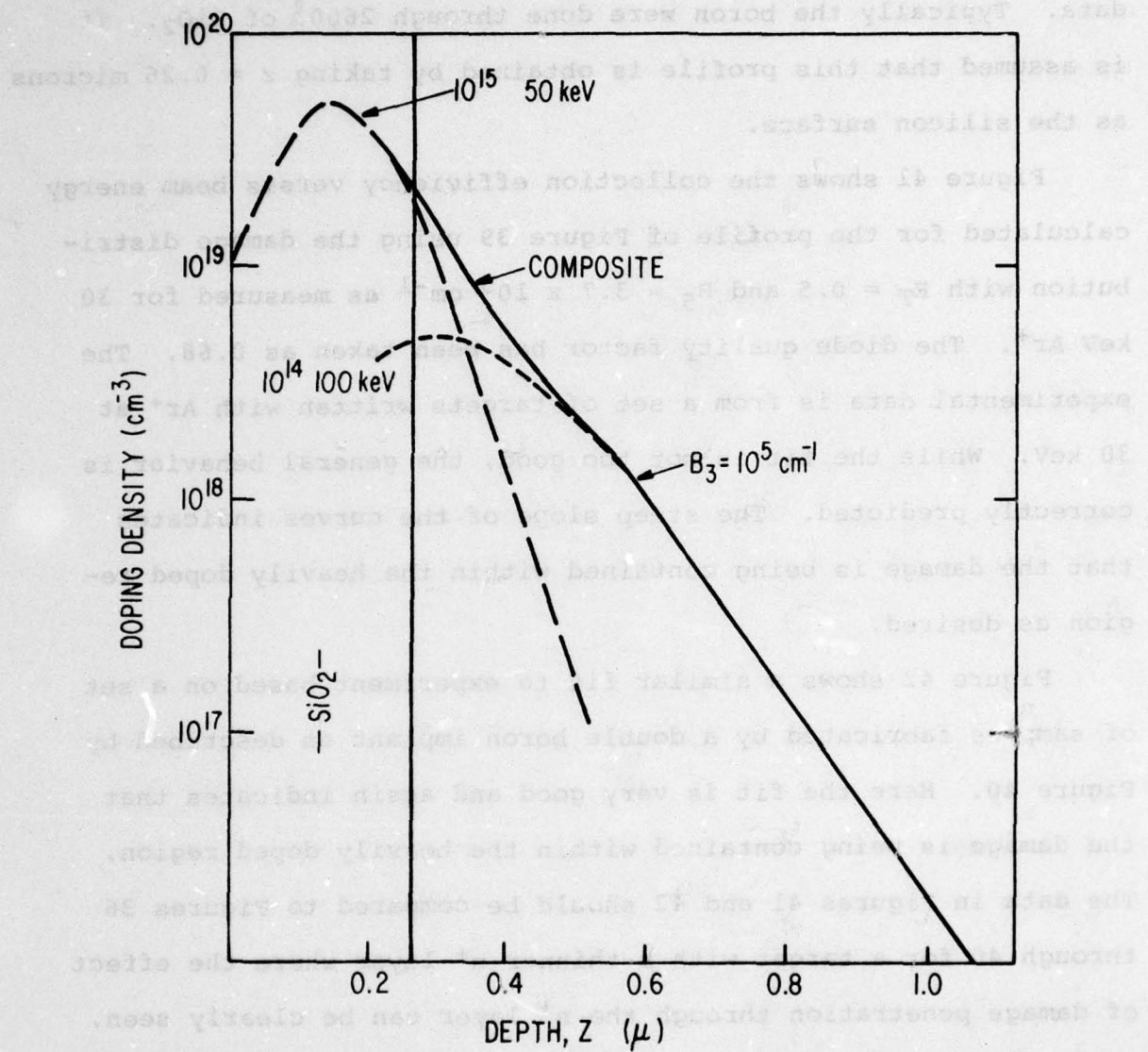


Figure 40. Doping Profile for Double B^+ Implant ($50 \text{ keV at } 10^{15} \text{ cm}^{-2}$ and $100 \text{ keV at } 10^{14} \text{ cm}^{-2}$) based on Crowder (*).

*B.L. Crowder, J.F. Ziegler, and G.W. Cole, The Influence of the Amorphous Phase on Boron Atom Distributions in Ion Implanted Silicon, International Symposium on Ion Implantation in Semiconductors and Other Materials, B.L. Crowder, ed. Plenum Press, New York, 1972, pp 257-265.

profile. The 100 keV data is taken from Crowder (see reference in Figure caption 40) and the 50 keV obtained by scaling this data. Typically the boron were done through 2600 \AA of SiO_2 . It is assumed that this profile is obtained by taking $z = 0.26$ microns as the silicon surface.

Figure 41 shows the collection efficiency versus beam energy calculated for the profile of Figure 39 using the damage distribution with $R_T = 0.5$ and $B_5 = 3.7 \times 10^5 \text{ cm}^{-1}$ as measured for 30 keV Ar^+ . The diode quality factor has been taken as 0.68. The experimental data is from a set of targets written with Ar^+ at 30 keV. While the fit is not too good, the general behavior is correctly predicted. The steep slope of the curves indicates that the damage is being contained within the heavily doped region as desired.

Figure 42 shows a similar fit to experiment based on a set of samples fabricated by a double boron implant as described by Figure 40. Here the fit is very good and again indicates that the damage is being contained within the heavily doped region. The data in Figures 41 and 42 should be compared to Figures 36 through 40 for a target with a thinner n^+ layer where the effect of damage penetration through the n^+ layer can be clearly seen. Hence, based on these measurements, it is seen that these new target structures can contain the damage within the n^+ region while still giving similar high gains at 2 keV.

The apparent deep location of the defects to which the archival target substrate is sensitive during readout could be due to several phenomena. The defects could penetrate deeper than predicted

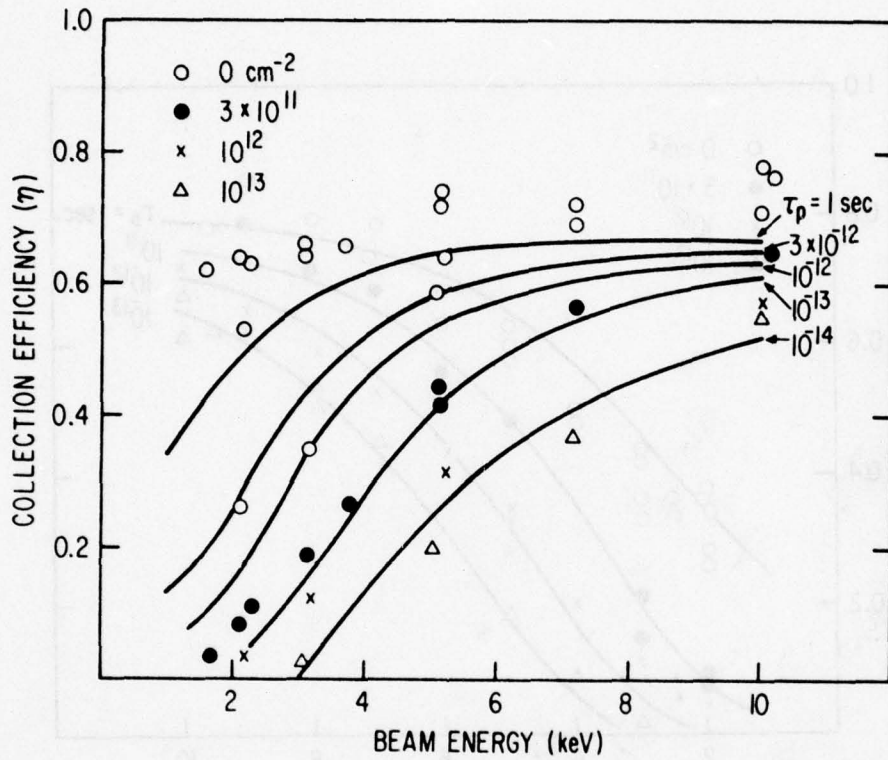


Figure 41. Comparison of Complete One-Dimensional Model to Experimental Data from Target Series 109-23 (3,4) and 109-27(1) Written with 30 keV Ar⁺ at Indicated Fluences. Model calculation based on doping profile in Figure 29 with $T_N = 0.8 \text{ micron}$ and a flat doping region $3.3 \times 10^{15} \text{ cm}^{-3}$. Damage profile described by $R_p = 0.03 \text{ micron}$, $R_T = 0.5$, $B_5 = 3.7 \times 10^5 \text{ cm}^{-1}$, diode quality factor = 0.68, and τ_p as indicated.

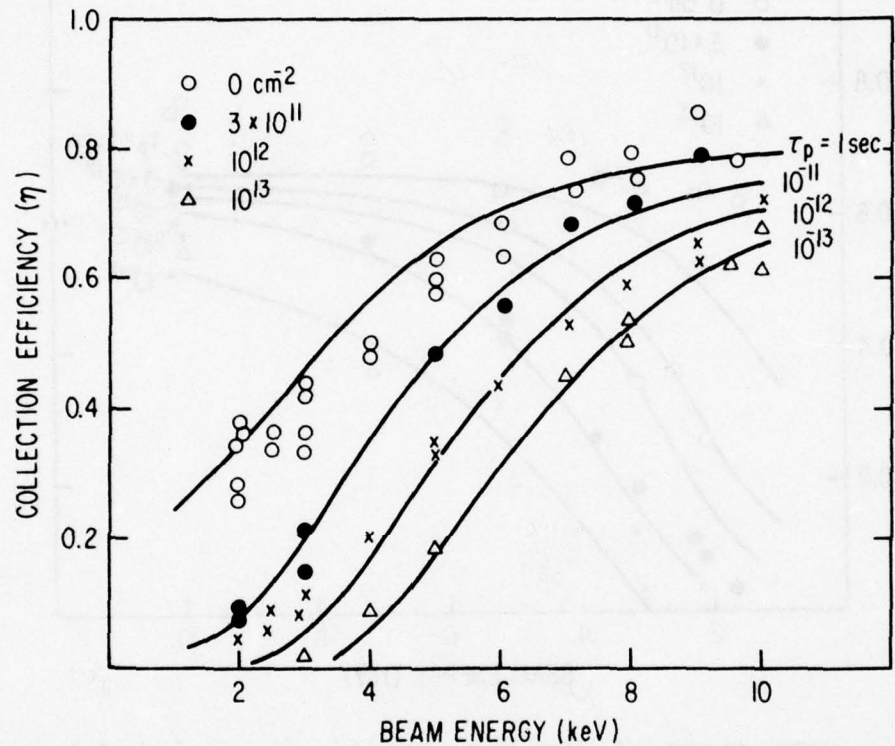


Figure 42. Comparison of Complete One-dimensional Model to Experimental Data from Target Series B2-9 Written with 30 keV Ar^+ at Indicated Fluences. Model calculation based on doping profile in Figure 40 with implantation through 0.26 micron of SiO_2 . Damage profile described by $R_T = 0.5$, $R_p = 0.03$ micron, and $B_5 = 3.7 \times 10^5 \text{ cm}^{-1}$. Diode quality factor = 0.85.

by Brice's energy calculations due to an anomalous diffusion of defects into the substrate, or the defects could be initially formed deeper than predicted by deeper ion penetration than anticipated, resulting perhaps from channeling. In another process, the defects could be driven deeper into the substrate during the implantation process itself as waves of newly formed defects and energy sweep through the lattice from the surface.

Whichever phenomenon or combination of these is involved, the problem might be alleviated by the appropriate writing conditions. Anomalous diffusion of defects into the substrate might be curtailed by trapping the defects closer to the surface by other defects. This may happen when the sample receives a large dose. It may also be expected that a very heavy mass ion, such as xenon, will exhibit somewhat less tailing. The defect clusters produced by a heavy ion may act as sinks for point defects migrating through the lattice.

Another approach could involve maintaining low sample temperature during the ion writing process. More defects result from a cold implant since fewer are annealed out during the writing process itself. However some types of defects are capable of moving and annealing at very low temperature, even as low as 4 K. A low temperature would tend to curtail the deep movement of many defects into the substrate as well. A liquid-nitrogen temperature implant could result in a defect distribution with less tailing into the device as well as possibly a lower fluence requirement. The effect of quenching-in the defects would persist to a large

degree even after the sample is returned at room temperature after ion temperature writing.

If the deep defect distribution is due to channeling phenomena, changing the sample temperature during implant might result in noticeable effects. At low temperatures, channeling of the implanted ions would be more marked, since the substrate ions remain closer to their lattice sites, leaving the channels more open. At elevated implantation temperatures, increased thermal energy causes greater lattice vibrations. The substrate ions move further from their sites in the lattice, obstructing the channels, and thus reducing the number of implanted ions that can scatter down these pathways. Using higher sample temperatures during the writing process to reduce the amount of channeling would be of dubious value, since a considerable portion of the defects would be annealed out, and defect migration would be promoted by the elevated temperature.

Perhaps the most desirable approach to reduce defect tailing would be to write harder, with heavy ions, because in this way the migrating defects may tend to be captured by other sites of radiation damage, curtailing their penetration, and increased defect annealing would not be promoted as much by this mode of implantation.

In summary, defect tailing has been discovered and measured for a number of planar diode structures. Ar^+ , Kr^+ , and Xe^+ damage implants have been evaluated at energies which give projected ranges of 0.03 and 0.06 microns. Structures formed with lightly doped P^+ , heavily doped As^+ and heavily doped B^+ regions all on

<111> Monex silicon, have all showed similar amounts of damage tailing. The size of the effect is ~ 0.05 microns with some defects penetrating as much as 0.2 microns beyond their generation depth according to the Brice model. One effect of damage tailing, the complete penetration of damage into the diode junction, can cause disconnection of the isolated unwritten dot patterns and increased diode leakage. The effects can be eliminated by deeper doping profiles. Large area writing tests of these structures have been successful. Evaluation of the packing density capabilities of these new diode structures is described in Section IV.

SECTION III
ION IMPLANT TARGET DESIGN AND PROCESSING

The deep penetration of the defects generated by ion writing precipitated several modifications in target substrate design and processing. Deep defect distributions necessitate deeper n⁺ (or p⁺) layers so that the defects do not penetrate to the diode depletion region.

This deeper diode structure alteration can be achieved by reducing or eliminating the surface oxide through which the implant providing then n⁺ (or p⁺) layer is performed (e.g. targets A210-A212), or using multiple energy implants to tailor the deeper profile (e.g. A206-A209). Another technique, which also functions to reduce the steepness of the doping gradient, is to increase the annealing temperature after implant. This causes diffusion of the dopant, moving the junction deeper, and spreading out the profile of implanted ions (e.g. B17-B23).

Another method for contending with the deep defect distributions is to produce a n⁺np (or p⁺pn) device by Figure 43 a double implant forming a shallow top doped layer which results in a driving field, with a deeper implanted dopant layer, forming the junction (see Figure 43). The junction implant is done first, generally at a low fluence $\approx 10^{12}$ ions/cm², and then annealed at high temperature, 1100°C, to produce a relatively flat profile of dopant extending deep ($\approx 1\mu$) into the substrate. The high annealing temperatures not only flatten the profile, but also serve to activate the dopant completely and to anneal ion implantation generated defects in the diode depletion region which can cause excess diode leakage and low

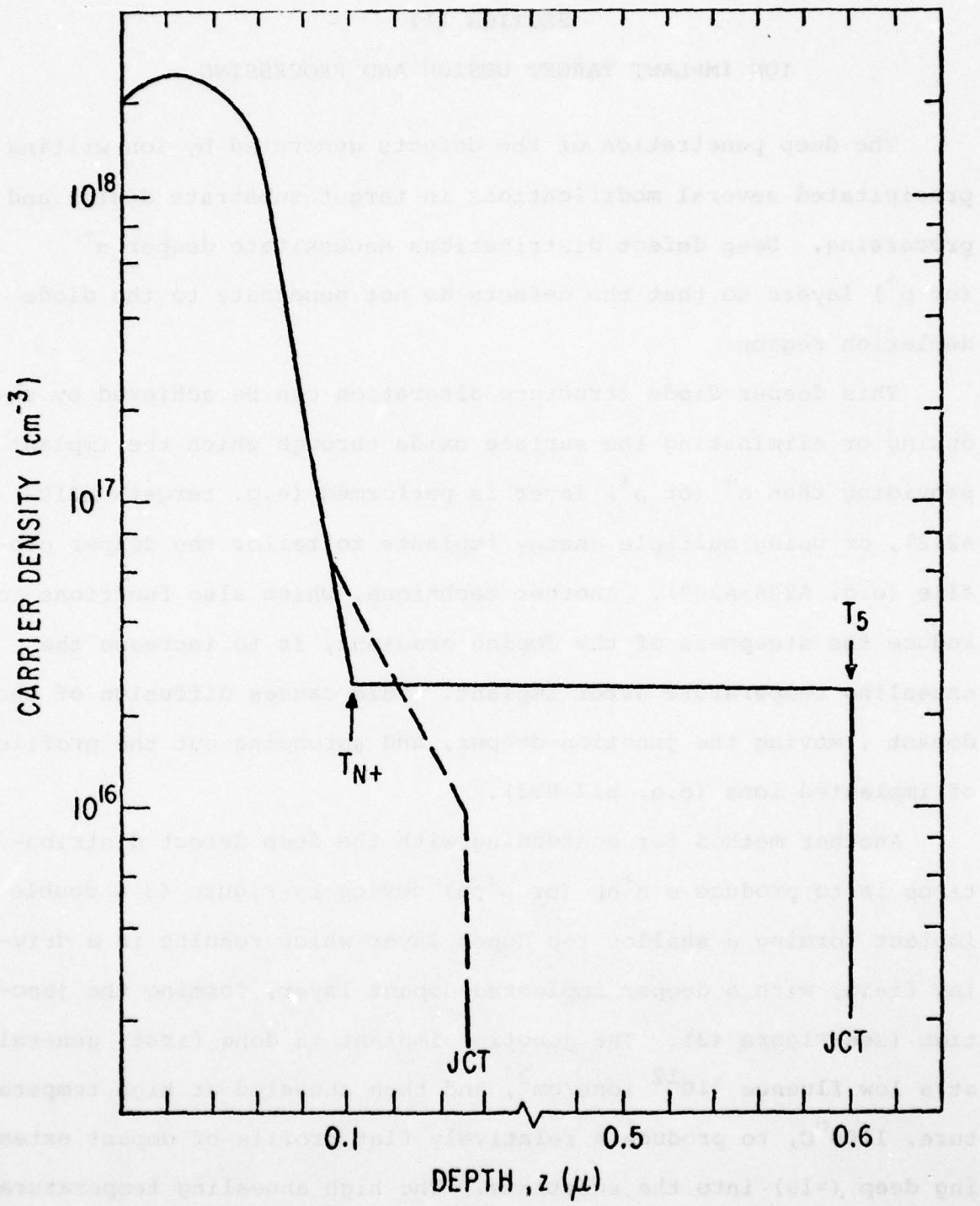


Figure 43. Doping Profiles for Typical Planar Diodes -- n^+p (dotted) and n^+-n-p (solid)

voltage breakdown. To produce the driving field, a second implant is performed through a surface oxide so that the peak just lands inside the oxide, producing a steep doping gradient away from the surface. This second higher fluence (10^{15} ions/cm⁻²) implant receives a lower temperature annealing cycle, usually 900°C, which is sufficient to activate the dopant and remove much of the resulting radiation damage. The low anneal temperature allows the profile to retain its steep slope. The unannealed remanents of radiation damage from this second implant are distant from the junction and are in a heavily doped region so that generation-recombination is suppressed and isolated from the junction. This assures higher quality diode characteristics.

Several lots of this target generation were produced at the Integrated Circuits Center in Syracuse, N.Y. These are given the designations BAR (BEAMOS to ARchival), where BEAMOS targets were stripped of oxide, an implant oxide was deposited, and the second implant and anneal performed; NAR (n⁺ top layer ARchival); and PAR (p⁺ top layer ARchival). Process steps for these variations are indicated in Tables 1, 2, and 3.

To improve the basic device structure as well as to facilitate the through-put of writing experiments, a new mask set was designed and a lot processed of the p⁺pn variety. In addition to double field implants, channel stopper, back implantation, diode passivation, and contact metallizations (see Figure 44 for cross section), the new masks provide a series of bar patterns in resist for writing experiments as well as Van der Pauw patterns. The bar patterns allow fast through-put of writing experiments in

design, induces a small electric field barrier at the cathode emitter
which must leak out some of which occurs at a point between the
end point where the electron passes through, where it is shown
as the origin of "leakage". First consider negative biases and assume
that the positive voltage is zero.

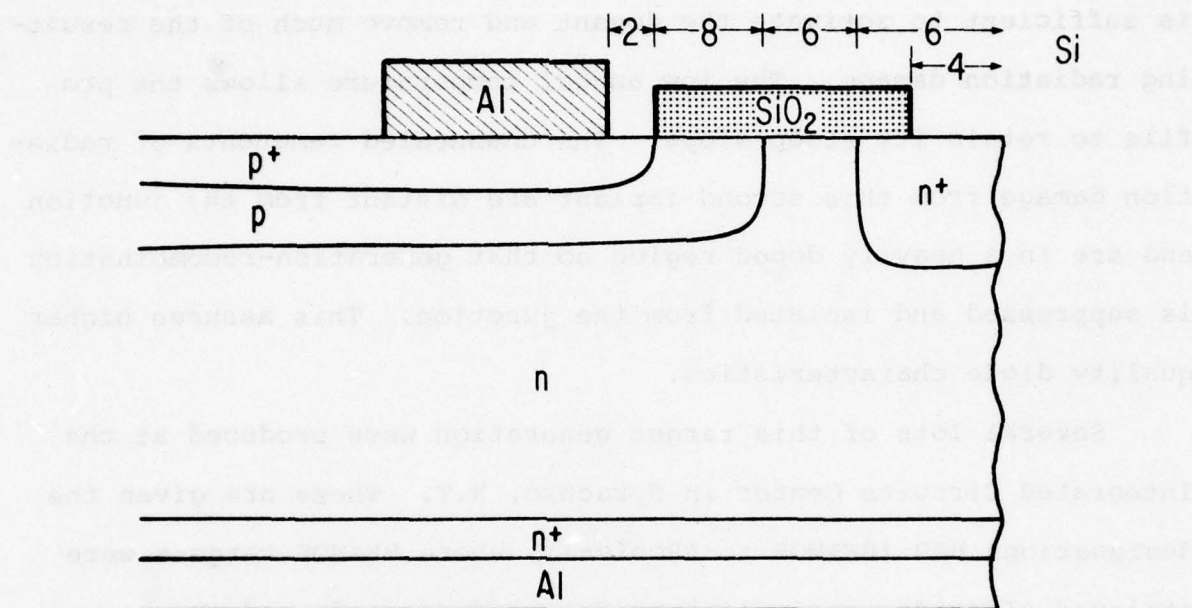


Figure 44. Cross Section of Planar Diode Device as Processed with New Mask Set Z. (All Dimensions in Mils).

which several implantation parameters are varied on the same substrate. This was achieved by masking, implant, mask strip, remask, implant, etc. In this way, for example, four different fluence patterns are produced on the same wafer in the Integrated Circuits Center, and shipped to CRD for evaluation. This method also reduces the effects of the individual substrate on the study of writing quality. Table 3 presents the process procedure for use with the new mask set and Target dimensions and mask layout for PAR lot are given in Appendix III.

A summary of targets produced or used in this period is presented in Appendix II. Implant and processing parameters are indicated for the various groups of targets.

TABLE 1

BAR (n^+np) PROCESS FOR ARCHIVAL PLANAR DIODE SUBSTRATES

1. Strip metallization in PAN etch
2. Photomask with diode mask #3B, (open field) double mask and expose
3. Strip oxide
4. Strip resist
5. Oxidize 14 minutes in Dry O_2 at $1150^\circ C$ for 800 \AA
6. Photomask with diode mask #3B
7. Implant with 100 kV As to $5 \times 10^{14} \text{ ions/cm}^{-2}$
8. Strip resist
9. Branson clean
10. Anneal 1 hour at $900^\circ C$ in N_2
11. Branson clean
12. Dip etch
13. Deposit thick aluminum on front 400°
14. Photomask with mask 2B, positive resist
15. Pattern aluminum
16. Strip resist
17. Deposit 2000\AA Al on back

TABLE 2

NAR (N^+NP) PROCESS FOR ARCHIVAL PLANAR DIODE SUBSTRATE

1. Starting Mat. P-type 10-30 ohm cm <111> Fz Si
2. Branson clean
3. Oxidize 10/90/10 @ 1050°C 6000 Å
4. Photomask with Mask Z1
5. Etch 82424 8 minutes
6. Branson clean
7. Ion implant B^+ , 30 keV, 10^{15} cm^{-2} for back contact
8. Ion implant B^+ , 50 keV, 10^{15} cm^{-2}
9. Remove resist $H_2SO_4 + H_2O_2 +$ rinse
10. Branson clean
11. Oxidize 10/90-10 @ 1050°C for 6000 Å
12. Photomask with Mask Z2
13. Coat back with resist
14. Etch 82424 for 8 minutes
15. Remove resist with $H_2SO_4 + H_2O_2 +$ rinse
16. Oxidize 17 minutes in dry O_2 at 1150°C for 1000 Å
17. Ion implant P^+ , 80 keV 10^{12} cm^{-2}
18. Etch in 82424 for 2 minutes
19. Oxidize at 1200°C in dry O_2 for ≈ 15 minutes for 800 Å
20. Photomask with mask Z3
21. $As^+ 100 \text{ keV } 5 \times 10^{14} \text{ cm}^{-2}$, etch 82424 clear
22. Branson clean
23. Anneal 900°C for 1 hour in N_2
24. Photomask with mask Z5
25. Etch 82424 for 8 minutes (clear back)
26. Strip resist $H_2SO_4 + H_2O_2 +$ rinse

TABLE 2 Continued

27. Thick Al E-beam $10,000 \text{ \AA}$ back
28. Thick Al E-beam evaporation for $10,000 \text{ \AA}$ on front
29. Photomask with mask Z4
30. Coat backside with resist
31. Etch front Al with spray etch
32. Strip resist A-20
33. Sinter Al contacts at 395°C for 10 minutes in N_2

TABLE 3

**PAR (p^+ _{pn}) PROCESS FOR ARCHIVAL PLANAR DIODE SUBSTRATES
PRODUCED USING NEW "Z" MASK SET**

1. Starting material n type 1030 ohm-cm <111> float zone Si
2. Branson clean
3. Oxidize 6000 Å at 1050°C
4. Photomask with mask Z1
5. Etch oxide in 82424 etch for 8 minutes
6. Branson clean
7. Ion implant back contact with 30 kV P⁺ to 10^{15} ions/cm²
8. Ion implant front with 50 kV P⁺ to 10^{15} ions/cm²
9. Remove resist, in H₂SO₄ + H₂O₂, A20, ultrasonic, repeat with fresh H₂SO₄ + H₂O₂ and rinse D.I. H₂O
10. Branson clean
11. Oxidize 6000 Å at 1050°C
12. Photomask with mask Z2
13. Coat back with resist
14. Etch oxide with 82424 etch 8 minutes
15. Remove resist with H₂SO₄ + H₂O₂, A20, ultrasonic, fresh H₂SO₄ + H₂O₂ and rinse D.I. H₂O
16. Oxidize 17 minutes in dry O₂ at 1150°C to grow 1000 Å
17. Ion implant with 50 kV B⁺ to 10^{12} ions/cm²
18. Etch oxide with 82424 2 minutes
19. Oxidize 1200°C dry O₂ 1 hour, in steam 1050°C to 2600 Å
20. Photomask with mask Z3, double coat
21. Ion implant with 50 kV B⁺ to 10^{15} ions/cm²
22. Branson clean
23. Anneal 900°C 1 hour in N

TABLE 3 Continued

24. Photomask with mask Z5
25. Etch residual glass from anneal with 82424 8 minutes (clears back too)
26. Remove resist with $H_2SO_4 + H_2O_2$, A20, ultrasonic, then fresh $H_2SO_4 + H_2O_2$ and rinse D.I. H_2O
27. Deposit with E-beam evaporator 10,000 Å Al on back
28. Deposit with E-beam evaporator 10,000 Å Al on front
29. Photomask front with mask Z4
30. Coat back side of wafer with resist
31. Etch aluminum on front with spray etch
32. H_2O with ultrasonic for mask removal
33. Sinter Al contacts at 395°C for 10 minutes in N_2

SECTION IV

HIGH RESOLUTION WRITING INVESTIGATIONS

The ion written archival target approach has been evaluated by flood beam ion implantation through Cr masks prepared on the surface of the diode targets. This simulates writing by a focused ion beam. The Cr masks are produced by electron beam lithography and chemical etching. After implantation, the Cr patterns are photographed by secondary emission in a scanning electron microscope (SEM). After stripping the Cr film, the diode readout signals are measured in the SEM.

The following section describes recent high resolution writing experiments. Improvements in the modeling of the two dimensional readout theory including defect tailing are also discussed. The first four parts of the section describe recent improvements in measurement and sample preparation techniques related to these studies.

A. Beam Current Control

The Coates and Welter scanning electron microscope system was used for electron beam resist exposure to form metal implantation masks for the ion writing experiments. To achieve greater uniformity and precision in the exposures, the beam current was intermittently monitored using a Faraday cup. The tip was operated in a built-up thermally cleaned field emission mode, at beam currents between 0.5 and 3 nanoamps. A landing potential of

16 kV was used for the electron beam to pattern the resist. The beam current was monitored (Figure 45) and a noise variation on the order of 15% was observed. This noise reduction was achieved by the TFE filament heater operating with mode control setting between 50 and 100. This stability could be reached in two ways: 1) By setting the filament heater Control at 75; about an hour later stable operation at the 1 or 2 nanoamp level could be attained; 2) If the setting was placed at about 200 (higher current) initially, this beam current level was achieved quickly, and by backing off to 50 or 100, stabilized beam current at this desired level was achieved quickly.

B. New Test Pattern

A new test pattern was developed for use in electron beam exposures of PMMA etch masks for producing chrome metal barrier implantation masks. This pattern is shown in Figure 46. This pattern provides both isolated written and unwritten lines of various dimensions. The data read from these line patterns is more reproducible than that from dot patterns because beam positioning during readout is not as critical. This pattern was used along with the isolated dot pattern shown in Figure 27 of the Fourth Quarter Phase I report.

C. Improved CR Etching

A number of improvements in Cr etching techniques for producing high resolution implant mask patterns have been implemented.

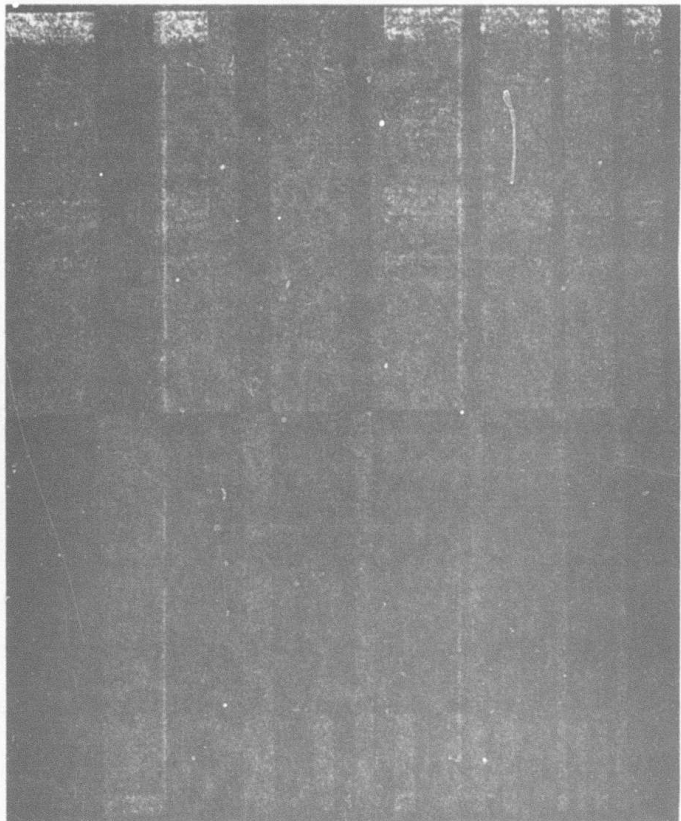


Figure 45. Plot of C&W SEM Emission Current
as a Function of Time Showing
Beam Stability

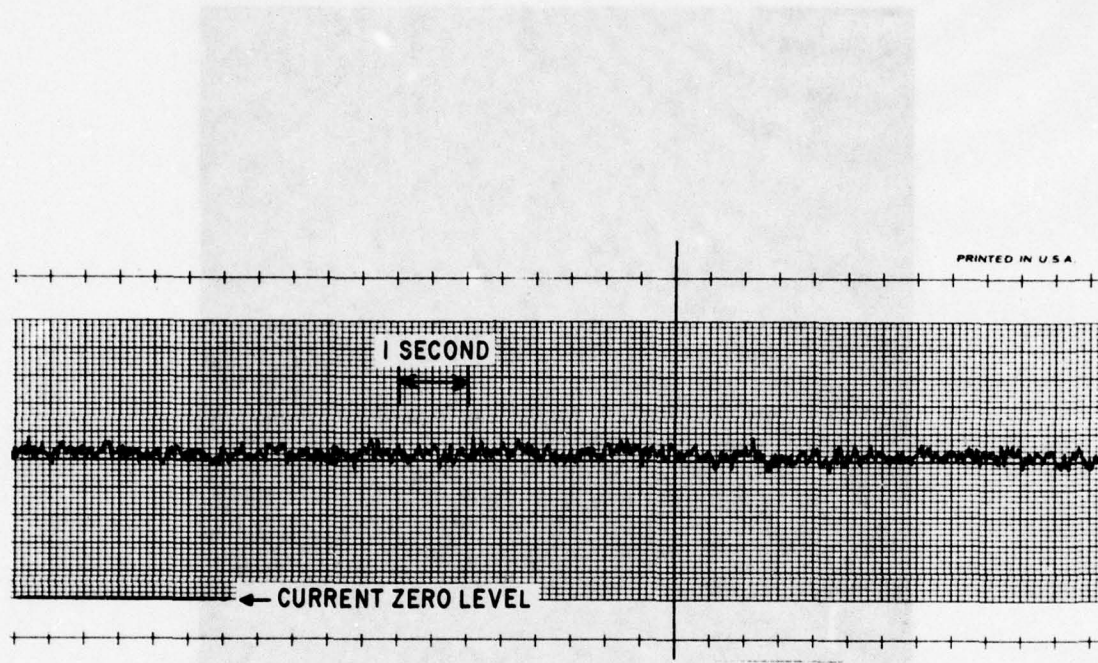


Figure 46. Test Pattern Used to Produce Isolated Written and Unwritten Lines

These largely involved greater precision in the etch reaction and improved cleanliness.

The steps preceding the etching operation include the deposition of 500 Å of sputtered chrome on the surface of clean diode substrates, the spinning of the polymethyl methacrylate resist for 1 minute at 2000 RPM, and the development and exposure of this resist. This leaves the areas to be stripped of chrome open for chemical action.

In addition to more cleaning steps and an isopropyl rinse following development to remove polymer residue, considerably greater care was exercised in regard to temperature control of the etch and rate calibration. Fresh etch solution and clean glassware is used for each wafer etch. The solution is heated to near the 50°C temperature, and not allowed to temperature overshoot past 55°C. During the etch operation, control is maintained within 0.5 degree of 50°C. Vigorous agitation is used to keep a fresh supply of active solution at the wafer surface at all times. The etch period is timed within 1 second accuracy.

For each sputter deposition of chrome and each new batch of etch (mixed from two components), the etch rate is calibrated from the time needed to clear a glass slide with the same Cr thickness as the wafers. The time required is tested in 5 second increments to achieve maximum clearance with minimum undercut. The minimum time increment is selected which removes the chrome film to the point of optical and reflected transparency.

At the end of the timed etch, the sample is immediately plunged into a distilled water bath, swirled vigorously, and then into a second distilled water bath, followed by a flowing distilled water rinse to remove all etch and possible accompanying residue.

The etched sample with the resist still on is then inspected in an optical microscope to insure that open areas indeed are clear, and then the resist is stripped. The resulting Cr pattern is then given a preliminary optical microscope evaluation to determine the quality of the resolution, and is then ready to serve as an implantation mask. The complete implant mask formation process is summarized in Table 4.

D. Lift-off Experiments

In an effort to produce better definition in high resolution chrome patterns, another method, commonly called lift-off was used to selectively remove metallization. With this technique, the bare semiconductor is coated with the electron sensitive polymer first, then patterned, and developed. The target, with the patterned areas open, is then metallized. When this structure is then soaked in the resist solvent, the metal layer which lies over polymer floats off, with the resist, while that which is in direct contact with the semiconductor adheres. In this way high resolution metal masks can be produced.

TABLE 4

PROCESSING ARCHIVAL SUBSTRATES FOR E-BEAM EXPOSURE AND ION WRITING

1. Complete planar diode structure
2. Clean in boiling solvents, trichlor, acetone, 2-propanol, then DI rinse
3. Sputter etch, then sputter 500 Å Cr
4. Spin on PMMA from bottle #2, 1 minute at 2000 RPM, bake 15 minutes 170°C
5. Expose and develop -

soak	1 min
spray	30 sec
6. Bake 10 minutes at 120°C
7. Etch at 50°C C-25 etch, about 35 seconds, fresh etch, clean beaker
8. Quench wafer immediately in DI bath, then second DI bath, then rinse in running DI
9. Examine etch in optical microscope
10. If satisfactory, remove PMMA

soak	5 min
spray	30 sec
11. Writing implant
12. Photograph chrome patterns in SEM
13. Three solvent clean in room temperature trichlor, acetone, 2-propanol DI rinse
14. Strip Cr with room temperature Bell and Howell CR etch
15. Three solvent clean, trichlor, acetone, ethyl, DI rinse
16. BHF back, edges of mesa
17. Examine diode signals

In a series of preliminary experiments, parameters for successful lift-off were studied using blank wafers. In the first test, PMMA resist was spun on at 2000 rpm for 1 minute to produce a 0.6 film, and baked 16 minutes at 170°C. After pattern exposure and development, 2 minute soak, 30 second spray, 600 A of Au was deposited by evaporation. Attempts at lift-off resulted in debris remaining in the pattern, indicating a longer spray cycle, and perhaps more complete development was needed. In a second test, a 20 minute soak cycle in ethyl acetate, with 15 second sprays at the 12 and 16 minute points, produced considerably superior results. However, still some areas of the pattern did not clear and sections of the gold did not adhere properly. One of the most critical points in the lift-off process is that a very clean surface is required for proper metal pattern adhesion through processes sufficient to lift the rest of the metal. In order to facilitate this, a longer development of the PMMA was deemed appropriate to increase undercutting of the resist patterns as well as an ethanol and DI rinse to provide good contact surface for the metal.

Lift-off techniques were used to pattern target B109D, a p⁺ top layer archival diode structure. Approximately 0.95 microns of PMMA resist was spun on for 1 minute at 2000 RPM and then prebaked 16 minutes at 170°C. After electron beam exposure and development for 1 minute with 30 second spray and thorough rinsing, 300A of gold was evaporated over the resist. A 20 minute soak of the PMMA in ethyl acetate with 60 second spray resulted in the gold lifting in most areas and no patterns.

The target was then put through the pattern process again, with the gold stripped, HF dip, repeated DI rinses, and solvent cleaning in trichloroethylene, acetone, and proponal. Again resist (0.95μ) was spun on, and baked 16 minutes at 170°C . Development proceeded with a 160 second soak, 30 second spray, followed by 120 second soak, 30 second spray. Chrome was then deposited by evaporation to a thickness of 600A. Three minutes in ethyl acetate, then 30 second spray then a 1 minute soak followed by 15 second spray, rinse in ethyl alcohol, rinse in DI and then a blow dry, resulted in fair lift-off and the retention of the coarse patterns on the order of 0.4μ .

Similar results were achieved with target B109A. The patterned PMMA was metalized with 500A evaporated chrome, and then lift-off was brought about by 1 minute soak in ethyl acetate, 30 second spray, 30 second ethanol soak, 25 second DI rinse, then another cycle of 5 minute ethyl acetate soak, 1 minute boil, ethanol rinse, DI rinse. Still fine parts of the pattern had not lifted. A 30 second ultrasonic ethyl alcohol clean, followed by ethanol and DI rinse, then a 4 minute soak in ethyl acetate, and 1 minute ultrasonic clean in ethyl acetate, 2 minutes ultrasonic treatment in ethyl alcohol, 5 minute ultrasonic in acetone, 5 second dip 50°C C-25 Cr etch, 21 minute ultrasonic clean in acetone resulted in 0.4μ patterns. Parts of the smaller ones were lost, and some of the very small areas would not lift.

Target 105-7(1) was exposed and patterned, and then 500A Cr was deposited by evaporation. Ethyl acetate was used to lift

off the chrome by a 2-1/2 minute spray, 30 second soak, 2 minutes ultrasonic, followed by 15 second rinse in ethanol, and a 10 second rinse in DI. A large portion of the patterns were again lost, however some useful line structures on the order of 0.5μ were preserved.

The lift-off technique did not prove satisfactory for the production of the very high resolution (on the order of 0.1μ) metal patterns of interest. Although, with cleanliness and care, high resolution patterns were produced, they did not consistently meet the quality standards needed. Finer structures were afforded by the conventional wet etching techniques for chrome metallizations, with considerably less debris interfering with the patterns. A better alternative to wet etching to produce metal patterns with greater edge definition would be ion beam etching. Although this process tends to erode the resist walls, resulting in some degradation of the pattern, it has been shown to be effective for high resolution work.

E. Bit Spacing Criterion

Figure 47 shows the format for both the theoretical and experimental studies. Two types of bit patterns are studied: The isolated written and unwritten areas. Each of these patterns can be described by a single feature or pattern size parameter W. In the case of focused ion beam writing, W is identified with the bit spacing. This identification is exact if the ion beam spot size and the bit spacing are each equal to W. For the Cr pattern experiments, W is the size of the hole in the

Cr film or the size of the island of Cr. From the readout gain measurements, isolated bit gain plots are determined as indicated in Figure 47. The crossing point of these two curves serves as a good estimate of the minimum achievable bit spacing. This can be seen from the following argument. If a simple level detection data recovery method were utilized, then the crossing point represents the minimum bit spacing achievable (if the signal-to-noise were infinite), and there were no other noise sources such as target defects.

More sophisticated data encoding and recovery techniques which rely on derivative processing can realize significant improvements, thereby permitting operation near the crossing point in realistic situations. The reduction in the gain of the isolated unwritten area is due to the interaction of at least eight adjacent bits. Sequentially, bits have four of these eight adjacent bits in common, so derivative processing can significantly remove the effect of cross-talk due to these four adjacent bits. This is similar to data recovery in BEAMOS targets. Derivative processing has been successfully applied to the BEAMOS memory device.

F. Two-dimensional Model

A two-dimensional model for the target bit spacing density was developed during Phase I and discussed in the First Quarter Report. The predictions of this model will be re-examined in light of the defect spreading measurements described earlier. Figure 48 shows cross sections of a written archival target. Two cases corresponding to isolated written and unwritten areas are shown. The feature size is 0.2 micron, which is the size of the corresponding feature in the Cr mask. In Figure 48, a typical

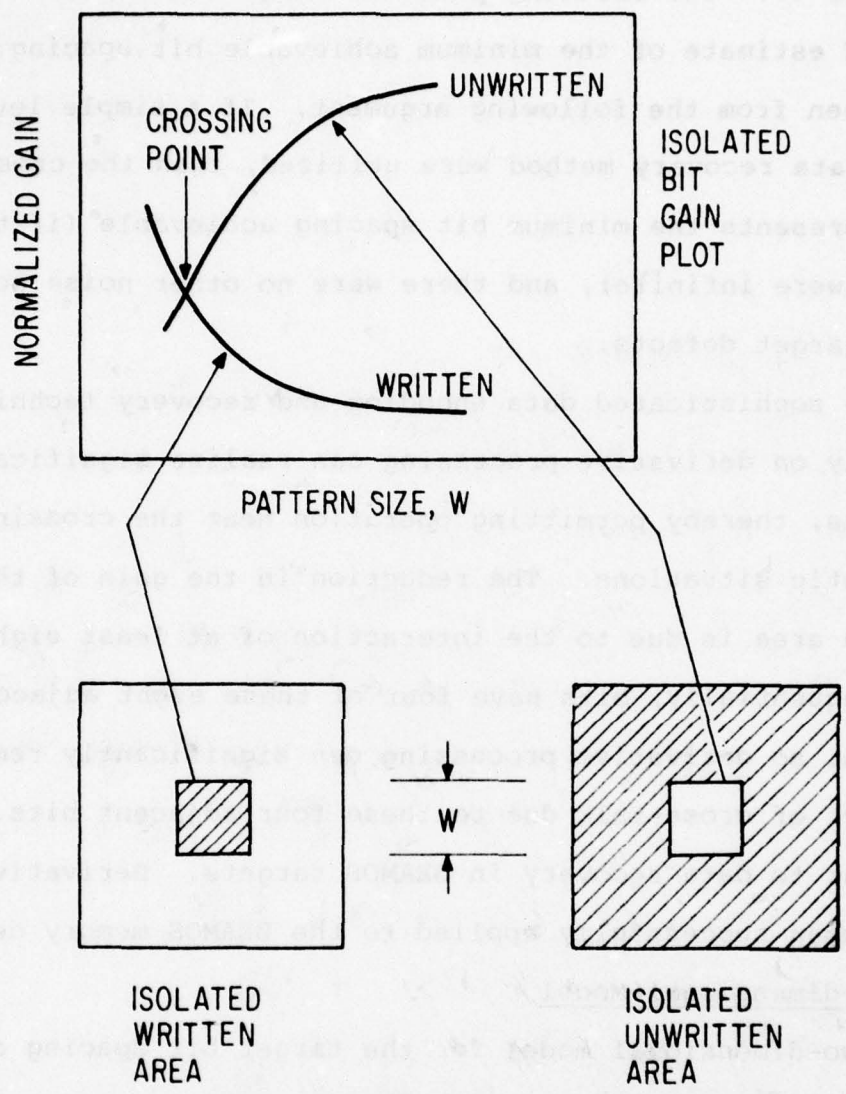


**Figure 47. Definition of Isolated Bit Gain Plot
for the Determination of the Minimum
Bit Spacing**

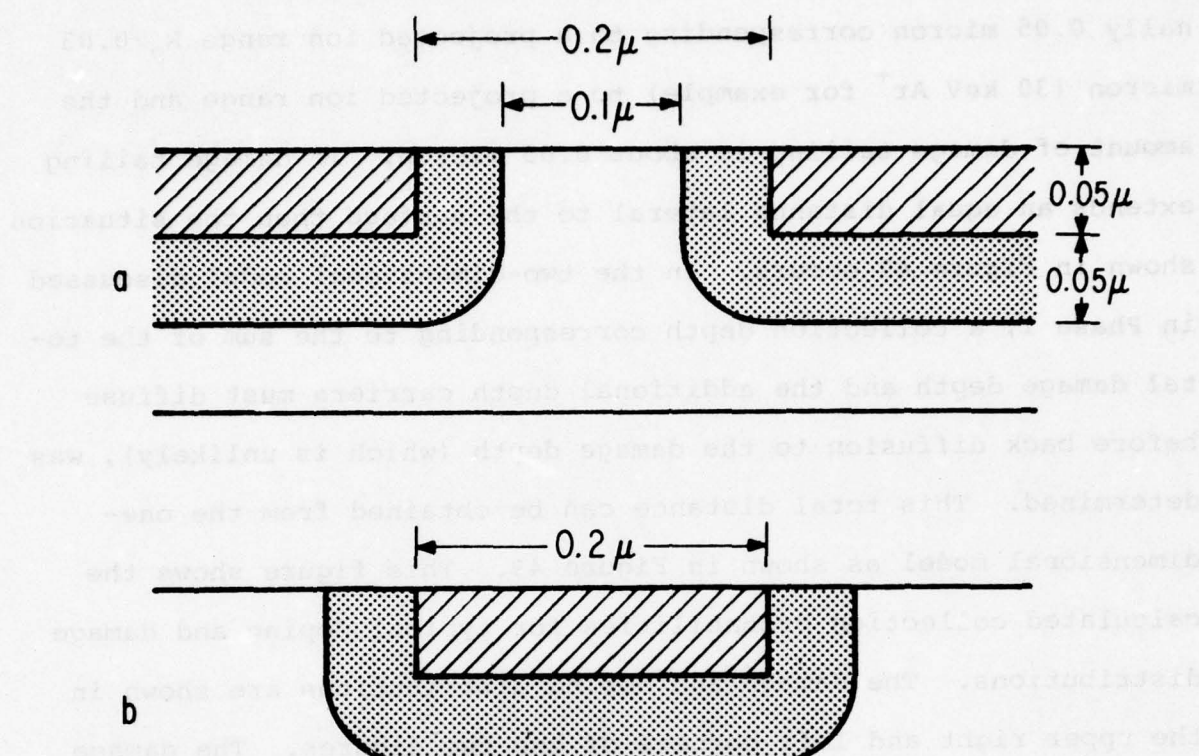


Figure 48. Cross Section of an Ion Written Archival Target for the Case of (a) An Isolated Unwritten Area and (b) An Isolated Written Area

writing condition is assumed where the depth of the main part of the damage distribution (the Brice or Gaussian part) is nominally 0.05 micron corresponding to a projected ion range $R_p \approx 0.03$ micron (30 keV Ar⁺ for example) to a projected ion range and the amount of damage tailing is about 0.05 micron. If damage tailing extends an equal distance lateral to the surface then the situation shown in Figure 48 occurs. In the two-dimensional model discussed in Phase I, a collection depth corresponding to the sum of the total damage depth and the additional depth carriers must diffuse before back diffusion to the damage depth (which is unlikely), was determined. This total distance can be obtained from the one-dimensional model as shown in Figure 49. This figure shows the calculated collection probabilities for typical doping and damage distributions. The damage and doping distributions are shown in the upper right and left corners of the two figures. The damage distribution corresponds to Ar⁺ at 30 keV. Shown in each figure are the collection probabilities versus depth for the three cases of the complete damage distribution, no damage, and damage without damage tailing. For the damage cases $\tau_p = 10^{-13}$ seconds which corresponds to ion writing fluences $\sim 10^{13} \text{ cm}^{-2}$. Figure 49b is typical of the steeper doping gradient archival targets; this figure will be used in the following discussion. Figure 49a is included for reference to show the effect of less steep doping gradients. For Figure 49b the collection probability in the written area reaches 0.9 at $z = 0.14$ micron as compared to 0.09 micron without the damage tail. Also the diameter of the unwritten region

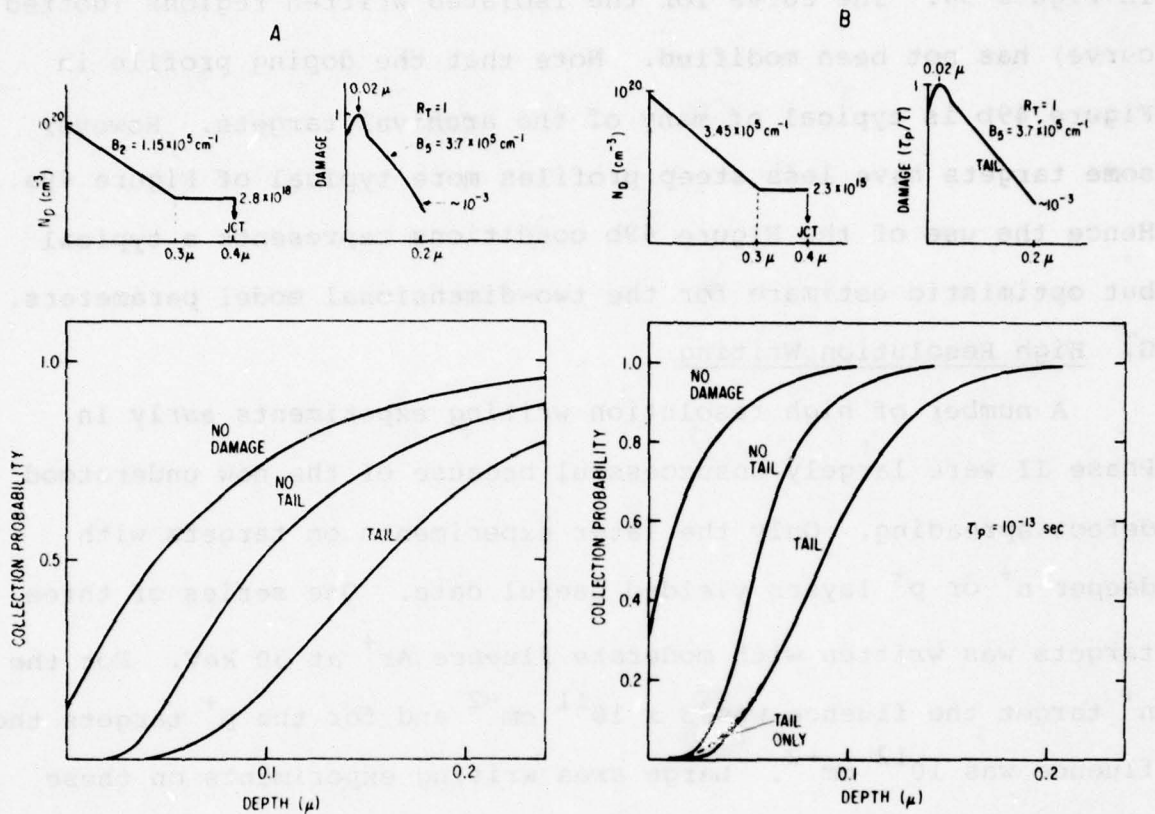


Figure 49. Calculated Collection Probability vs Depth for Typical Doping and Damage Profiles Shown in the Upper Part of the Figures for N^+P Diode. Damage Cases are for $\tau_p = 10^{-13}$ sec. For the No Damage Cases, $S_v = 10^6$ cm/sec.

is decreased because of the increased lateral diffusion of the defects. The result of these two effects on the model is shown in Figure 50. The curve for the isolated written regions (dotted curve) has not been modified. Note that the doping profile in Figure 49b is typical of many of the archival targets. However some targets have less steep profiles more typical of Figure 49a. Hence the use of the Figure 49b conditions represents a typical but optimistic estimate for the two-dimensional model parameters.

G. High Resolution Writing

A number of high resolution writing experiments early in Phase II were largely unsuccessful because of the now understood defect spreading. Only the later experiments on targets with deeper n⁺ or p⁺ layers yielded useful data. One series of three targets was written with moderate fluence Ar⁺ at 30 keV. For the n⁺ target the fluence was $3 \times 10^{11} \text{ cm}^{-2}$ and for the p⁺ targets the fluence was 10^{12} cm^{-2} . Large area writing experiments on these or similar targets predicted written areas collection efficiencies of about 0.05 at 2 keV. More important, these writing conditions are consistent with the expected performance of the focused ion column, which will provide up to $6 \times 10^{11} \text{ ions/cm}^2$ in a 0.1 micron spot, at 30 to 60 keV and 10 mbits/sec. The results for isolated bit and bar measurements are summarized in Figures 51 through 53. The three samples behave almost identically. Figure 54 compares the isolated bit or dot data to the predictions of the model. The model has been adjusted for the high written gain level of the targets by scaling it according to the equation:

$$G = (G(0) + G_w)/(1 + G_w),$$

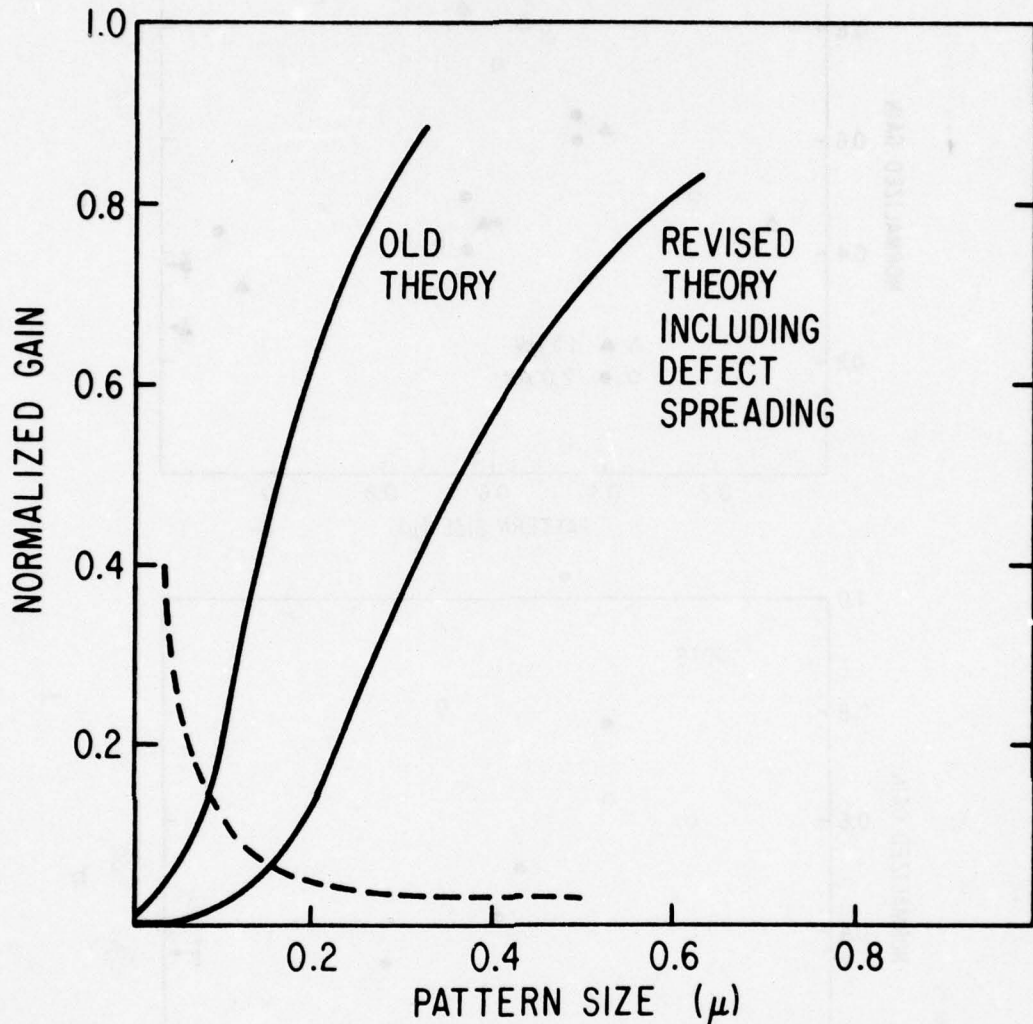


Figure 50. Normalized Gain Versus Pattern Size Based On the Two-dimensional Resolution Model. Curve labeled "old" assumes no defect tailing and a very steep N^+ doping profile. The revised theory includes the effect of defect tailing for a 30 keV Ar^+ writing beam at a fluence 10^{13} cm^{-2} and a less steep doping profile.

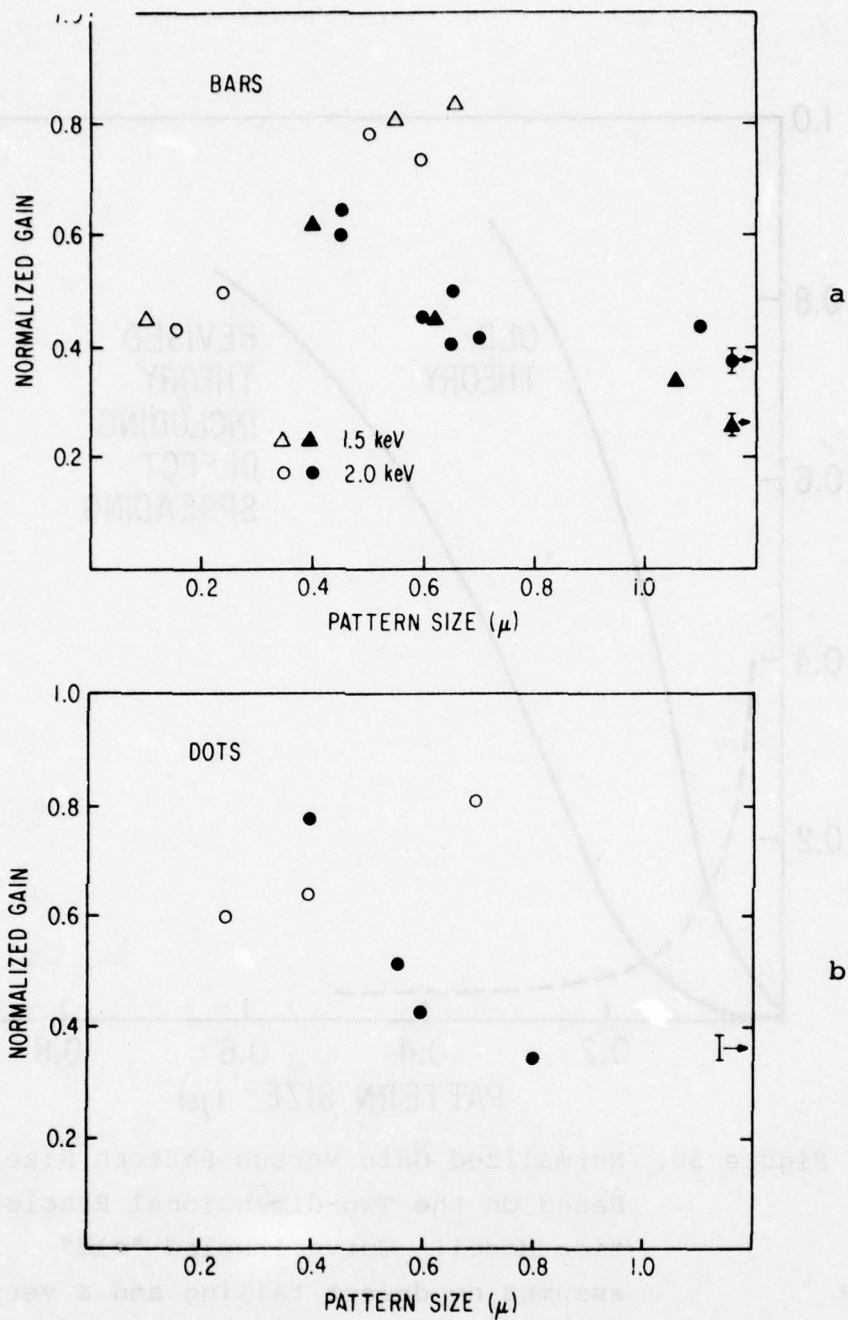


Figure 51. Normalized Readout Gain at 1.5 and 2 keV for N^+ NP Sample 109-23(3) written with Ar^+ at 30 keV and $3 \times 10^{11} \text{ cm}^{-2}$. Solid point are isolated written and open points isolated unwritten (a) bars and (b) dots.

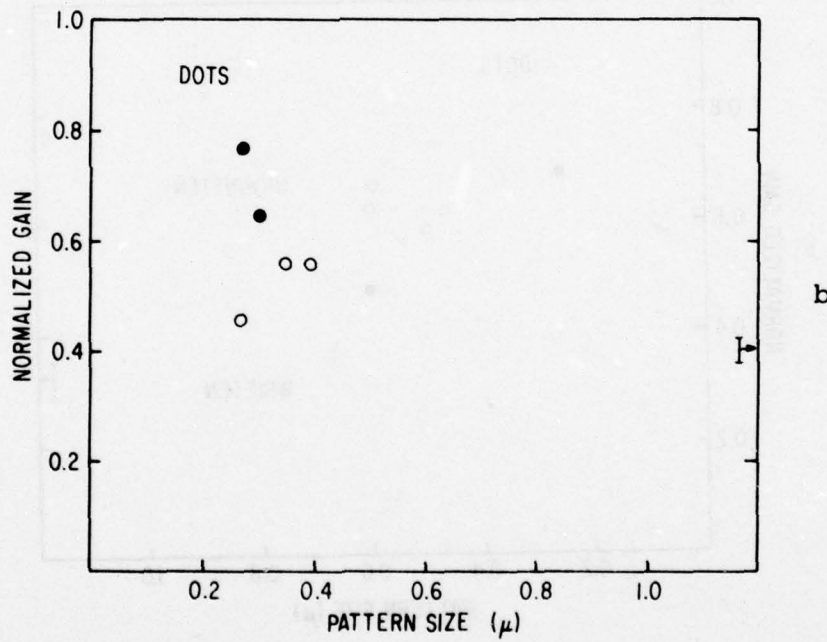
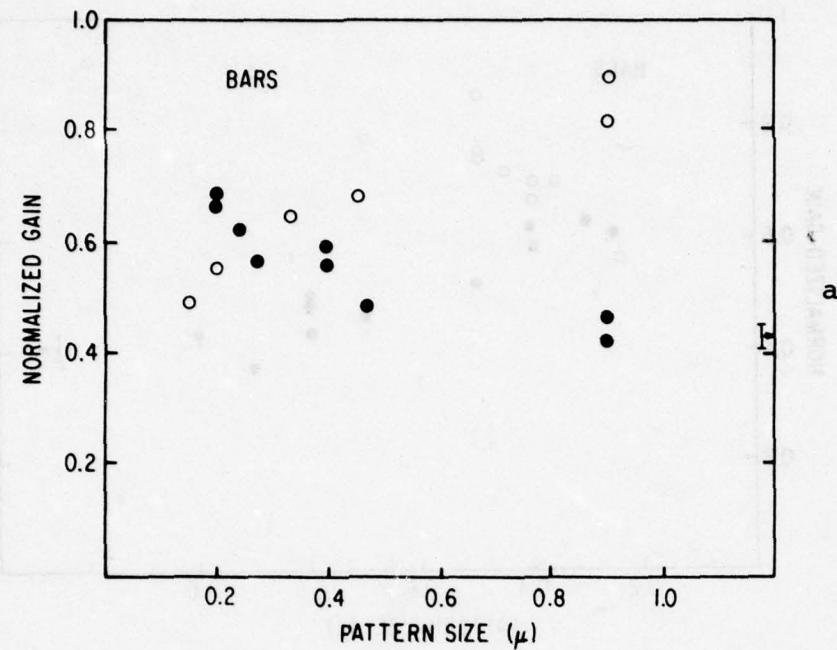


Figure 52. Normalized Readout Gain at 2 keV for P^+N
 Sample B2-1C Written with 30 keV Ar^+ at
 10^{12} cm^{-2} . Open points are isolated
 unwritten and solid points isolated
 written (a) bars and (b) dots.

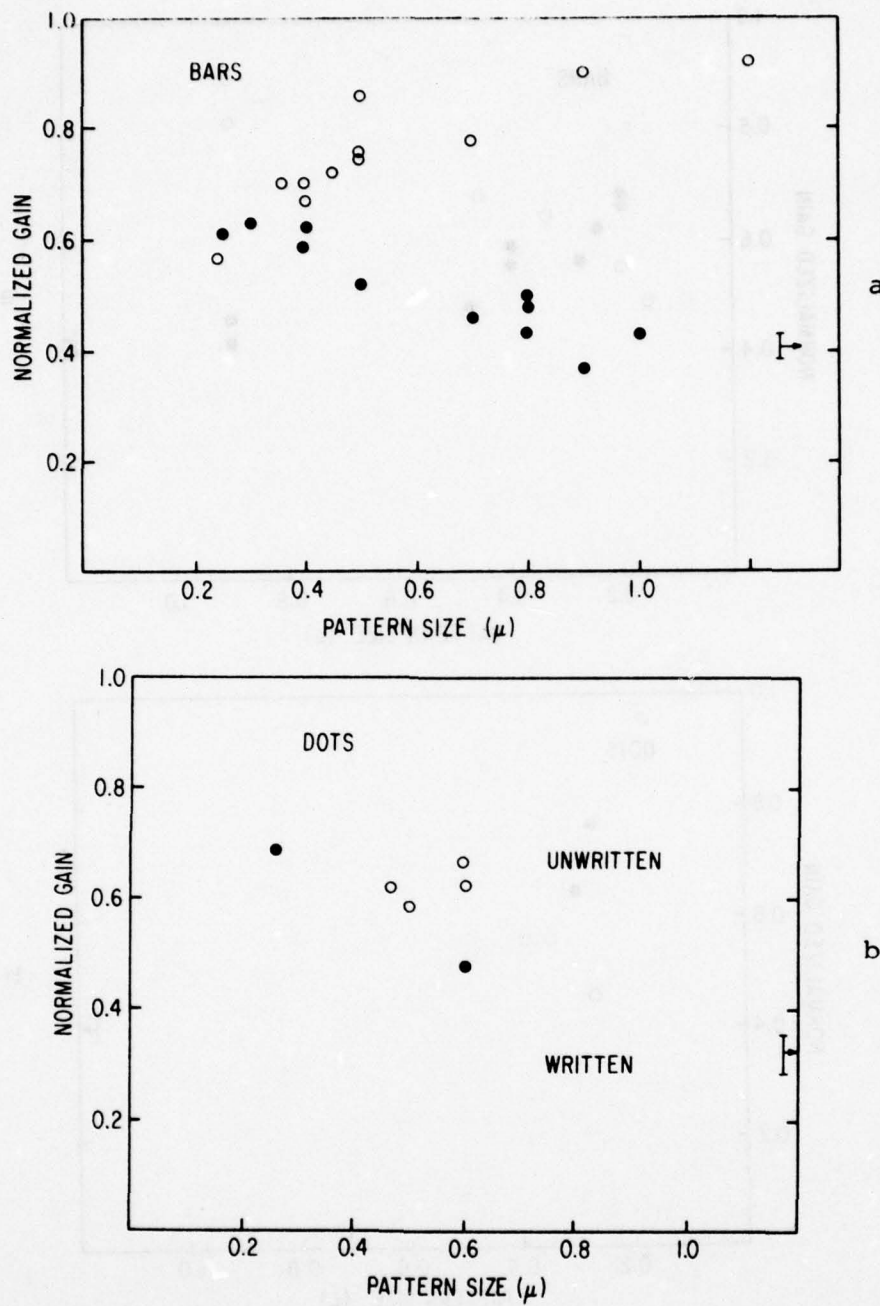


Figure 53. Normalized Readout Gain at 2 keV for P^+N
 Sample B2-5A Written with 30 keV Ar^+ at
 10^{12} cm^{-2} . Solid points are isolated
 written and open points are isolated
 unwritten (a) bars and (b) dots.

and at 109-23(3) the step height between baseline and at 20 microns
evidences no change and each .0 = 0.0 micrometers
-as of periodicity of 20 microns and the same utilization
of the 109-23(3) sample.

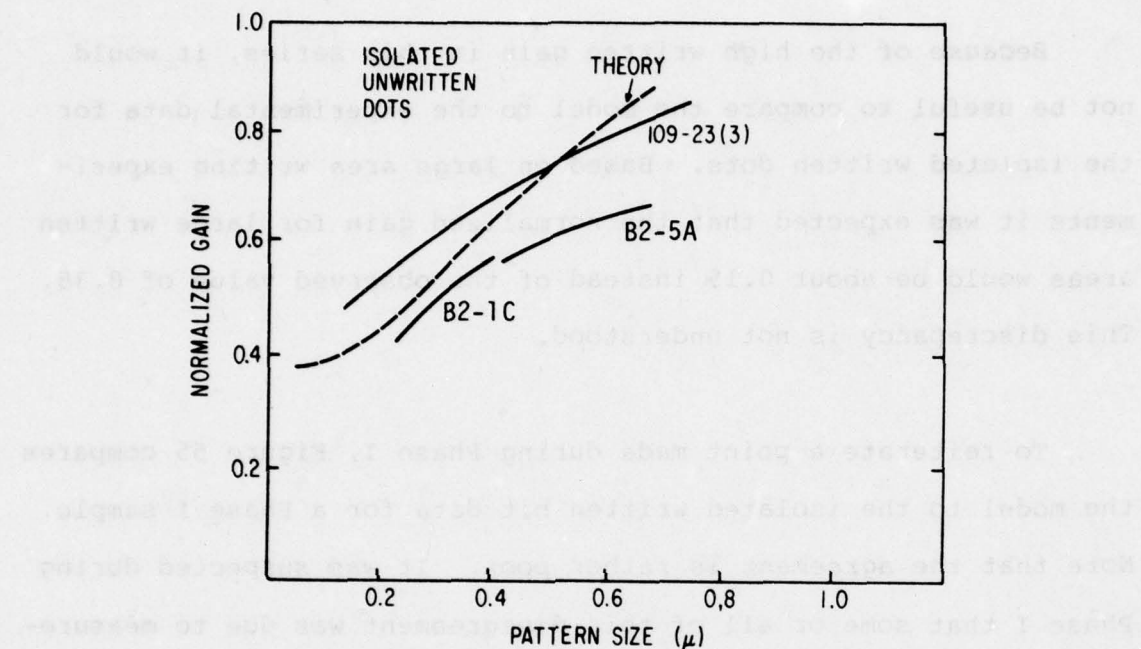


Figure 54. Comparison of Isolated Unwritten Dot Data
for the three Samples of Figures 5, 6, and 7
vs pattern size. Theory based on two-
dimensional diffusion model as described
in text.

where G_w is the normalized large-area written gain and $G(0)$ is the normalized gain when $G_w = 0$. Note that agreement is reasonably good, indicating that the poor resolution may be attributed to defect spreading.

Because of the high written gain in this series, it would not be useful to compare the model to the experimental data for the isolated written dots. Based on large area writing experiments it was expected that the normalized gain for large written areas would be about 0.15 instead of the observed value of 0.35. This discrepancy is not understood.

To reiterate a point made during Phase I, Figure 55 compares the model to the isolated written bit data for a Phase I sample. Note that the agreement is rather poor. It was suspected during Phase I that some or all of this disagreement was due to measurement errors and electron beam spot size effects. One principal measurement problem was 60 Hz noise on the electron beam sweeps which prevented accurate positioning of the beam during readout of small patterns. This has been reduced by improvements in the electronics and increased magnetic shielding. An additional measurement problem was a difficulty in determining the size of the openings at the bottom of the Cr mask. Experiments during Phase II have generally used 0.05 instead of 0.1 micron thick Cr. Only 0.02 micron is required to stop most of the writing ion beam. This 0.05 micron thickness gives a reasonable safeguard against penetration of the writing ion beam while permitting a more accurate measurement of the size of the bottom of the Cr hole.

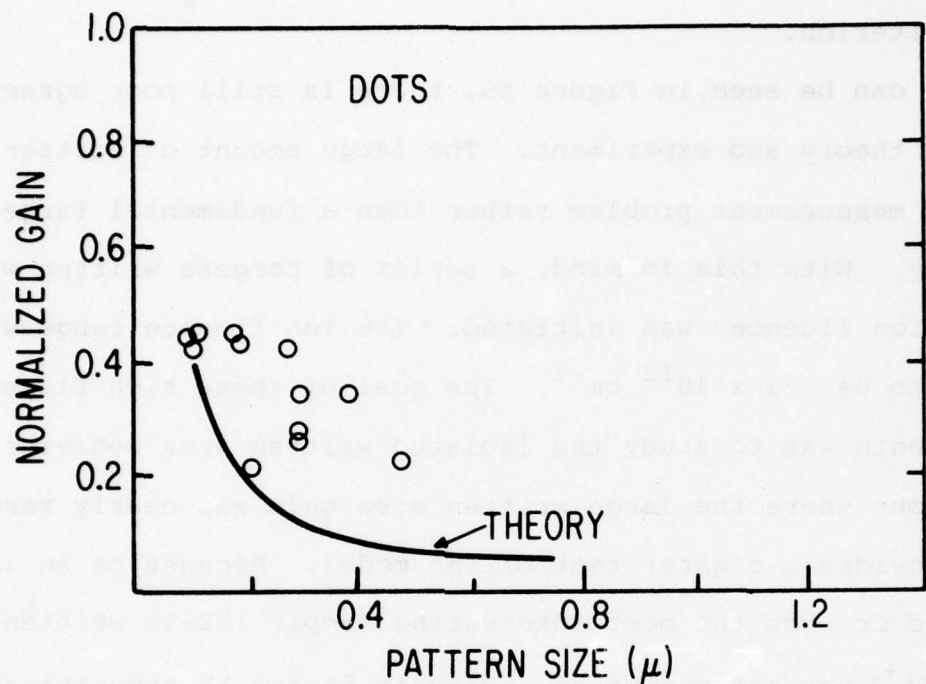


Figure 55. Isolated Written Dot Data vs Pattern Size for Sample Bl3A Written with 145 keV Xe^+ at 10^{12} cm^{-2} and 40 keV Xe^+ at 10^{11} cm^{-2} from Phase I. Theory based on two-dimensional model from Phase I.

This problem was discussed in the Fourth Quarter Phase I Report. All hole sizes in this report are the diameter of the black hole in the center of the SEM image. The data in Figure 9 has been replotted from the Phase I Report using this criterion.

this criterion.

As can be seen in Figure 55, there is still poor agreement between theory and experiment. The large amount of scatter suggests a measurement problem rather than a fundamental target property. With this in mind, a series of targets written with higher ion fluences was initiated. The ion fluence range was chosen to be $3 \times 10^{12} \text{ cm}^{-2}$. The goal of these high fluence experiments was to study the isolated written area behavior under conditions where the large written area gain was nearly zero. This provides a clearer test of the model. Because of an incomplete Cr etch the most interesting sample (B2-5D written with 30 keV Ar⁺) was not evaluated. Figures 56 and 57 show the results for a P⁺ type of target written with fluence of 50 keV As⁺ at $2 \times 10^{14} \text{ cm}^{-2}$. As⁺ should produce damage similar to Kr⁺. The ultimate goal of this sample is to compare doping writing to damage writing. However, before anneal, the only expected effect of the As⁺ implant is to produce damage writing. Hence it provides a good sample for the study of the anomalous behavior of the isolated written bits. Note that, as expected, for this high writing fluence the written gain at large W is very low. The small amount of residual gain was not expected and the reason for this is under investigation. Figure 56 also compares these measurements to the two-dimensional model. The agreement for

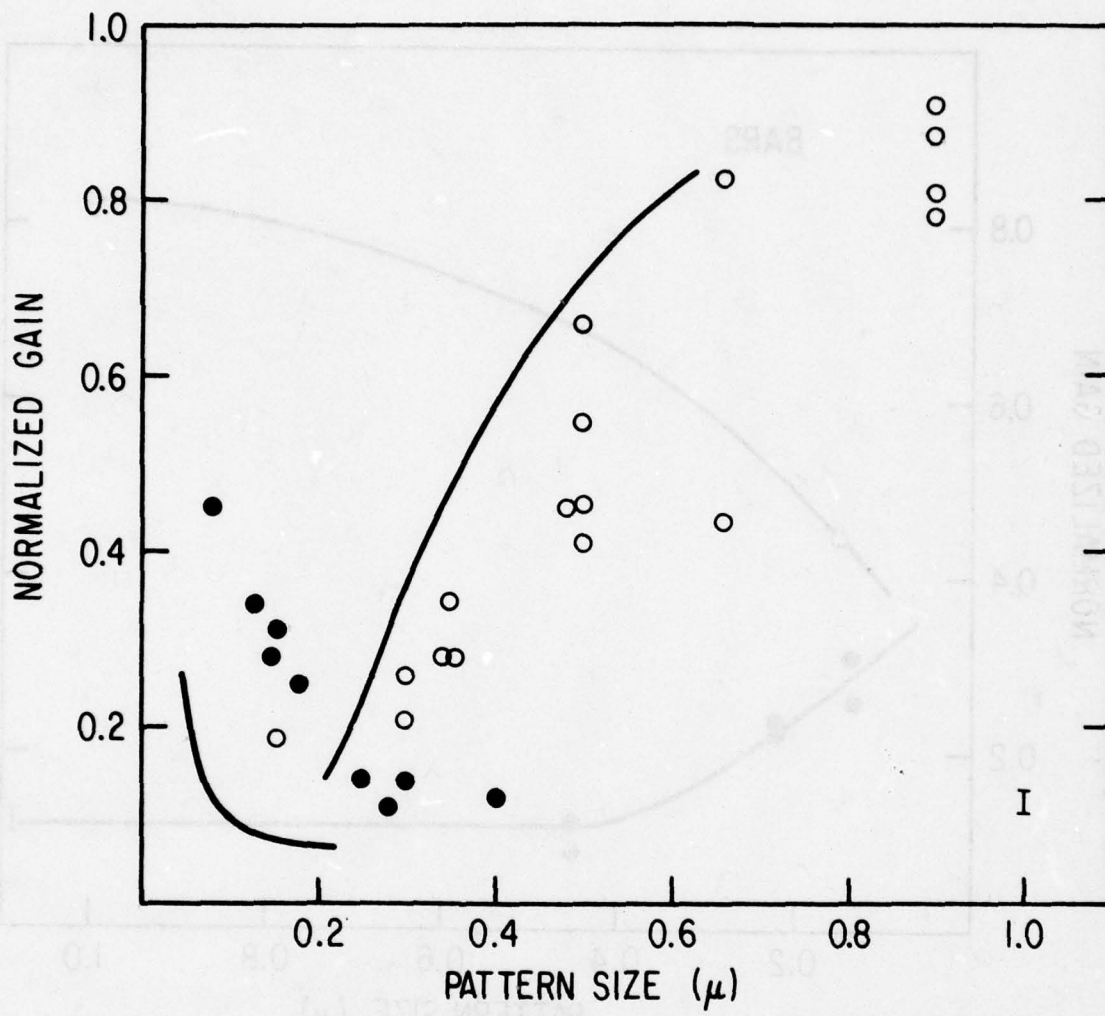


Figure 56. Normalized Gain Vs Pattern Size for Isolated Written and Unwritten Dots for Sample B2-1b Written with 50 keV As⁺ at $2 \times 10^{14} \text{ cm}^{-2}$. Solid lines are theory including the effect of defect tailing. Beam current 0.5 nA at 2 keV in field emission mode.

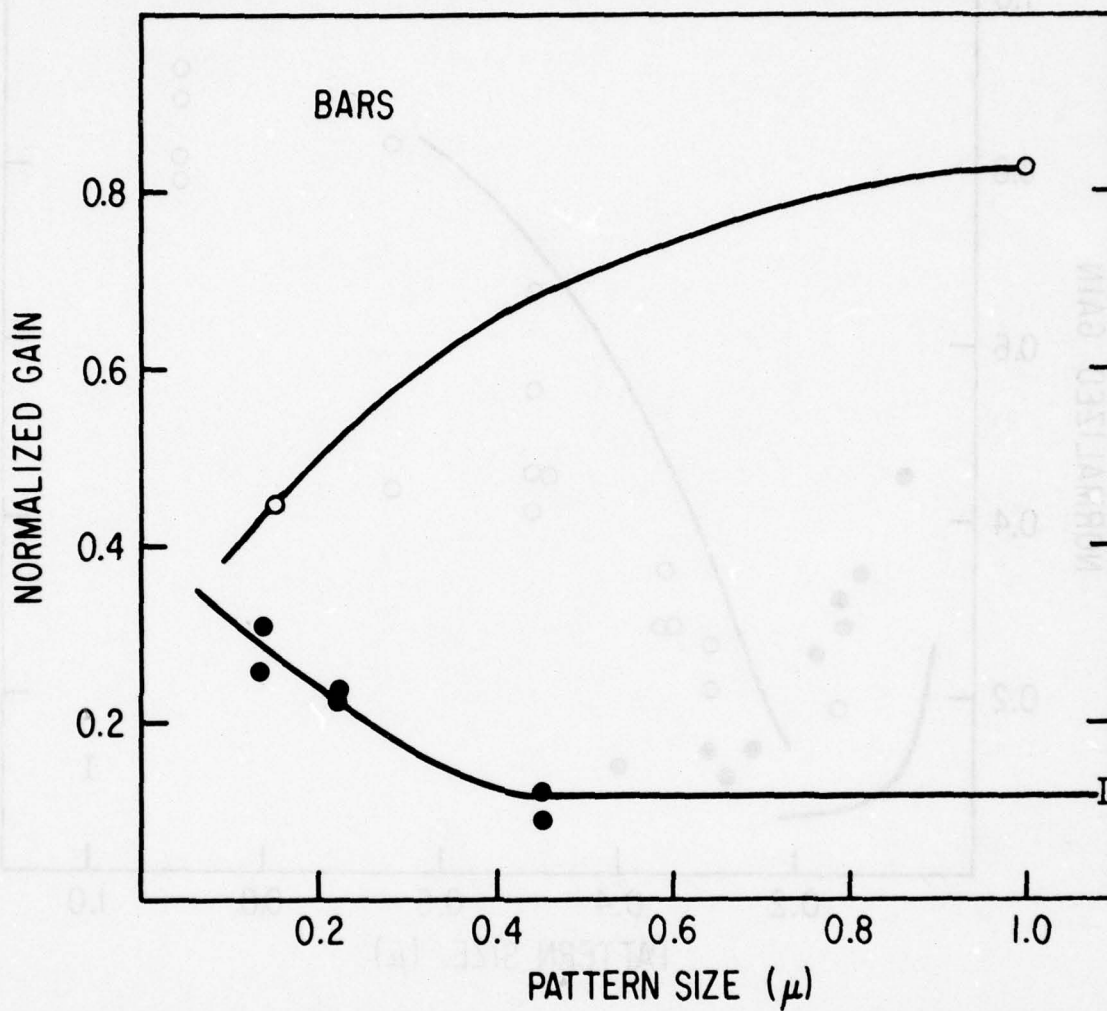


Figure 57. Normalized Gain vs Pattern Size for Isolated Written and Unwritten Bars for Sample B2-1B Written with 50 keV As⁺ at $2 \times 10^{14} \text{ cm}^{-2}$. Beam current 0.5 nA at 2 keV in field emission mode.

the isolated unwritten areas is reasonably good. If the model were refined to match these very heavy writing conditions the fit would be further improved. The agreement for the isolated written areas is not as good. This disagreement is surprising since, for these heavy writing conditions, the size of the actual damage region is much larger than the feature size. The most likely explanations for this poor disagreement are poor focus of the reading electron beam and saturation effects in the carrier recombination process. Data were also taken in the thermally assisted field emission (TFE) mode of the C&W SEM. The plotted points of Figure 56 were taken in the cold field emission (FE) mode. The TFE points were taken at 5nA while the FE points were taken at 0.5 nA. Comparison of secondary electron images indicated that the focus was better for the FE condition. The resolution data have been taken when the secondary image resolved better than 0.05 micron structures. This should have insured that the spot size was less than 0.05 micron. However, a spot profile such as shown in Figure 58 could give 0.05 micron resolution in secondaries but much poorer resolution in diode readout because the diode signal sums the contribution from the entire beam, while the secondary signal tends to display the derivative of the signal. During the next quarter of Phase II an examination of the spot profile of the C&W SEM is planned.

The second possibility is a saturation effect in the recombination process. One way to check for this is to look for a change in the written gain level as a function of beam current density. This was done on sample B2-1C, and Figure 59 shows a plot of

BEAM CURRENT DENSITY

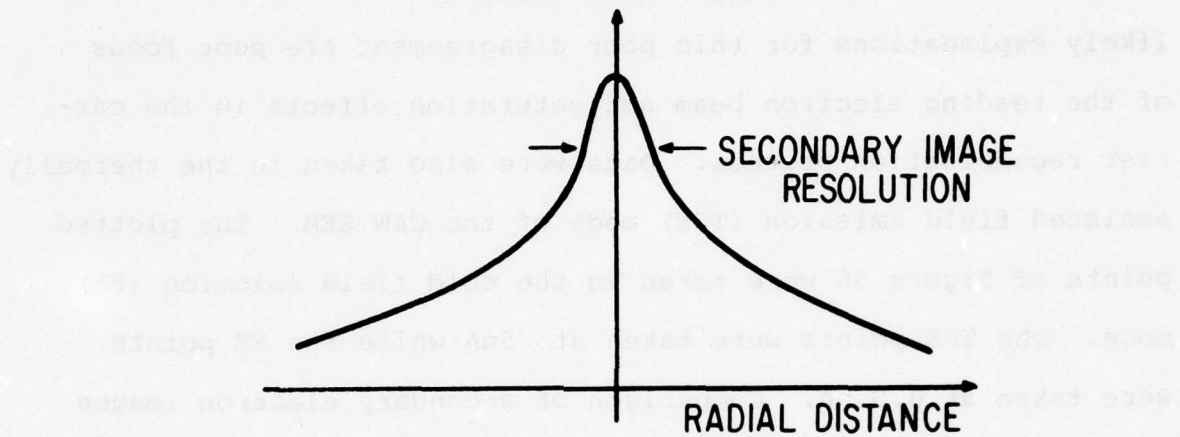


Figure 58. Possible Beam Profile Which Could Explain Good Secondary Images and Poor Resolution in Diode Readout

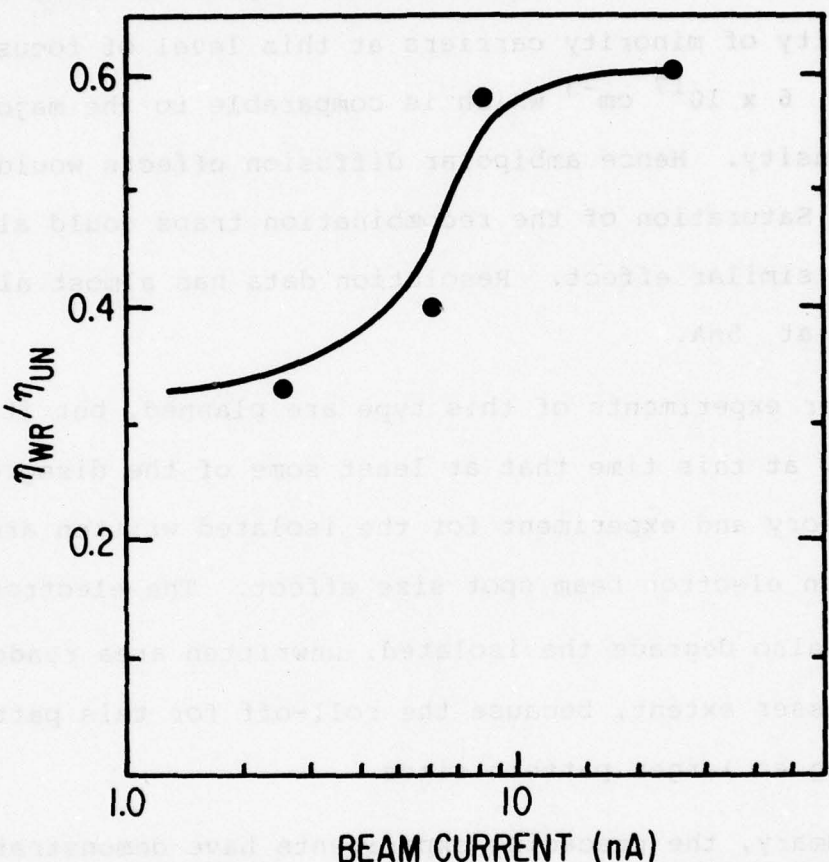


Figure 59. (Written Gain)/(Unwritten Gain) vs Beam Current

for a Large Written Area of Sample B21-C.

(See Figure 56) Beam well focused. High

current points in thermally aided field

emission mode.

the normalized gain in the large written areas as a function of beam current for a well focused beam (estimated spot size between 0.05 and 0.1 micron). Note that around 7nA there is a rapid change in the gain. This is not surprising since the estimated density of minority carriers at this level of focused beam current is $6 \times 10^{17} \text{ cm}^{-3}$ which is comparable to the majority carrier density. Hence ambipolar diffusion effects would be expected. Saturation of the recombination traps could also occur and give a similar effect. Resolution data has almost always been taken at 5nA.

Further experiments of this type are planned, but it seems most likely at this time that at least some of the disagreement between theory and experiment for the isolated written areas is due to an electron beam spot size effect. The electron spot size would also degrade the isolated, unwritten area readout, but to a lesser extent, because the roll-off for this pattern is occurring at larger pattern sizes.

In summary, the preceding experiments have demonstrated the feasibility of 0.4 micron bit spacing with ion fluences and energies compatible with the present ion column and source design. At higher ion fluences 0.25 micron spacing was demonstrated. It is projected that 0.25 micron spacing could be achieved at an ion fluence of 10^{13} cm^{-2} , which is a factor of 10 in excess of the present column capabilities. There is some possibility that the present results are pessimistic because of a spot size problem in the C&W microscope. This will be investigated in more detail during the remainder of Phase II.

SECTION V

ION IMPLANT TARGET - FOUR-POINT PROBE MEASUREMENTS

Four point probe measurements of the ion written targets were initiated to further contribute to our understanding of the ion damage process. The principal effects of ion implantation damage on the electrical properties of silicon are free carrier removal, mobility degradation, reduction in minority carrier lifetime, and increase in generation-recombination centers. Measurements of the conductivity as a function of the ion damage fluence provide information on the rate of carrier removal and the spatial distribution of the carrier removal traps.

The principal motivation for these experiments was to determine the depth of the deep traps responsible for carrier removal. This would have further confirmed the measurement of the damage depth by electron beam methods described in Section IV. This approach was not completely successful because of measurement problems at the higher fluences. A new mask set with Van der Pauw patterns has been designed to overcome this problem.

The four point probe technique is a fast, nondestructive method for measuring the electrical conductivity of ion implanted layers. Four colinear probe tips are set down on the semiconductor surface. As current goes through the two outer probes, the voltage IR drop between the two inner probes is measured. The conductivity, or $1/R_{\square}$, is calculated by using the relation

$$\sigma = \frac{1}{R_{\square}} = (0.2206) \frac{I}{V} \quad (8)$$

where V and I are the measured voltage and current and the multiplying prefactor includes corrections for probe spacing and geometry.

Clean surfaces are required for accurate measurements; however, HF dips are avoided since high recombination rates at the surface are desirable. Measurements are made in the dark to avoid light generation of carriers and possible modulation effects on the conductivity. A range of low operating currents is used to assure that the sheet resistance remains consistent. For thin layers such as these, broad probe tips with some loading are used to reduce possible "skidding" across the surface. A number of sites both in the written and unwritten regions of each target were tested both forward and reverse.

Several series of four point probe measurements were made on n^+ on p , and p^+ on n planar diode substrates, which were written with various fluences of inert gas ions at ion energies selected to locate the peak of the ion distribution profile at the same distance into the silicon for each ion.

The effects of ion damage on the electrical properties of silicon such as carrier removal by deep traps, mobility degradation, reduction in minority carrier lifetime, and increase in generation recombination are not independent since a given defect can participate in all these processes. Silicon is somewhat unusual because radiation damage will almost always cause carrier removal in both n and p type material, hence radiation damage causes all silicon to tend towards intrinsic.

Determination of Carrier Removal

Analysis of four point probe measurements provide a convenient measure of the carrier removal rate. The conductivity is given by

$$\sigma = q_e \mu N \quad (9)$$

where μ is the mobility and N the density of free carriers. We assume that the mobility depends only on the doping level and not on the ion generated damage. This should be a good approximation for low damage levels because the mobility is phonon scattering limited at room temperature, thus this is a region where additional defects will not significantly affect the mobility.

The sheet conductivity of the top diode layer is given by

$$G = \int_0^{T_N} \sigma dz \quad (10)$$

where T_N is the distance to the diode depletion region. The substrate is isolated from the four point probe by the diode depletion region. Let

$$H(z) = F_1 f(z) \quad (11)$$

represent the spatial density of defects generated by writing with ion fluence F_1 . H represents only those defects involved in the carrier removal process and we assume each defect can trap only one carrier. This assumes a linear defect generation process which again should be valid for low ion doses. The carrier removal rate per ion is given by:

$$E = \int_0^{T_N} f(z) dz \quad (12)$$

The sheet conductivity is given by:

$$G = qe \int_0^{T_N} \mu(N) [N(z) - H(z)] dz \quad (13)$$

The slope S of the sheet conductivity versus F curve is given by:

$$S_G = \frac{\partial G}{\partial F_I} = -q_e \int_0^{T_N} vF(z) dz = -q_e vE \quad (14)$$

so that

$$E = \frac{S_G}{q_e \mu} \quad (15)$$

assuming that the mobility does not depend on damage and that the mobility is approximately independent of z in the damaged region.

Figures 60, 63, 64, 65, 66, 68, and 69 show the measured sheet conductivity versus ion fluence for a number of diode constructions, ion energies, and species. As can be seen, there is usually a well-defined linear behavior at low fluence. In each case this slope has been converted to a carrier removal rate assuming a constant mobility based on the doping level of the diode near the surface.

Figures 60, 61, and 67 show the results from four point probe measurements on written areas of simple n+p and p+n planar diode structures. The targets were written with inert ions at various fluences, at energies selected to place the peak of the implanted ion distribution at approximately the same depth into the substrate, 500 Å. The devices referred to in Figure 60 were formed on <111> P type Monex 10-20 ohm-cm Si, by 100 kv A_S⁺ implantation through 800 Å of SiO₂ to a fluence of 10¹⁴ ions/cm² on the front with 10¹⁵ boron on the back for contact. Mesa diodes were then formed, masked, and written. The devices described by the results in

Figure 61 were formed on <111> n-type Monex 10-30 ohm-cm Si by 50 kV B^+ implantation through 2600 \AA of SiO_2 to a fluence of 10^{15} ions/cm² on the front with 10^{15} arsenic on the back for contact.

Figure 60 shows the linear region very clearly, especially for the Ne^+ implanted sample. Almost no systematic trend is apparent in the data of Figure 61 for the P^+ samples. This is probably because the carrier removal rate for p type silicon is much less, and mobility and lifetime degradation effects tend to obscure the linear decrease in conductance.

Table 5 shows the calculated carrier removal rate for the data of Figure 60. Figure 62 shows a plot of this carrier removal rate versus atomic number of the incident ion. As expected, the heavier ions have a higher carrier removal rate, both because of their higher defect generation efficiency and because of their higher energy. The solid curve is based on the Brice calculation of the damage rate in silicon (see Section II). This curve is constructed for a fixed ion projected range, $R_D = 0.06$ micron. The ordinate represents the total energy into damage processes. The energy required to create a carrier removal trap (in $10^{18} \text{ cm}^{-3} \text{ As}^+$ doped <111> Si) is 500 ev/trap, independent of ion species.

Figures 63, 64, and 65 show a series of experiments on targets fabricated by varying only the As^+ implantation fluence. This permits the measurement of the carrier removal rate as a function of doping level. Figure 66 shows a similar measurement on a flat profile target fabricated by P^+ implantation. Figure 67 shows the carrier removal rate versus estimated doping

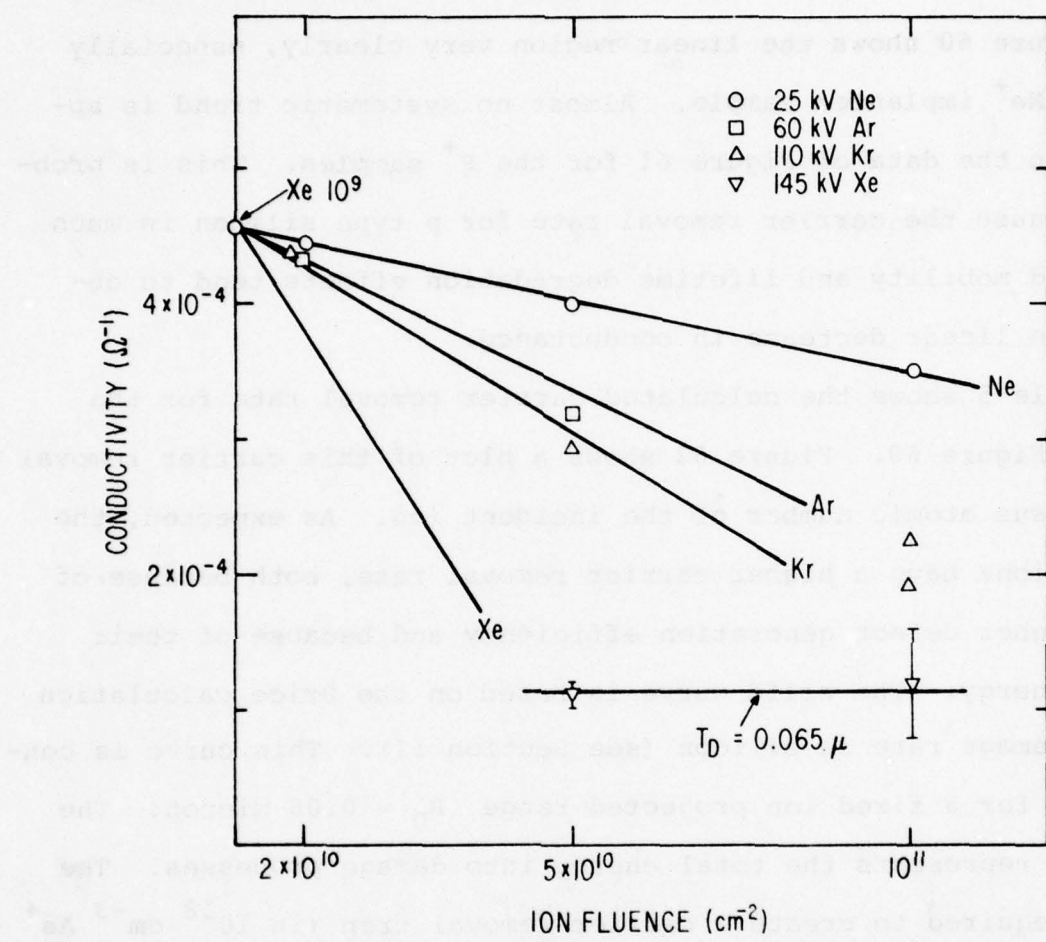


Figure 60. Conductivity vs Fluence Measurements for Unit Ion Writing on n+p Archival Planar Diode Devices Formed by 100 kV As^+ $10^{14}/\text{cm}^2$ Through 800 Å Oxide (Targets A72D, A73B, A74B, A72C, A74C, A75D, A73C, A72B, A75C, A71C)

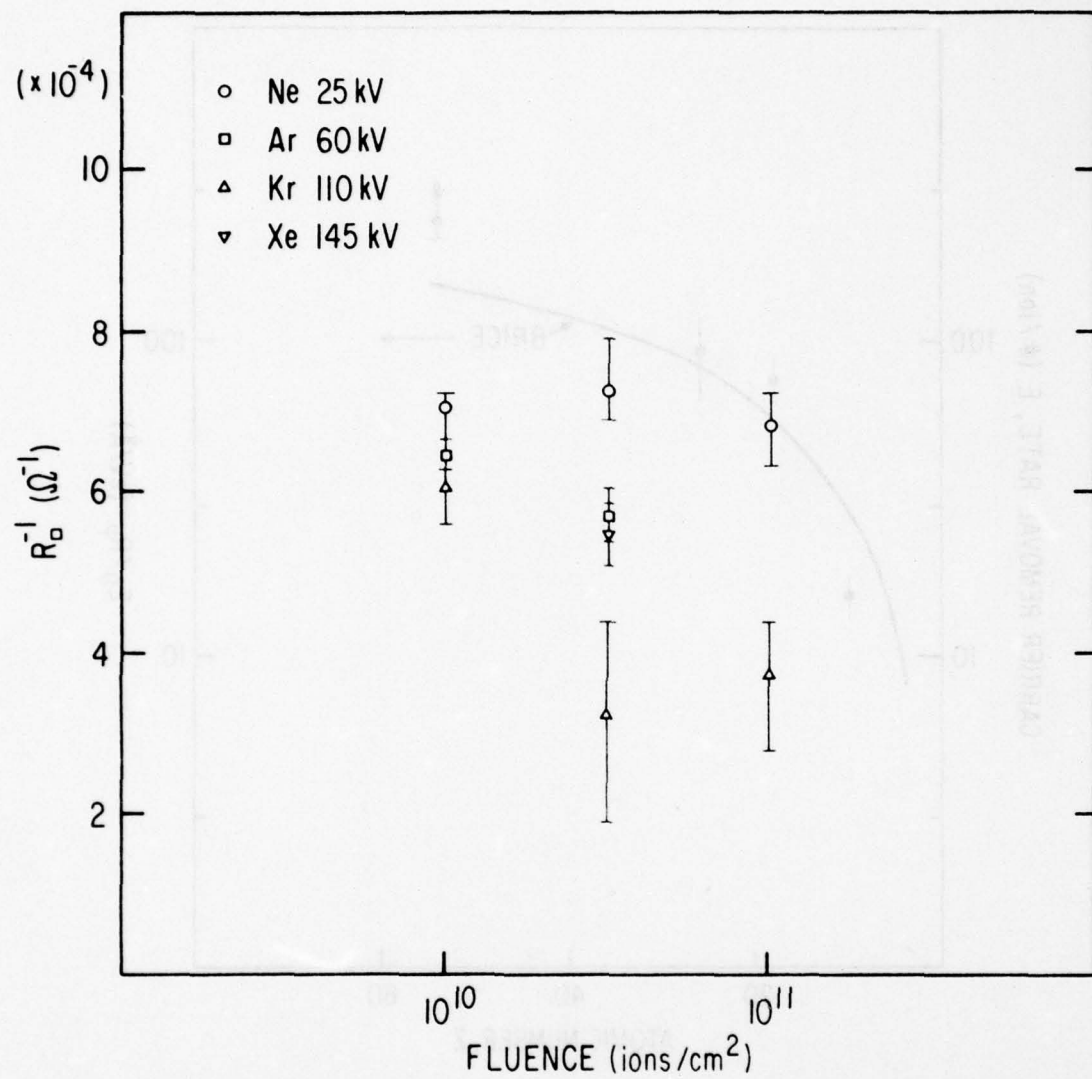


Figure 61. Conductivity vs Fluence Measurements for Ion-Written p^+n Archival Planar Diode Devices Formed by 50 kV 10^{15} B^+ /cm² Through 2600 Å Oxide (Targets B13C, B12C, B15C, B14C, B16C, B14A, B11A)

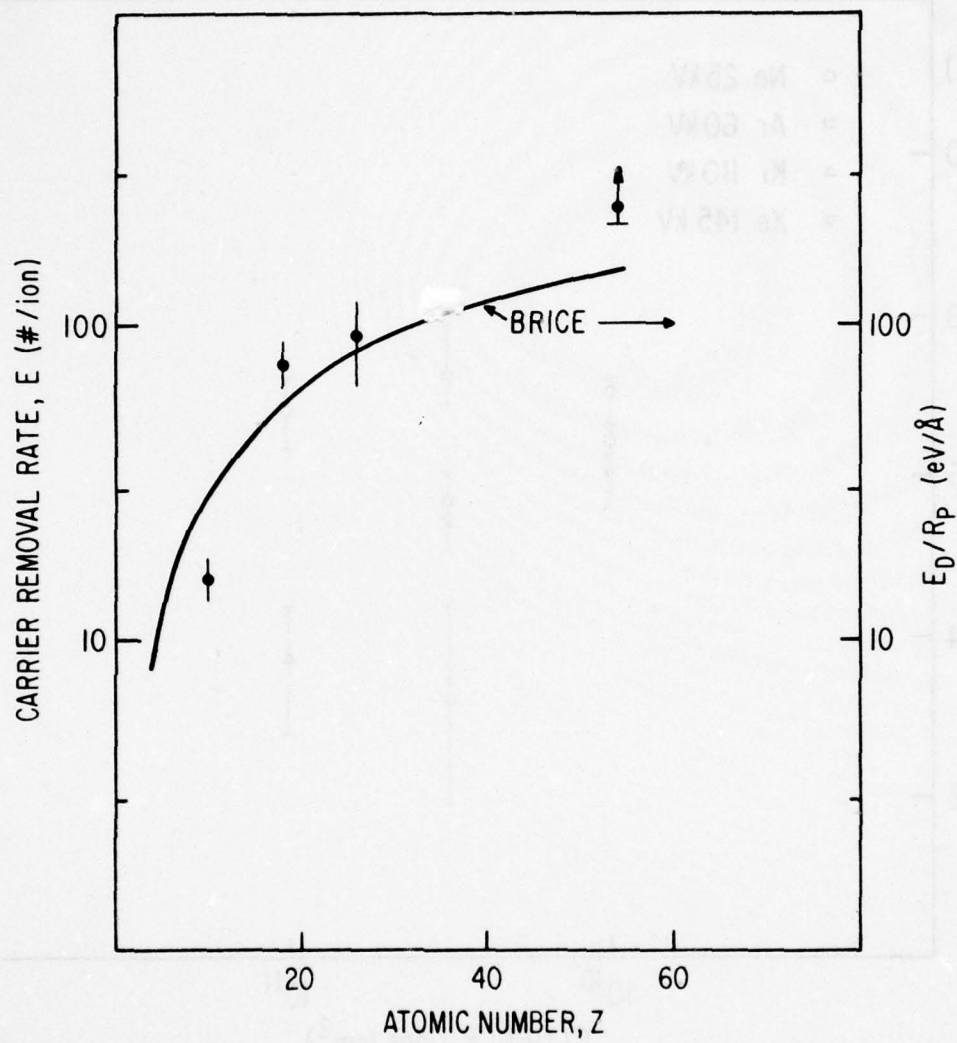


Figure 62. Carrier Removal Rate vs Atomic Number Compared to the Energy Loss Model of Brice

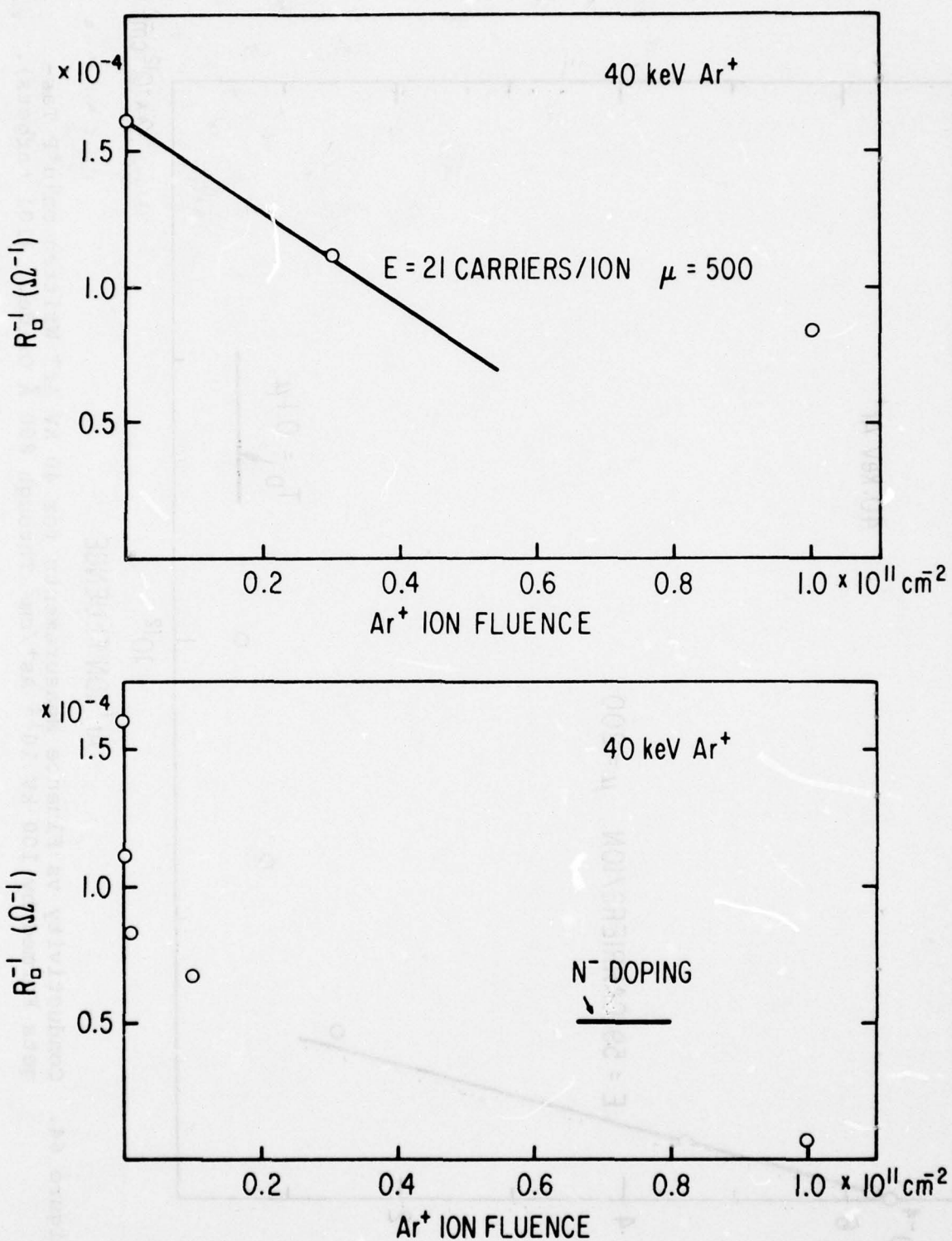


Figure 63. Conductivity vs Fluence Measurements for 40 kV Ar⁺ onto n+p Targets Formed by 100 kV 10^{13} As⁺/cm² Through 800 Å Oxide. (101 targets).

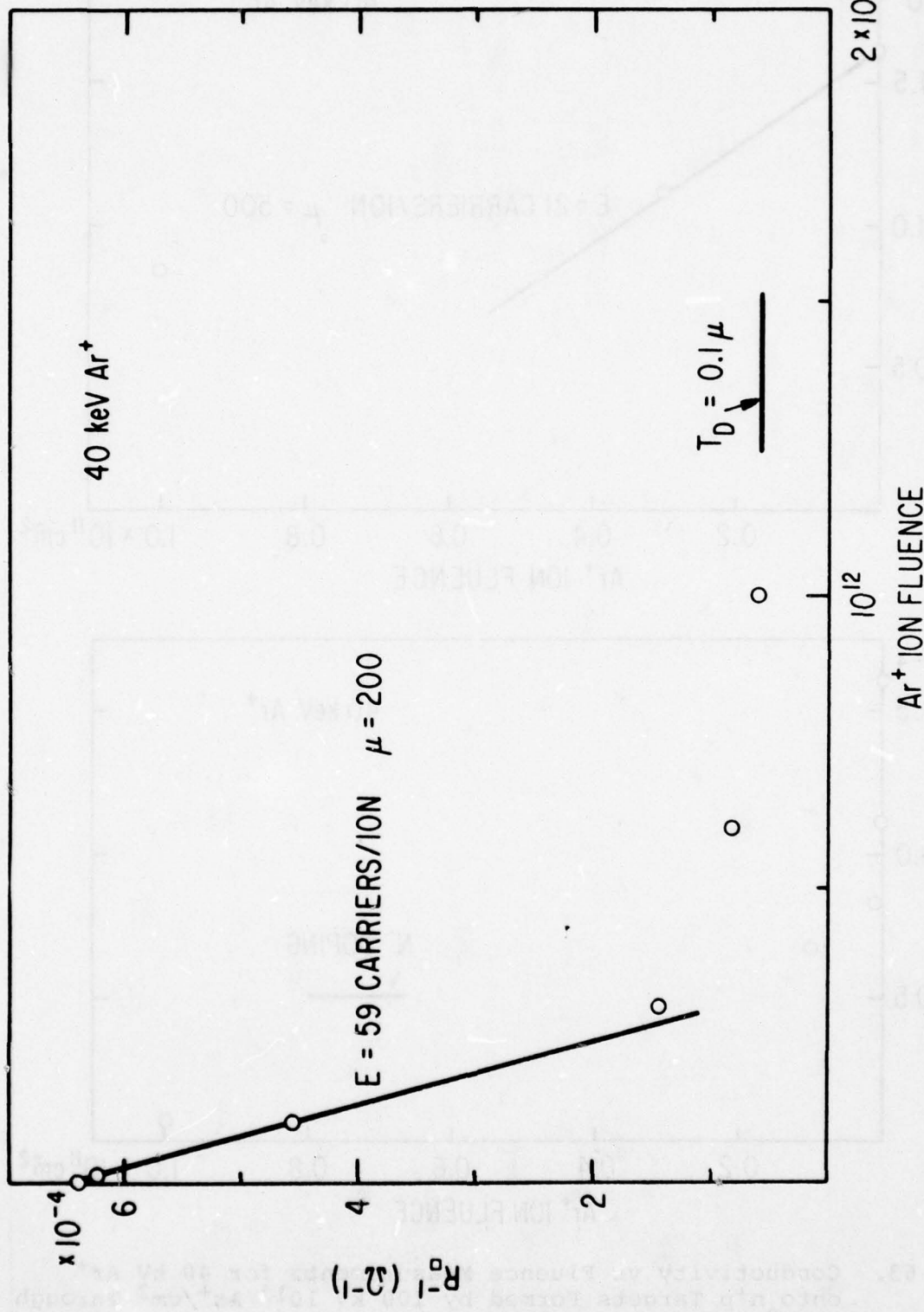


Figure 64. Conductivity vs Fluence Measurements for 40 kv Ar⁺ Written on n+p Targets Formed by 100 kv 10^{14} As⁺/cm² Through 800 Å Oxide. (101 targets).

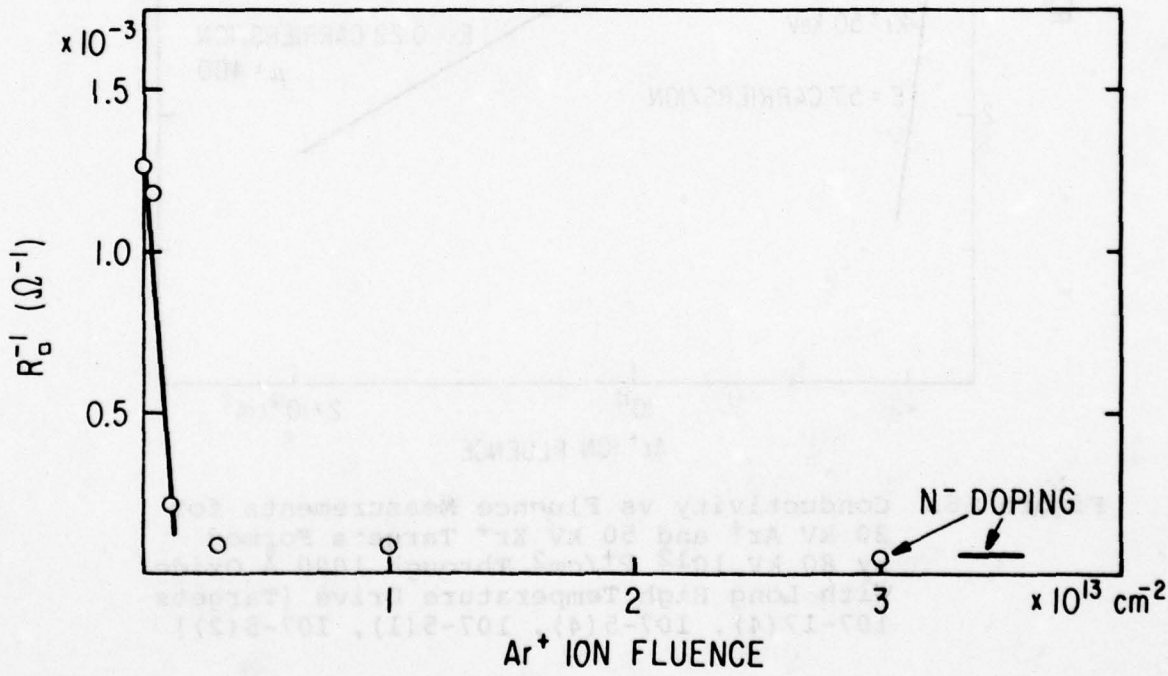
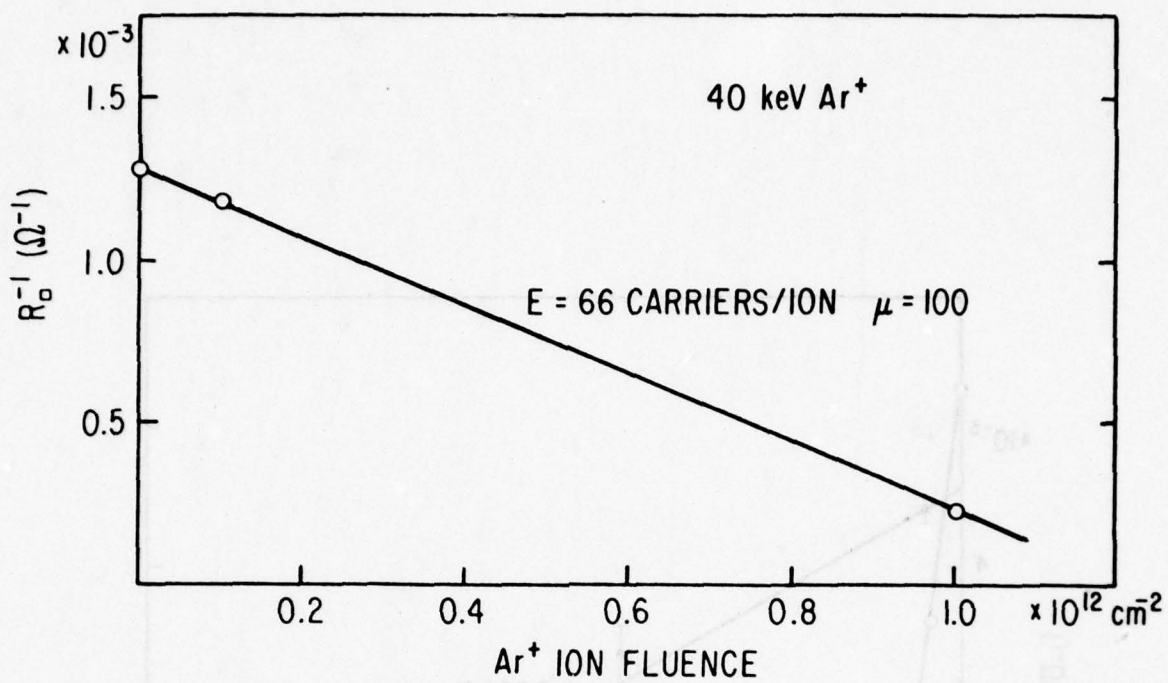


Figure 65. Conductivity vs Fluence Measurements for 40 kV Ar^+ Written n^+ Targets Formed by 100 kV $5 \times 10^{14} \text{ As}^+/\text{cm}^2$ Through 800 Å Oxide. (101 targets).

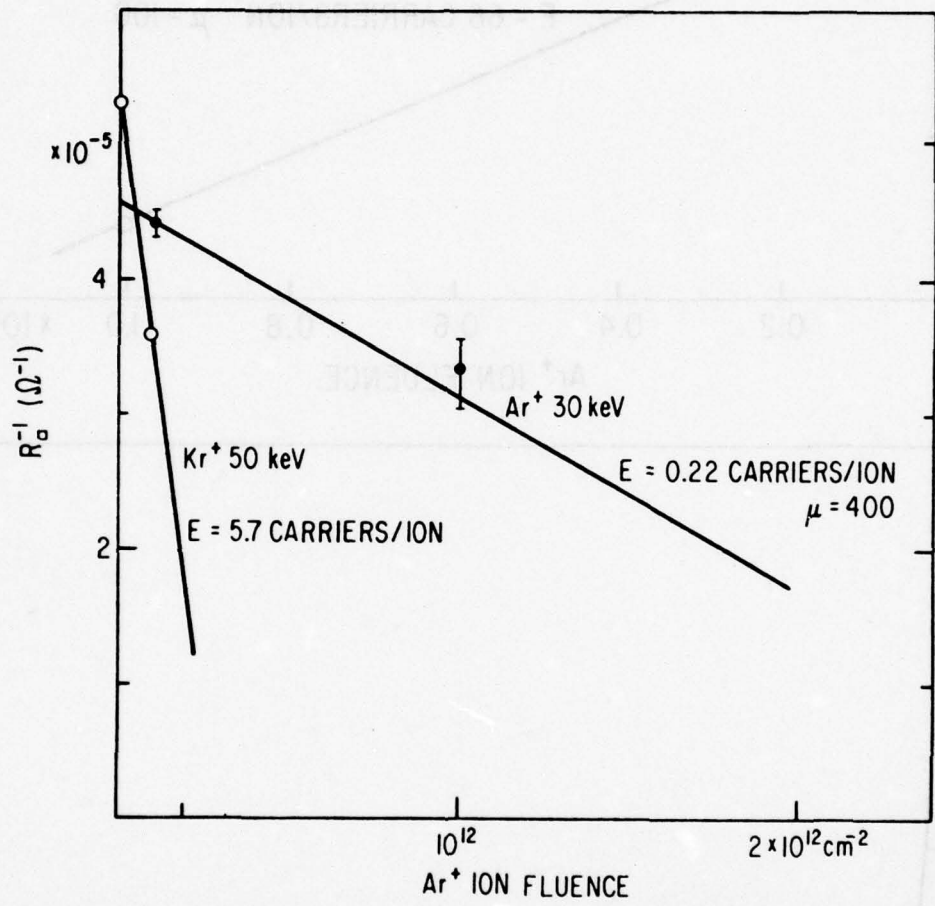


Figure 66. Conductivity vs Fluence Measurements for 30 kV Ar^+ and 50 kV Kr^+ Targets Formed by 80 kV $10^{12} \text{ P}^+/\text{cm}^2$ Through 1000 Å Oxide with Long High Temperature Drive [Targets 107-17(4), 107-5(4), 107-5(1), 107-5(2)]

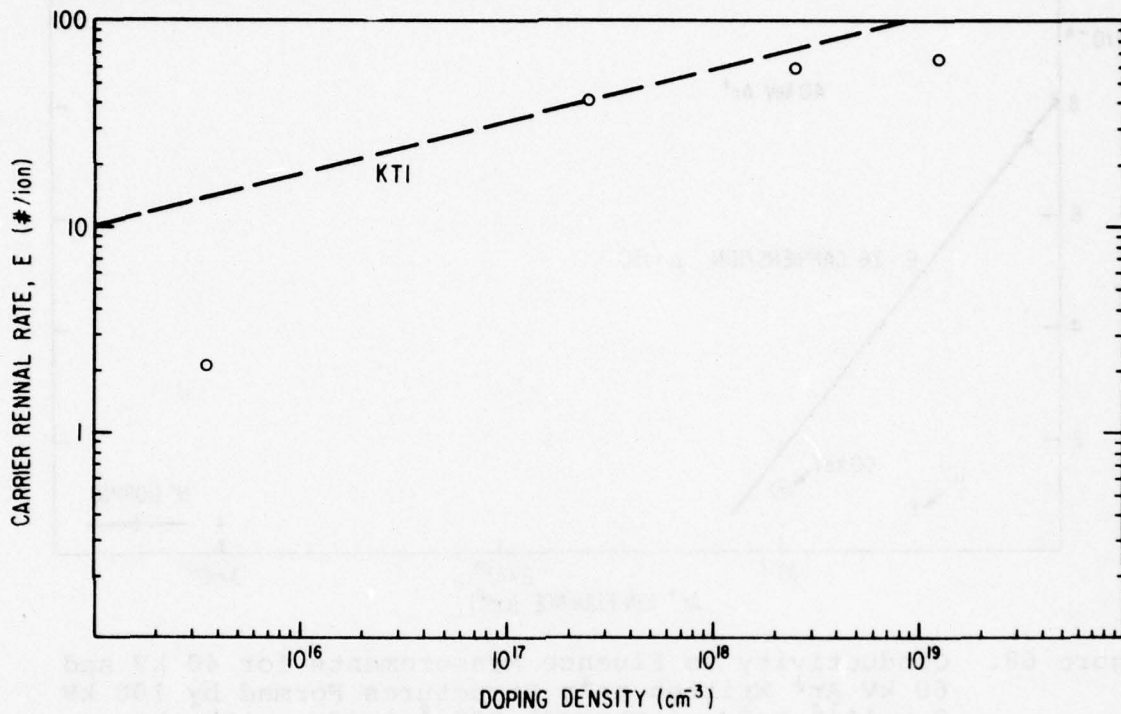


Figure 67. Carrier Removal Rate vs Doping Density for the Sample Series of the Preceding Four Figures. The dashed line "KTI" represents fission fragment irradiation of silicon. (See Hisao Kobayashi, Yasukio Takami, and Tetsuo Ikeda "Carrier Removal Rate for n-Type and p-Type Silicon by Fission Fragment Irradiation," Applied Physics Letters, Vol. 30, April 1977, pp. 389-91.)

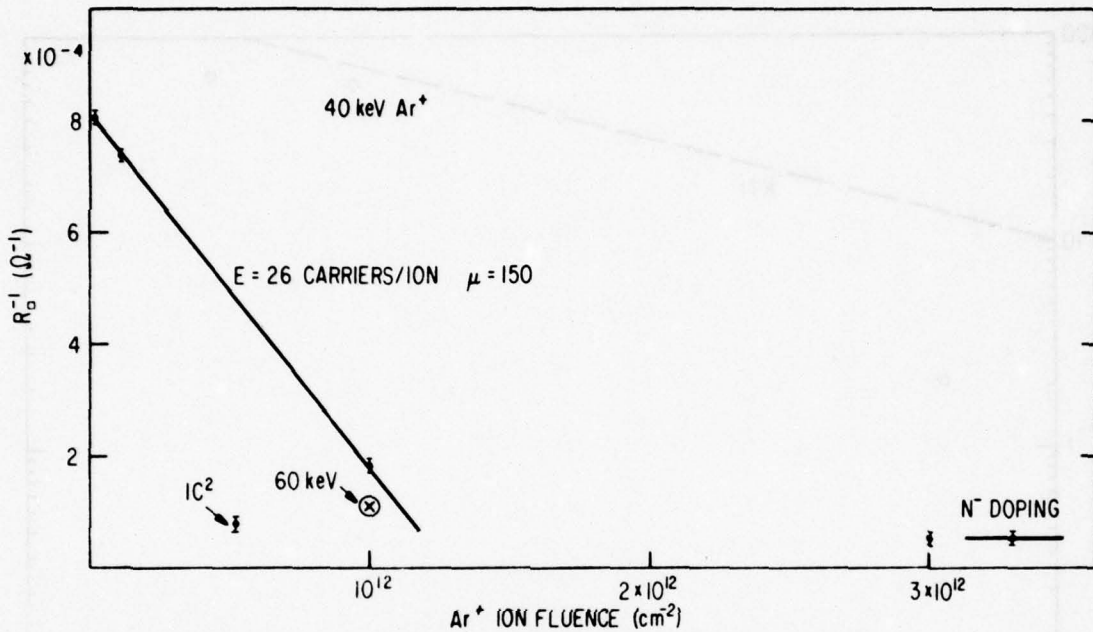


Figure 68. Conductivity vs Fluence Measurements for 40 kV and 60 kV Ar^+ Written $\text{n}n^+\text{p}$ Structures Formed by 100 kV $2 \times 10^{14} \text{ As}^+/\text{cm}^2$ Through 800 Å Oxide, with the Diode Formed by 80 kV $10^{12} \text{ p}^+/\text{cm}$ Through 1000 Å with a Long High Temperature Drive. [Targets 105-7 (3), 105-7(4), 105-10(1), 105-10(2), 105-10(3)]

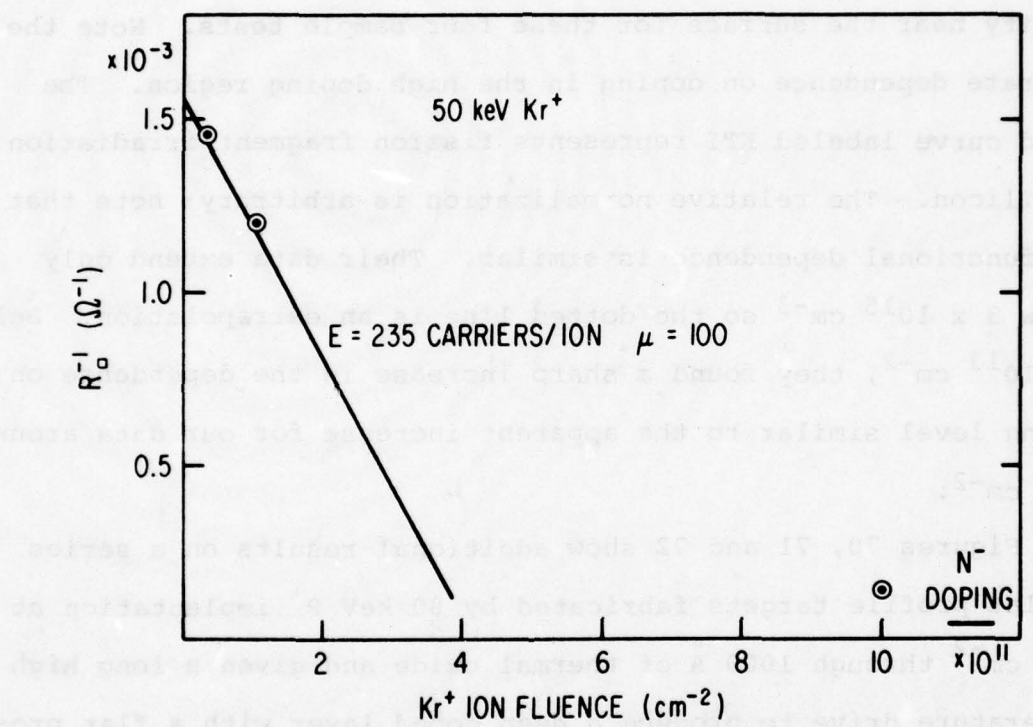


Figure 69. Conductivity vs Fluence Measurements on 50 kV Kr⁺ Written n+p Targets Formed by 100 kV 5 x 10^{14} As⁺/cm² Through 800 Å Oxide. [Targets 101-9(3), 101-9(2), 101-30(3), 101-23(4)]

TABLE 5

CARRIER REMOVAL RATES FOR ION SPECIES AND ENERGIES SELECTED
 TO PLACE ION DISTRIBUTION PEAKS AT SAME DEPTHS FROM FOUR
 POINT PROBE DATA BASED ON DATA IN FIGURE 60
 WITH $v = 200 \text{ CM/V-SEC}$

Ion	Z	E (kV)	Carrier Removal Rate
Ne^+	10	25	15.6
Ar^+	18	60	75
Kr^+	36	110	94
Xe^+	54	145	234

density near the surface for these four sample tests. Note the moderate dependence on doping in the high doping region. The solid curve labeled KTI represents fission fragment irradiation of silicon. The relative normalization is arbitrary; note that the functional dependence is similar. Their data extend only below $3 \times 10^{15} \text{ cm}^{-3}$ so the dotted line is an extrapolation. Below $3 \times 10^{13} \text{ cm}^{-2}$, they found a sharp increase in the dependence on doping level similar to the apparent increase for our data around 10^{16} cm^{-2} .

Figures 70, 71 and 72 show additional results on a series of flat profile targets fabricated by 80 keV P^+ implantation at 10^{12} cm^{-2} through 1000 Å of thermal oxide and given a long high temperature drive to produce a deep doped layer with a flat profile. These again give small carrier removal rates because of the low doping level.

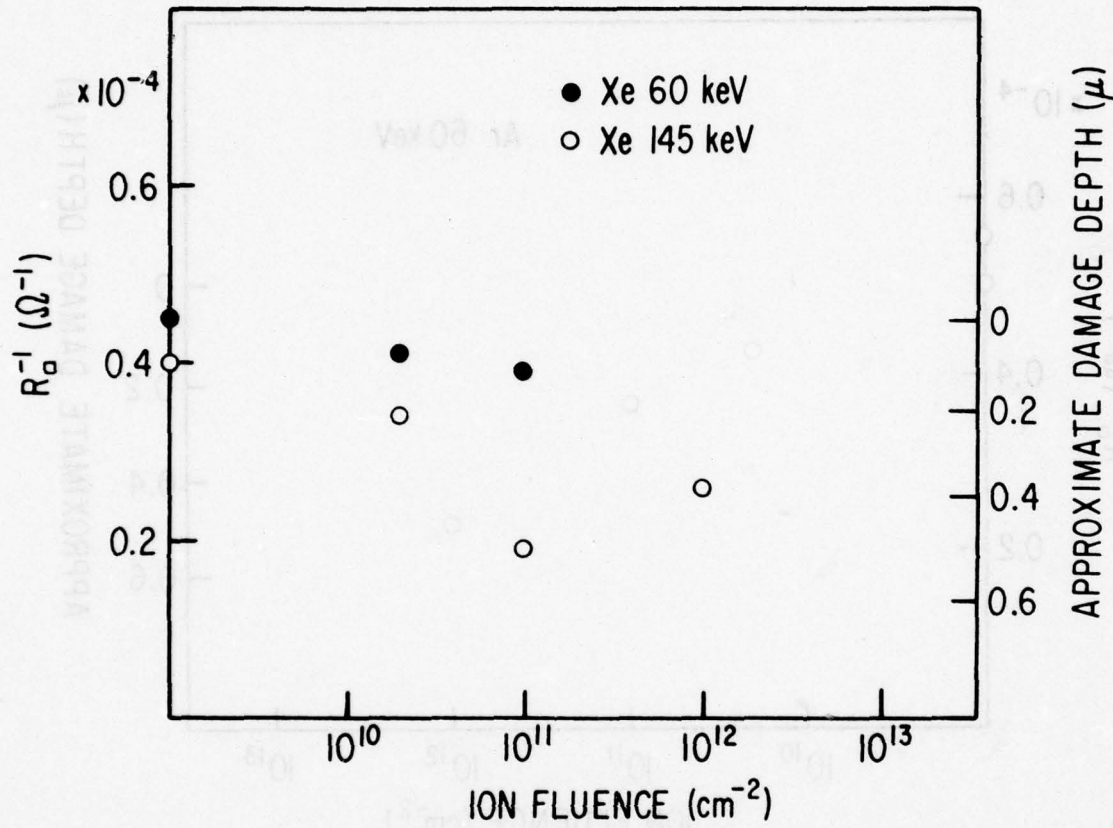


Figure 70. Conductivity vs Fluence Measurements for 110 kV Kr⁺ Written Targets Formed by 80 kV $10^{12} \text{ p}^+/\text{cm}^2$ Through 1000 Å Oxide with Long High Temperature Drive. [Targets 110-17(3), 109-8(1), 109-8(2), 110-17(1), 110-17(2)].

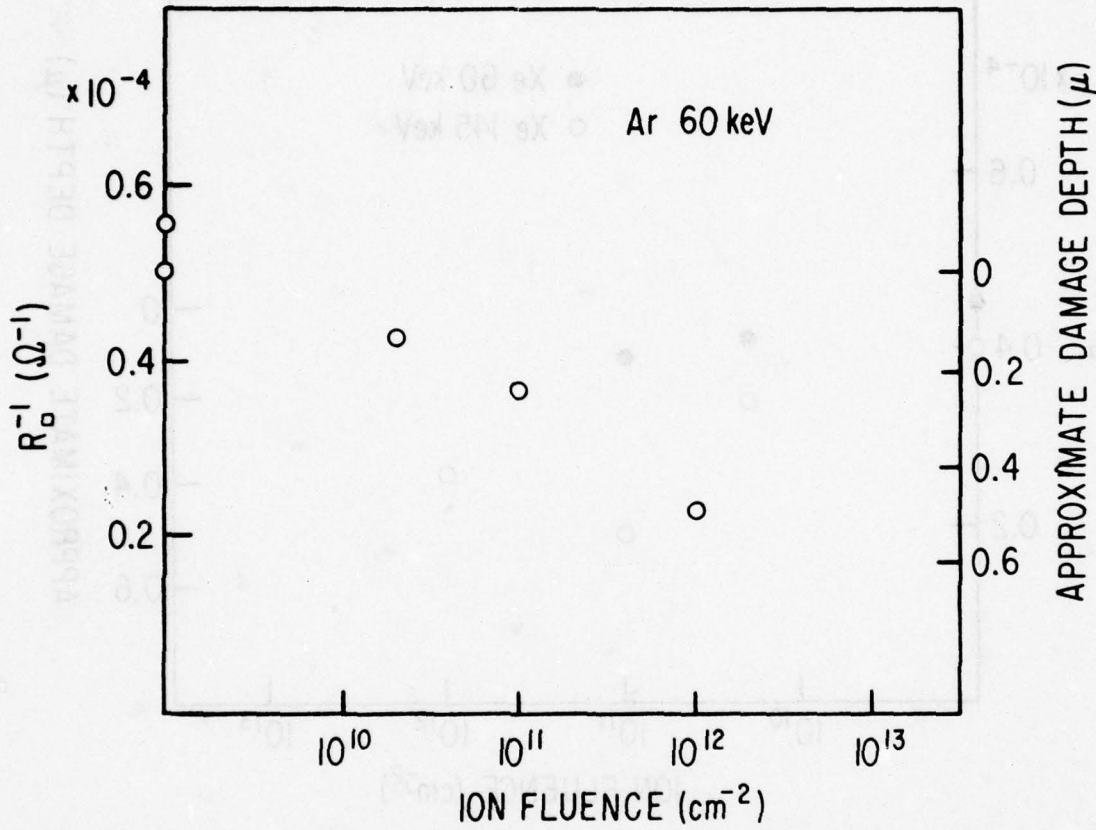


Figure 71. Conductivity vs Fluence Measurements for 60 kV Ar^+ Written n^+p Targets Formed by 80 kV p^+/cm Through 1000 Å Oxide with Long High Temperature Drive [Targets 110-5(3), 110-5(2), 110-5(1)]

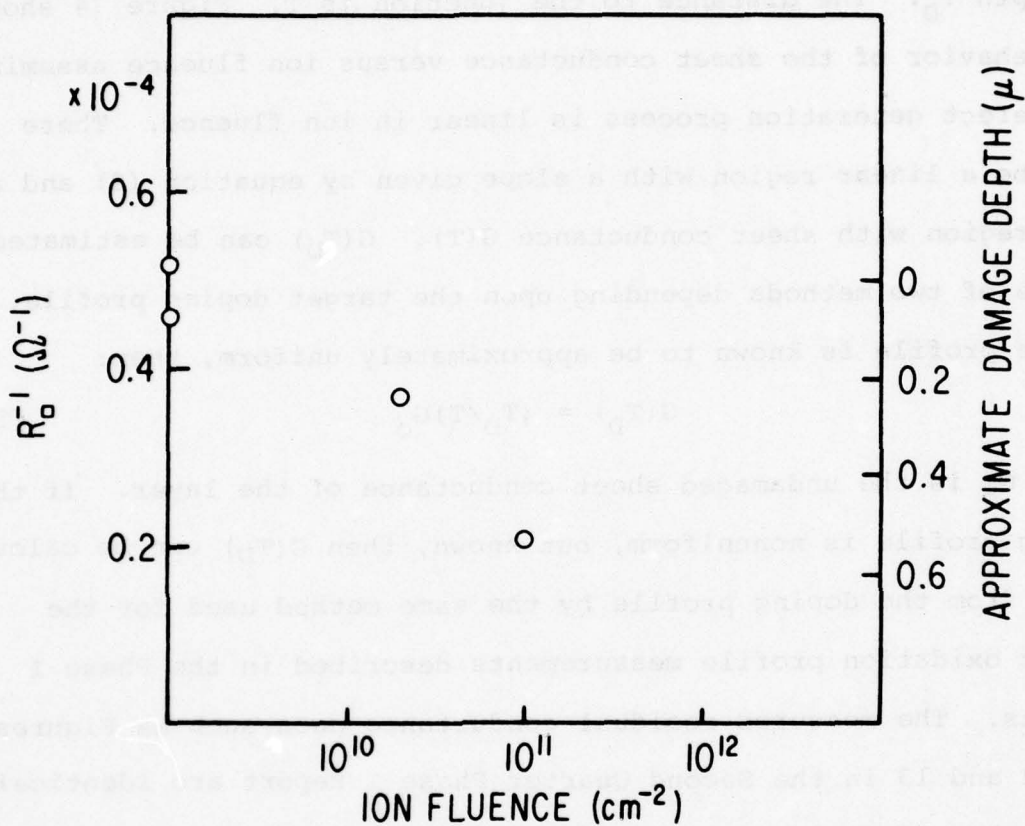


Figure 72. Conductivity vs Fluence Measurements for 110 kV Kr⁺ Written Targets Formed by 80 kV 10¹² p⁺/cm² Through 1000 Å Oxide with Long High Temperature Drive. [Targets 110-14(1), 110-14(2)]

DETERMINATION OF DAMAGE DEPTH

Figure 73 shows an idealized two layer model for the carrier compensation damage in a diode target. The damaging ion beam is assumed to generate carrier removal traps uniformly in a layer of depth T_D . The distance to the junction is T . Figure 74 shows the behavior of the sheet conductance versus ion fluence assuming the defect generation process is linear in ion fluence. There will be a linear region with a slope given by equation (8) and a flat region with sheet conductance $G(T)$. $G(T_D)$ can be estimated by one of two methods depending upon the target doping profile. If the profile is known to be approximately uniform, then:

$$G(T_D) = (T_D/T)G_0 \quad (16)$$

where G_0 is the undamaged sheet conductance of the layer. If the doping profile is nonuniform, but known, then $G(T_D)$ can be calculated from the doping profile by the same method used for the anodic oxidation profile measurements described in the Phase I reports. The measured residual conductance data such as Figures III-12 and 13 in the Second Quarter Phase I Report are identical to $G(T_D)$ as defined here. In these cases, T_D can be determined directly from this data.

Such a flat conductance region can be distinguished in Figures 60, 64, 65, 68, and 69. In Figures 61 and 64, these have been converted to damage depths by method 2 above. Note that in Figures 60 and 64, the ion fluences are still moderate and the damage depths of ≈ 0.2 micron determined in Section IV have not yet been reached.

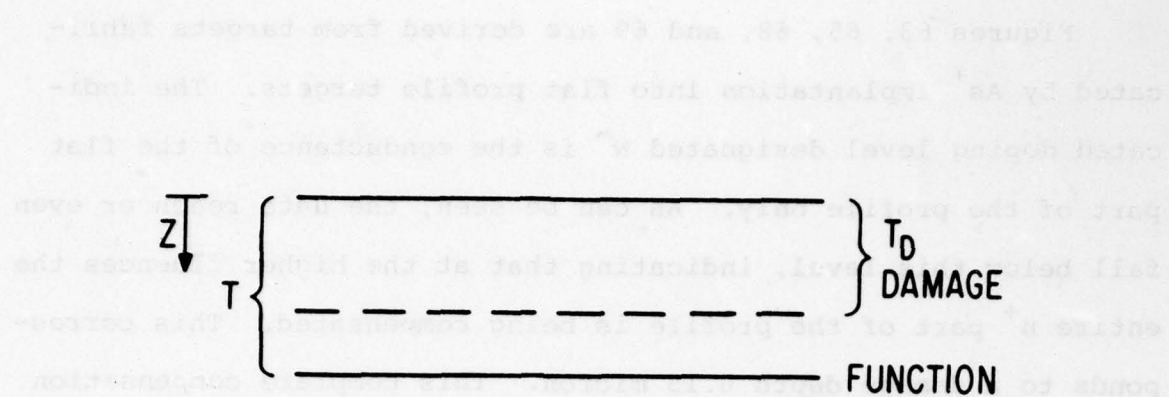


Figure 73. Idealized Two-Layer Damage Model

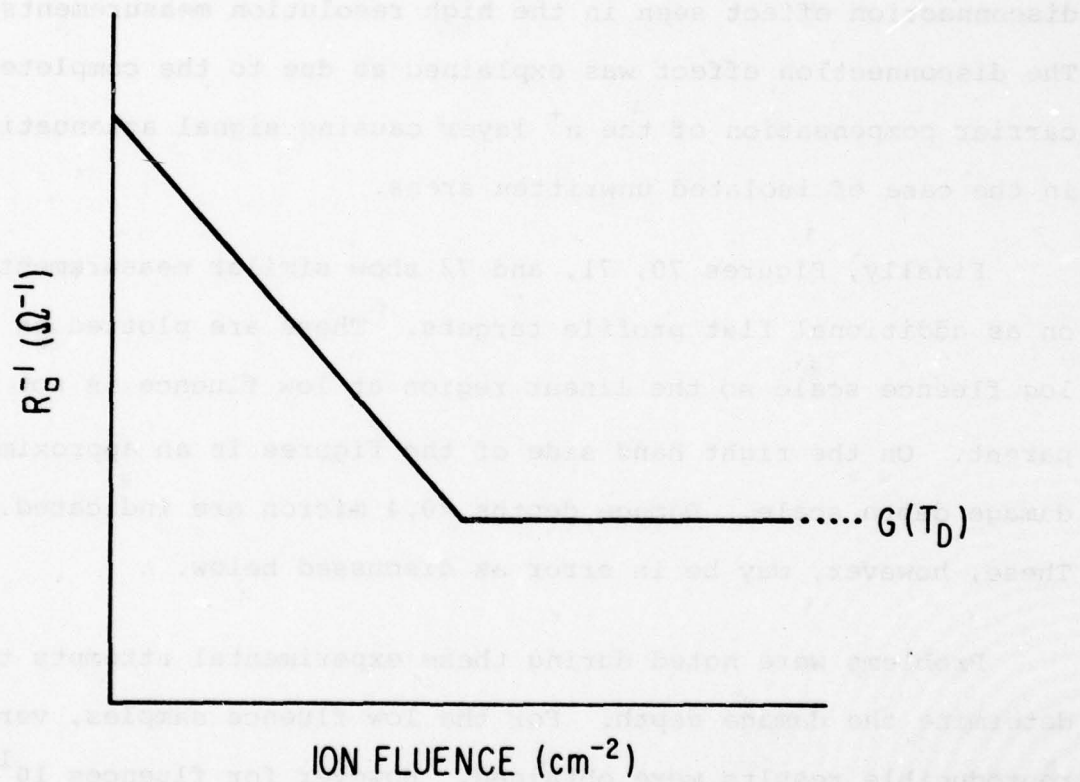


Figure 74. Sheet Conductance vs Ion Fluence for Idealized Two-layer Model

Figures 63, 65, 68, and 69 are derived from targets fabricated by As⁺ implantation into flat profile targets. The indicated doping level designated N⁻ is the conductance of the flat part of the profile only. As can be seen, the data reach or even fall below this level, indicating that at the higher fluences the entire n⁺ part of the profile is being compensated. This corresponds to a damage depth 0.15 micron. This complete compensation of the n⁺ layer is also consistent with the explanation of the disconnection effect seen in the high resolution measurements. The disconnection effect was explained as due to the complete carrier compensation of the n⁺ layer causing signal attenuation in the case of isolated unwritten areas.

Finally, Figures 70, 71, and 72 show similar measurements on as additional flat profile targets. These are plotted on a log fluence scale so the linear region at low fluence is not apparent. On the right hand side of the figures is an approximate damage depth scale. Damage depths \approx 0.4 micron are indicated. These, however, may be in error as discussed below.

Problems were noted during these experimental attempts to determine the damage depth. For the low fluence samples, very reproducible results were obtained. However for fluences 10^{12} cm⁻², and larger, considerably more scatter in the data was observed. For 10^{13} cm⁻², no data points are shown because reproducible results could not be obtained. This is believed to be due to the heavy damage (mobility degradation, carrier compensation, lifetime degradation) near the surface which prevents

adequate contact and also may cause some junction isolation effects. Because of these problems, data for $\geq 10^{12} \text{ cm}^{-2}$ should be discounted. Hence the very large damage depths indicated in Figures 63 and 68 through 70 may not be real.

Because of the above problem, Van der Pauw patterns were designed into one test quadrant (see Section V). This will eliminate the contact problems inherent in the four point probe technique. This should permit an independent measurement of the damage depth by the carrier compensation technique described here. With better data, methods analogous to those used in the data analysis in Section IV can be applied to provide an independent measurement of the damage tailing.

In summary, the four point probe measurements are consistent with damage depths ≈ 0.1 micron. Van der Pauw patterns will be necessary to quantitatively determine the damage depths at the higher fluences $\geq 10^{12} \text{ cm}^{-2}$. The measured compensation rates indicate that the carrier compensation efficiency increases with increasing ion mass and decreases with increasing substrate doping. Both of these are consistent with the current understanding of radiation damage in Si.

SECTION VI
OPTICAL DESIGN CONSIDERATIONS
FOR THE ION WRITER

As a result of the Phase I archival memory target research and optics study, the focussed ion beam writing concept was selected as the primary memory approach for further pursuit in Phase II of the Archival Memory System Development. It has been planned that an ion write station be designed and fabricated with goals of $0.1\mu\text{m}$ bit spacing, 10 megabit writing rate and a field size of approximately 10^5 bits. Also a separate electron beam read station with 10 megahertz readout capability as a goal is to be designed and fabricated during the Phase II contract period.

During this first reporting period, the major portion of the optics effort was spent on the design of the focussing optics for the ion write station. Although a preliminary optics study had been made in Phase I, finalized target requirements and new ion source specifications mandated a complete redesign of the ion write optics. This section of the report describes the ion writer optics design.

BACKGROUND AND GENERAL OPTICS CONSIDERATIONS

During Phase I of this contract, the ion writing optics centered around neon ions at a landing potential of 40 kV. It was shown[1] that a two electrostatic einzel lens collimating column using a gas phase field ionization (FI) ion source (Figure 75), with post-final-lens deflection, was capable of delivering $6.4 \times 10^{-11}\text{A}$ into a $0.1\mu\text{m}$ spot. This corresponds to a mean number of 40 ions per bit at a 10 mHz writing rate. Based on an estimate of

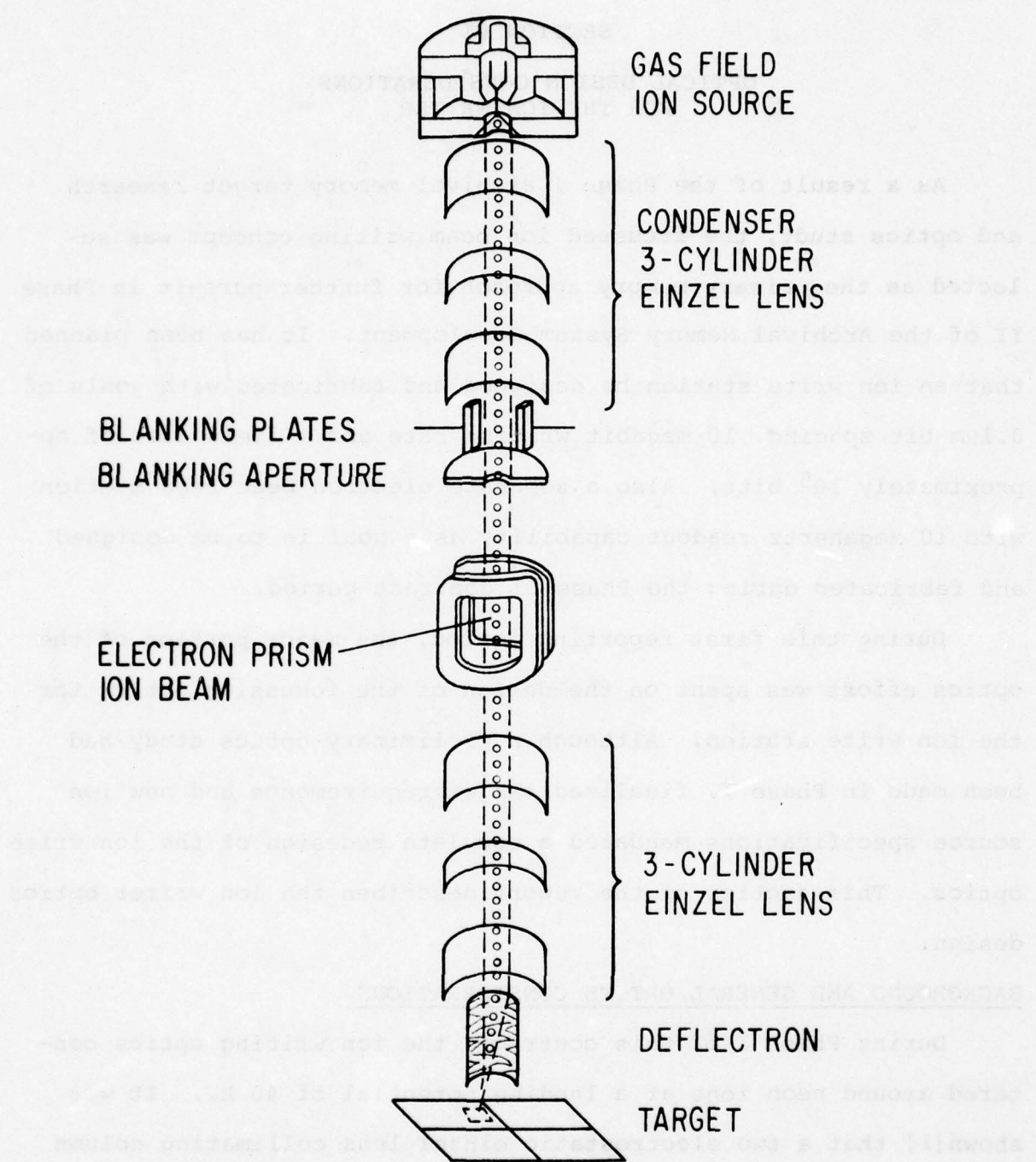


Figure 75. Phase I Ion Optics Column

10 ions per bit being adequate, and using a Poisson distribution, the probability for achieving less than 10 ions per bit was estimated to be $\approx 4 \times 10^{-9}$. Thus, 10 Mhz ion writing with 40 kV Ne^+ ions appeared feasible.

Near the end of Phase I and in the early portion of Phase II, further target research indicated that a more suitable choice of writing ion would be Xe^+ at 60 kV or Ar^+ at 30 kV landing potential. A closer examination of the field ion source structure (Figure 76) indicated that the maximum operating voltage from cathode to tip was 15 to 20 kV. The source developers at the Oregon Graduate Center felt that higher voltage tips could be fabricated by making a larger tip radius. However, voltage breakdown along the glass structure between the filament leads and cathode cap would limit operation to 20 kV maximum. Due to this voltage restriction, the all-einzel lens configuration of the Phase I optics study could not be used for landing voltages higher than 20 kV. Furthermore, a revamped specification of the angular brightness of the FI source set this value at 5×10^{-7} A/str as opposed to the value of 1×10^{-6} A/str assumed in the Phase I Study. In view of these changes in ion species and source capabilities a detailed redesign of the optics was required for Phase II.

For the Phase II optics the basic column concept, i.e. using a gas field ion source, electrostatic optics, and a two lens collimating system, remained the same as in Phase I. As shown in Phase I, the spot size for equivalent performance from a field ionization source and a duoplasmatron ion source is

$$d_{eq} = \sqrt{2.18 (\Omega_{\beta_0}/\beta_i)} \quad (17)$$

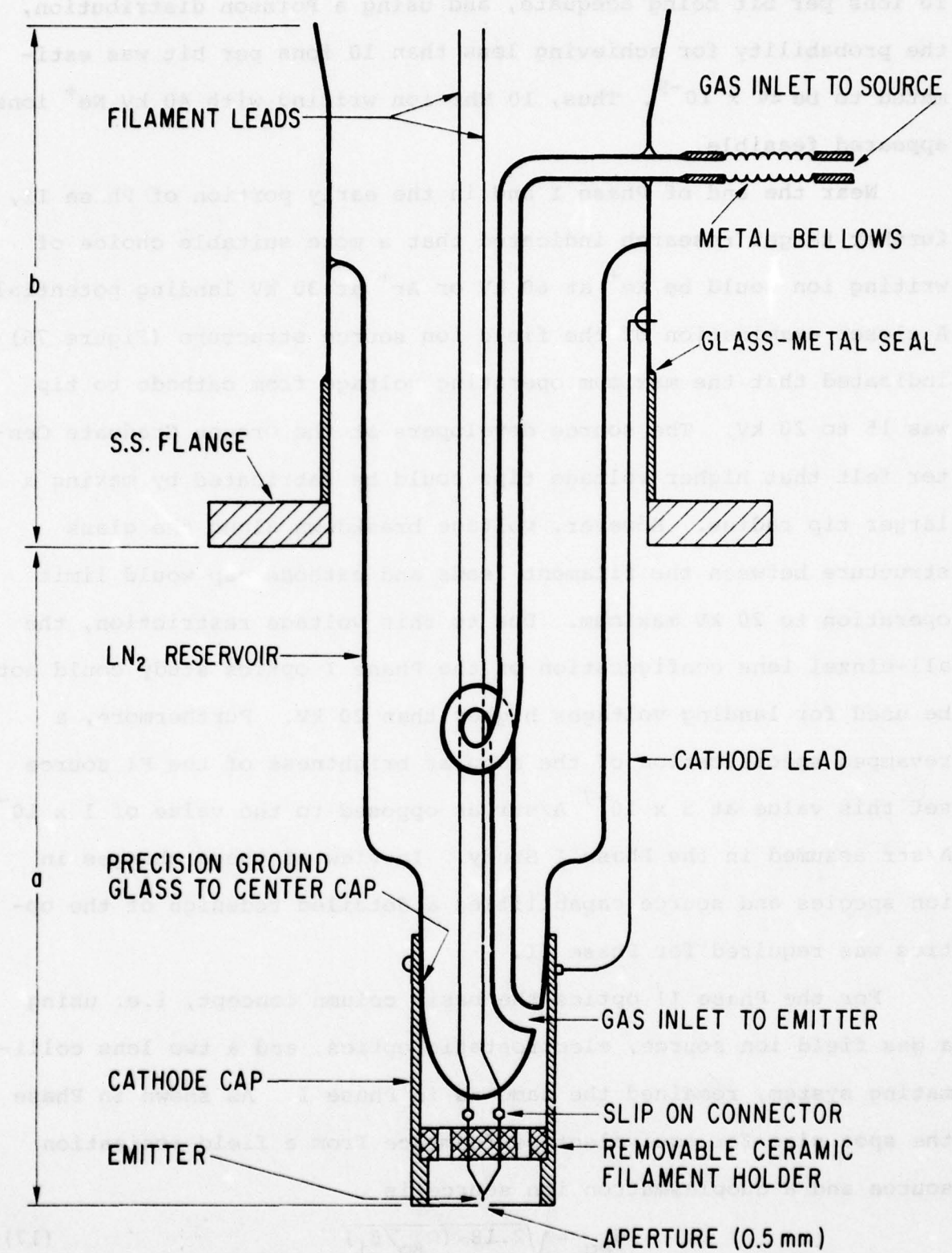


Figure 76. Gas Field Ionization Source Cross Section

where Ω_{β_0} is the angular brightness in amp/str of the FI source and β_i is the brightness in amps/cm²/str of the duoplasmatron source. For spot sizes greater than d_{eq} , the duoplasmatron produces more current per spot, whereas the converse is true for spot sizes less than d_{eq} . Using the new value of 5×10^{-7} A/str for Ω_{β_0} and keeping $\beta_i = 10^3$ A/cm²/str as in Phase I, Eq. 17 gives $d_{eq} \approx 3300\text{\AA}$. Since a bit size of $\leq 1000\text{\AA}$ is sought, the FI source is still the best choice. Electrostatic lenses are still required since their focusing properties are not dependent on the ion charge to mass ratio. Both lenses, however, cannot be of the einzel type (as used in Phase I) because the landing potential is required to be greater than the source voltage limit of 20 kV. A two lens collimated configuration as used in Phase I is still appropriate because of its lower aberrations and insensitivity to lens spacing.

Various types of electrostatic lenses can be considered; some of the simpler structures comprised of aligned apertures and tubes are shown in Figure 77. More exotic lens structures incorporating shaped electrodes have been considered in other work [2,3], however, the advantages of these in optical performance is not necessarily clear [4]. In view of this and because of the ease of fabrication, only those lens structures of simple tube and aperture construction were considered for the Phase II optics. An interesting fact concerning tube and aperture lenses is that the normalized spherical aberrations are equivalent for lenses of the same normalized dimensions of the two types. The tube lenses, however, require less voltage drop between elements to achieve a given lens-to-image-distance than the aperture lenses. Therefore, when voltage stress

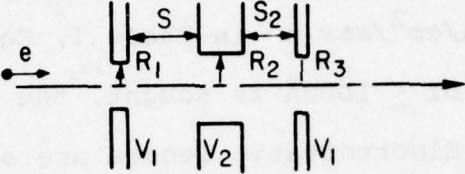
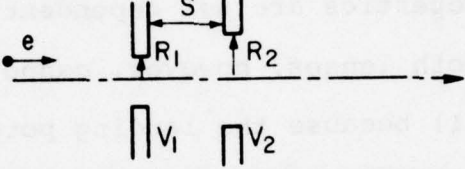
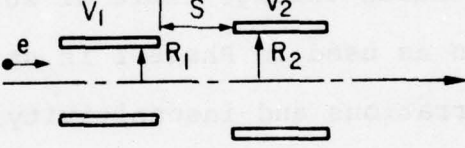
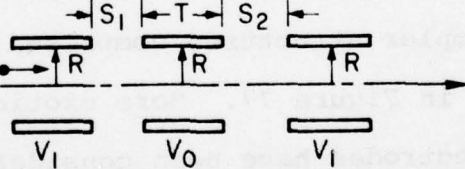
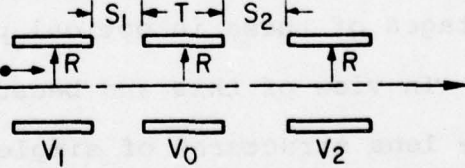
LENS TYPE	ELECTRON OPTICAL SYMBOL
3 APERTURE EINZEL	
2 APERTURE IMMERSION	
2 CYLINDER IMMERSION	
3 CYLINDER EINZEL	
3 CYLINDER TRIPOTENTIAL	

Figure 77. Cross Sections of Various Aperture and Cylinder Electrostatic Lenses

between lens elements is of concern, the tube lenses have a slight advantage. Aperture lenses require less total length for a given set of element spacings and therefore have a slight advantage when space must be conserved.

Considering the lenses of Figure 77, the combinations for use in a two lens collimating column are:

<u>Case</u>	<u>Lens 1</u>	<u>Lens 2</u>
1	Einzel	Einzel
2	Immersion	Einzel
3	Tripotential	Einzel
4	Einzel	Immersion
5	Einzel	Tripotential
6	Immersion	Immersion
7	Tripotential	Tripotential

Several of these lens configurations can be eliminated or ruled less attractive due to practical consideration. The einzel lens structure has the same potential on the two outer electrodes. Therefore, as noted previously, the two-einzel-lens configuration of case 1 cannot be used due to the landing potential requirement of ≥ 30 kV and the source voltage limit ≤ 20 kV. Some of the lens structures are made less attractive by the location of electrical ground in the column. For cases 4-7, either the target plane, or the region between lenses must be floated off ground, possibly by as much as 40 kV. If the target is at high potential, the readout electronics would have to be floated, and the mechanical motion of the stage would be more complicated. In the region between lenses, electrodes for electronic beam centering, astigmatism correction, beam blanking,

etc. are installed. Having to float these electrodes at high voltage adds to their complexity. Therefore, unless these configurations show significant optical advantages (i.e. lower aberrations which would allow a great increase in current for a given spot size), they are less appealing than cases 2 and 3. Cases 2 and 3 have all the acceleration in the first lens. By using an einzel lens for the final lens, both the region between lenses and the target region operate at ground potential. From a practical standpoint, these two cases (2 and 3) are considered the preferred options for the Phase II optics configuration.

Optical properties for the immersion, tripotential, and einzel lenses were determined using the Liebmann ray tracing method[6]. With this ray tracing method, paraxial and third order aberrated rays are built up in a step by step manner using recursion formulae which are functions of the axial potential, its derivatives, and the past history of the ray. Axial potentials and derivatives for the tube lenses were determined with the well-known integral solution of Laplace's equation based on the Fourier Transform[7]. This method of solution has been previously used to obtain the potentials for two tube immersion lenses[8], three cylinder lenses [5], symmetrical magnetic lenses[9], and extended to the tripotential lens for work within GE. The axial potential for the aperture lenses were obtained by numerical solution of Laplace's equation using a modified form of the Liebmann five point relaxation technique due to Shortly and Weller[10]. The optical properties of interest for the present study are the paraxial focal lengths, lens-to-image-plane distance, and the spherical and chromatic aberration

coefficients. The evaluation of the optical properties for the lenses of cases 2 and 3 with minimum spherical and chromatic aberrations are discussed in the next section of this report.

INVESTIGATION OF LENS PROPERTIES

As was noted during Phase I, aberrations of the first lens of a two lens system become significant when the overall optics magnification approaches or becomes greater than unity as it does with field emission or field ionization sources. Riddle[4], has introduced an interesting and practical way to investigate the aberration properties of the first lens in such a system. The concept is shown schematically in Figure 78. The aberrations are referred to the object plane and normalized to z_o , which is the working distance of the lens and not the lens center to target distance, z_m , as is often used. Normally the working distance for an electron or ion lens is taken from the object or image distance to the edge of the first electrode or first lens gap. The advantage of using z_o instead of z_m is that z_o is the same for all lenses since the lens length L does not enter into its definition. Hence it provides a unified comparison of normalized spherical, C_s/z_o , and chromatic, C_c/z_o , aberrations for various lens types. This method of aberration characterization was used to study and compare three cylinder einzel lenses, two cylinder immersion lenses, and three cylinder tripotential lenses during this phase of the contract. Only the cylinder lenses were studied in detail because (as previously noted) their optical properties are quite similar to the aperture lens types.

The first lens type studied was the three cylinder einzel lens shown schematically in Figure 79. The working distance, z_o , is

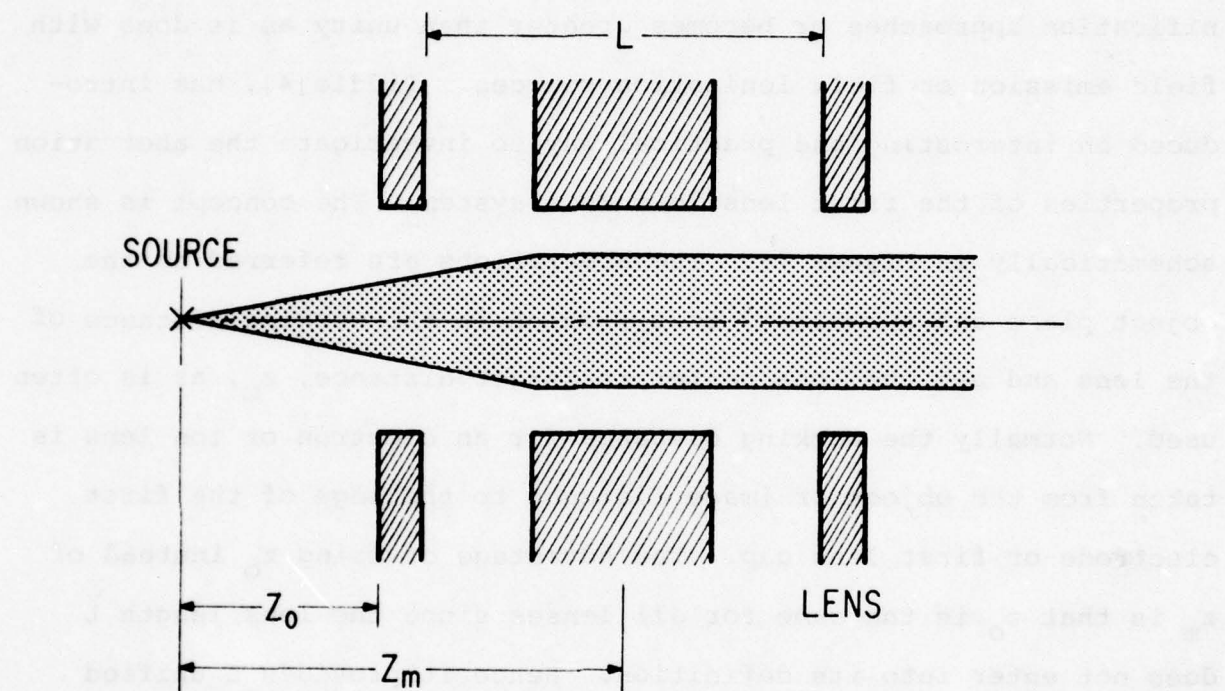


Figure 78. Parameter Definitions for the First Lens and Source

will add to right side of charge to one side and move between cylinders by itself until it meets one of the two charges and will then stop moving due to the repulsion of the other cylinder. This is due to the fact that the two charges have opposite signs.

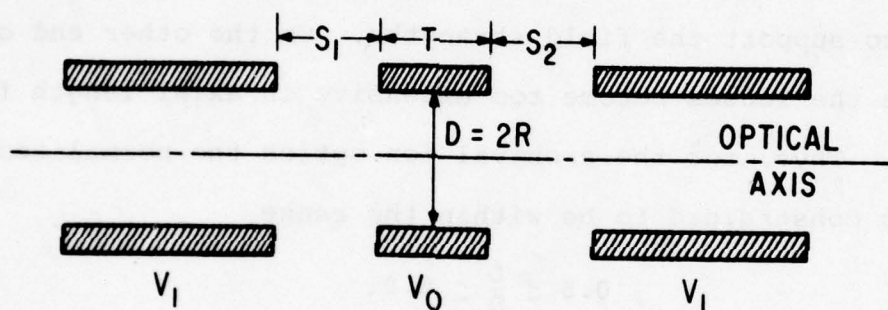


Figure 79. Three Cylinder Einzel Lens

measured from the object side focal point to the edge of the first gap. If the lens gaps S_1 and S_2 are equal, the lens is referred to as a symmetrical einzel, and $S_1 \neq S_2$ is referred to as an asymmetrical einzel lens. The length of the lens, L , normalized to lens diameter D is

$$\frac{L}{D} = \frac{S_1}{D} + \frac{T}{D} + \frac{S_2}{D}. \quad (18)$$

As shown in the Phase I optics study, the aberrations of electrostatic lenses are reduced by maximizing the field strength in the lens gaps, S_1 and S_2 . Under these conditions, lens dimensions become excessively large for $L/D \leq 0.5$ due to the gap sizes required to support the field strengths. On the other end of this range the lenses become too extensive in axial length for $L/D > 5.0$. Thus, for the archival ion optics the normalized lens length was constrained to be within the range

$$0.5 \leq \frac{L}{D} \leq 5.0. \quad (19)$$

The normalized lens dimensions for the lens cases studied in detail are summarized in Table 6. For each value of L/D , a sufficient number of cases were investigated to evaluate the significance of the gap widths and central electrode thickness on the lens aberrations. Optical properties for all of the lenses given in Table 6 were calculated as a function of the lens voltage factor V , which is given by:

$$V = \frac{V_C - V_t}{V_O - V_t} \quad (20)$$

where V_C = central electrode potential

V_O = outer electrode potential

V_t = ion source tip potential

TABLE 6
THREE CYLINDER EINZEL LENS DIMENSIONS
NORMALIZED TO LENS RADIUS D FOR CASES STUDIED

Lens Case	Normalized Lens Length L	Normalized Lens Dimensions		
		S_1/D	S_2/D	T/D
1.1		0.1	0.1	0.3
1.2		0.1	0.2	0.2
1.3	0.5	0.1	0.3	0.1
1.4		0.2	0.1	0.2
1.5		0.3	0.1	0.1
1.6		0.2	0.2	0.1
2.1		0.1	0.1	0.8
2.2		0.25	0.25	0.5
2.3		0.4	0.4	0.2
2.4	1.0	0.1	0.4	0.5
2.5		0.1	0.8	0.1
2.6		0.4	0.1	0.5
2.7		0.8	0.1	0.1
3.1		0.1	0.1	2.8
3.2		1.0	1.0	1.0
3.3		1.4	1.4	0.2
3.4		0.1	0.4	2.5
3.5	3.0	0.1	1.4	1.5
3.6		0.1	2.8	0.1
3.7		0.4	0.1	2.5
3.8		1.4	0.1	1.5
3.9		2.8	0.1	0.1
4.1		0.1	0.1	4.8
4.2		1.0	1.0	3.0
4.3		2.0	2.0	1.0
4.4		2.4	2.4	0.2
4.5	5.0	0.1	4.8	0.1
4.6		0.1	3.0	1.9
4.7		0.1	1.0	3.9
4.8		0.1	0.4	4.5
4.9		3.0	0.1	4.9

For the present analysis, V was restricted to the range $0 \leq V \leq 1$, since operation outside of this range implies an additional power supply. Working distance, z_o , normalized to lens radius, R , and the normalized spherical aberration coefficient, C_s/z_o , and chromatic aberration coefficient, C_c/z_o , were plotted as a function of the voltage factor V . Representative graphs of the optical properties for the minimum spherical aberration symmetrical and asymmetrical lens cases for each value of L/D are shown in Figures 80, 81, and 82.

Referring to these figures, several general statements are made: As shown in Figure 80, z_o/R increases as V increases for all values of L/D , that is, weaker lenses have longer focal lengths. As V increases, z_o/R is initially larger for asymmetrical lenses than symmetrical lenses for lenses of equal L/D . This remains true for all values of V in the range $0 \leq V \leq 1$ for lenses of small L/D ratio. However, for larger values of L/D (≥ 3.0), the z_o/R curves cross over as V increase. Similar statements pertain to lenses of the same symmetry as L/D is increased over the range of voltage ratio $0 \leq V \leq 1$.

As shown in Figure 81, the normalized spherical aberration coefficient, C_s/z_o , shows a minimum at a particular value of V for each lens type. For the smaller values of L/D , the minimum occurs for values of $V < 0$ and, therefore, does not show up on the curves in the restricted range $0 \leq V \leq 1$. In general, the value V_{\min} at the minimum of C_s/z_o is smaller for smaller values of L/D for lenses of the same type of symmetry. Furthermore, the asymmetrical lenses show lower values of V_{\min} and $C_s/z_o \min$

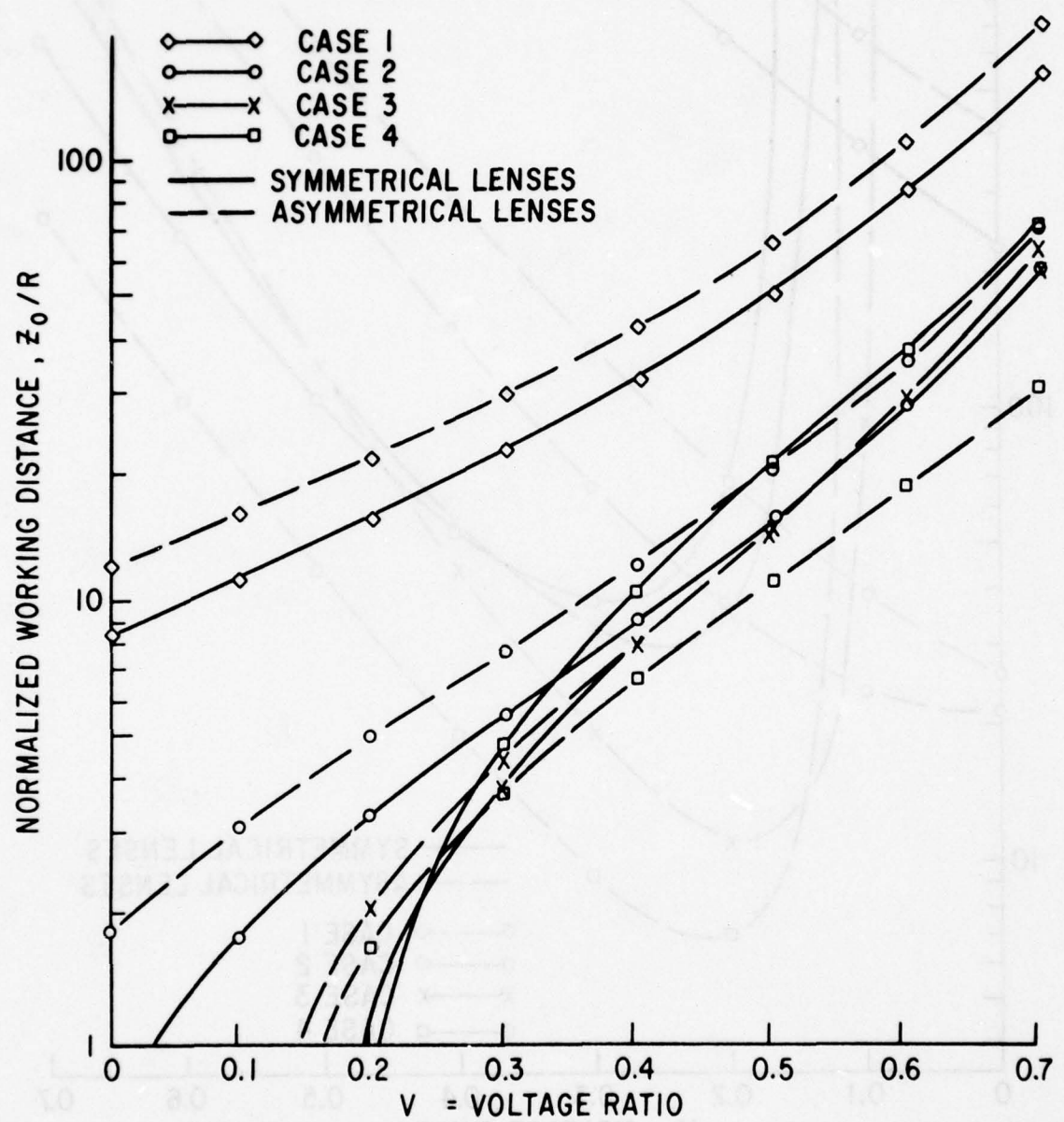


Figure 80. Normalized Working Distance vs Lens Voltage Ratio for Three Cylinder Einzel Lens Cases

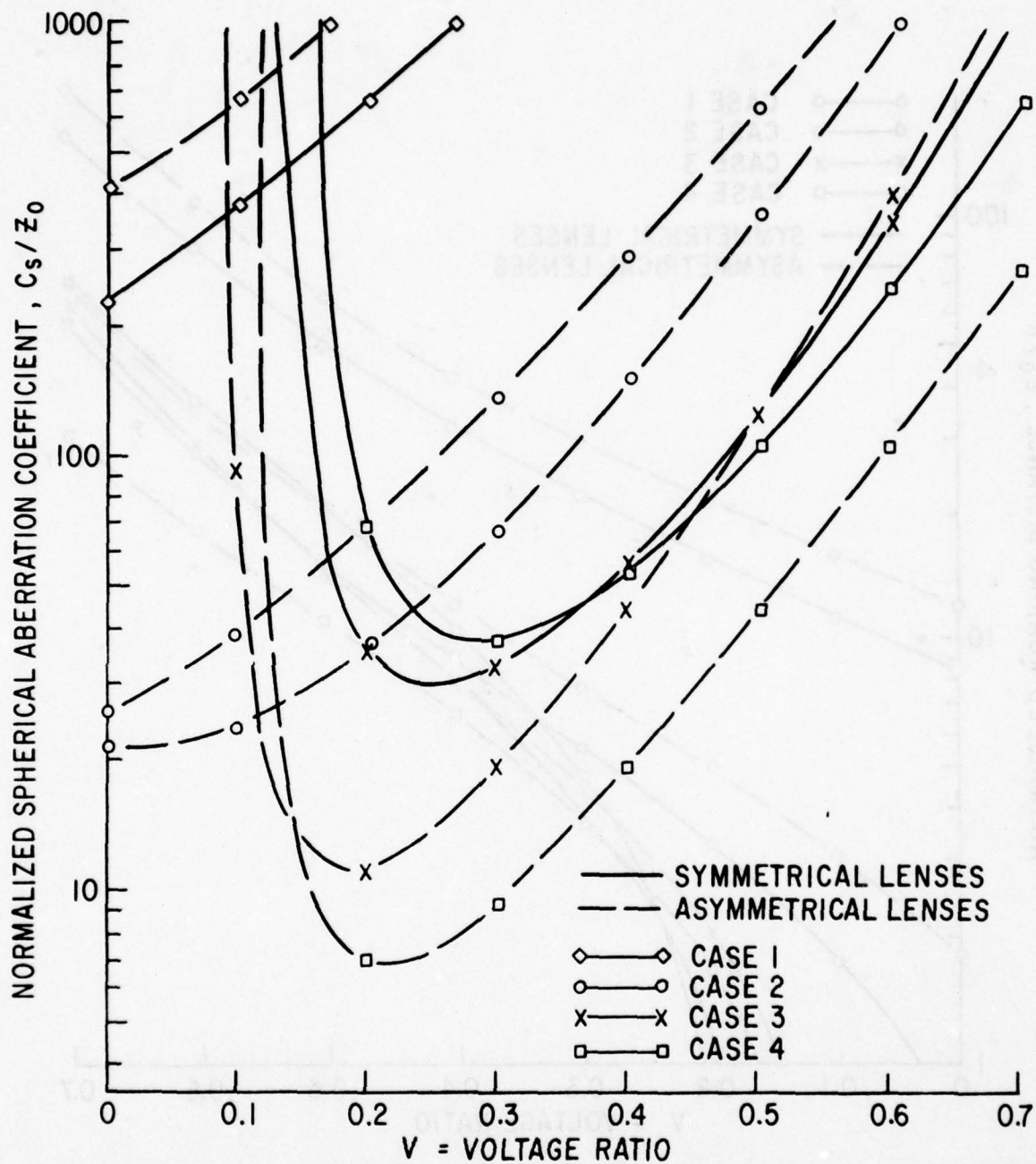


Figure 81. Normalized Spherical Aberration Coefficient vs Lens Voltage Ratio for Three Cylinder Einzel Lens Cases

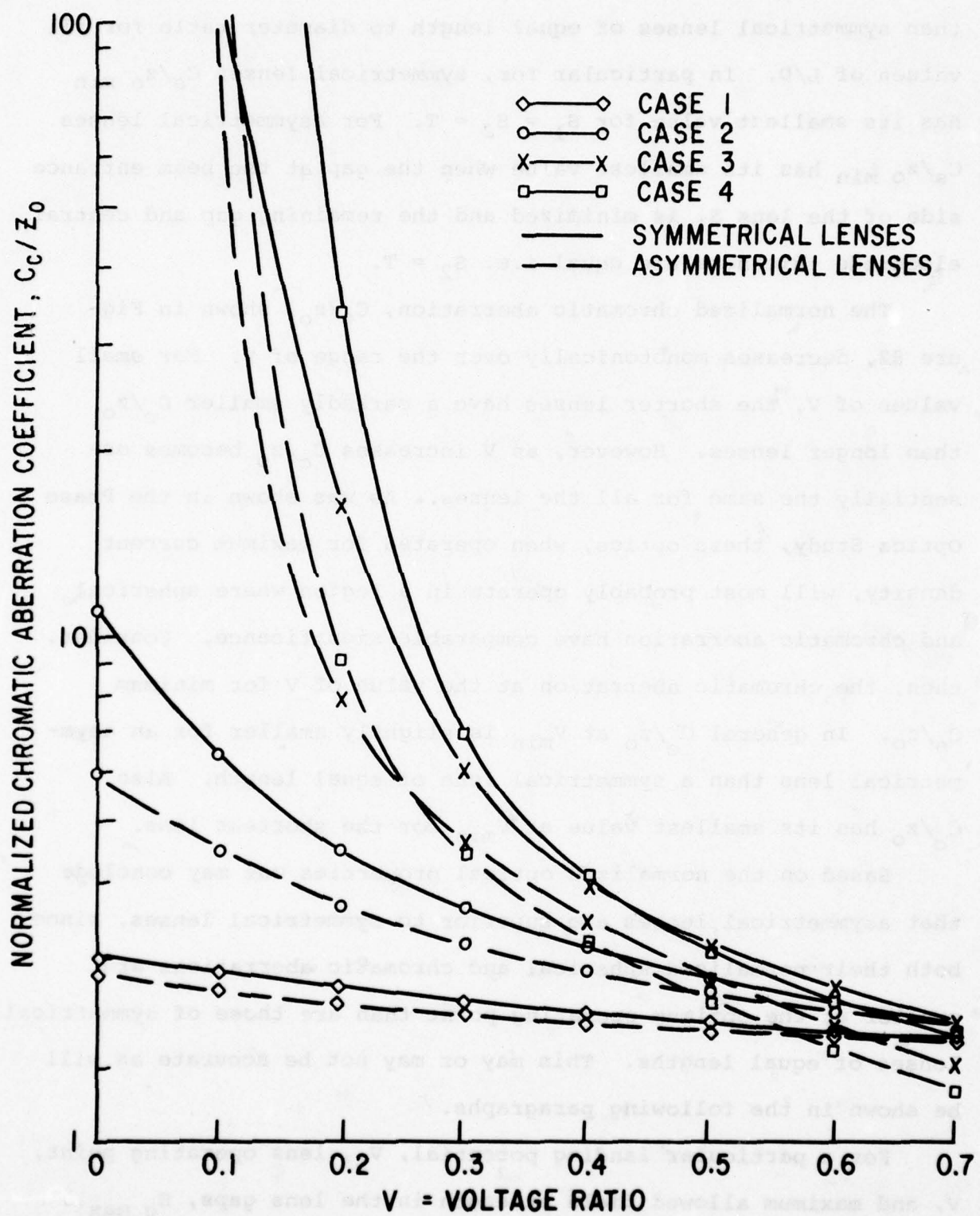


Figure 82. Normalized Chromatic Aberration Coefficient vs Lens Voltage Ratio for Three Cylinder Einzel Lens Cases

than symmetrical lenses of equal length to diameter ratio for all values of L/D. In particular for, symmetrical lenses $C_s/z_o \text{ min}$ has its smallest value for $S_1 = S_2 = T$. For asymmetrical lenses $C_s/z_o \text{ min}$ has its smallest value when the gap at the beam entrance side of the lens S_1 is minimized and the remaining gap and central electrode thickness are equal i.e. $S_2 = T$.

The normalized chromatic aberration, C_c/z_o , shown in Figure 82, decreases monotonically over the range of V. For small values of V, the shorter lenses have a markedly smaller C_c/z_o than longer lenses. However, as V increases C_c/z_o becomes essentially the same for all the lenses. As was shown in the Phase I Optics Study, these optics, when operated for maximum current density, will most probably operate in a region where spherical and chromatic aberration have comparable significance. Consider, then, the chromatic aberration at the value of V for minimum C_s/z_o . In general C_c/z_o at V_{\min} is slightly smaller for an asymmetrical lens than a symmetrical lens of equal length. Also C_c/z_o has its smallest value at V_{\min} for the shortest lens.

Based on the normalized optical properties one may conclude that asymmetrical lenses are superior to symmetrical lenses, since both their normalized spherical and chromatic aberrations are smaller at the optimum operating point than are those of symmetrical lenses of equal lengths. This may or may not be accurate as will be shown in the following paragraphs.

For a particular landing potential, V_L , lens operating point, V, and maximum allowed field strength in the lens gaps, $E_g \text{ max}$, the minimum gap spacing can be expressed as

TABLE 7
OPTICAL PROPERTIES FOR BEST LENSES OF TABLE 1

Lens	V_{min}	z_o/R	C_s/z_o	C_c/z_o	$R_{min}\text{cm}$	$z_o\text{ cm}$	$C_s\text{cm}$	$C_c\text{ cm}$
1.1	0	8.53	226.95	3.01	2.5	21.33	4840	64
1.2	0	12.04	411.33	2.80	2.5	30.10	12381	84
2.1	0	.66	22.16	12.55	2.5	1.63	36.56	20.05
2.4	0	1.79	25.47	6.00	2.5	4.48	114.00	26.85
3.2	.25	2.41	30	9.25	.19	0.45	13.56	4.18
3.5	0.2	2.01	11.47	8.11	2.0	4.02	46.11	32.60
4.3	.29	4.05	38	8.25	.09	0.36	13.75	2.99
4.6	.22	2.04	6.7	7.51	1.95	3.98	26.65	29.88

$$S_{\min} = \frac{V_L (1-V)}{\frac{E}{g} \max} \quad (21)$$

Since the lens gap S is minimized, so is the lens radius at this operating point for a given lens because

$$R_{\min} = \frac{1}{2} \frac{S_{\min}}{S/D} . \quad (22)$$

Therefore z_o , C_s , and C_c are also minimized by operating with these conditions:

$$z_o \min = (z_o/R) R_{\min}, \quad (23)$$

$$C_s \min = (C_s/z_o) z_o \min, \quad (24)$$

$$C_c \ min = (C_c/z_o) z_o \ min. \quad (25)$$

The method of combined aberration minimization that we have used is to operate a given lens at the voltage factor V_{\min} for the minimum in C_s/z_o and then designed for a maximum field strength of 5×10^4 volts/cm according to equations 5-9. The normalized optical properties and actual optical properties for the lenses of Figures 80, 81, 82 are summarized in Table 7. As was noted previously, the assymetrical lenses appear much more favorable in normalized aberrations. However, in terms of actual aberrations at a given set of operating conditions the larger length symmetrical lenses have lower spherical and chromatic aberration than their asymmetrical counterparts. This is because the S/D ratio is larger for the symmetrical lens and therefore, for a given S_{\min} , (Eq. 21) R_{\min} is lower (Eq. 22) leading to lower aberrations. It is for this same reason that lenses with small L/D have larger aberrations. However, it must be realized that in order to achieve these small aberrations the lens must be small in dimensions and

also operate with a small working distance. Therefore, these considerations must be compatible with mechanical and manufacturing constraints for the symmetrical lens to be effectively used.

A further comparison of the optical properties of symmetrical and asymmetrical lenses can be made by referring to Figures 83 and 84. In these figures the actual spherical and chromatic aberration coefficients in cm are plotted against z_0 in cm's for the 25 kV landing potential case. These curves are generated by starting at the minimum operating points summarized in Table 7 and increasing R above R_{\min} thereby increasing other lens dimensions and optical properties. From these curves it can be seen that smaller values of z_0 can be reached with symmetrical lenses, leading to considerable reduction in aberrations. However, for longer working distances the asymmetrical lens has the lowest aberrations. Therefore the best lens to use depends on operating parameters such as minimum tolerable working distance and landing potential.

Thus, the choice between symmetrical and asymmetrical einzel lens designs is too dependent on system parameters and operating conditions to be made by general rules. Lenses with larger normalized lens lengths, L/D , result in lower aberrations for both symmetrical and asymmetrical lenses. Minimum aberrations for symmetrical lenses are achieved for the geometric conditions $S_1 = S_2 = T$. For the asymmetrical lens, minimum aberrations are achieved by making the beam entrance gap S_1 small and then setting $S_2 \approx T$.

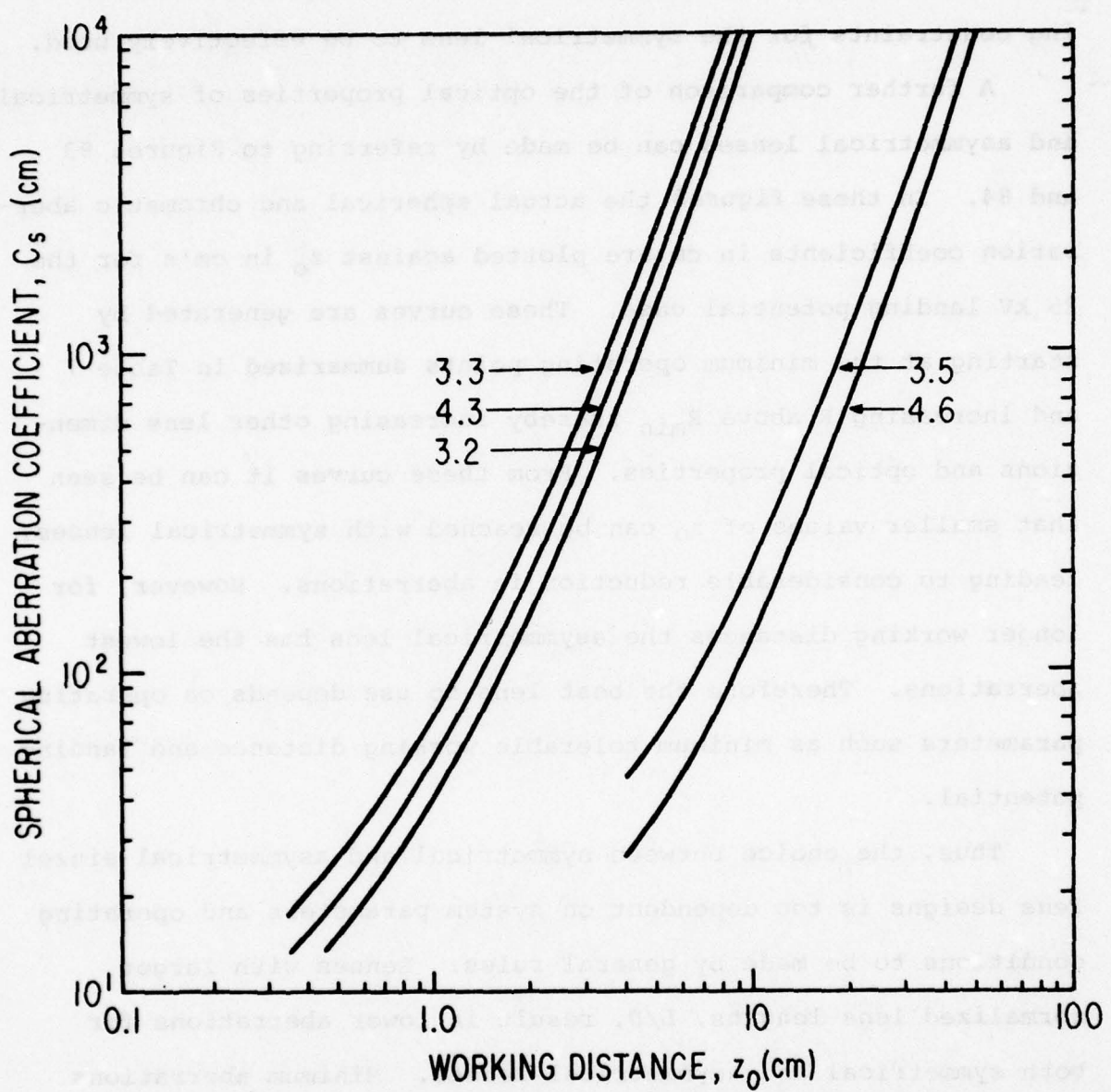


Figure 83. Spherical Aberration Coefficient vs Lens Working Distance for Symmetrical and Asymmetrical Einzel Lenses

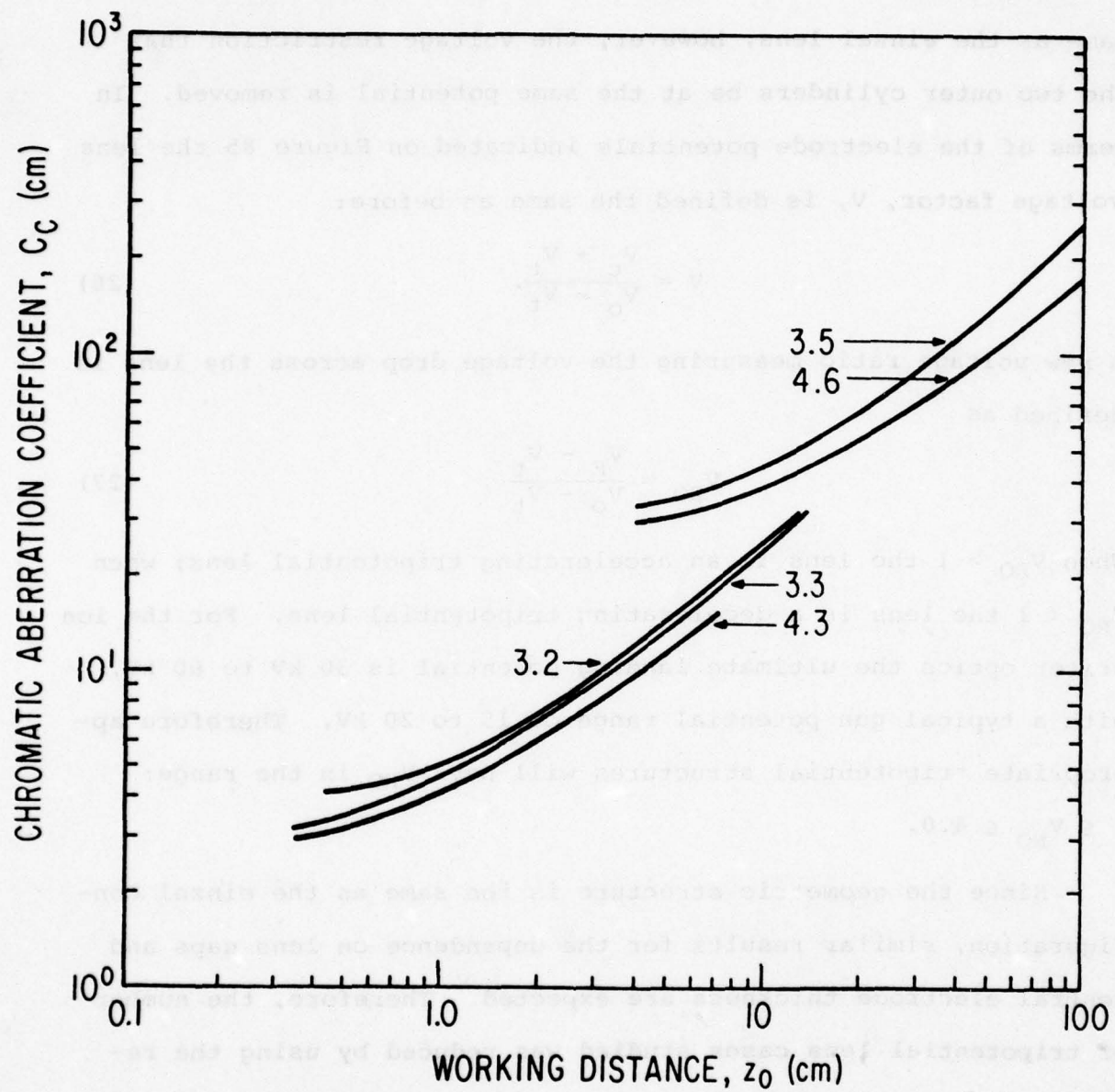


Figure 84. Chromatic Aberration Coefficient vs Lens Working Distance for Symmetrical and Asymmetrical Einzel Lenses

The next lens type studied was the tripotential lens shown in cross section in Figure 85. The geometrical structure is the same as the einzel lens, however, the voltage restriction that the two outer cylinders be at the same potential is removed. In terms of the electrode potentials indicated on Figure 85 the lens voltage factor, V , is defined the same as before:

$$V = \frac{V_c - V_t}{V_o - V_t}. \quad (26)$$

A new voltage ratio measuring the voltage drop across the lens is defined as

$$V_{RO} = \frac{V_R - V_t}{V_o - V_t}. \quad (27)$$

When $V_{RO} > 1$ the lens is an accelerating tripotential lens; when $V_{RO} < 1$ the lens is a decelerating tripotential lens. For the ion writer optics the ultimate landing potential is 30 kV to 60 kV, with a typical gun potential range of 15 to 20 kV. Therefore appropriate tripotential structures will have V_{RO} in the range: $2 \leq V_{RO} \leq 4.0$.

Since the geometric structure is the same as the einzel configuration, similar results for the dependence on lens gaps and central electrode thickness are expected. Therefore, the number of tripotential lens cases studied was reduced by using the results of the einzel lens analysis as a guide. Small values of normalized lens length were not considered. Furthermore, since the einzel lens cases 3 and 4 gave similar results for the lenses of the same symmetry, only case 3 was extended to the tripotential case for study.

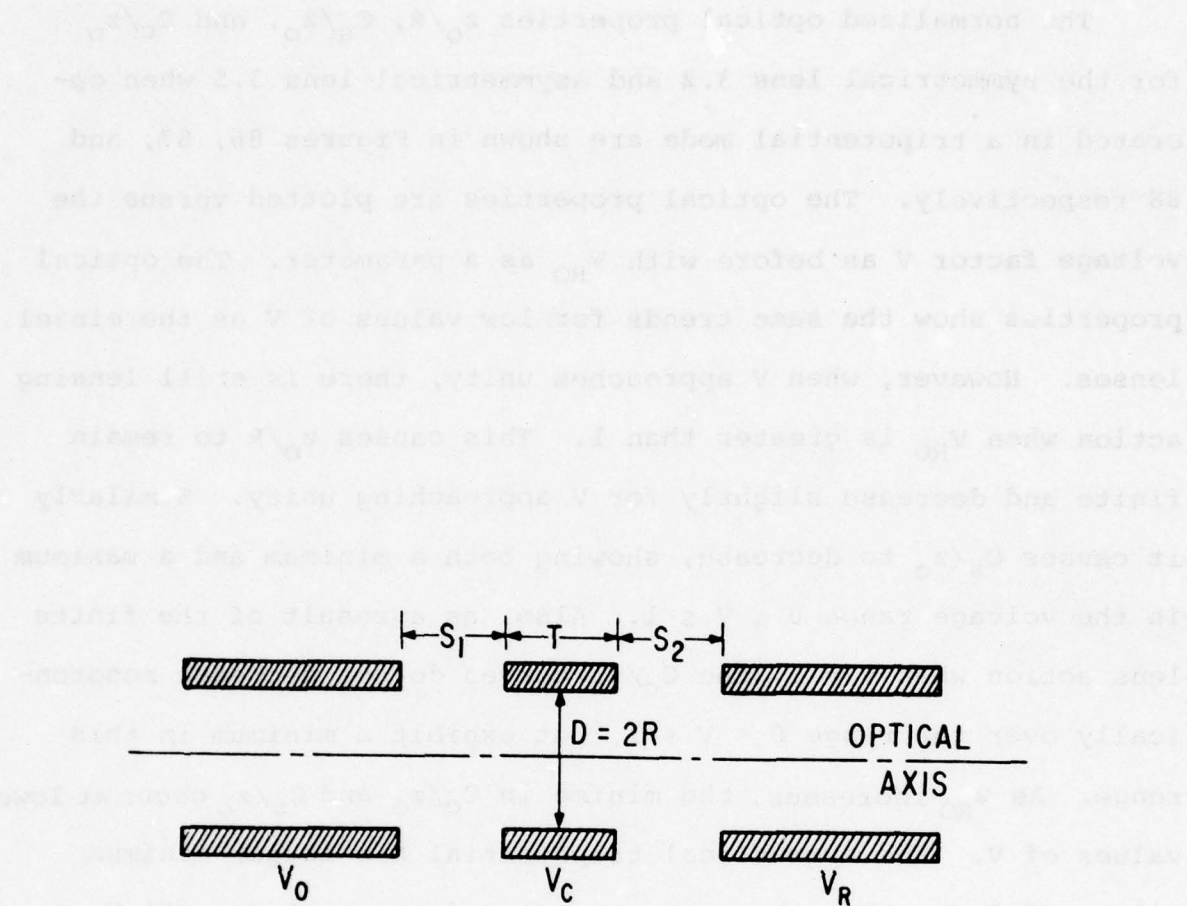


Figure 85. Three Cylinder Tripotential Lens

The normalized optical properties z_o/R , C_s/z_o , and C_c/z_o for the symmetrical lens 3.2 and asymmetrical lens 3.5 when operated in a tripotential mode are shown in Figures 86, 87, and 88 respectively. The optical properties are plotted versus the voltage factor V as before with V_{RO} as a parameter. The optical properties show the same trends for low values of V as the einzel lenses. However, when V approaches unity, there is still lensing action when V_{RO} is greater than 1. This causes z_o/R to remain finite and decrease slightly for V approaching unity. Similarly it causes C_s/z_o to decrease, showing both a minimum and a maximum in the voltage range $0 \leq V \leq 1$. Also, as a result of the finite lens action when $V = 1$, the C_c/z_o curves do not decrease monotonically over the range $0 < V < 1$, but exhibit a minimum in this range. As V_{RO} increases, the minima in C_c/z_o and C_s/z_o occur at lower values of V . The symmetrical tripotential has larger minimum values of C_s/z_o than the asymmetrical tripotential for all V_{RO} . Based on these curves for the normalized optical properties, the asymmetrical tripotential lens would appear to have an electron optical advantage over the symmetrical tripotential. However, as noted above, the use of normalized aberrations for comparisons may be misleading, and the symmetrical and asymmetrical tripotential should be evaluated on a case by case basis.

The final lens type considered was the two tube immersion lens shown schematically in Figure 89. This lens provides acceleration ($V_i > 1$) or deceleration ($V_i < 1$) across the gap, S , similar to V_{RO} in the tripotential lens. The parameter V_i is the immersion lens voltage factor and is defined as

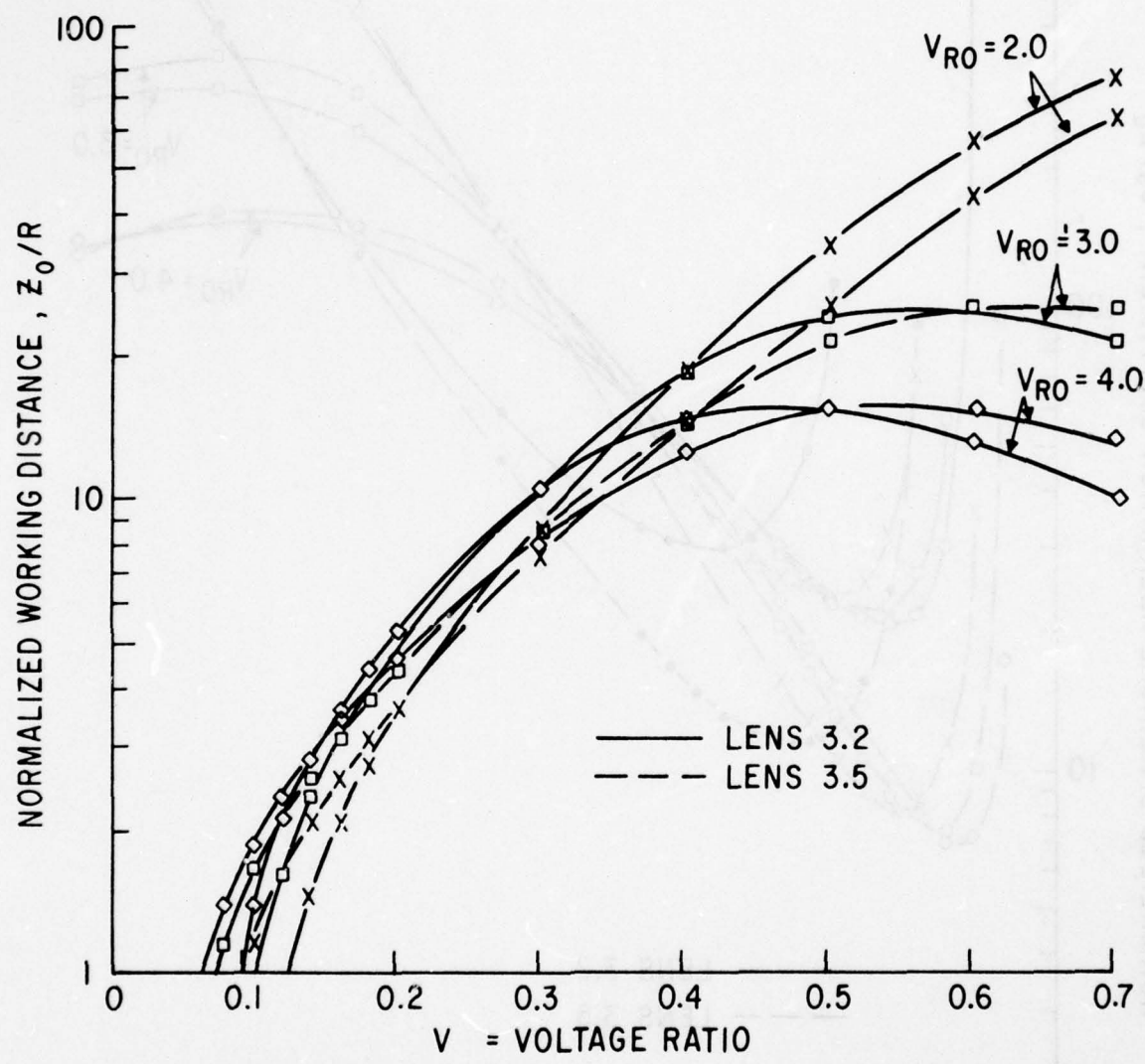


Figure 86. Normalized Working Distance vs Lens Voltage Ratio for Three Cylinder Tripotential Lens Cases

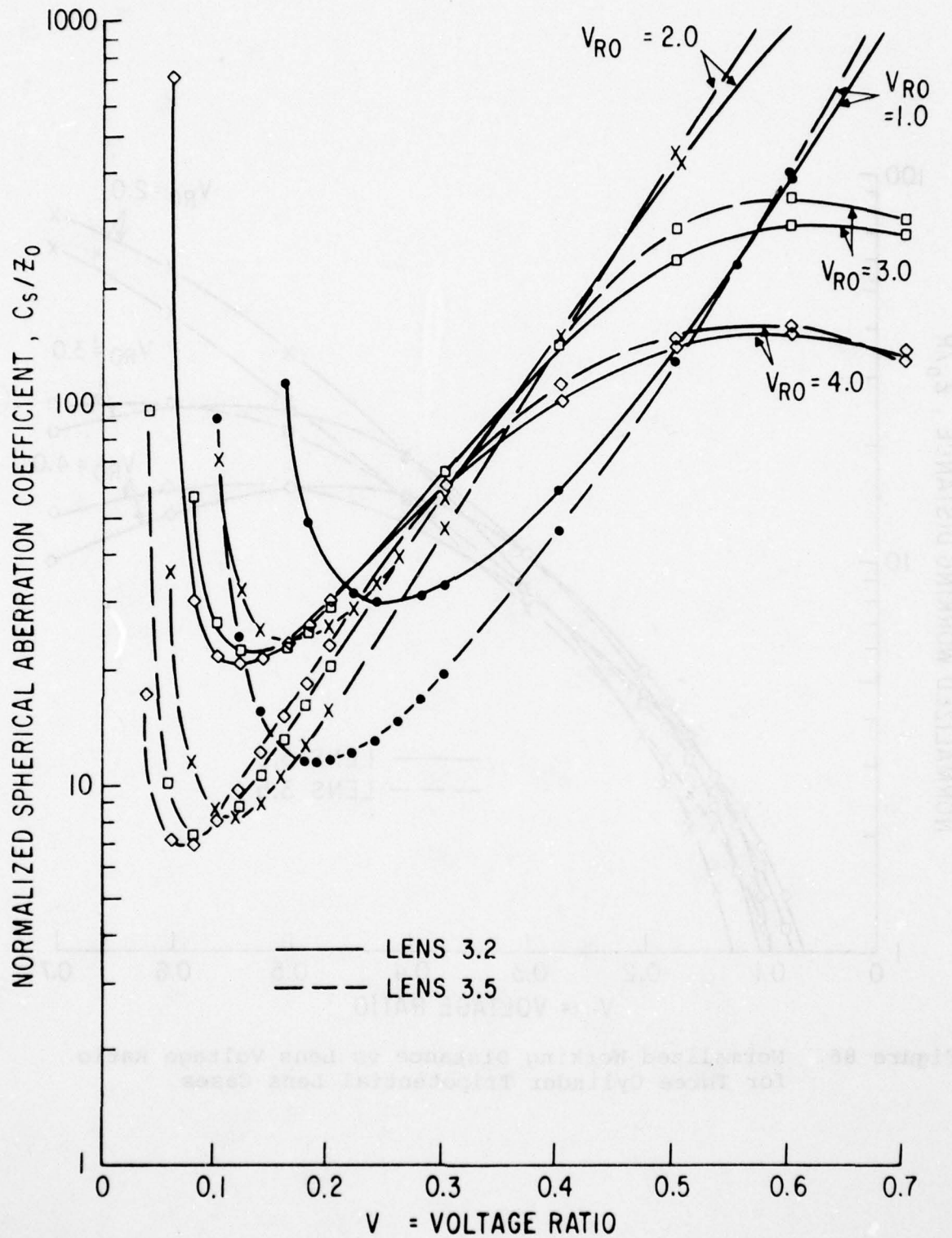


Figure 87. Normalized Spherical Aberration Coefficient vs Lens Voltage Ratio for Three Cylinder Tripotential Lenses

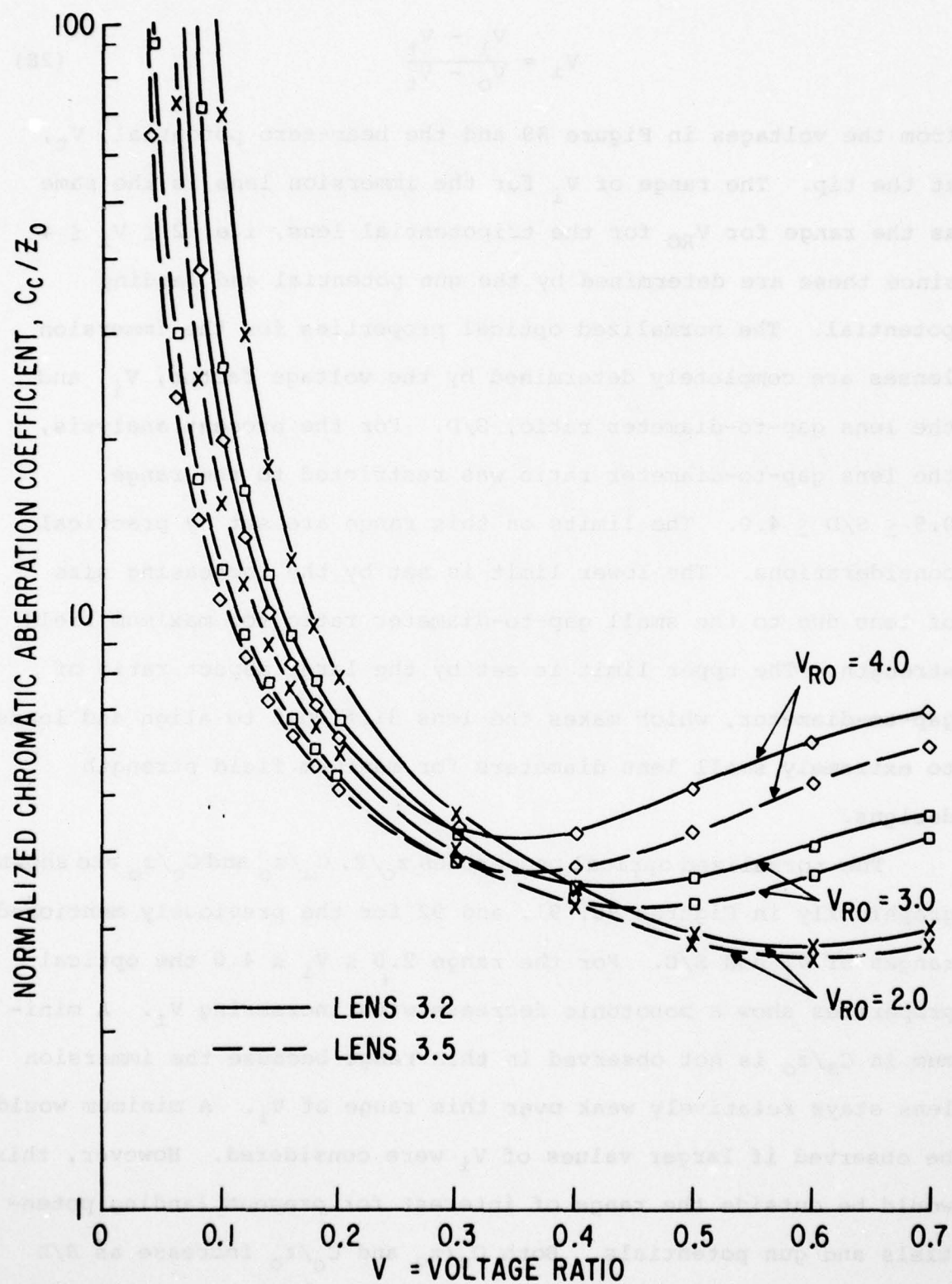


Figure 88. Normalized Chromatic Aberration Coefficient vs Lens Voltage Ratio for Three Cylinder Tripotential Lenses

$$v_i = \frac{v_1 - v_t}{v_o - v_t} \quad (28)$$

from the voltages in Figure 89 and the beam-zero potential, v_t , at the tip. The range of v_i for the immersion lens is the same as the range for v_{RO} for the tripotential lens, i.e. $2 \leq v_i \leq 4$ since these are determined by the gun potential and landing potential. The normalized optical properties for the immersion lenses are completely determined by the voltage factor, v_i , and the lens gap-to-diameter ratio, S/D. For the present analysis, the lens gap-to-diameter ratio was restricted to the range, $0.5 \leq S/D \leq 4.0$. The limits on this range are set by practical considerations. The lower limit is set by the increasing size of lens due to the small gap-to-diameter ratio for maximum field strength. The upper limit is set by the large aspect ratio of gap-to-diameter, which makes the lens difficult to align and leads to extremely small lens diameters for maximum field strength designs.

The normalized optical properties z_o/R , C_s/z_o and C_c/z_o are shown graphically in Figures 90, 91, and 92 for the previously mentioned ranges of v_i and S/D. For the range $2.0 \leq v_i \leq 4.0$ the optical properties show a monotonic decrease with increasing v_i . A minimum in C_s/z_o is not observed in this range because the immersion lens stays relatively weak over this range of v_i . A minimum would be observed if larger values of v_i were considered. However, this would be outside the range of interest for present landing potentials and gun potentials. Both C_s/z_o and C_c/z_o increase as S/D increases at a given value of v_i . The significance of this trend

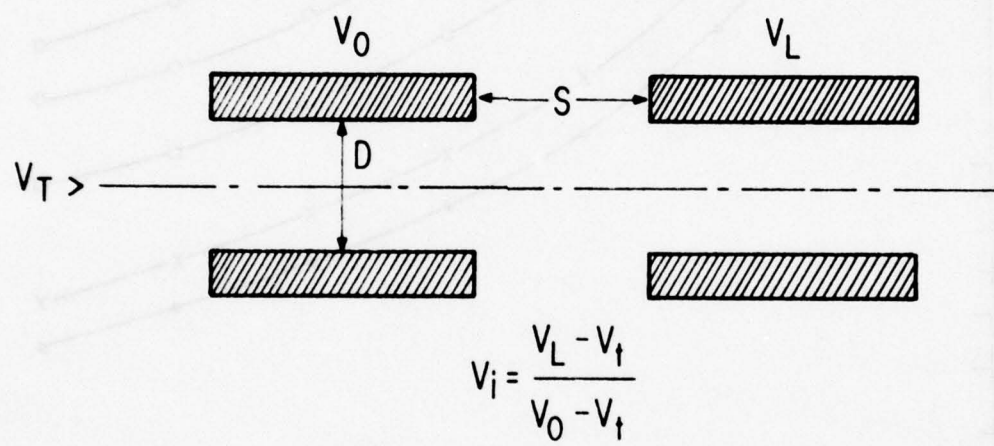
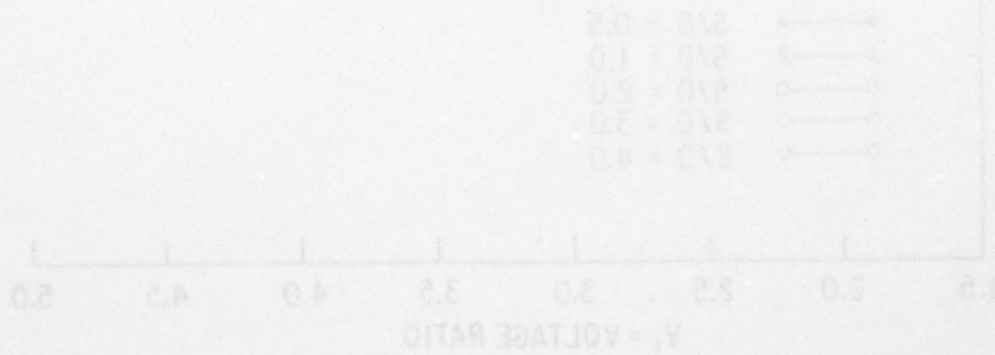


Figure 89. Two Cylinder Immersion Lens



The following table gives the optical ratios for various voltages. The values are approximate and may differ slightly from those obtained by direct measurement.

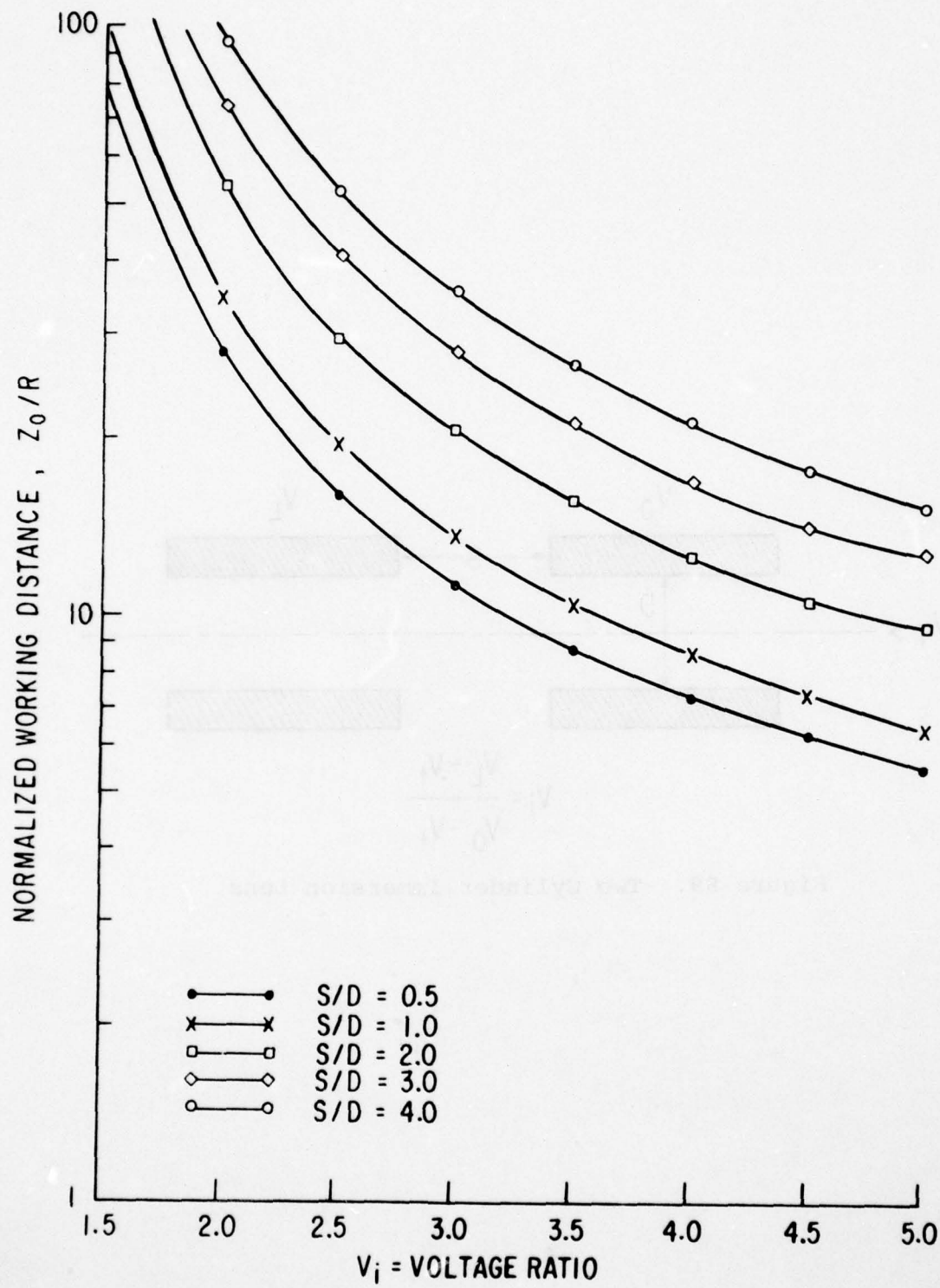


Figure 90. Normalized Working Distance vs Lens Voltage Ratio for Two Tube Immersion Lenses

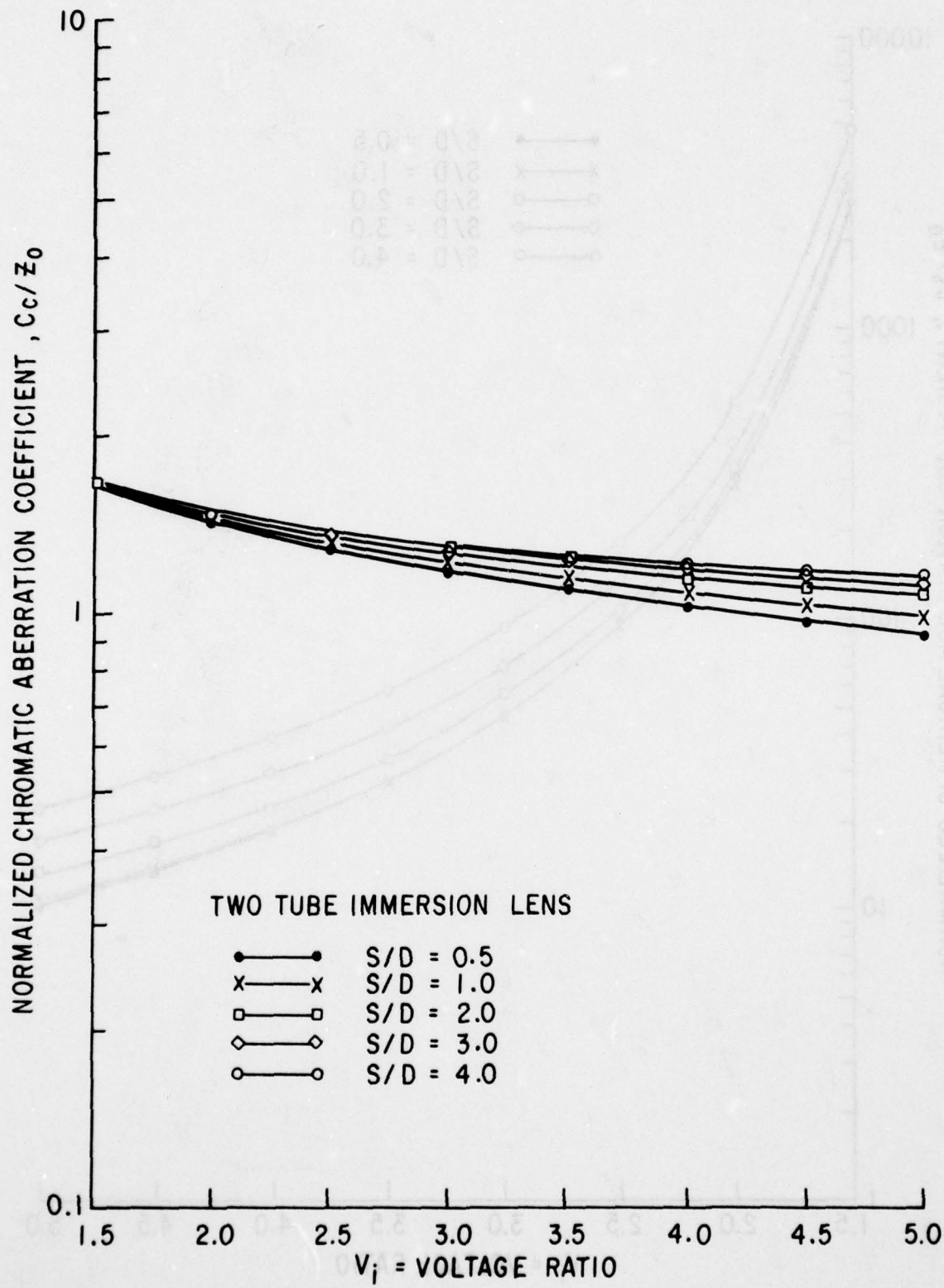


Figure 91. Normalized Chromatic Aberration Coefficient vs Lens Voltage Ratio for Two Tube Immersion Lenses

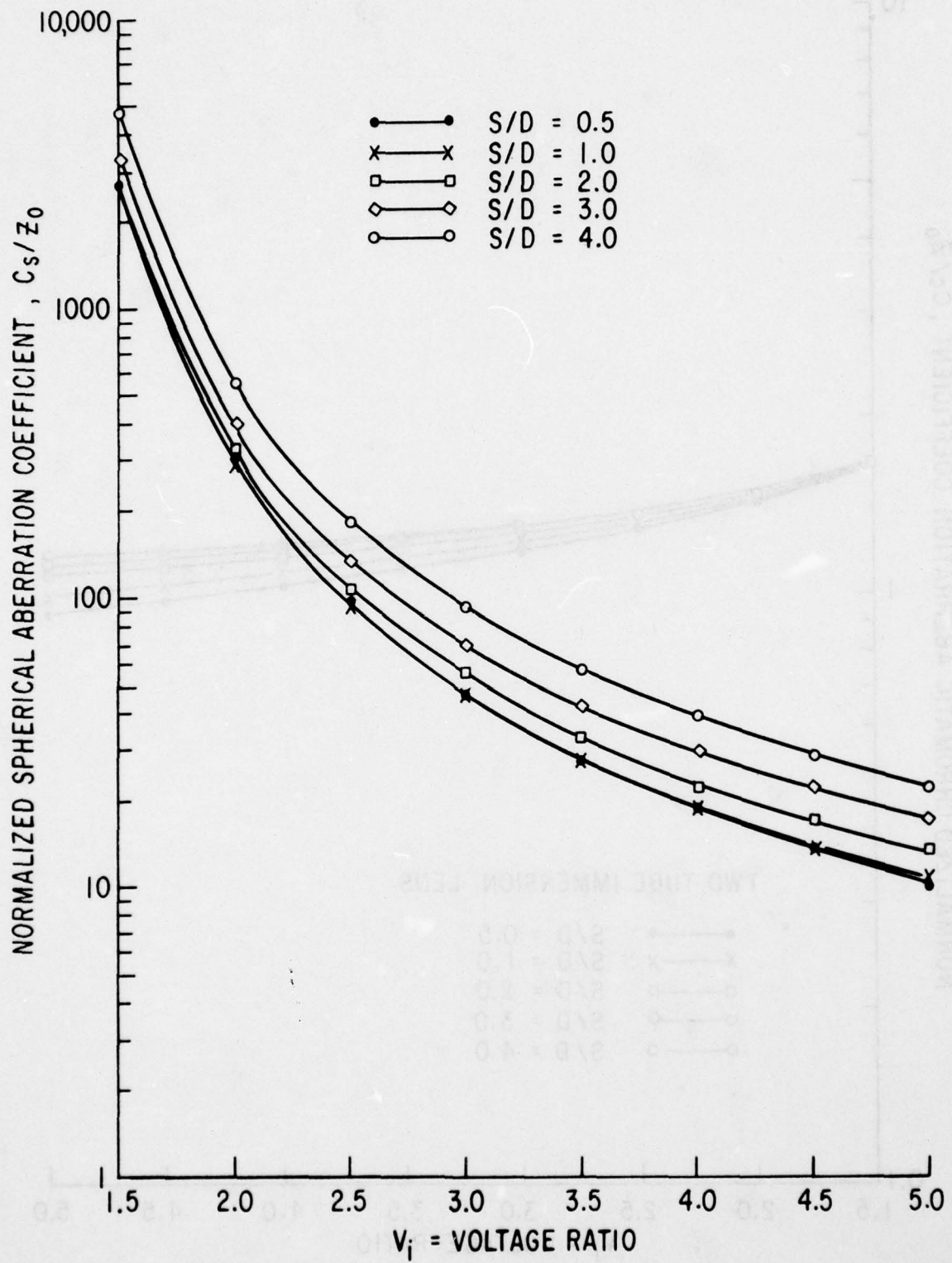


Figure 92. Normalized Spherical Aberration Coefficient vs Lens Voltage Ratio for Two Tube Immersion Lenses

cannot be ascertained from the normalized optical parameters; the lowest aberration configuration can only be determined from a case study when the optical properties are actually evaluated.

In this section, the normalized optical properties for the einzel, tripotential, and immersion electrostatic tube lenses have been presented. The use of these optical properties in the designs for positive ion columns of Xe^+ at 60 kV landing potential and Ar^+ at 30 kV landing potential will be discussed in the following sections of this report.

60 kV Xe^+ , ION COLUMN DESIGN

In this section, the design of a 60 kV, Xe^+ ion column using the optical properties discussed in the preceding section will be presented. The design criteria are a final landing potential of 60 kV, gun accelerating potential of 15-20 kV, and an optical column with all the acceleration in the first lens. The design criteria are a final landing potential of 60 kV and a gun potential of 15-20 kV. Also a column with all the acceleration in the first lens is assumed, so that the region between lenses and the target plane can be operated at electrical ground. In more specific terms, these requirements dictate an initial lens of either the three element tripotential or two element immersion type operating with an accelerating ratio of 3-4 and a final lens of the three element einzel type.

Normalized optical properties for the lenses meeting the column design conditions are summarized in Tables 3 and 9. For analysis, the three element symmetrical lens 3.2 and asymmetrical lens 3.5 were chosen. These lenses were chosen over lenses 4.3

TABLE 8
NORMALIZED OPTICAL PROPERTIES THREE CYLINDER
TRIPOTENTIAL AND EINZEL PROPERTIES

Lens	V_{RL}	V_{min}	z_o/R at V_{min}	C_s/z_o at V_{min}	C_c/z_o at V_{min}	f_o/R at V_{min}
3.2	1.0	.25	2.41	30	9.25	5.7
	3.0	.12	1.63	22.16	16.25	5.45
	4.0	.14	2.06	20.42	13.49	6.65
3.5	1.0	.20	2.01	11.47	8.11	4.40
	3.0	.09	1.42	7.35	14.40	3.00
	4.0	.075	1.25	6.85	16.25	3.55

TABLE 9
NORMALIZED OPTICAL PROPERTIES TWO CYLINDER IMMERSION LENS

S/D	V_i	z_o/R	C_s/z_o	C_c/z_o	f_o/R
0.5	3	11.33	47.37	1.18	8.81
	4	7.24	18.54	1.03	5.27
1.0	3	13.70	46.68	1.23	10.94
	4	8.58	18.80	1.08	6.50
2.0	3	20.48	54.47	1.28	16.66
	4	12.52	22.71	1.15	9.78
3.0	3	27.92	68.85	1.30	22.85
	4	16.85	28.99	1.19	13.30
4.0	3	35.67	92.88	1.32	29.32
	4	21.37	38.38	1.21	16.97

and 4.6 after comparison of their optical properties and consideration of the compactness of an $L/D = 3.0$ design, which would be simpler to build. Both symmetrical and asymmetrical configurations were considered. The design procedure was to operate the lenses under maximum field strength conditions at the operating point for the minimum in C_s/z_o for the three element lenses.

The two element immersion lens does not show a minimum in C_s/z_0 and the operating point is set entirely by the accelerating ratio (V_i) for the lens.

For the einzel lens maximum field strength considerations lead to the equation for minimum gap dimension

$$S_{\min} = \frac{V_L (1-V_{\min})}{Eg_{\max}} \quad (29)$$

Since the einzel lens is symmetrical in voltage, the minimum lens diameter is given by:

$$D_{\min} = \frac{S_{\min}}{S/D}, \quad (30)$$

where S/D is interpreted to be the smallest S/D ratio for the particular lens. Once D_{\min} is known, the other lens dimensions can be calculated from the normalized dimensions given in Table 6 and the optical properties from the data in Table 8. The maximum field strength conditions must be considered for each gap independently for the tripotential lens since this lens is asymmetrical in voltage (and perhaps in geometry as well). For the beam input side the minimum gap width is

$$S_{1\ min} = \frac{V_g (1-V_{\min})}{Eg_{\max}}, \quad (31)$$

leading to a minimum diameter of

$$D_{1\ min} = \frac{S_{1\ min}}{S_{1/D}} \quad (32)$$

The minimum gap width for the exit side of the lens is given by

$$S_{2\ min} = (V_{RO} - V_{\min}) \frac{V_g}{Eg_{\max}} \quad (33)$$

and its associated diameter is

$$D_{2 \text{ min}} = \frac{s_2 \text{ min}}{s_2/D} \quad (34)$$

The lenses as considered have a constant bore diameter. To prevent exceeding the maximum field strength at any point in the lens, the maximum value of $D_{1\text{min}}$ or $D_{2\text{min}}$ must be taken for the lens diameter. Once the diameter is known the remaining lens dimensions and optical properties can be evaluated from the data in Tables 6 and 8 respectively. The minimum gap for the immersion lens is given by

$$s_{\text{min}} = \frac{(V_i - 1) V_g}{Eg_{\text{max}}} \quad (35)$$

and the minimum diameter by

$$D_{\text{min}} = \frac{s_{\text{min}}}{s/D} \quad (36)$$

Once again with D_{min} and s_{min} known, the lens dimensions are known and the optical properties can be evaluated from the normalized data which is given in Table 9.

The maximum field design conditions were used in conjunction with the data in Tables 6, 8, and 9 to specify the dimensions and optical properties for the first lens of the column. As a design condition, all of the acceleration for the lens system occurs in the first lens. Therefore the symmetrical tripotential, 3.2, the asymmetrical tripotential, 3.4, and the immersion lenses were considered for this lens. The gun potential is in the range of 15-20 kV and can vary slightly from gun to gun. For design, a gun potential of 15 kV was assumed, since this produces the maximum voltage

drop across the lens and therefore sets the most stringent requirements on lens dimensions. The maximum field strength in the lens gaps was taken as 5×10^4 volts/cm so that the enhanced field at the edge of the gap and inner cylinder wall remain within safe limits[1]. The resulting lens dimensions and optical properties for the first lens candidates are summarized in Table 10. Immersion lenses with $S/D > 3.0$ were not considered because the lens diameters were too small. The immersion lenses have a much lower chromatic aberration than the tripotential lenses; however, their spherical aberration coefficient is much greater. The symmetrical and asymmetrical tripotential lenses have comparable aberrations, the former having a lower chromatic aberration coefficient and the latter a lower spherical aberration coefficient.

The optimum first lens cannot be selected without considering the combined effects of its performance with the final lens. As was shown in the Phase I Optics Study, the beam current versus spot size at the image plane has the characteristic shape of the curve in Figure 93. At the largest spot sizes, the optics are limited by spherical aberration and the beam current varies as the two-thirds power of the spot size. In the intermediate spot size range, the optics are chromatic-aberration limited and the beam current varies as the square of the spot size. Ultimately, for small spot sizes, the optics become diffraction limited and the beam current drops rapidly. For a two lens field-ion source column designed for maximum current density, the aberrations of both lenses make significant contributions to the current versus spot size characteristic. The method of maximizing the beam current

TABLE J 0
PROPERTIES OF FIRST LENS CANDIDATES IN cm

Type	s_1	s_2	T	D	z_{ol}	C_{s1}	C_{c1}	f_1
Symm Tripot 3.2	1.16	1.16	1.16	1.16	1.19	24.35	16.09	3.85
Asym Tripot 3.5	0.28	3.89	4.17	2.78	1.74	11.88	28.19	4.93
Immersion $S/D = .5$	0.9			1.8	6.52	120.81	6.71	7.93
Immersion $S/D = 1.0$	0.9			0.9	3.86	72.59	4.17	2.93
Immersion $S/D = 2.0$	0.9			0.45	2.82	63.97	3.24	2.20
Immersion $S/D = 3.0$	0.9			0.3	2.53	73.27	3.01	2.00

adopted in this study was to optimize the magnification in the spherical aberration limited region and search for the lens combination to meet these conditions at the desired spot size. With this method of optimization, the beam current per unit spot size is made as large as possible in the spherically aberrated region. Thus, even if operation ends up in the chromatic aberration limited region, the beam current per unit spot size is larger because it starts its characteristic d^2 fall off at a higher value of beam current. Furthermore, the energy spread of 2 eV for the ion sources is an estimated worst case value not yet confirmed by experiment. Therefore the column may well run in the spherical aberration limited range of operation.

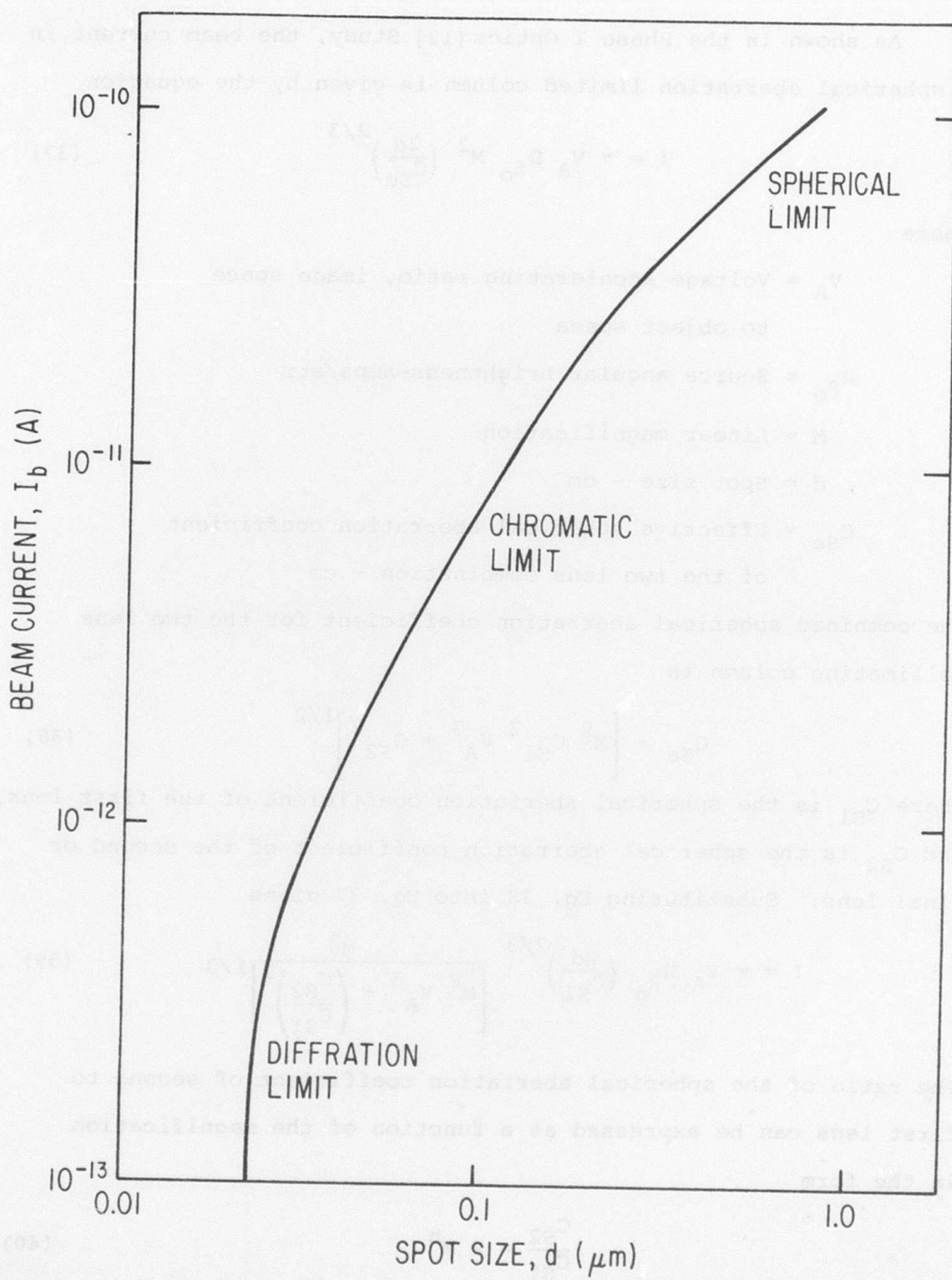


Figure 93. Typical Beam Current vs Spot Size Curve Showing Regions of Various Aberration Limits for a Two Lens Field Ion Source Column

As shown in the Phase I Optics [12] Study, the beam current in a spherical aberration limited column is given by the equation

$$I = \pi V_A \Omega_{\beta_0} M^2 \left(\frac{2d}{C_{Se}} \right)^{2/3} \quad (37)$$

where

V_A = Voltage accelerating ratio, image space
to object space

Ω_{β_0} = Source angular brightness-amps/str

M = Linear magnification

d = Spot size - cm

C_{Se} = Effective spherical aberration coefficient
of the two lens combination - cm

The combined spherical aberration coefficient for the two lens collimating column is

$$C_{Se} = \left[M^8 C_{S1}^2 V_A^3 + C_{S2}^2 \right]^{1/2} \quad (38)$$

where C_{S1} is the spherical aberration coefficient of the first lens, and C_{S2} is the spherical aberration coefficient of the second or final lens. Substituting Eq. 38 into Eq. 37 gives

$$I = \pi V_A \Omega_{\beta_0} \left(\frac{2d}{C_{S1}} \right)^{2/3} \frac{M^2}{\left[M^8 V_A^3 + \left(\frac{C_{S2}}{C_{S1}} \right)^2 \right]^{1/3}} \quad (39)$$

The ratio of the spherical aberration coefficient of second to first lens can be expressed as a function of the magnification in the form

$$\frac{C_{S2}}{C_{S1}} = k M^n \quad (40)$$

where k and n are constants dependent on the lens types. Substitution of this equation into Eq. 39 yields:

$$I = \pi V_A \Omega \beta_0 \left(\frac{2d}{kC_{SL}} \right)^{2/3} \frac{M \left(2 - \frac{2}{3} n \right)}{\left[M^{8-2n} \frac{V_A^3}{k^2} + 1 \right]^{1/3}} \quad (41)$$

The optimum magnification for maximum current may now be found by setting the derivative of Eq. 41 with respect to M , equal to zero and solving for M . This results in the optimum magnification given by:

$$M_{opt} = \left[\frac{k^2}{V_A^3} (3-n) \right] \left(\frac{1}{8-2n} \right) \quad (42)$$

This equation illustrates the interaction of the two lenses on the final column design through the constants k and m , relating their aberration coefficients.

The next step in the design is to select the final lens configuration. As noted previously, the final lens is to be of the three element einzel type. The choice has been limited to the symmetrical einzel 3.2 and the asymmetrical einzel 3.5 (cf. Table 7). The normalized optical properties for these lenses are given in Table 8 for operation at the C_S/z_O minimum. Using Eqs. 29 and 30, the minimum bore diameters for these lenses operating under maximum field strength conditions are 0.9 cm for the symmetrical lens 3.2, and 9.6 cm for the asymmetrical lens 3.5. Now, because of the optimum magnification criterion, there is no guarantee that the final lens will be used at this operating point. However, it is desirable to operate as nearly to this operating point as possible, to minimize the final lens aberration contribution. A result of

the Phase I Optics Study was that the linear magnification is optimized at a value near unity. Since the linear magnification is the ratio of the focal lengths of the second to first lenses, these lens diameters used with the data of Tables 8 and 10 show that the symmetrical lens 3.2 is the most compatible with the first lens candidates.

The next step in the optics design is to select the combination of lens 1 from Table 10 and the symmetrical einzel, 3.2, that produces the most current per unit spot size for spot sizes in the range of 800 to 1000 \AA . In order to do this, each of the lens combinations were optimized for maximum current within the limits of a maximum field strength of 5×10^4 volts/cm in either lens. This was done by calculating the optimum magnification for the optics system under spherical aberration limits and using this to specify the focal length of the final lens 3.2 since the focal length of the first lens is known. This focal length was used with the normalized optical properties of the symmetrical einzel, 3.2, at the minimum spherical aberration operating point, listed in Table 8, to obtain the dimensions of the final lens. If these dimensions were greater than those specified by maximum field strength considerations, the lens was operated at the optimum magnification. If, however, the optimum magnification called for dimension less than the maximum field strength allowed, the final lens was operated with dimensions as set by the field strength limit.

The equation for the optimum magnification for a spherical aberration limited system was given previously in Eq. 42. The derivation of this equation, assuming the ratio of spherical aber-

ration coefficients of the second to first lens, is related to the magnification, n , by an equation of the form:

$$\frac{C_{S2}}{C_{S1}} = k M^n \quad (43)$$

The constants k and n can be evaluated in terms of the optical constants of the lenses for the method of changing magnification by changing final lens size adopted here. At the minimum operating C_{S2}/z_{o2} point for the final lens let the optical constants be

$$A_1 = \frac{C_{S2}}{R_2} = \frac{C_{S2}}{z_{o2}} \frac{z_{o2}}{R_2} \quad (44)$$

and

$$A_2 = \frac{f_2}{R_2} \quad (45)$$

where the subscript 2 is used to indicate the second lens. Parameters with subscript 1 will indicate first lens properties. Therefore, the spherical aberration of the second lens can be expressed in terms of the optical properties as

$$C_{S2} = A_1 R_2 = \frac{A_1}{A_2} f_2 \quad (46)$$

Now, the first lens operating point is set at a fixed value as indicated in Table 10 and thus

$$C = \frac{C_{S1}}{f_1} = \text{constant.} \quad (47)$$

With this equation and Eq. 46 the desired result is given by

$$\frac{C_{S2}}{C_{S1}} = \frac{A_1}{A_2 C} \frac{f_2}{f_1} = \frac{A_1}{A_2 C} M \quad (48)$$

Comparing Eqs. 48 and 43 the desired constants are:

$$n = 1 \quad (49)$$

and

$$k = \frac{A_1}{A_2 C} \quad (50)$$

Using the preceding equations, the optimum magnification and second lens radius for the symmetrical einzel lens 3.2 used in combination with the various first lenses of Table 10 were calculated. The results of these calculations are summarized in Table 11. It was shown previously that the minimum lens radius for the symmetrical einzel final lens based on field strength considerations is 0.45 cm. Therefore, the optimum magnification conditions of Table 11 cannot be met without exceeding a field strength of 5×10^4 /cm in the lens gaps of the final lens for first lenses of the immersion type with $S/D \geq 1.0$. Thus for optical calculations, the final lens for these cases, as indicated previously, is set at the dimensions dictated by the maximum field strength. The resulting optical properties for the final lens in combination with the first lenses of Table 10 are given in Table 12. The actual magnification M_{act} , for these lens systems shows the deviation from the optimum conditions of Table 11 for the immersion first lens systems with $S/D \geq 1$.

Beam current versus spot size calculations were made for the lens systems listed in Table 12 with a computer program developed during the Phase I Optics Study. In this program, the spot size calculation takes account of geometric magnification, spherical aberration, chromatic aberration, and diffraction effects. The

TABLE 11

OPTIMUM MAGNIFICATION AND OPTIMUM RADIUS (cm) FOR A SYMMETRICAL
THREE CYLINDER EINZEL LENS WITH FIRST LENSES OF TABLE 10

First Lens Type	k	M_{opt}	R_{2opt}
Sym Tripot 3.2	2.00	0.709	0.478
Asym Tripot 3.5	5.26	0.976	0.844
Immersion S/D = 0.5	0.83	0.527	0.734
Immersion S/D = 1.0	0.51	0.449	0.23
Immersion S/D = 2.0	0.44	0.426	0.16
Immersion S/D = 3.0	0.35	0.394	0.14

TABLE 12

SECOND LENS DIMENSIONS ON OPTICAL PROPERTIES FOR
OPERATION WITH FIRST LENSES OF TABLE 10

First Lens	R_2 cm	z_{o2} cm	f_2 cm	C_{s2} cm	C_{c2} cm	M_{act}
Sym Tripot 3.2	0.478	1.15	2.73	34.56	10.66	.709
A Sym Tripot 3.5	0.844	2.03	4.81	61.02	18.82	.976
Immersion S/D = 0.5	0.734	1.77	4.18	53.07	16.36	.527
Immersion S/D = 1.0	0.45	1.085	2.57	32.54	10.03	.877
Immersion S/D = 2.0	0.45	1.085	2.57	32.54	10.03	1.168
Immersion S/D = 3.0	0.45	1.085	2.57	32.54	10.03	1.285

program was updated to include the revised source angular brightness of 5×10^{-7} amps/str, Xe^+ ions, and 60 kV landing potential. The resulting beam current versus spot size characteristics are shown in Figure 94. From this figure, it is seen that the immersion first lens with $S/D = 1.0$ and the symmetrical einzel second lens operating in the field strength limit gives the most current in the 800 to 1000 \AA spot size range of interest. The tripotential first lens systems are limited by the larger chromatic aberration of the first lens in this spot size region and therefore do not produce as much current. Even though the aberrations of the first lens are smaller for $S/D > 1.0$ immersion lenses, these systems do not have the current capability in the spot size range of interest of the $S/D = 1.0$ immersion first lens system. The reason for this is that the final lens is limited by field strength in all of these cases. Since the $S/D = 1$ immersion lens system operates closer to the optimum magnification for maximum current, it has higher current capability, and is the best choice for the lens system. The ion fluence, F in ions/cm^2 , delivered to the target with this system can be calculated with the formula

$$F = \frac{4\tau I}{\pi q d^2} \quad (51)$$

where

τ = bit dwell time - sec

I = beam current - amps

q = electronic charge - coul

d = spot size

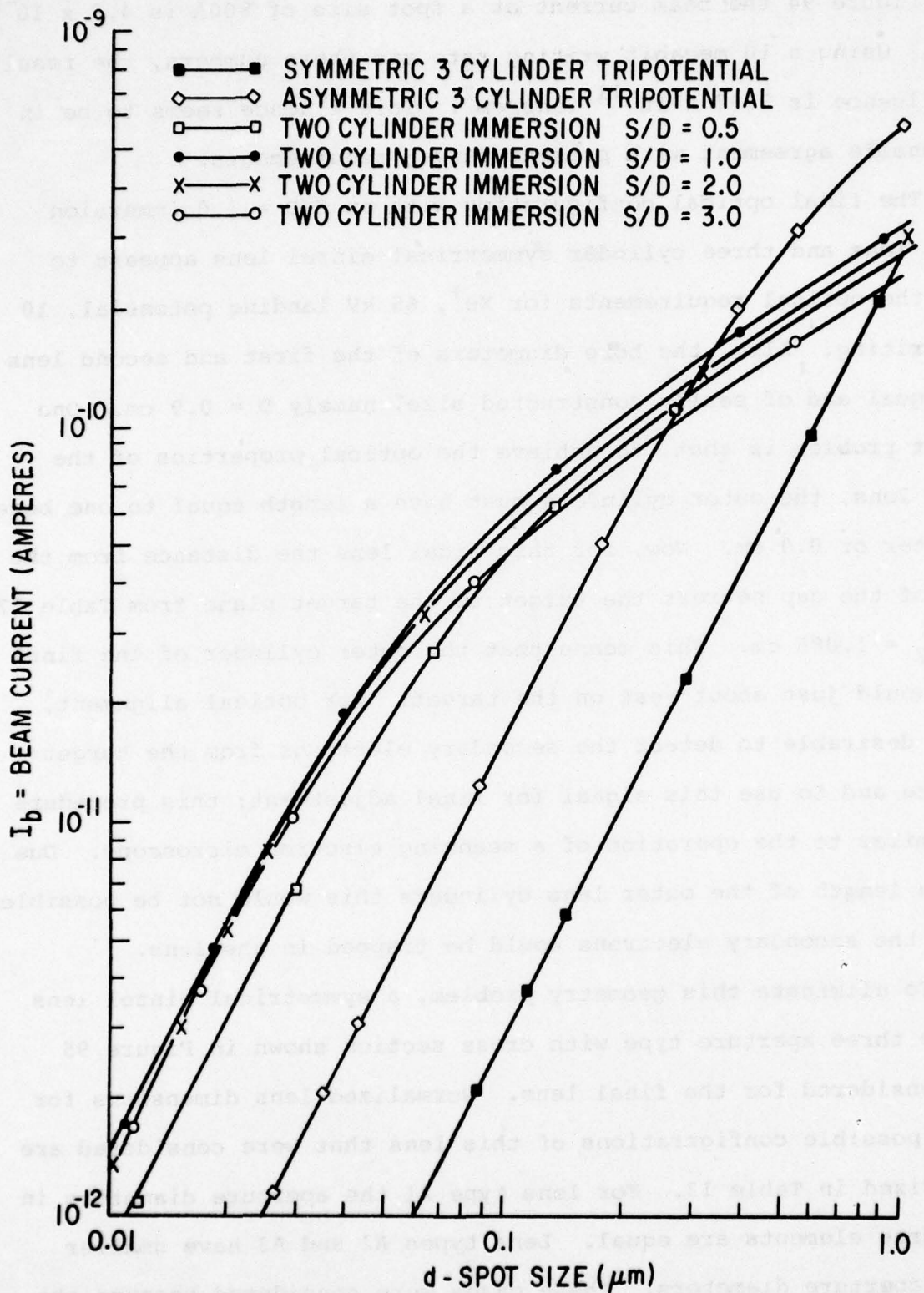


Figure 94. Beam Current vs Spot Size for Xe^+ 60 kV Column with Various First and Final Lens Combinations

From Figure 94 the beam current at a spot size of 800\AA is 4.8×10^{-11} amps. Using a 10 megabit writing rate and these numbers, the resulting fluence is 5.97×10^{-11} ions/cm². This fluence seems to be in reasonable agreement with present target requirements.

The final optical configuration with an S/D = 1.0 immersion first lens and three cylinder symmetrical einzel lens appears to meet the optical requirements for Xe^+ , 60 kV landing potential, 10 MHz writing. Also, the bore diameters of the first and second lens are equal and of easily constructed size, namely D = 0.9 cm. One slight problem is that, to achieve the optical properties of the final lens, the outer cylinders must have a length equal to one bore diameter or 0.9 cm. Now, for this final lens the distance from the edge of the gap nearest the target to the target plane from Table 12 is $z_{o2} = 1.085$ cm. This means that the outer cylinder of the final lens would just about rest on the target. For optical alignment, it is desirable to detect the secondary electrons from the target surface and to use this signal for final adjustment; this procedure is similar to the operation of a scanning electron microscope. Due to the length of the outer lens cylinders this would not be possible since the secondary electrons would be trapped in the lens.

To eliminate this geometry problem, a symmetrical einzel lens of the three aperture type with cross section shown in Figure 95 was considered for the final lens. Normalized lens dimensions for three possible configurations of this lens that were considered are summarized in Table 13. For lens type A1 the aperture diameters in the three elements are equal. Lens types A2 and A3 have smaller outer aperture diameters. These cases were considered because the

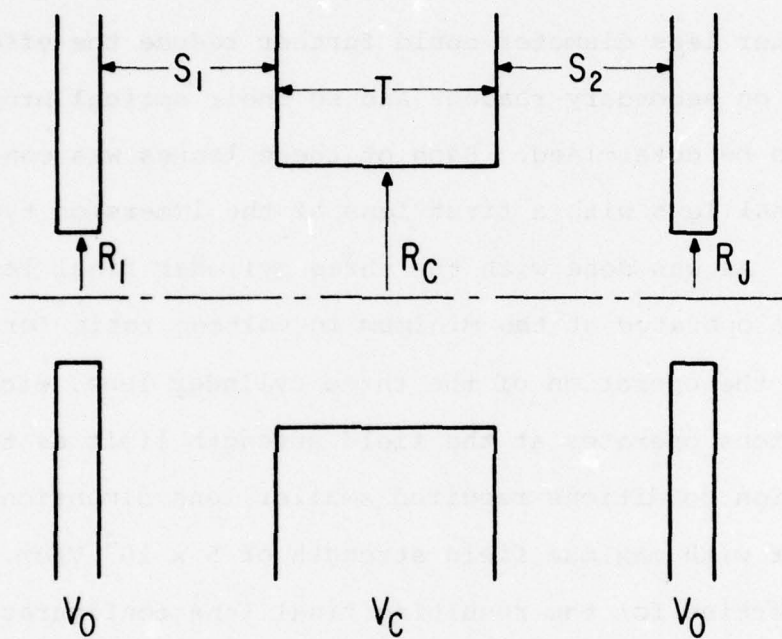


Figure 95. Three Aperture Einzel Lens

TABLE 13
NORMALIZED LENS DIMENSION FOR 3 APERTURE
EINZEL SECOND LENS

Lens Type	S_1/D_I	S_2/D_I	T/D_I	D_O/D_I
A1	1.0	1.0	.625	1
A2	1.0	1.0	.625	0.5
A3	1.0	1.0	.625	0.25

reduced outer lens diameter could further reduce the effect of the lens field on secondary readout and so their optical properties should also be determined. Each of these lenses was considered for the final lens with a first lens of the immersion type with $S/D = 1.0$. As was done with the three cylinder final lens, these lenses were operated at the minimum in voltage ratio for the C_S/z_o . Similar to the operation of the three cylinder lens, each of these configurations operates at the field strength limit as the optimum magnification conditions required smaller lens dimensions than allowed for with maximum field strength of 5×10^4 V/cm. The optical properties for the resulting final lens configurations are summarized in Table 14. Beam current versus spot size was calculated for these final lens configurations and the results are shown in Figure 96. As seen from this figure, the results are quite similar for all cases and almost identical with the results for a three cylinder lens. For example, with the equal diameter final lens, A1, the beam current at 800Å spot size is 5.2×10^{-11} amps giving a fluence at a 10 megabit writing rate of 6.47×10^{11} . In fact this fluence is slightly higher than the three cylinder einzel configuration because the overall system operates closer to the optimum magnification in the field strength limit. The working

TABLE 14

OPTICAL PROPERTIES FOR 3 APERTURE EINZEL FINAL LENSES
FOR OPERATION WITH AN IMMERSION FIRST LENS S/D = 1.0

Final Lens Type	R _I cm	z _{O2} cm	f ₂ cm	C _{S2} cm	C _{c2} cm	M _{act}
A1	0.48	0.984	2.38	36.53	9.02	.81
A2	0.48	0.850	2.25	29.35	8.25	.77
A3	0.48	0.794	2.21	28.79	7.94	.76

distance, z_{O2} , for the aperture final lens is comparable to that of the cylinder lens; however, because of the thin outer electrodes, the lens is considerably displaced from the target. Therefore collection of secondaries should be no problem. Furthermore, these calculations show that, if necessary, the outer electrodes of the lens could be reduced in size to further reduce the effect of the lens on the secondary collection without compromising the optical performance. However, from a fabrication point of view, the equal diameter lens is preferred because it can be more accurately assembled.

Based on the preceding design considerations, a proposed final design for the focusing optics of an Xe^+ , 60 kV, 10 megabit ion writer is shown in Figure 97. The optics consist of a two cylinder immersion lens with a gap to diameter ratio of 1.0. The final lens is of the equidiameter three aperture symmetrical einzel configuration. Both lenses operate in a maximum field strength limiting condition of 5×10^4 volts/cm in the lens gaps. All pertinent lens dimensions, voltages, and field strengths are indicated on the figure. The dimension between lenses is not specified at this point

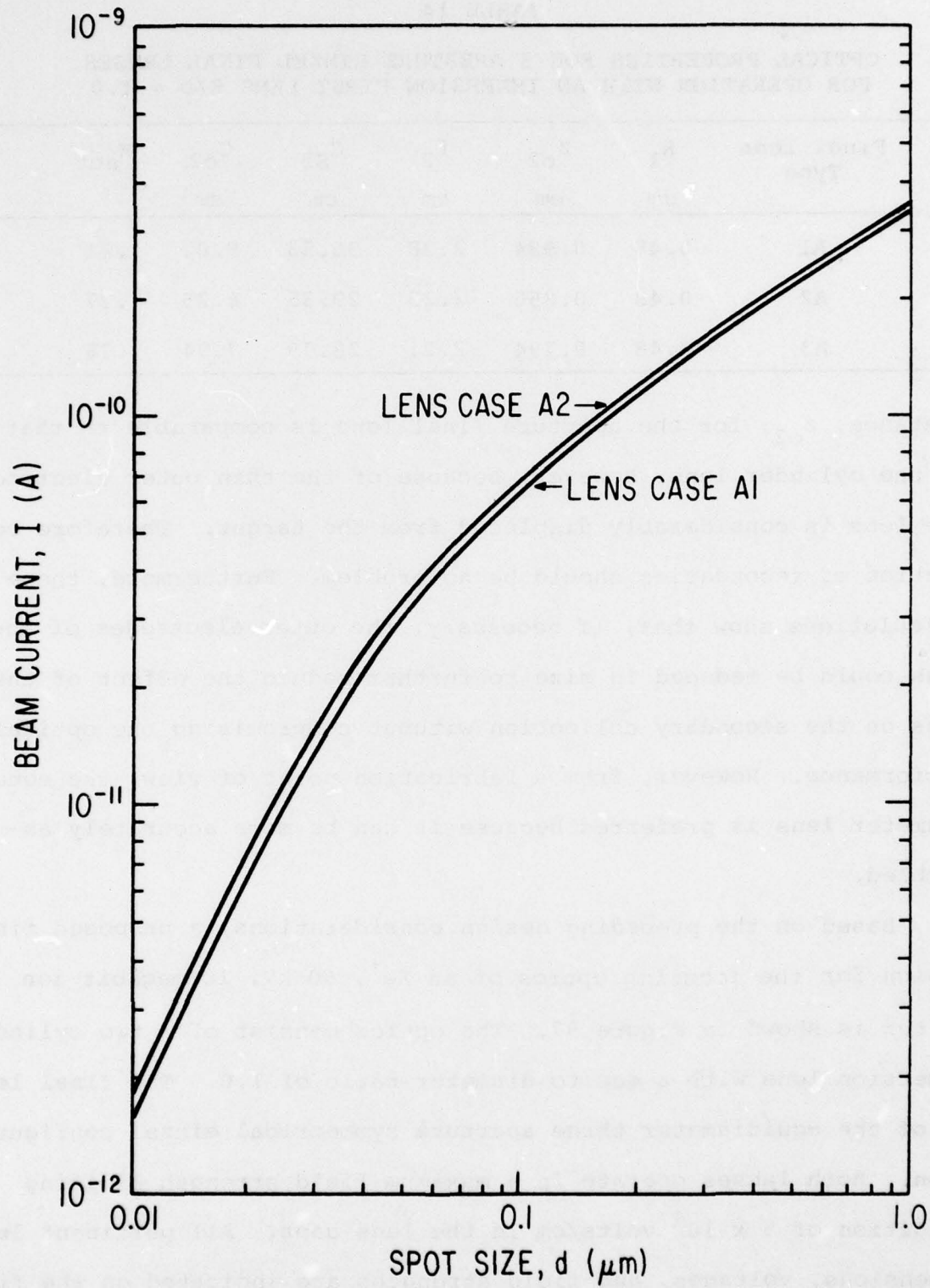


Figure 96. Beam Current vs Spot Size for Xe^+ , 60 kV Ion Column with Three Aperture Final Lenses

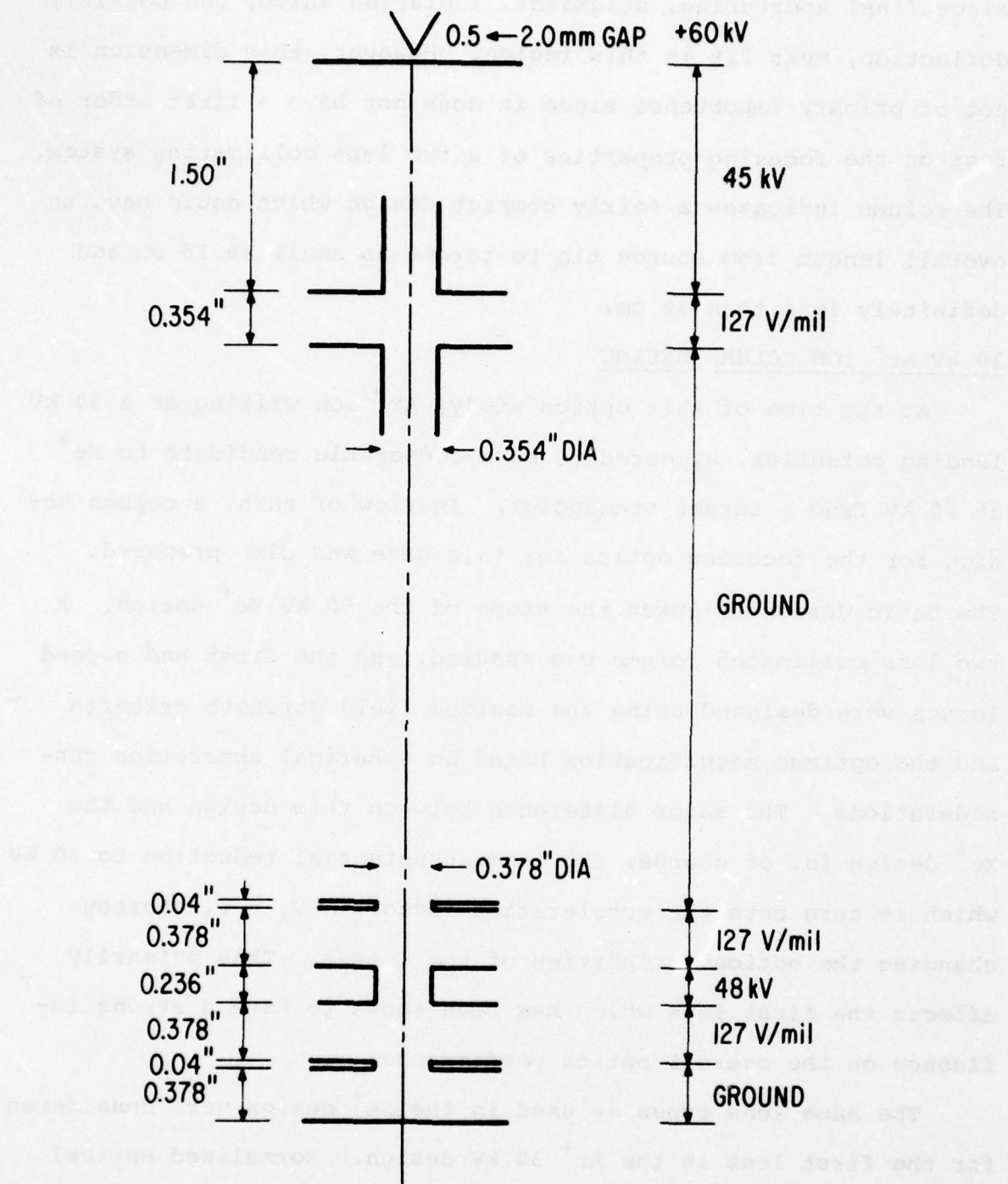


Figure 97. Cross-sectional Diagram of Xe^+ 60 kV Ion Optics Design

since final aperturing, stigmator, isolation valve, and possibly deflection, must fit in this region. However, this dimension is not of primary importance since it does not have a first order effect on the focusing properties of a two lens collimating system. The column indicates a fairly compact design which could have an overall length from source tip to target as small as 18 cm and definitely less than 30 cm.

30 kV Ar⁺ ION COLUMN DESIGN

At the time of this optics study, Ar⁺ ion writing at a 30 kV landing potential, appeared to be a comparable candidate to Xe⁺ at 60 kV from a target standpoint. In view of this, a column design for the focusing optics for this case was also prepared. The basic design followed the steps of the 60 kV Xe⁺ design. A two lens collimated column was assumed, and the first and second lenses were designed using the maximum field strength criteria and the optimum magnification based on spherical aberration considerations. The major difference between this design and the Xe⁺ design is, of course, the landing potential reduction to 30 kV which in turn cuts the acceleration factor to $V_A = 2$, thereby changing the optical properties of the lenses. This primarily affects the first lens which has been shown to have a strong influence on the overall optics performance.

The same lens types as used in the Xe⁺ design were considered for the first lens in the Ar⁺ 30 kV design. Normalized optical properties for these lenses operating with an accelerating voltage factor of 2.0 are listed in Table 15 for the three cylinder lenses and in Table 16 for the two cylinder immersion lenses. The operating

points for the three cylinder lenses are taken at the minimum in C_s/z_0 as was done in the Xe design. The first lens dimensions, and hence their aberrations were minimized using the maximum field strength conditions, Eqs. 31 through 34 for the tripotential lenses and Eqs. 35 and 36 for the immersion lenses. The resulting lens dimensions and optical properties for the Ar^+ , 30 kV, first lens candidates, are summarized in Table 17. Immersion lenses with $S/D > 2.0$ were not considered as the lens dimension became too small. The spherical aberration for the immersion lenses is noted to be drastically bigger than for the Xe^+ first lens candidates. This happens because the strength or refracting power of an immersion lens is a strong function of the accelerating ratio for low voltage ratios. For an accelerating ratio of two, the immersion lens is a very weak lens characterized by large spherical aberration. However, when the accelerating ratio increases to four as in the Xe design, the immersion lens becomes quite strong and the spherical aberration coefficient decreases markedly. The spherical aberration coefficients for the three element lenses, on the other hand, are quite comparable to those of the Xe design. Therefore, we might expect the immersion lenses to become less important in this design.

In order to achieve comparable fluence from the Ar^+ column as from the Xe column, one might expect that the working distance will again have to be small. Therefore, anticipating from the results of the Xe design, an equal diameter three aperture einzel lens, type A1, was assumed for the final lens right at the start of the design. The normalized optical properties for this lens operating at the minimum C_s/z_0 point are

TABLE 15

NORMALIZED OPTICAL PROPERTIES - THREE CYLINDER
TRIPOTENTIAL LENSES FOR Ar⁺ 30 kV FIRST LENSES

Lens	V _{RL}	V _{min}	z _o /R	c _s /z _o	c _c /z _o	f _o /R
3.2	2.0	.165	2.25	24.10	11.80	5.8
3.5	2.0	.12	1.65	8.4	11.40	4.2

TABLE 16

NORMALIZED OPTICAL PROPERTIES - TWO CYLINDER
IMMERSION LENSES

S/D	V	z _o /R	c _s /z _o	c _c /z _o	f _o /R
0.5	2.0	28.11	308.71	1.43	23.93
1.0	"	34.75	293.33	1.46	29.89
2.0	"	53.24	325.25	1.48	46.15
3.0	"	73.49	403.56	1.49	63.86
4.0	"	94.70	561.07	1.50	82.47

TABLE 17

PROPERTIES OF FIRST LENS CANDIDATES (in cm) Ar⁺, 30 kV DESIGN

Lens Type	S ₁	S ₂	T	D	z _{o1}	c _{s1}	c _{c1}	f ₁
Sym Tripot 3.2	.55	.55	.55	.55	0.619	14.92	7.0	1.60
A Sym Tripot 3.5	.264	3.70	3.96	2.64	2.178	18.29	24.82	5.54
Immersion S/D = 0.5	0.6				1.20	8.433	2603.35	12.06
Immersion S/D = 1.0	0.3				0.30	5.213	1528.98	7.61
Immersion S/D = 2.0	0.15				.075	3.993	1298.72	5.91
								3.46

$$V_{\min} = 0.2$$

$$f_2/R = 4.95$$

$$z_{o2}/R = 2.05$$

$$C_{s2}/R = 76.11$$

$$C_{c2}/R = 18.79$$

The minimum radius for this lens based on a maximum field strength of 5×10^4 volts/cm in the lens gaps is 0.24 cm. This gives the optical properties at the field strength limit for the final lens:

$$z_{o2} = 0.492$$

$$f_2 = 1.188$$

$$C_{s2} = 18.266$$

$$C_{c2} = 4.510$$

The optimum magnification and lens dimensions using the methods developed in the Xe design were sought for combinations of this lens and the first lenses of Table 17. The resulting optical properties for the final lens with the various first lens combinations are summarized in Table 18. For all the lens combinations, except the S/D = 2.0 immersion first lens case, the optimum magnification and lens dimensions could be used. For this case, the optimum radius was less than the radius allowed by the field strength limit and therefore the field strength limited optical properties were assumed.

Beam current versus spot size calculations were made for the lens combinations given in Tables 17 and 18 for Ar⁺ ions at 30 kV. The results of these calculations are shown in Figure 98. From this figure, the best lens system for the Ar⁺ ions at 30 kV is the

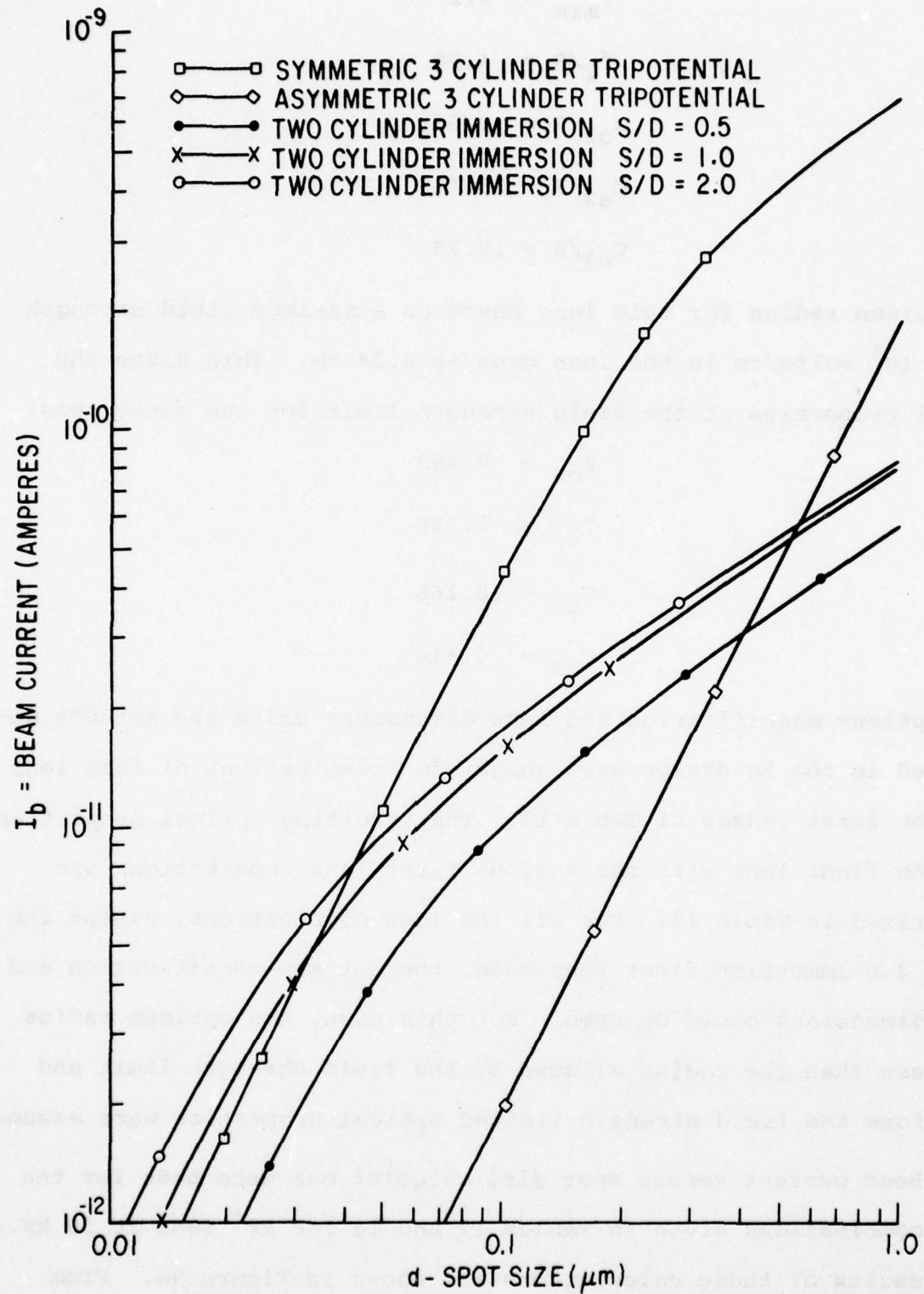


Figure 98. Beam Current vs Spot Size Curves for Various First and Final Lens Combinations, for an Ar^+ , 30 kV Design

TABLE 18
SECOND LENS RADIUS AND OPTICAL PROPERTIES
FOR OPERATION WITH FIRST LENSES OF TABLE 17

First Lens Type	R_2 cm	Z_0^2 cm	f_2 cm	C_{S^2} cm	C_{C^2} cm	M
Sym Tripot 3.2	.303	.622	1.501	23.07	5.70	.938
A Sym Tripot 3.5	1.484	3.042	7.346	112.95	27.88	1.326
Immersion $S/D = 0.5$.402	.842	1.99	30.60	7.55	.277
Immersion $S/D = 1.0$.256	.523	1.267	19.48	4.81	.282
Immersion $S/D = 2.0$.24	.492	1.188	18.266	4.51	.343

three cylinder symmetrical tripotential first lens and the three aperture einzel final lens operating at the optimum magnification of 0.938. The immersion first lens systems, as was expected due to the large spherical aberrations of the first lens, do not perform well in the 30 kV configuration. The beam current at 800\AA for the best configuration is 3.0×10^{-11} amp which gives a fluence at a 10 megabit writing rate of 3.73×10^{11} ions/cm². A cross-sectional diagram of the 30 kV focusing optics showing pertinent dimensions, voltages, and voltage stresses is given in Figure 99.

ION BEAM DEFLECTION CONSIDERATIONS

In the preceding sections of this report, lens designs for an Xe^+ , 60 kV landing potential optical column, and an Ar^+ , 30 kV landing potential column, were presented. The lens designs represent the first major step in any optical design. It is through the lens designs that it is determined whether the final spot size and beam current requirements can be met. Generally the next question of

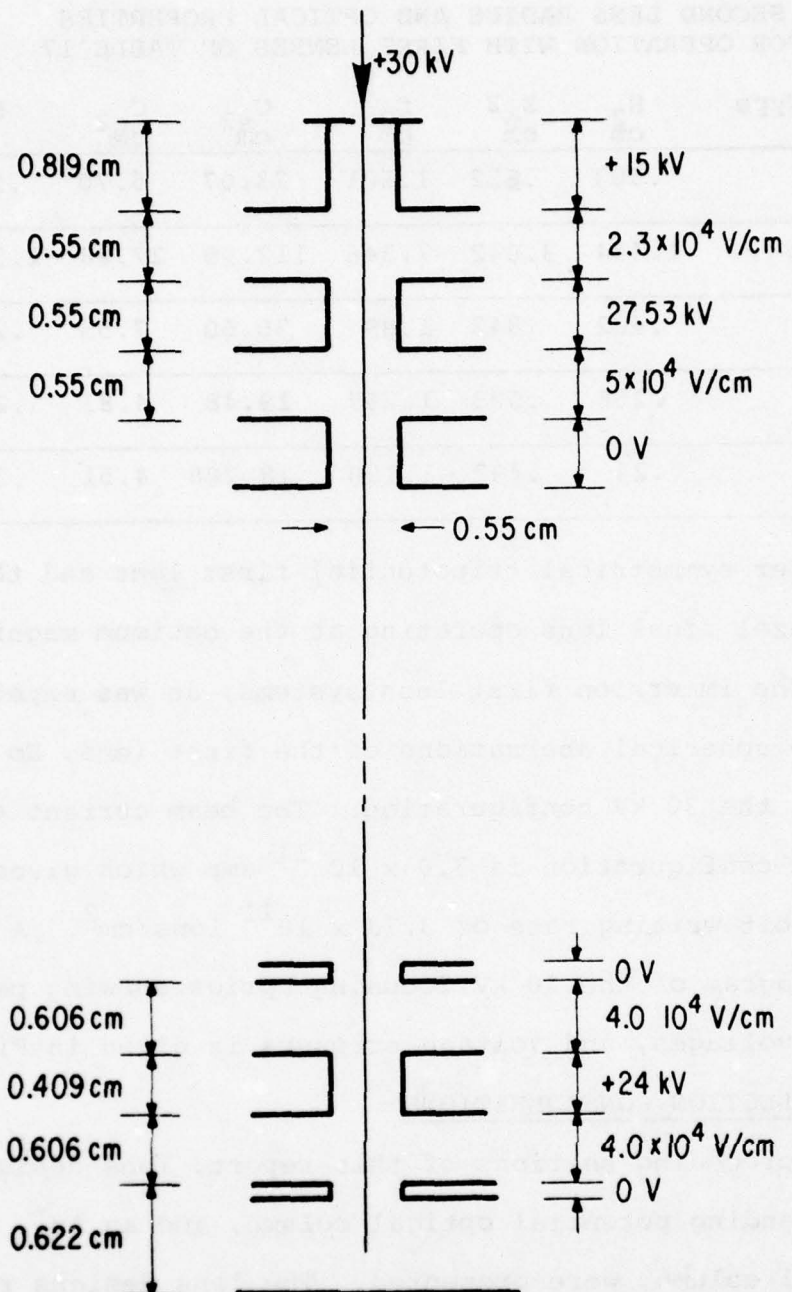


Figure 99. Cross-sectional Diagram of Ar^+ 30 kV Ion Optics Design

importance concerns the deflection system, namely, can certain requirements on overall field size be met. In many cases there is either more compatibility in one area of the design than required, or sufficient freedom to relax the design requirements to implement a suitable deflection system. This allows an interactive trade-off design procedure between the focusing and deflection design. Such is not the case for the present archival memory ion write optics. The focusing system is designed to the limit to meet the beam current requirements for $0.1 \mu\text{m}$ bit size at a 10 mHz writing rate. The primary reason for this is relatively poor angular brightness and large projected energy spread of gas field ionization sources, as compared to electron sources. In view of this, the design procedure adopted for the ion writer is to maximize the current capability for the spot size range of interest with the lens design, and then design the deflection system around this configuration to achieve the largest possible field size. A goal for the deflection system is a $1 \text{ mm} \times 1 \text{ mm}$ field-of-view corresponding to a 10^8 bit total electronically addressable field for a $0.1 \mu\text{m}$ bit spacing. During this first period of Phase II, the major effort in the optics area was spent on optimizing the lens design, for the Xe^+ 60 kV column and the Ar^+ 30 kV column. Preliminary consideration was, however, given to the type of deflection system and the voltage drive requirements.

Characteristic of the lens designs for the ion writer is a very short working distance from the final lens to target. For the Xe^+ 60 kV design, the working distance is .984 cm; and for the Ar^+ 30 kV design, the working distance is .622 cm. These short

working distances, coupled with the desire for a secondary electron detector to aid in the optics alignment, preclude the use of post-final-lens deflection. Therefore a pre-lens deflection assembly similar in concept to a scanning electron microscope deflection system is required. However, as with the ion lenses, the deflector must also be of the electrostatic type, since, then, the deflection properties are independent of the ion mass. Such pre-lens deflectors are considerably more complicated than post-lens deflectors. In general, the pre-lens deflector consists of a two-state unit in contrast to a single stage post lens unit that basically pivots the beam at a given point about the principal optics axis. As a result, the final lens sees an off axis virtual source under deflection conditions, and thereby produces a proportionately off axis image at the target plane. Such a deflection system has larger aberrations than a comparative single stage post lens deflection system. This is not only because of the increased complexity of the deflector, but also because the off axis final lens aberrations contribute to the overall deflection aberrations.

Estimates of the first order deflection properties, voltage drive requirements, and deflector size were made during this contract period. For these purposes a simplified model of the pre-lens deflection system as shown in Figure 100 was assumed. The model consists of two parallel plate deflection structures, separated by a drift space l_d , of length l_1 and l_2 and plate separation s_1 and s_2 respectively. The first set of plates is driven with the differential voltage of $\pm V_d/2$ and the second set of plates by the differential voltage $\pm k V_d/2$. The sign of the voltages is reversed

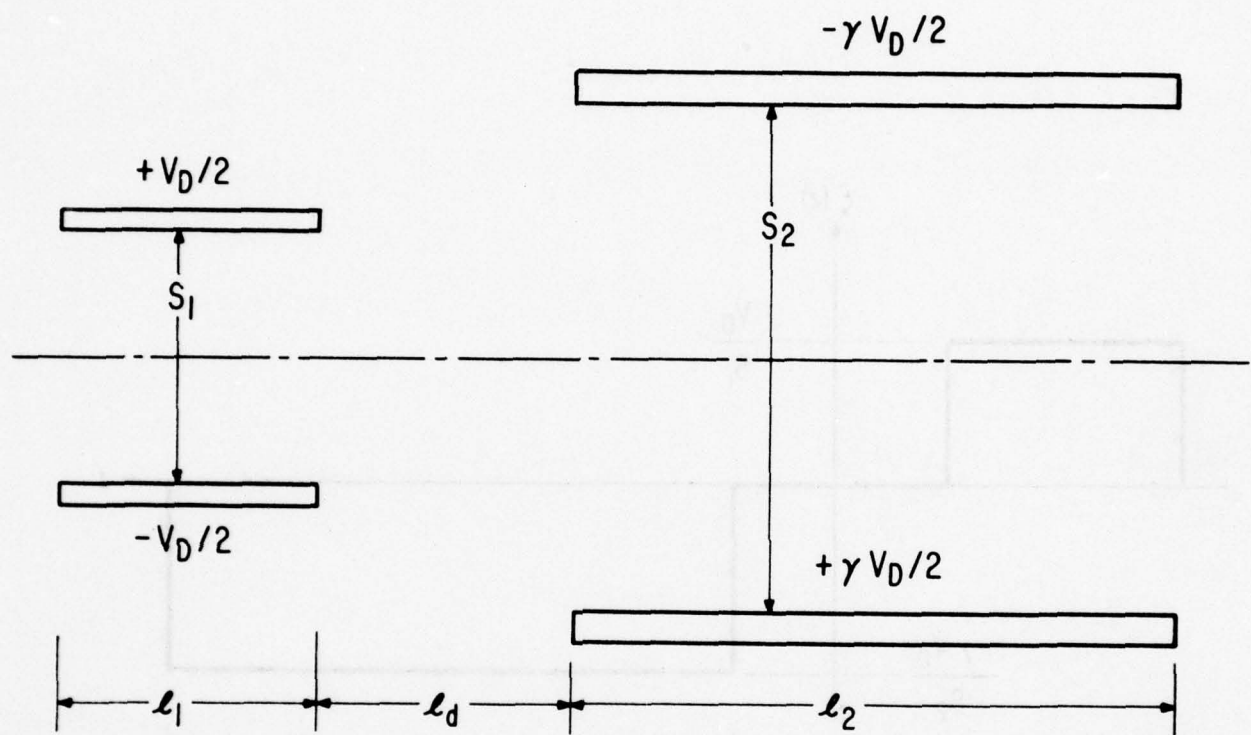


Figure 100. Cross-sectional Diagram of Double Deflector Optics

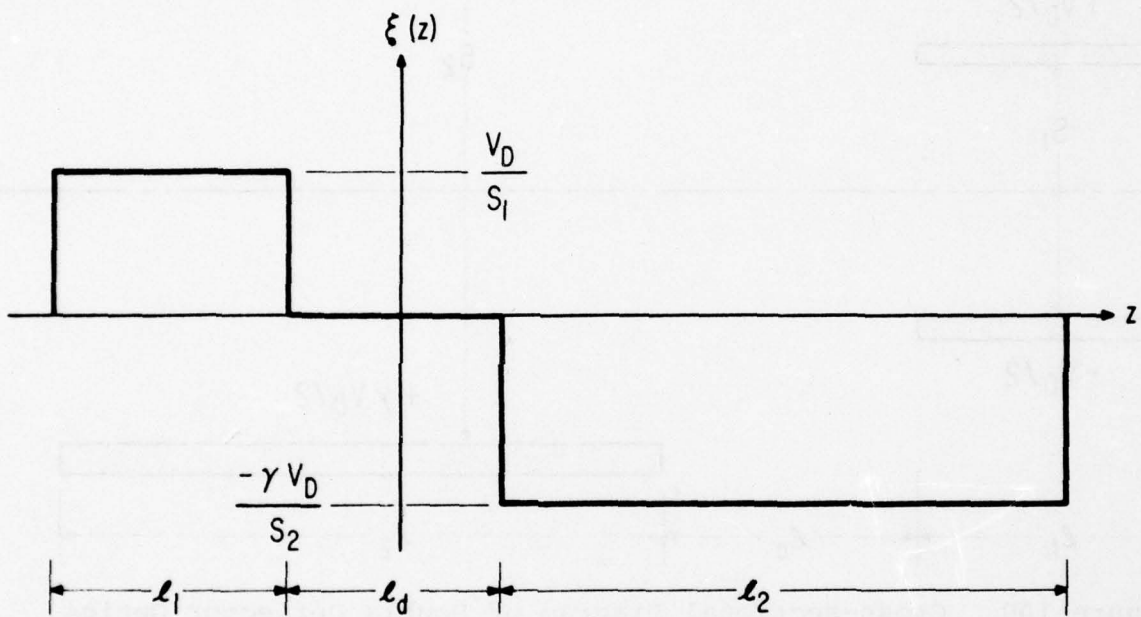


Figure 101. Uniform Field Model for Double Deflector

in the two sections of the deflector so that the first deflector moves the beam off axis and the second deflector bends the beam back toward the axis in such a way that it crosses the axis at a distance L_2 from the second set of plates. For these initial calculations the simple uniform field of Figure 101 was assumed for the deflection system. This type of field (although simplified) does allow complete analytical treatment of the deflector and is known to give pessimistic predictions of the drive requirements since the additional deflection due to fringe fields is neglected. [13]

The first order deflection $y_s(z)$ at a point z for a ray entering a deflector at z_0 orthogonally and on axis is given by: [14]

$$y_s(z) = \int_{z_0}^z d\zeta \int_{z_0}^\zeta \frac{E(u)}{2V_B} du \quad (52)$$

and the slope of the ray $y_s'(z)$ by

$$y_s'(z) = \int_{z_0}^z \frac{E(u)}{2V_B} du \quad (53)$$

where E is the deflection field and V_B is the beam potential.

Taking $z_0 = 0$ at the deflection entrance and assuming the aforementioned deflection model the solutions of (52) and (53) give

$$y_s(L_T) = - \frac{v_d}{2V_B} \left[\frac{l_1}{s_1} \left(L_1 + \frac{l_1}{2} \right) - \frac{k l_2}{s_2} \left(L_2 + \frac{l_2}{2} \right) \right] \quad (54)$$

and

$$y_s'(L_T) = - \frac{v_d}{2V_B} \left[\frac{l_1}{s_1} - \frac{k l_2}{s_2} \right] \quad (55)$$

For the pre-lens double deflection system $y_s(L_T) = 0$ and thus equation (54) gives the condition:

$$\frac{l_1}{s_1} \left[L_1 + \frac{l_1}{2} \right] = \frac{k l_2}{s_2} \left[L_2 + \frac{l_2}{2} \right] \quad (56)$$

Since the beam is collimated in the deflector the beam enters the final lens at an angle $\theta = Y_s'$ as indicated in Figure 102 resulting in a deflection at the target, h , of

$$h = f_o \tan \theta \quad (57)$$

where f_o is the object side focal length of the final lens.

The preceding equations have been extended to aid in the first order design of a pre-lens deflector. The approach is to reformulate these equations so that, given the deflection requirements at the target, various deflection geometries can be developed and compared with a minimum of input information, such as drive voltage and total deflection length. For these purposes the deflector geometry (refer to Figure 100) was cast in the form

$$\begin{array}{lll} l_1 = l & s_1 = S & k = 1.0 \\ l_2 = nl & s_2 = mS & l_d = 0 \end{array} \quad (58)$$

Substituting the parameters of (58) into the Eq. (56) and solving for L_2 gives

$$L_2 = \frac{nm + m/2 - n^2}{n - m} l \quad (59)$$

Substituting the parameters of (58) into Eq. (55) and solving for l gives

$$l = v \frac{mS}{n-m} \quad (60)$$

where

$$v = \frac{2Y_s' V_B}{V_d} \quad (61)$$

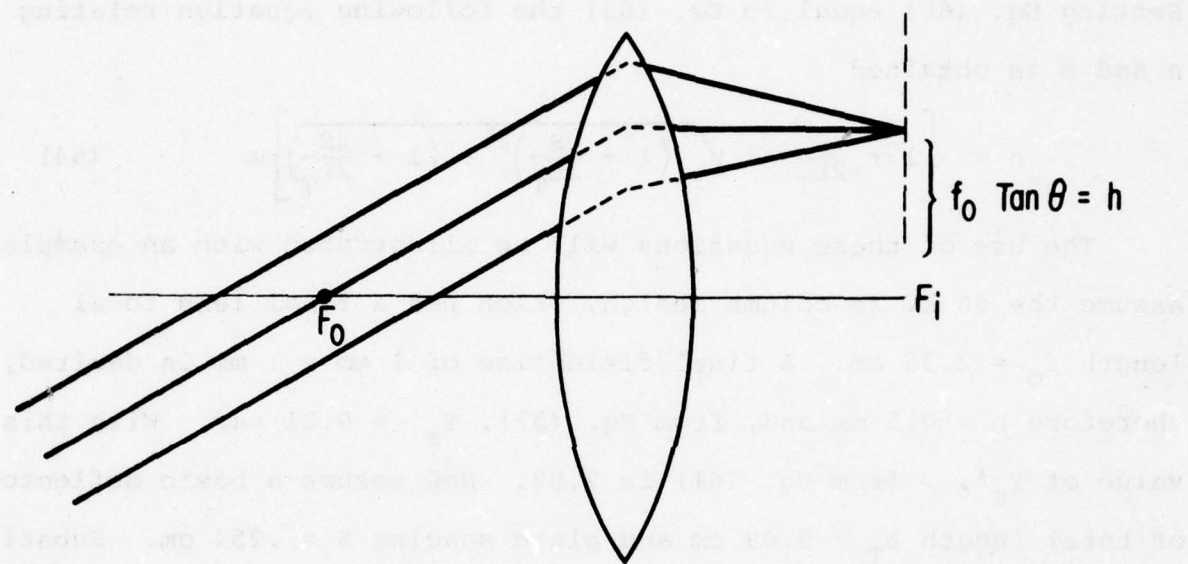


Figure 102. Pre-lens Deflection of a Collimated Beam

Inherent in these equations is the condition $n > m$ since l cannot be negative. The total deflector length L_T for the parameters of (58) is

$$L_T = l + nl + L_2 \quad (62)$$

Using L_2 from Eq. (59) in Eq. (62) and again solving for l gives

$$l = \left[\frac{n-m}{n-m/2} \right] L_T \quad (63)$$

Setting Eq. (60) equal to Eq. (63) the following equation relating n and m is obtained

$$n = \left[1 + \frac{vS}{2L_T} \pm \sqrt{\left(1 + \frac{vS}{2L_T} \right)^2 - \left(1 + \frac{vS}{2L_T} \right)} \right] m \quad (64)$$

The use of these equations will be illustrated with an example. Assume the 60 kV Xe column design, which has a final lens focal length $f_o = 2.38$ cm. A final field size of 1 mm x 1 mm is desired, therefore $h = 0.5$ mm and, from Eq. (57), $Y_s' = 0.21$ rad. With this value of Y_s' , v from Eq. (61) is 2.52. Now assume a basic deflector of total length $L_T = 5.08$ cm and plate spacing $S = .254$ cm. Substituting these values in Eq. (64) gives

$$\text{and } n = 1.3218 \text{ m} \quad (65)$$

$$n = 0.8042 \text{ m} \quad (66)$$

As mentioned previously $n > m$ since l cannot be negative, and therefore substituting (65) into (63) gives

$$l = 1.989 \text{ cm.}$$

Thus the deflector length l is set and assuming various values for m , n can be evaluated from (65), L_2 from (59), and the rest of the deflector geometry from the parameters of (58). For example with $n = 0.5$

$$l_1 = l = 1.989$$

$$l_2 = nl = 1.316$$

$$L_2 = 1.776$$

$$s_1 = 0.25$$

$$s_2 = 0.127$$

A useful estimate of how close the beam comes to the deflection bars is

$$\Delta s = s_2/2 - y_s' \left[\frac{l_2}{2} + L_2 \right] \quad (67)$$

which gives 0.127 mm for this example.

Despite the approximations made in this model, it does provide equations that yield a deflector design in a straightforward manner that can easily be evaluated and compared with other designs. For example, the deflector resulting in the above illustration might be rejected in favor of another design with wider plate spacing so that the beam misses the deflection bar by a larger amount. Therefore these techniques can be used to rapidly evaluate various deflector configurations so that a promising configuration can be found. This configuration can then be further investigated for its deflection and aberration properties with more accurate and extensive calculations. A more refined method of evaluating the deflection system will be pursued in the next period of this contract.

SECTION VII

SYSTEM APPLICATIONS STUDY

A series of design models was used to compare the expected prices and performance features of two different systems based on the GE Advanced Archival Memory technology with a system based on magnetic tape cartridge media, and with a system based on optical disk media, as they might appear in 1985.

Three kinds of application demands were imposed on each system, over a wide range of total storage requirements and a wide range of input/output demand rates.

Advanced Archival Memory (AAM) systems using the "small" (7×10^{10} -bit) media plates showed better price/performance features than tape-cartridge systems, and price/performance features comparable to those of optical disk systems for file sizes above about 10^{13} bits in all cases.

Systems using the "large" (1.5×10^{12} -bit) media plates showed better price/performance features than all other systems for all applications; at file sizes above 10^{13} bits.

A. FILE SYSTEM STRUCTURES CONSIDERED

Figure 103 is a schematic diagram of the file systems modeled for all of the technologies examined.

The user systems and the possible high-level file system controllers at the top of the figure were not included in the model. It was assumed that high-level file system functions such as the computation of physical addresses, data-base management, and management of file space would be performed either by the high-level

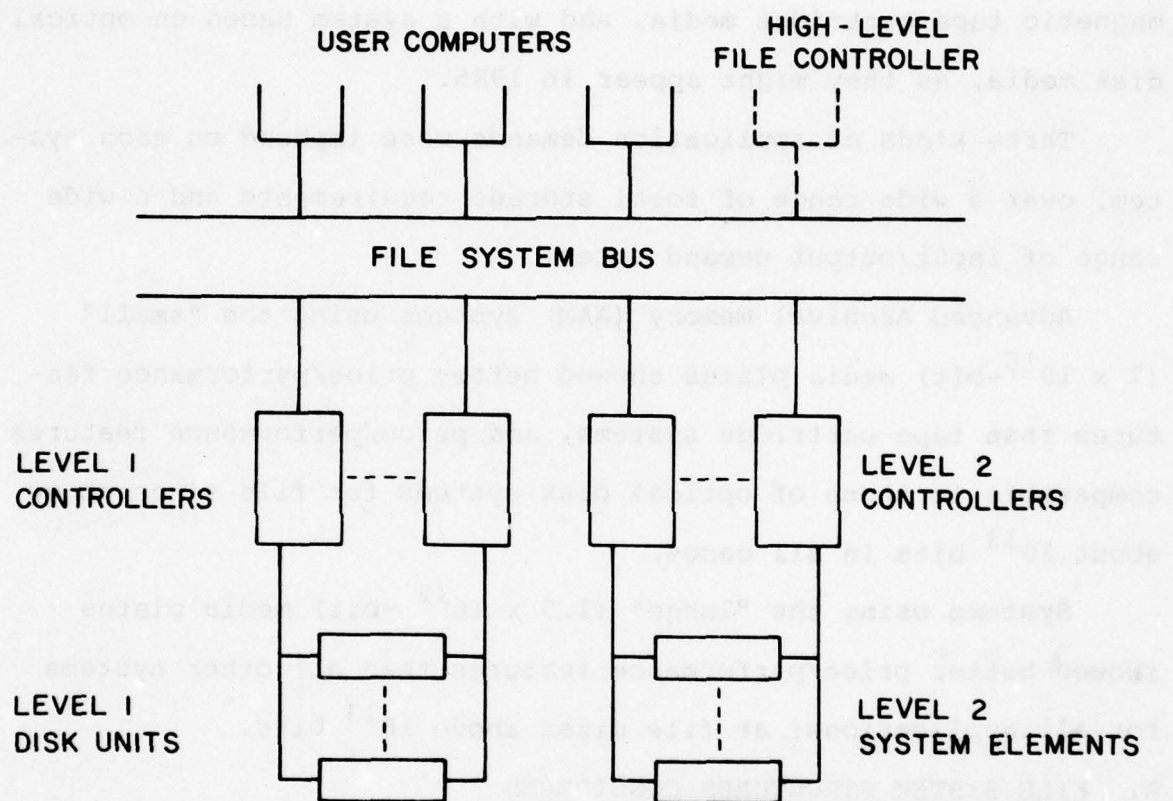


Figure 103. Two-level File System

controller, or by software executed in the user computers. Some of the high-level addressing functions would result in accesses to the catalogs maintained in the modeled system.

All transfers of commands and data between user computers and high-level controllers, if any, and the file system controllers are passed via a bus with ports for all of the directly-attached elements.

A first level in each of the system was assumed to be assembled from 1985 moving-head disk machinery. This level is required in the small-plate AAM systems to store some amount of recently-written data to which immediate access is needed, because of the relatively long delay in moving the small AAM plates from writing stations to reading stations. It is available in all of the systems to store selected fractions of the data and the catalog information, so that overall system prices can be minimized by trading off disk space for additional access rates to the larger media elements.

In all of the cases run with the design models, a minimum of two disk controllers, and a minimum of two disks was assumed to provide redundancy assurance against system failures.

A minimum of two controllers was assumed in all systems at this level. Each controller was assumed to be able to control a reasonably large number of the units appropriate to the technology of the media under consideration, as outlined below for each case.

Small-Plate AAM Systems

Figure 104 shows a small AAM plate. It is about 4 cm. square. The diode surface is not structured, except that it may be made

4 cm. 0.2 cm.

NOTCHES FOR MECHANICAL IDENTIFICATION

WRITE - PROTECT PIN

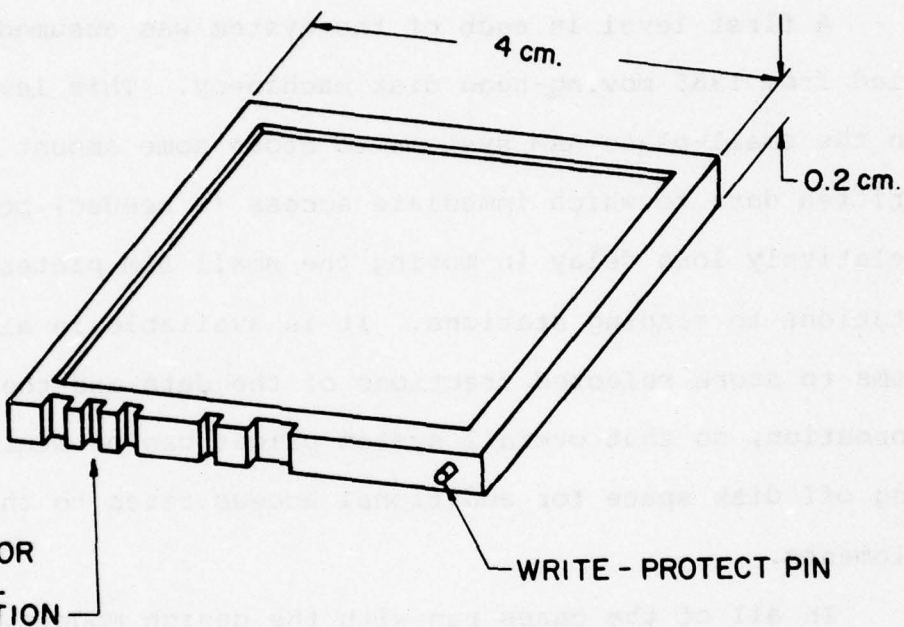


Figure 104. Small Plate AAM Plate

of mosaic of smaller chips. The surface is divided under software control into about 10,000 data blocks, each holding about 3,000 by 3,000 bit-sites, surrounded by a guard-band of empty bit-sites, as shown in Figure 105. Each block is pre-formatted under software control, either in the factory, or in a customer's system. The physical address (plate number/block number), together with alignment information is written into each block.

Figure 106 shows the layout of data fields within a block. Each field is preceded by an alignment line. It was assumed that 100 lines of data could be written in close-packed format after each alignment line.

Figure 107 shows the line formats assumed. The alignment line is mainly composed of alternate "zero" (unrecorded) and "one" (recorded) bit-sites. This sequence is interrupted at intervals to inscribe a numeric value of the number of bit-sites from the beginning of the number back to the beginning of the line.

Each data line on the plate is preceded by a preamble of 64 bits for synchronization purposes. This preamble is followed by a mixture of data bits and Error-Detecting-And-Correcting (EDAC) code, so that about 2,500 "useful" data bits are written on each line. If data cannot be verified during the writing of a field, the write mechanism comes back and fills in certain bit-sites in the preamble so that the reading process will know that the line is to be ignored.

For some of the reasoning behind this media format, see Section G.

Figure 108 is a schematic diagram of the small-plate ADAR organization at level 2 in the file system.

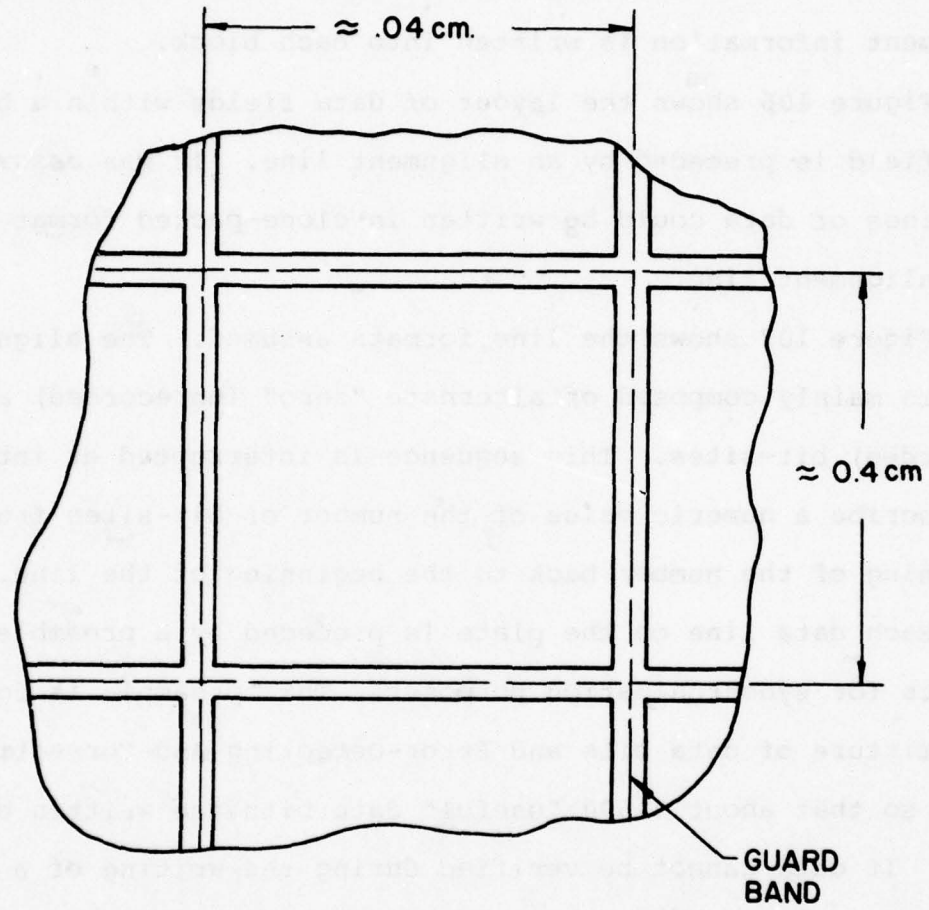


Figure 105. One Small-plate AAM Data Block

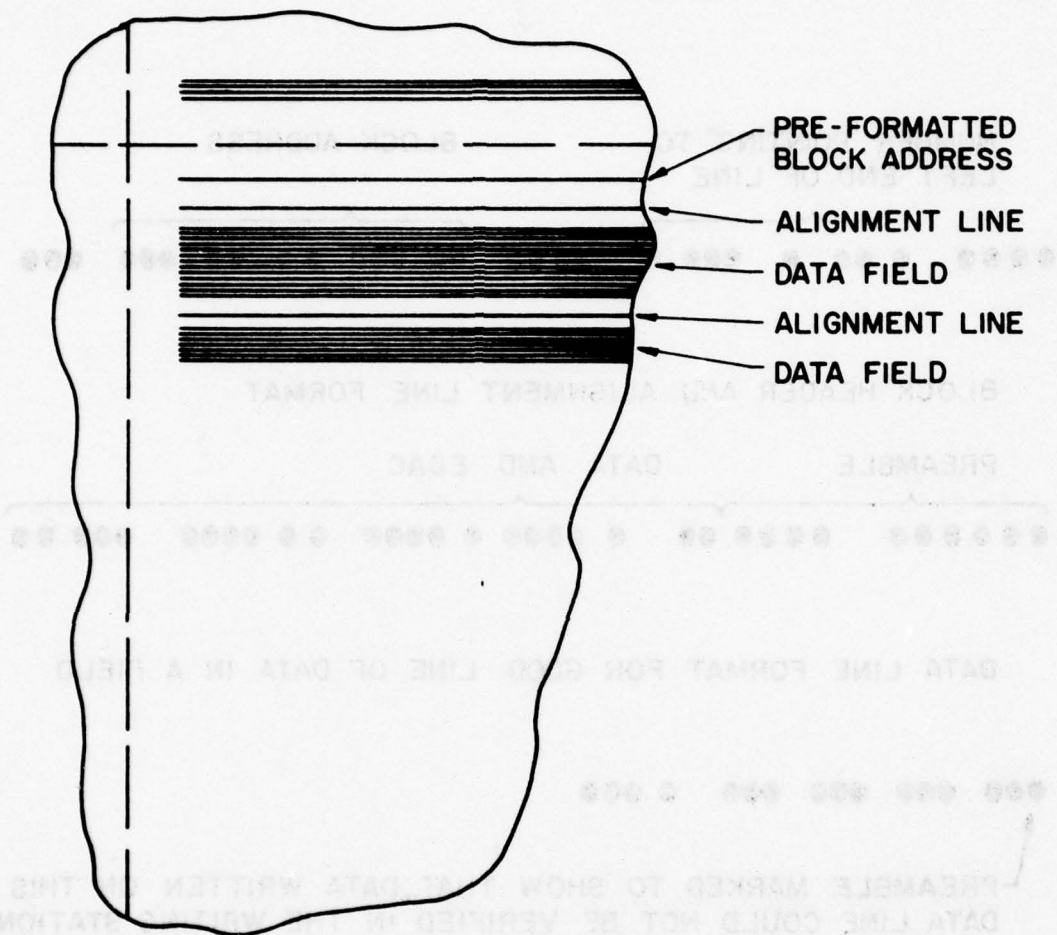


Figure 106. Layout of Data Fields Within Small Plate AAM Block

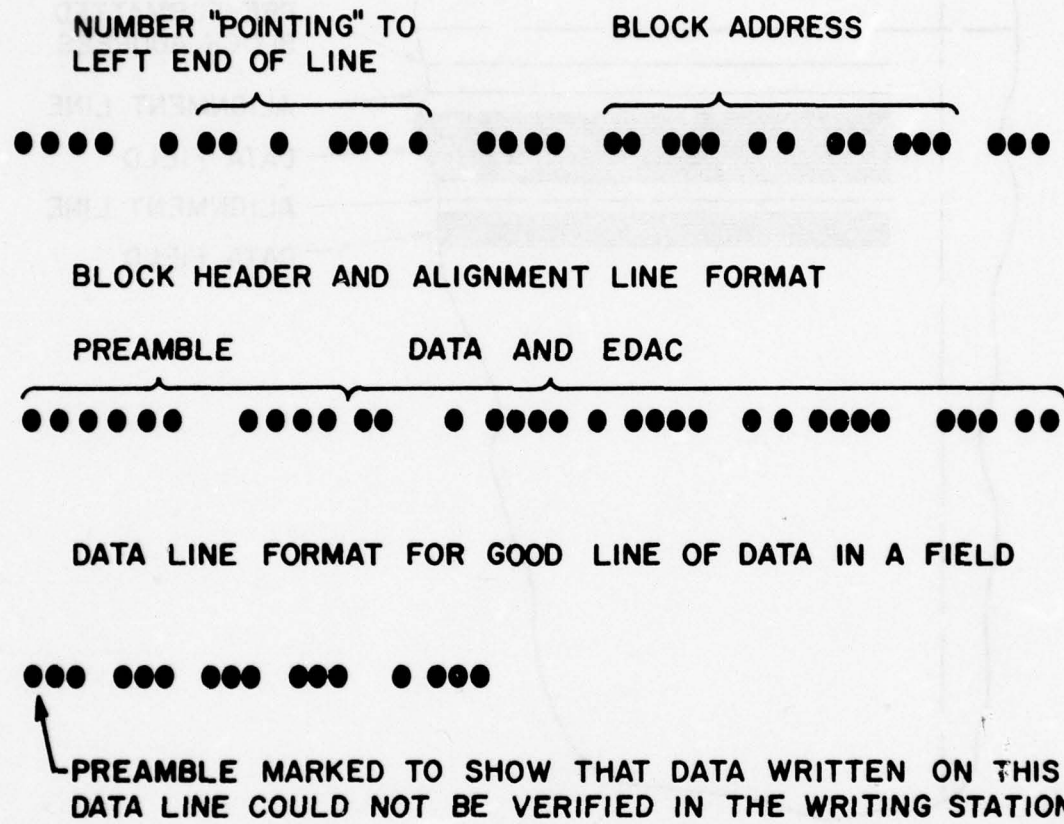


Figure 107. Line Format for Small-plate AAM

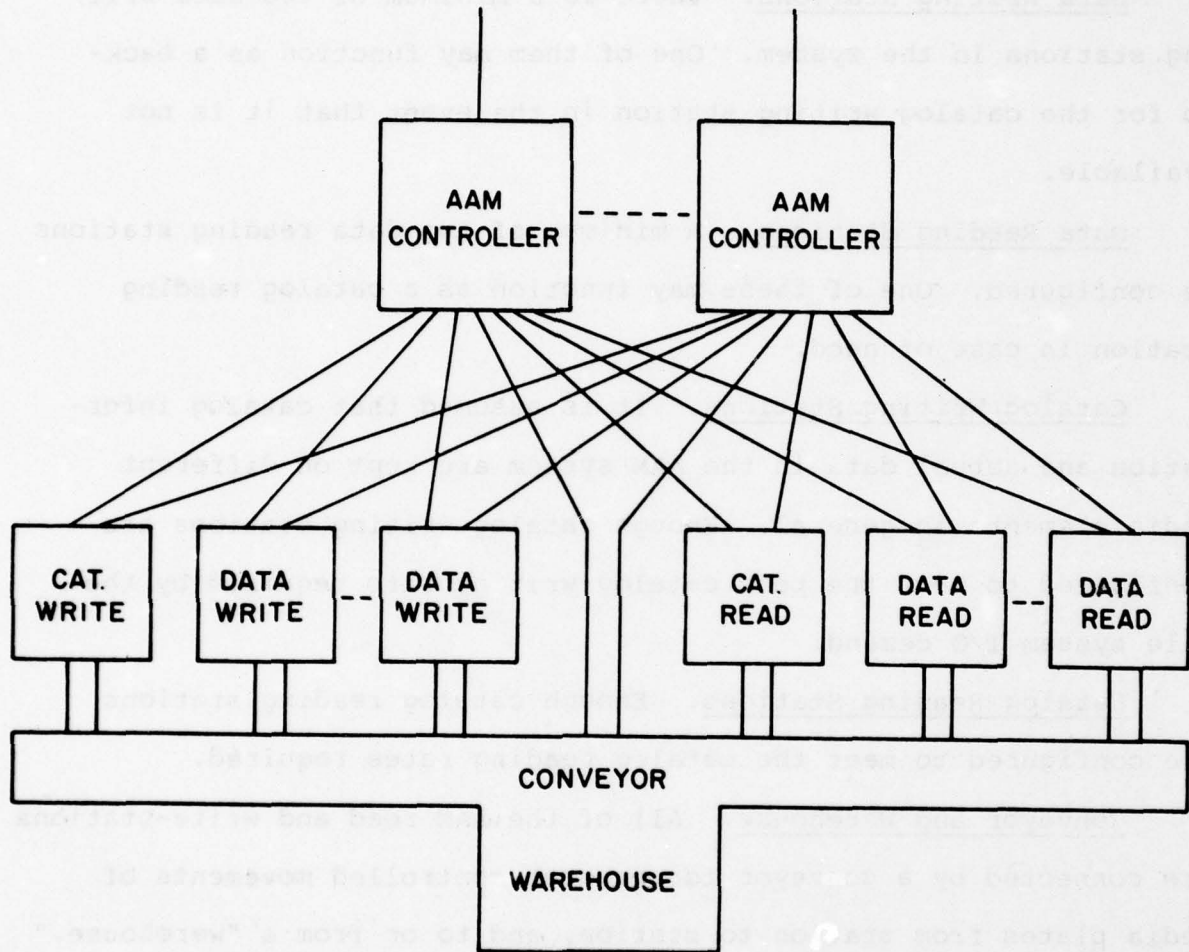


Figure 108. Small Plate AAM System Schematic

Controllers. There is a minimum of two AAM controllers, arranged for redundant connections between the file system bus and the ADAR units. These machines direct the operations of all of the units.

Data Writing Stations. There is a minimum of two data writing stations in the system. One of them may function as a back-up for the catalog writing station in the event that it is not available.

Data Reading Stations. A minimum of two data reading stations is configured. One of these may function as a catalog reading station in case of need.

Catalog Writing Stations. It is assumed that catalog information and actual data in the AAM system are kept on different media elements in general. Enough catalog writing stations are configured to meet the peak catalog writing rate required by the file system I/O demand.

Catalog Reading Stations. Enough catalog reading stations are configured to meet the catalog reading rates required.

Conveyor and Warehouse. All of the AAM read and write-stations are connected by a conveyor for program-controlled movements of media plates from station to station, and to or from a "warehouse." In many systems, the warehouse is not required, because there is adequate storage within the stations for the plates.

In the small-plate AAM writing station, writing is accomplished with a focused beam of ions, impinging at fairly high voltage at

precise locations on the medium surface. A limited reading capability within the write-station is implemented by switching an electron beam to project through the writing lenses onto the same locations as the writing beam. The write optics can move the writing beam so as to cover a single block of the plate surface by electronic deflections. A mechanical "stage" is required to move the plate from block to block. In addition to the medium plate, which is in the read-write position in the station, there is a "stack" of plates stored within the station vacuum chamber. A "changer" mechanism exchanges the plate on the "stage" for a plate in the stack, and also moves plates in and out of the station via a vacuum lock.

Plates which are on the conveyor or in the warehouse are kept in small, individual containers to protect them from dust. The changer mechanism removes a plate from its container as it enters the vacuum port, and re-inserts it in the container as it leaves the vacuum port to be moved somewhere by the conveyor.

The small-plate AAM reading station uses a matrix lens in the electron column to select the data block on the medium plate from which data are to be read, so that the "stage" on which the plate is held has no need for mechanical motion. It has a "stack" of plates within the station vacuum chamber, a changer mechanism and a vacuum port similar to those of the writing station.

Figure 109 shows the large AAM plate. It is about 15 cm. square, or about fourteen times the surface area of the smaller plate. Here also, the surface of the diode is not structured, except that it may be a matrix of individual chips, with individual electrical connections so as to improve the frequency response

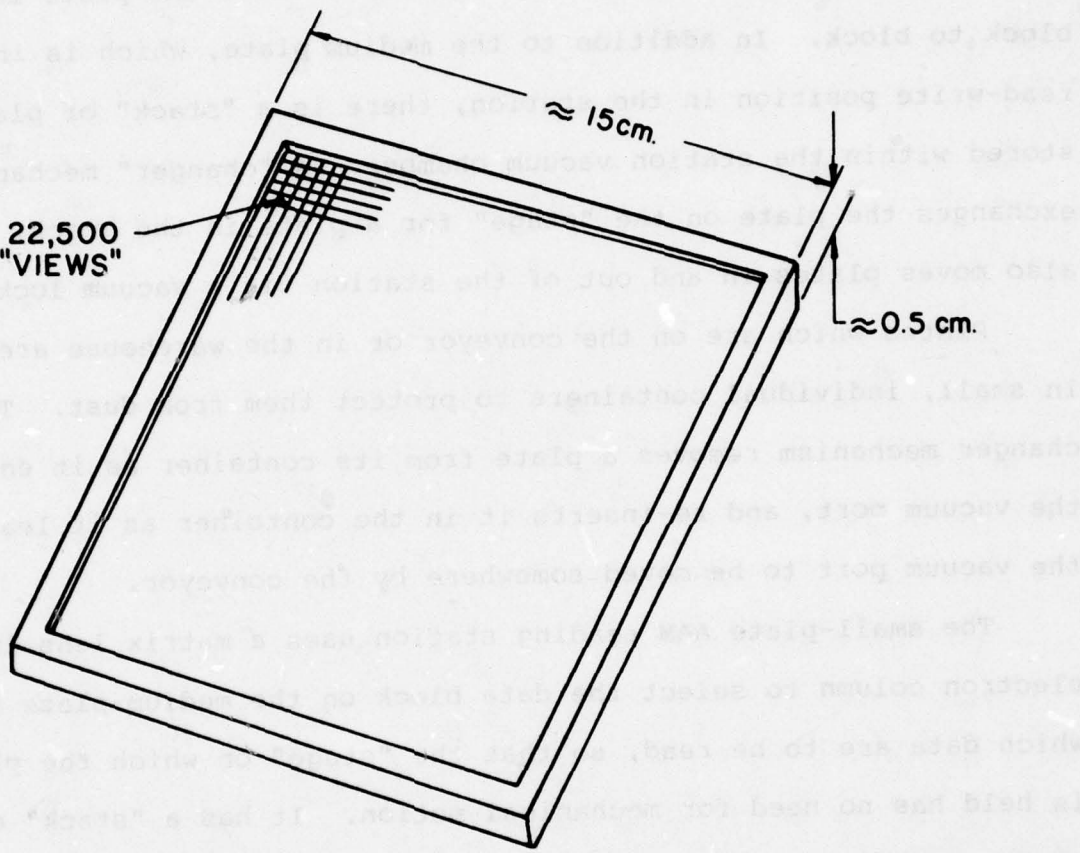


Figure 109. Large-plate AAM Plate

of the diodes in the read-out process. The surface is divided into "views," which are about 1 mm square, corresponding to the largest area which can be addressed at high resolution by the writing and reading beams.

As shown in Figure 110, each "view" on the plate is surrounded by a guard-band of nonrecorded bit-sites, and it is further subdivided into "blocks" which are about 500 bit-sites square. These correspond to the largest number of bit-sites which can be scanned dynamically at high accuracy with easily realizable control electronics.

As shown in Figure 111, each "block" of data starts with an alignment/block address line, which may be prerecorded during plate manufacture, or when the plate is first put into use in the user facilities. The "block" is broken up into a number of "fields," each of which is preceded by its own alignment line. Within each field, data lines are close-packed. The line formats are shown in Figure 112. The alignment line is partially alternating zero and one, but it also contains numbers which "point" to the left end of the line, and one or more copies of the block address. Each data line begins with a 32-bit preamble, followed by a mixture of data and EDAC code. With formatting, guard-band, EDAC losses, and with some allowance for "bad" blocks, the plate holds more than 10^{12} "useful" data bits.

Figure 113 is a schematic diagram of the large-plate AAM system. Assumptions concerning the design of the equipment and the operating rules of the system make it somewhat different from the small-plate system.

belebte ergebnisse mit verschiedenem Aussehen und so
und mit unterschiedlichen Ergebnissen im Laufe des Körpers "weil" nicht
wirkt und verschiedene Arten von Reaktionen auf den Körper auslösen kann

beschreibt die Ergebnisse der Untersuchungen in der Literatur.

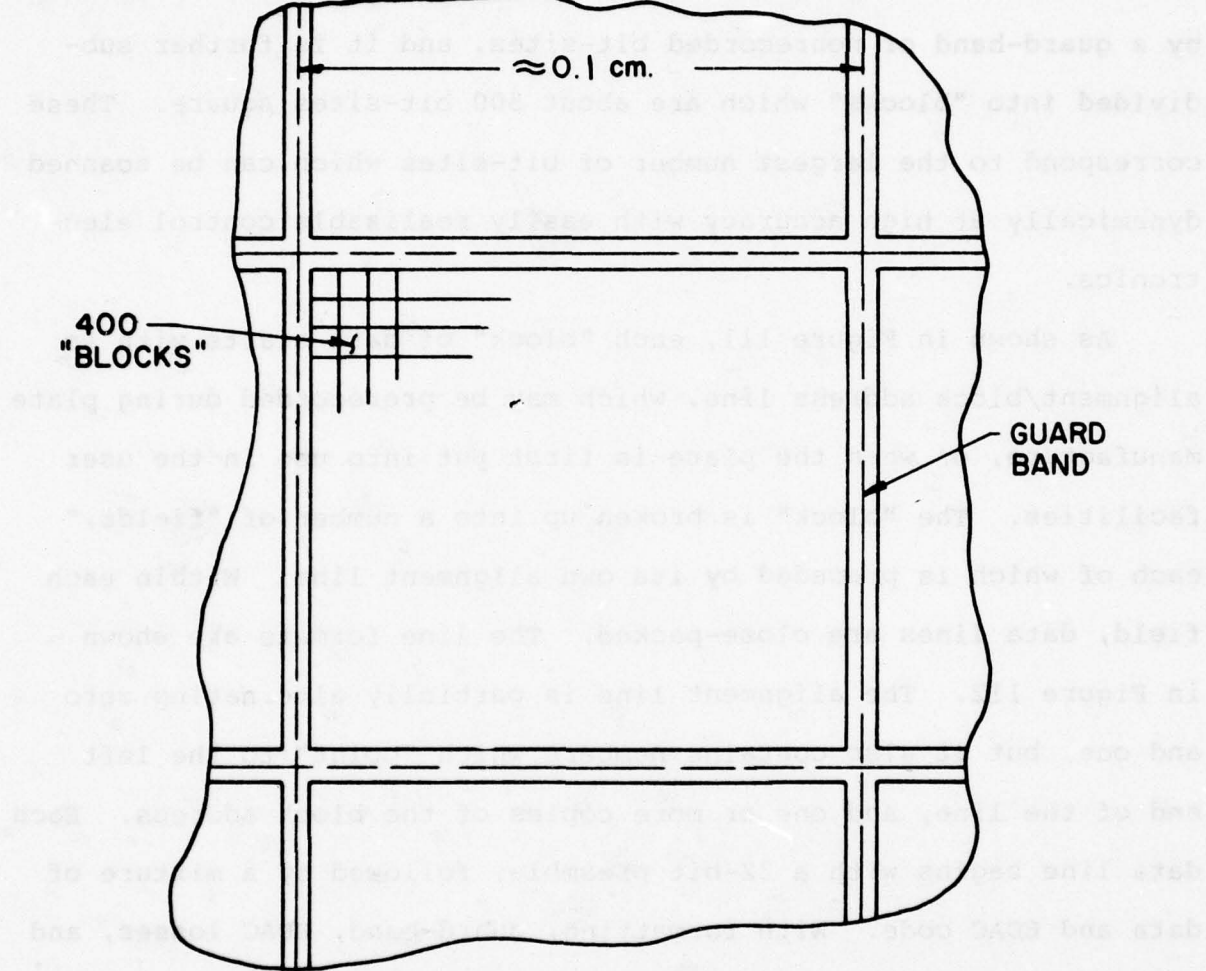


Figure 110. One View on Large AAM Plate

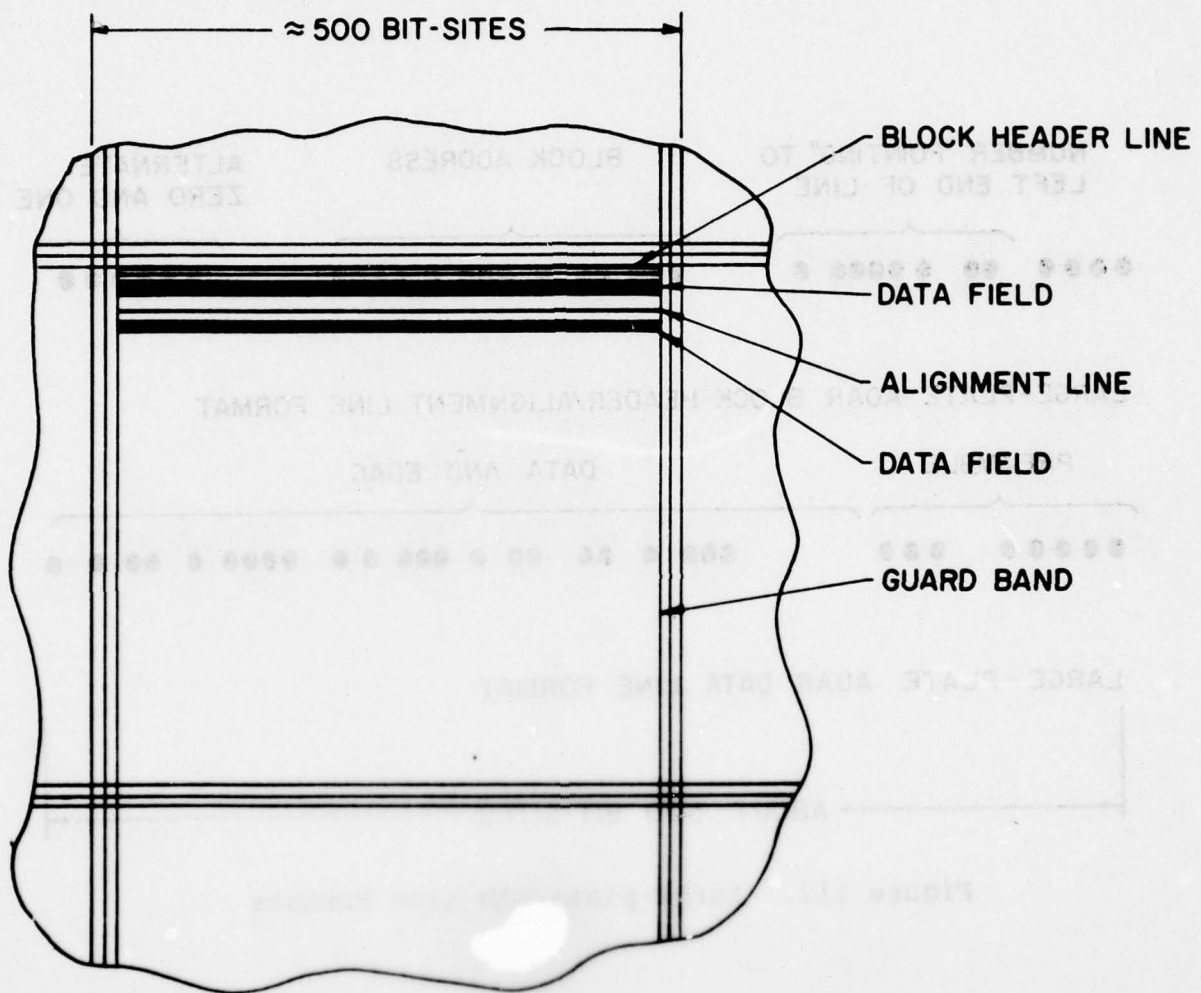


Figure 111. Large-plate AAM Block Format

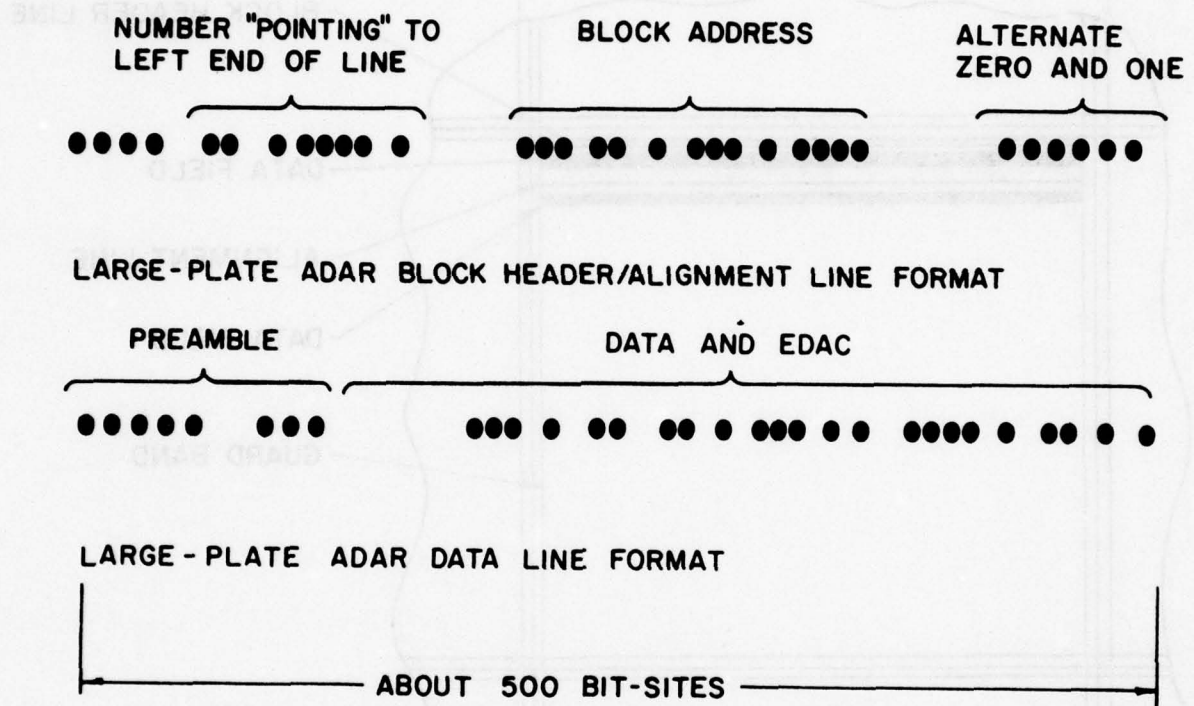


Figure 112. Large-plate AAM Line Formats

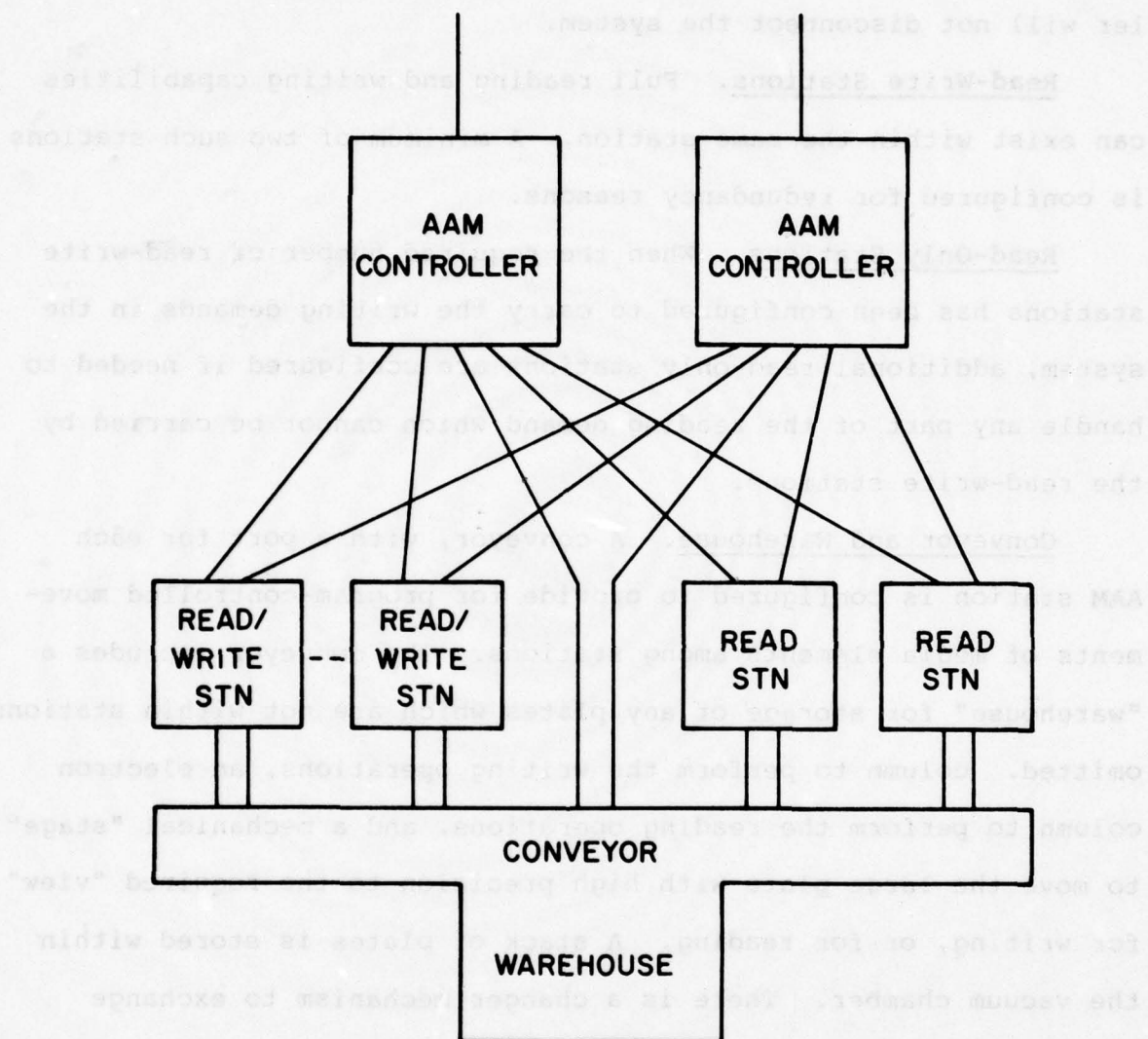


Figure 113. Large-plate AAM System Schematic

Controllers. A minimum of two level 2 controllers is configured to direct the operations of all of the level 2 elements. Redundant paths are provided, so that failure of a single controller will not disconnect the system.

Read-Write Stations. Full reading and writing capabilities can exist within the same station. A minimum of two such stations is configured for redundancy reasons.

Read-Only Stations. When the required number of read-write stations has been configured to carry the writing demands in the system, additional read-only stations are configured if needed to handle any part of the reading demand which cannot be carried by the read-write stations.

Conveyor and Warehouse. A conveyor, with a port for each AAM station is configured to provide for program-controlled movements of media elements among stations. The conveyor includes a "warehouse" for storage of any plates which are not within stations. omitted. column to perform the writing operations, an electron column to perform the reading operations, and a mechanical "stage" to move the large plate with high precision to the required "view" for writing, or for reading. A stack of plates is stored within the vacuum chamber. There is a changer mechanism to exchange plates between the stage and the stack and to move plates in and out of the station via the vacuum port. When a plate is on the conveyor or in the warehouse, it is enclosed in its own dust-proof container. The read-only station for the large-plate AAM system is identical with the read-write station, except that the write column and other features associated with the writing operation are omitted.

Tape-Cartridge System

The storage medium of this system is a cartridge containing a spool of magnetic tape, similar to that now in use in the IBM 3850 mass storage system. It was assumed that by 1985 this cartridge would hold 100 million characters in place of today's 50 million.

Figure 114 is a schematic diagram of the elements which are configured at level 2 in the tape-cartridge system to provide for data storage, and for the I/O rates demanded.

Controllers. A minimum of two controllers is configured to direct the operations of all of the other equipment, and to provide redundant paths in case of controller failure.

Read-Write Stations. Each read-write station can accept a cartridge, remove the spool from the cover, thread the tape to the take-up spool, move the tape at high speed to a given physical address, and transfer data. It can also rewind the tape onto the cartridge spool, put the spool back in the cover, and deliver the cartridge to an output location. A number of read-write stations can be stacked vertically, so that all of them can be served by a single, vertically-moving "gofer."

Gofers. A gofer can exchange tape cartridges with each of the read-write stations which it serves. It also has "pockets" in which it can retain some number of frequently-used cartridges so as to reduce the access time for a cartridge not currently mounted in a read-write station. Some number of gofers can be grouped around a set of carrousels. The gofer moves vertically to reach a selected carrousel wheel, while the wheel turns to put

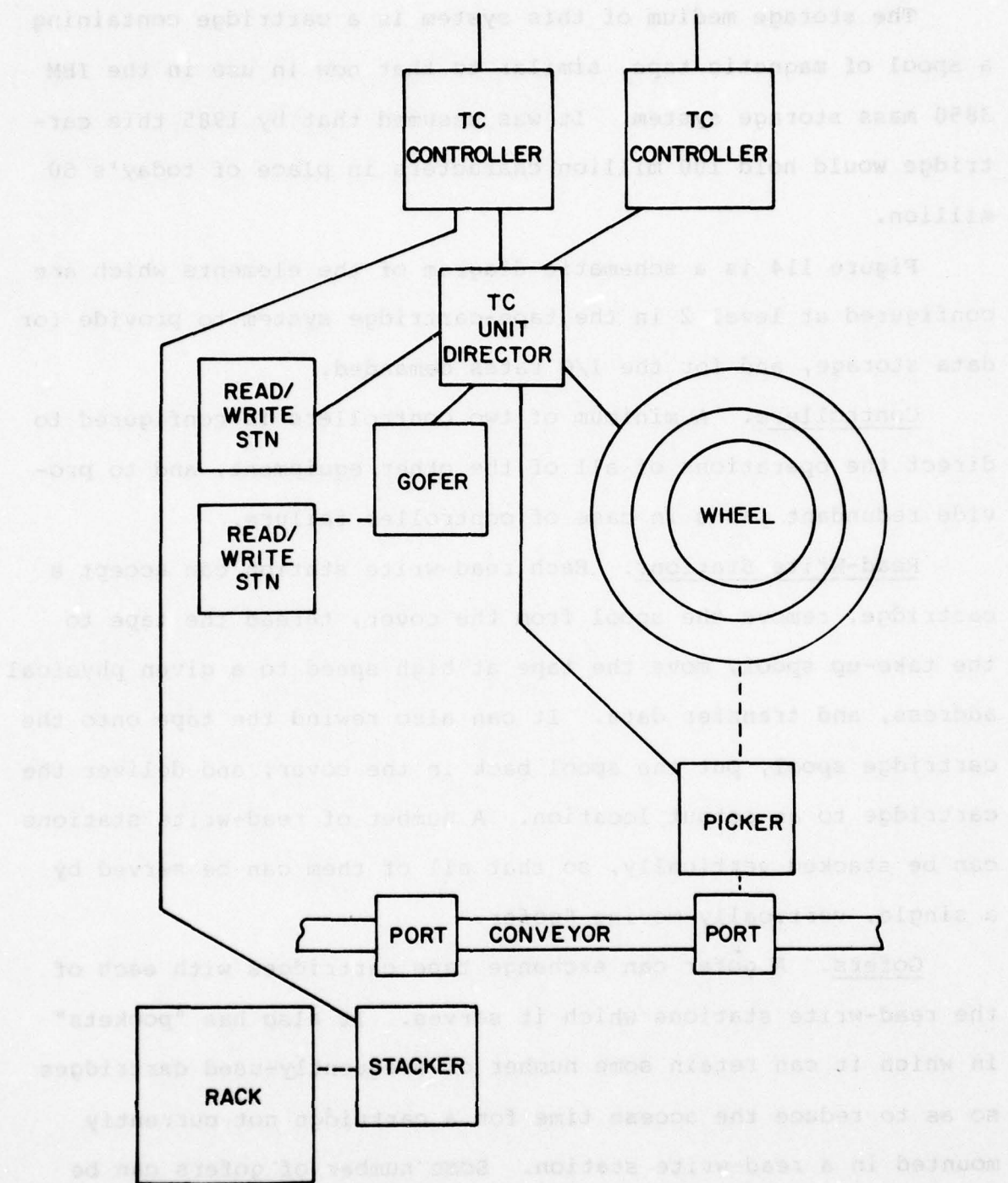


Figure 114. Elements of the Tape-cartridge System

a selected cell in front of the gofer, so that the gofer can exchange a cartridge it is carrying for a cartridge from the wheel.

Carrousel. The "heart" of each unit is a stack of some number of carrousel wheels. Each wheel holds a number of cartridges in cells along the outer edge. The gofer can exchange cartridges with a selected cell of a selected wheel.

Picker. Some number of pickers can be positioned around each carrousel. The pickers move vertically, and exchange cartridges brought from the conveyor for cartridges in specified cells on specific wheels. At one end of its travel, each picker can exchange cartridges with a conveyor port. Pickers are not used if the carrousels have enough spaces for all of the media elements required.

Conveyor. The conveyor moves cartridges among ports which serve the pickers on each unit and ports which serve the stackers. The conveyor is omitted from the system if there is no need for it.

Stackers. Each stacker moves in two dimensions so as to transfer cartridges between its conveyor port and a large storage rack. Stackers and racks are omitted if all of the cartridges can be stored in the carrousels.

Racks. If needed, static storage racks are configured to hold cartridges for which there is no room in the carrousels.

Optical Disk Systems

Figure 115 is a partial radial section of the optical disk medium element. It is a sandwich formed by joining two outer plastic disks with ring spacers. The inner surface of each disk is initially coated with a thin layer of some volatile metal, such as tellurium.

the disk surface and can be used to detect the presence of
readily available materials such as paper or plastic.
The thickness of the medium which leaves room for recording
is reported separately from the rest of the disk area.
The thickness of the medium is 15 cm. The thickness of the
disk is indicated by the dimension line.

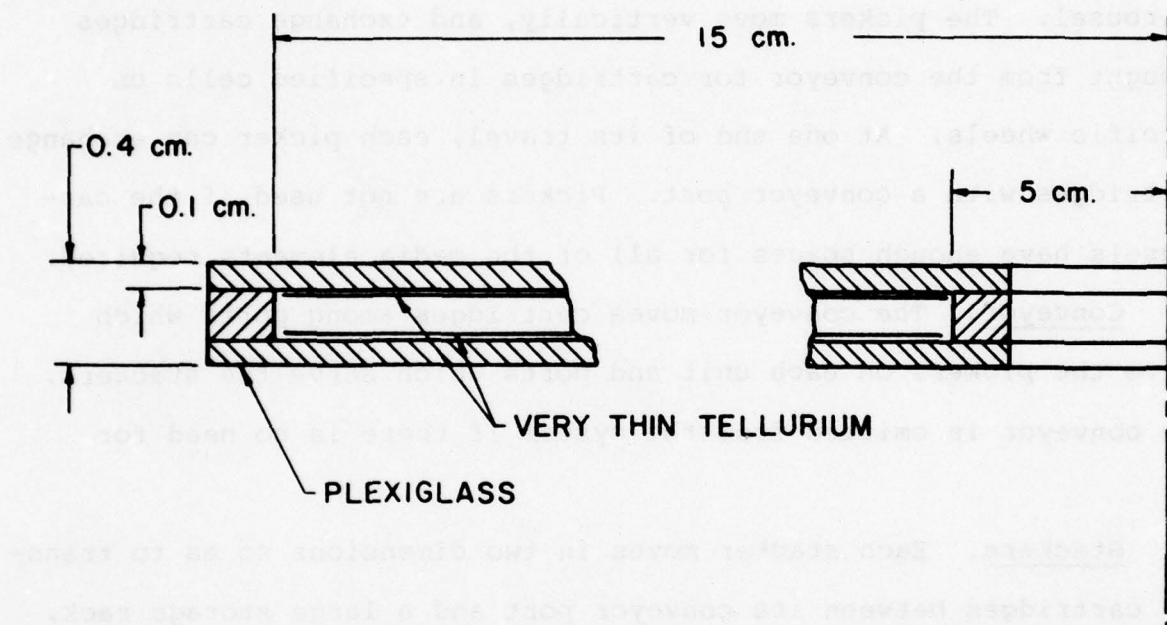


Figure 115. Partial Radial Section of Optical Disk Medium

Where this coating is undisturbed, it has quite high, mirror reflectivity. Figure 116 shows schematically the method of writing and reading. A laser is pulsed at relatively high power in the writing process, so as to blast small "pits" in the metal surface. Operated at relatively low power, the laser is used to project a very small spot on the metal layer. Where no pit has been blasted, the signal in the reading photocell is quite large. The signal is much reduced in the pit area, because the mirror reflectivity of the surface is greatly reduced. The high signal-to-noise ratio available in this system allows the recording of multiple bits per pit through variation of the recording pulse length. With three bits per bit-site, and asynchronous operation, the disk can hold more than 10^{11} bits on each side.

Figure 117 shows the elements of the level 2 organization assumed. It is very similar to the level 2 organization for the tape-cartridge system described above.

Controllers. A minimum of two controllers is configured per system in order to provide a redundant path. These controllers direct the operations of all of the level 2 elements in writing, reading, and moving the media.

Read-Write Stations. A minimum of two read-write stations is configured in the system. More are added as necessary to meet the peak I/O demands. A number of read-write stations may be "stacked" vertically to be served by a single gofer.

Gofers. A gofer moves vertically to reach a selected read-write station, or a selected carrousel wheel. It is required to invert the disk on a read-write station for access to the other side, or for exchange of a disk with the read-write station.

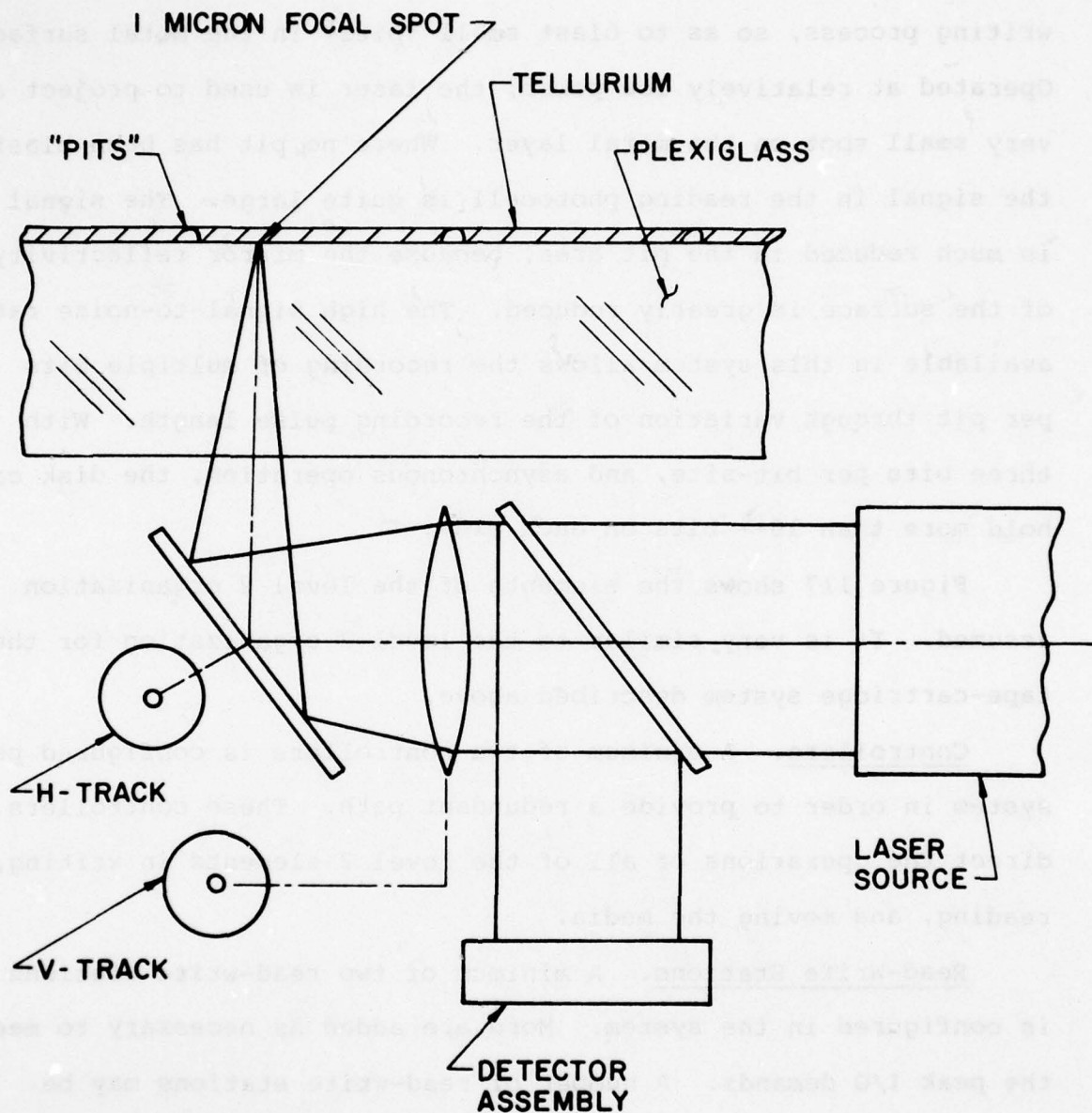


Figure 116. Schematic Diagram of Optical Disk

Read/Write Assembly

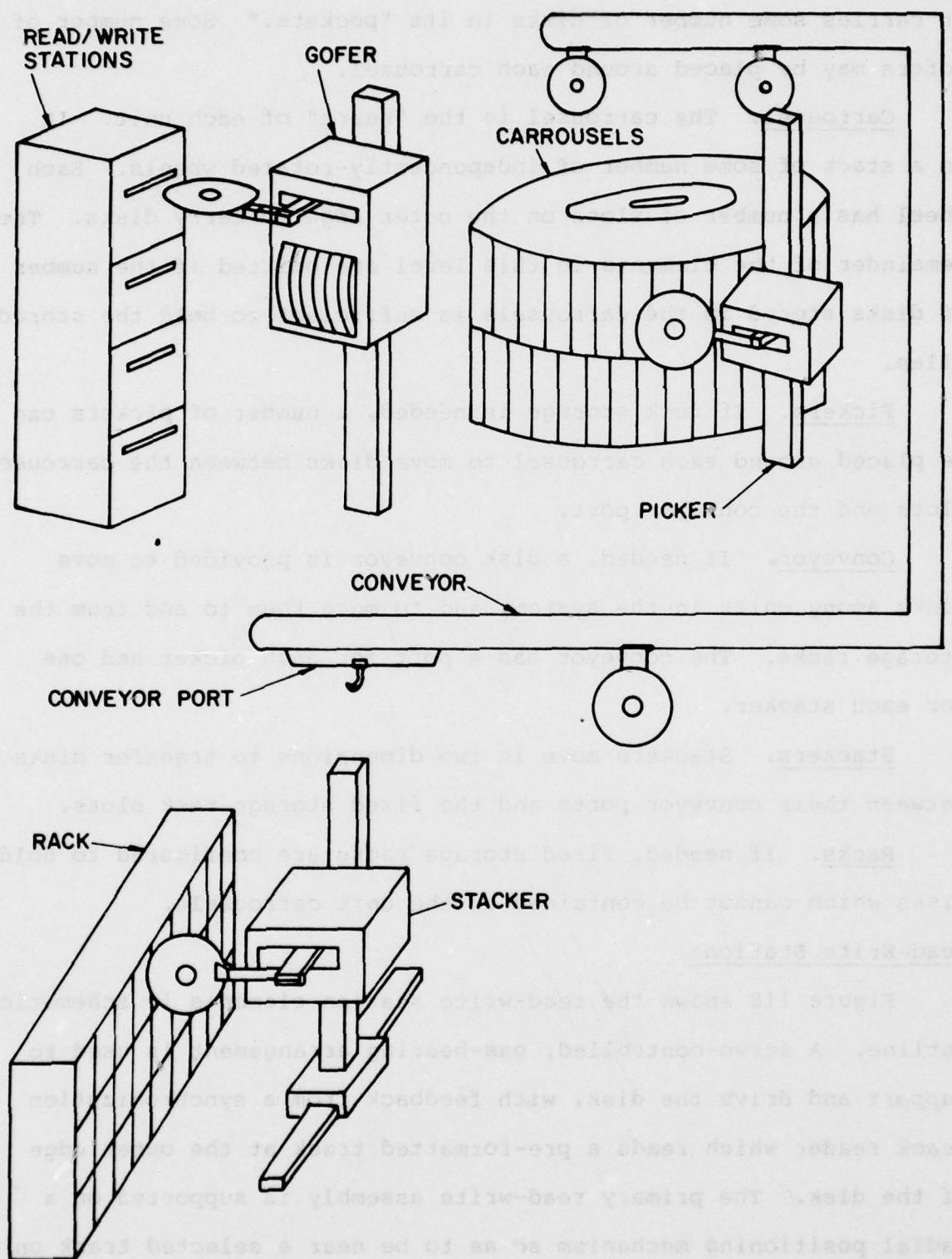


Figure 117. Very Large Optical Disk File System

It carries some number of disks in its "pockets." Some number of gofers may be placed around each carrousel.

Carrousel. The carrousel is the "heart" of each unit. It is a stack of some number of independently-rotated wheels. Each wheel has a number of slots on the outer edge to carry disks. The remainder of the elements in this level are omitted if the number of disks stored in the carrousels is sufficient to hold the stored files.

Pickers. If rack storage is needed, a number of pickers can be placed around each carrousel to move disks between the carrousel slots and the conveyor port.

Conveyor. If needed, a disk conveyor is provided to move disks among units in the system, and to move them to and from the storage racks. The conveyor has a port for each picker and one for each stacker.

Stackers. Stackers move in two dimensions to transfer disks between their conveyor ports and the fixed storage rack slots.

Racks. If needed, fixed storage racks are configured to hold disks which cannot be contained in the unit carrousels.

Read-Write Stations

Figure 118 shows the read-write station elements in schematic outline. A servo-controlled, gas-bearing arrangement is used to support and drive the disk, with feedback from a synchronization track reader which reads a pre-formatted track at the outer edge of the disk. The primary read-write assembly is supported on a radial positioning mechanism so as to be near a selected track on

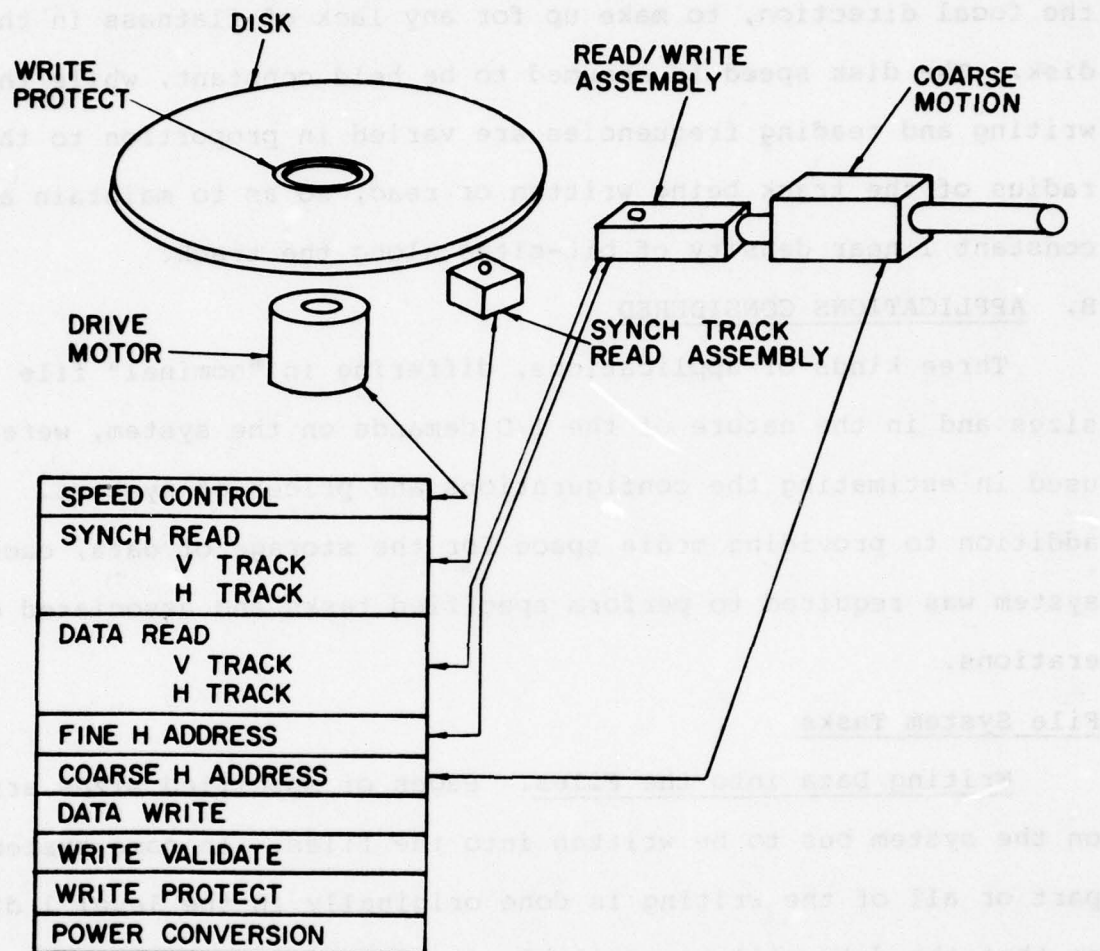


Figure 118. Optical Disk Read/Write Station

the lower surface of the disk. Fine positioning is accomplished with a small mirror which is servo-controlled by tracking signals from a dual-channel reading assembly. Both this assembly and the synchronization reading assembly must also be servo-controlled in the focal direction, to make up for any lack of flatness in the disk. The disk speed is assumed to be held constant, while the writing and reading frequencies are varied in proportion to the radius of the track being written or read, so as to maintain a constant linear density of bit-sites along the track.

B. APPLICATIONS CONSIDERED

Three kinds of applications, differing in "nominal" file sizes and in the nature of the I/O demands on the system, were used in estimating the configurations and prices of systems. In addition to providing media space for the storage of data, each system was required to perform specified tasks and associated operations.

File System Tasks

Writing Data into the Files. Pages of specified sizes arrive on the system bus to be written into the files. In some systems, part or all of the writing is done originally in the level 1 disks, so that the data will be available for immediate reading, and so that the overall price of the system can be reduced by reducing the number of level 2 units needed.

Reading Data from the Files. Commands to read specified pages arrive on the system bus. In some systems, part of these refer to data stored in level 1, but generally most of them require access to level 2.

Copying Data from Level 1 to Level 2. When part or all of the write demands are carried out in level 1, a backlog of spare-time copying demands is built up. These are executed when there is excess system capacity, unless the data in level 1 overflows the space allocated, in which case some of them must be executed immediately.

Restructuring Data Files. Many kinds of data files require restructuring from time to time in order to improve access efficiencies and reclaim wasted spaces. It was assumed here that such demands would be proportional to the rate of writing data into the file, and that they would be executed in spare time, so as not to interfere with peak period operations of the system.

Catalog Operations Associated with Tasks

Although it was assumed that all high-level control functions would be performed by software in the user computers, or by a high-level file system controller, which was not included in the model, it was also assumed that such control processes would require access to catalogs or file directories in their operations, and that such "accessory" files might become large enough to warrant storage in the file system itself. Some number of catalog read and write operations is thus associated with each execution of each of the tasks outlined above, and space is provided for the catalog information.

I/O Demand Scheduling

Three-shift operation of the file system is assumed. The demand during each shift is described in terms of the total number of pages written and the total number of pages read during

the shift, and by a single number giving the ratio of peak demand rate to average demand rate during the shift.

Distribution of Access Requirements Across the File Space

It is well-known that certain files on any system are used more frequently than other files, and that when random access is possible, certain pages of a file are referenced much more frequently than others. Beyond these matters of common knowledge, there is very little factual information. For lack of such data, and because it is easily computed, it was assumed in all of the applications considered that if the pages in the file were arranged in descending order of access frequency, and if the access rate were then stated as a function of the distance along the file address space, it would approximate an inverse exponential function; i.e., the access rate to the page at location S would be given by the equation:

$$R = R_0 e^{-As} \quad (68)$$

where R is the access rate to the most frequently-used page in the system, s is the fraction of the total address space in the system, and A is a constant determined by the application. While there are cases in which this assumption is clearly not true, it is probable that a large mix of demands on behalf of a large number of users will yield a distribution which approximates this. Assumptions regarding all three kinds of demand are tabulated in Table 19.

Table 19
MAJOR FEATURES OF THE APPLICATIONS
CONSIDERED IN THIS STUDY

APPLICATION	LIBRARY	IMAGERY	TIME-SHARING
Useful Bit Stored	1×10^{14}	1.6×10^{14}	1.6×10^{13}
Redundant Bits Stored	1×10^{14}	3.2×10^{13}	3.2×10^{12}
Catalog Bits Stored	2×10^{11}	1.92×10^{11}	1.92×10^{11}
Total Storage	2.002×10^{14}	1.922×10^{14}	1.639×10^{13}
Writes-Bits/Page	1×10^6	1×10^7	1.1×10^4
Pages/Sequences	10	200	10
Distribution Coefficient	10	10	10
First Shift Pages	1×10^4	3×10^3	8.67×10^5
Second Shift Pages	1×10^3	3×10^3	5×10^5
Third Shift Pages	0	3×10^3	1×10^5
Catalog Writes/Sequence	1	1	1
Catalog Reads/Sequence	2	2	2
Peak/Average Demand			
First Shift	3	3.33	3
Second Shift	2	3.33	2
Third Shift	1.5	3.33	1.5
Reads-Bits/Page	1×10^5	1×10^7	1.1×10^4
Pages/Sequence	5	5	5
Distribution Coefficient	8	8	10
First Shift Pages	1×10^5	5.4×10^4	5×10^6
Second Shift Pages	1×10^4	5.4×10^3	2.5×10^6
Third Shift Pages	1×10^3	5.4×10^2	5×10^5
Catalog Writes/Sequence	1	1	1
Catalog Reads/Sequence	2	2	2

The Library Application

In this application, it is assumed that all input to the files is prepared and added by a small group of specialists, primarily during the first shift. Output goes on demand to a large group of independent users, primarily at on-line terminals. Response time in accessing the required output pages is therefore quite important.

The Imagery Applications

Image data are received at any time of the day or night and recorded in the system. Personnel using computers to analyze and compare the images work mainly on the day shift. Access time is less critical because a large part of the work can be pre-planned. Page sizes are large, making data transfer rate an important feature of the file system.

The Time-Sharing Application

File sizes and page sizes are relatively small, but the access rate, particularly on first shift is very high, and most of the reading refers to pages written the same day.

C. FILE SYSTEM DESIGN PROCESS

Computer programs were written to design file systems from the given technologies to meet the given demands. One program was prepared for each of the kinds of systems considered. All of them followed the same general outline, and worked from the same demand descriptions.

1. The number of media elements required to store the "nominal" data, the redundant data, and the catalog information was computed by determining the capacity of a medium element and then dividing the total storage required by the element capacity, at a given degree of space utilization.

2. The task demand rates from the demand data were converted into peak operation rates for a set of operations appropriate to the system under consideration.

3. The units required at level 2 were configured by:

- Setting the initial number equal to the minimum number required in the data.
- Finding the fraction of the data and the catalogs available for each access delay and using that data to compute "hit" probabilities for each amount of time the device is kept busy.
- Summing the use rates multiplied by holding times over all hit probabilities to find the expected device busy times per second.
- Dividing by the number of devices to find device utilization ratios.
- Comparing device utilizations with those specified in the data. If no over-utilized devices are found, skip to step 4.
- Else, augment the configuration to reduce the over-utilization and iterate, beginning at the second bullet above.

4. Configure the level 2 controllers to connect all of the units, or to carry out the required operating rate, whichever is more demanding.

5. Configure the level 1 units and controllers to store the required amount of data, or to operate at the required I/O rate, whichever is more demanding.

6. Configure the file system bus to transfer the required commands, data, and status information.
7. Estimate service times and queue-waiting times for all of the devices in the system.
8. Estimate the times required to execute the required write sequences and read sequences.
9. Find the total price for the system, the price per bit actually stored, and the price per access to the data.

Certain "free" parameters in the process are left to the choice of the program user during the configuration process. These include:

1. The Load Factor. This number can be set to multiply all I/O demand rates uniformly, so that system designs for differing demand rates can be produced.
2. The fraction of "old" file data kept in level 1 to improve access times and reduce the need for level 2 I/O capacity.
3. The number of AAM plates-full of data which can be stored in level 1 before copying must be started to level 2.
4. The fraction of catalog information referring to data in level 2 which is kept in level 1 to reduce access delays and reduce the I/O rate of catalog information in level 2.
5. The fraction of all writes which are directed to level 1 (applies to large-plate AAM model only).
6. A switch which tells whether catalog information is kept on the same medium plate as the data to which it refers (used only in large-plate AAM system design).

Configuring the Small-Plate AAM Systems

In these systems, it was assumed that all of the writing of data was done in level 1, with later copying to level 2.

Each execution of a system task required some number (possibly zero) of executions of the following listed operations:

- Write Data Level 1.
- Read Data Level 1.
- Write Catalog Level 1.
- Read Catalog Level 1.
- Write Data at Random Address Level 2.
- Write Data at Sequential Address Level 2.
- Read Data at Random Address Level 2.
- Read Data at Sequential Address Level 2.
- Write Catalog Level 2.
- Read Catalog Level 2.

It was assumed that reading, except to verify writing, would not be done in the writing stations, and that catalog information kept on AAM plates would be assigned to plates reserved for that purpose, rather than being mixed with data on common plates. Separate clusters of AAM stations were thus configured for:

- Writing Data.
- Reading Data.
- Writing Catalog.
- Reading Catalog.

Minimums of two stations each were specified for writing data and reading data, and minimums of one station each were specified for writing catalog and reading catalog. This arrangement tended to make systems with small files and/or small I/O rates more expensive than they might otherwise have been.

Configuring Large-Plate AAM

In these systems a variable amount of original writing was specified to be done in level 1 for later copying to level 2. Writing of files which need not be available for immediate reading could be done directly to level 2, although in most cases it turned out that little of this kind of operation was economical.

A longer list of system operations was defined to take advantage of the large amount of data which could be on a single plate:

- Write Data Random Level 1.
- Write Data Sequential Level 1.
- Read Data Random Level 1.
- Read Data Sequential Level 1.
- Write Catalog Level 1.
- Read Catalog Level 1.
- Write Data Random Level 2.
- Write Data on Same Plate Level 2.
- Write Data Sequential Level 2.
- Read Data Random Level 2.
- Read Data on Same Plate Level 2.
- Read Data Sequential Level 2.
- Write Catalog Random Level 2.

- Write Catalog on Same Plate Level 2.
- Write Catalog Sequential Level 2.
- Read Catalog Random Level 2.
- Read Catalog on Same Plate Level 2.
- Read Catalog Sequential Level 2.

Assuming that routine reading could be done in a station equipped for writing made it possible to reduce the total number of stations in some cases. A minimum number of write stations, usually two, was specified. If additional writing stations were required to handle the peak writing demand, they were added to the configuration. The number of stations required to handle the entire I/O rate was then found, and any excesses over the number of writing stations were configured as read-only stations.

Configuring the Tape-Cartridge Systems

All stations were assumed capable of both reading and writing, and no special distinctions were made between cartridges for storage of catalog information and for storage of data.

System Operations Considered. The following list of operations in response to system task demands was included in the calculations. This is essentially the same list as for the small-plate AAM system.

- Write Data Level 1.
- Read Data Level 1.
- Write Catalog Level 1.
- Read Catalog Level 1.
- Write Data Random Level 2.
- Write Data Sequential Level 2.

- Read Data Random Level 2.
- Read Data Sequential Level 2.
- Write Catalog Level 2.
- Read Catalog Level 2.

Because of the fairly complex relations among minimum numbers of elements required, numbers of elements permitted by interconnection constraints, numbers of elements configured and hit probabilities, the configuration process:

- Found the minimum configuration.
- Found hit probabilities, element busy-times.
- Found the utilization ratios of all elements.
- Checked for over-utilization. If none, proceeded to complete the configuration of other parts of the system.
- Increased the number of the most over-utilized element configured, harmonized the new trial configuration in accord with the interconnection constraints, and iterated to above.

Configuring the Optical Disk System

Except for minor differences in treatment of hit probabilities caused by the two-sided recording disk, this system is very similar to the tape-cartridge system. The same set of system operations was computed, and the same iterative technique was used to determine the final configuration.

TYPICAL CONFIGURATIONS, COSTS AND SERVICE TIMES

The tabulations which follow show the system configurations, prices, and expected elapsed service times for completion of write sequences and read sequences during the peak load period on the system. The "base" case data given in Section B are used for all configurations shown here.

Generally, some number of file pages is written or read sequentially, so that a sequence time includes:

- The elapsed time for all file bus transfers of data, commands, and status returns.
- The elapsed time for all catalog operations.
- The elapsed time for random access and transfer of the first page.
- The elapsed time for sequential access and transfer of all subsequent pages, if any.

The configurations, and the time calculations in the models are somewhat pessimistic in comparison with those calculated from a detailed simulation, or with those to be expected in actual practice, but they are probably adequate for comparison purposes.

D. SYSTEM PRICE AND PERFORMANCE RESULTS

One set of designs for each of the storage technologies and for each application was made on the assumption that demand for file I/O remained fixed, independent of file size. These results would apply to an installation serving a fixed demand as the total amount of data stored increased with time.

A second set of designs for each of the systems was made on the assumption that I/O demand rate would be proportional to the total amount of stored data. These results would apply to the "pooling" of some number of smaller sets of files on the same system in order to achieve lower costs, if possible.

A third set of designs was made for each system, holding the file size constant, and varying the I/O demand rate over a wide range to "separate" the price of raw storage from the price of input output, and to explore the effects on read-sequence times.

In each case, the free parameters of the file system design model were adjusted to yield a system design with the lowest price to meet the given storage and I/O requirements.

Results for the Library Application

File Growth at Constant I/O Demand. Figure 119 shows expected 1985 end-user prices for complete file systems based on each of the media as a function of total bits stored. Note that both scales are logarithmic. A system using magnetic disks only is also plotted for comparison purposes. Within the probable precisions of the many assumptions made in the design model, the small-plate AAM system and the optical disk system show comparable results for file sizes up to about 10^{15} bits, and both are better than the tape cartridge system for file sizes above 10^{13} bits. The large-plate AAM system appears clearly better than all other systems for all file sizes.

Economy of Scale. Figure 120 shows expected 1985 end-user prices for complete file systems over a range of sizes, on the assumption that the I/O demand rate varies proportionally with the file size. The small-plate AAM system looks somewhat better than tape cartridge and optical disk systems for file sizes of 10^{14} bits and up. The large-plate AAM system looks much better than all other systems for file sizes larger than 10^{13} bits.

Figure 121 shows the same results plotted on a price per bit scale, to indicate that modest scale economies can be expected out to the largest file sizes examined, for the large-plate AAM system. The others lose scale economy beyond about 10^{15} bits.

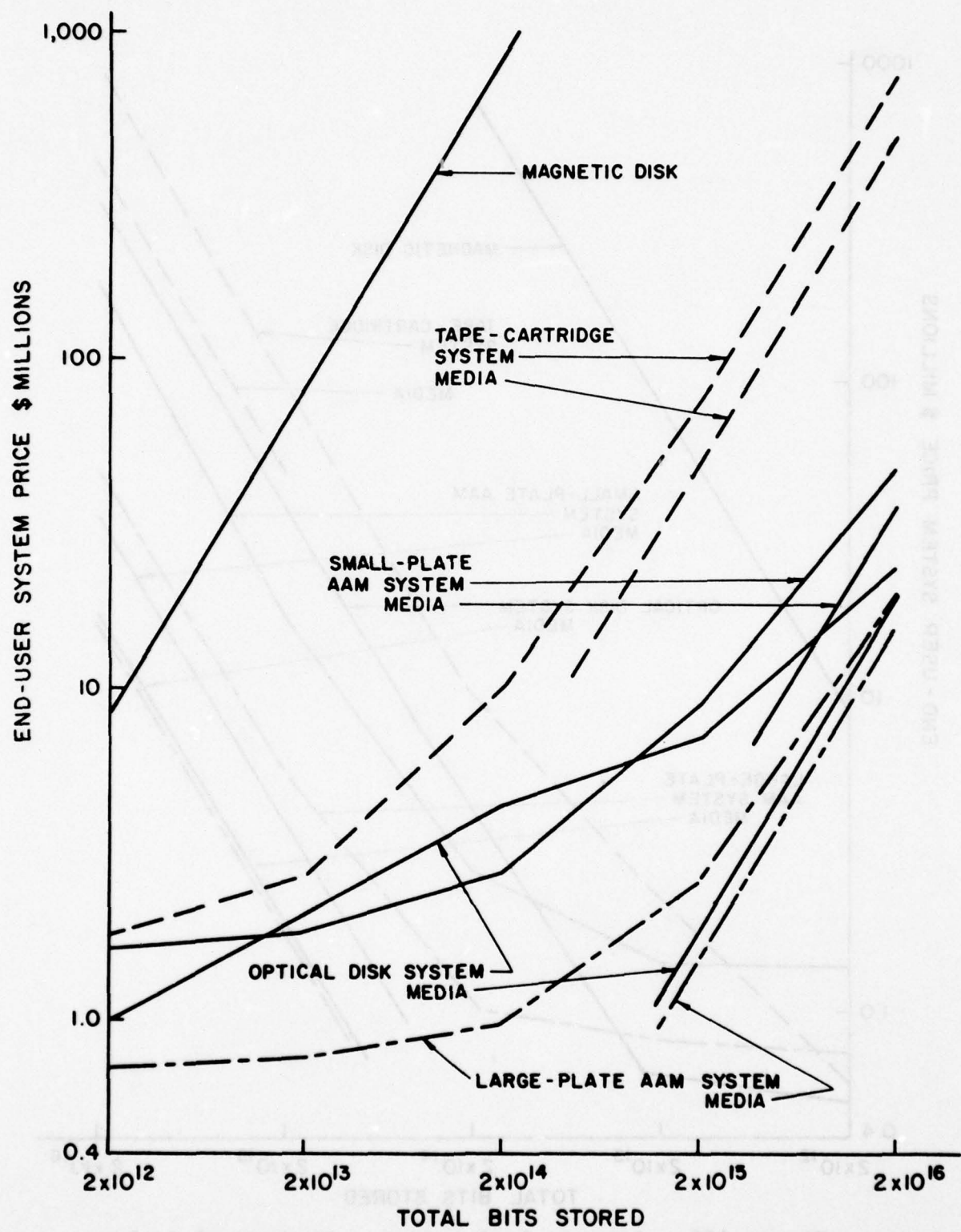


Figure 119. Library Application at Constant I/O Rate

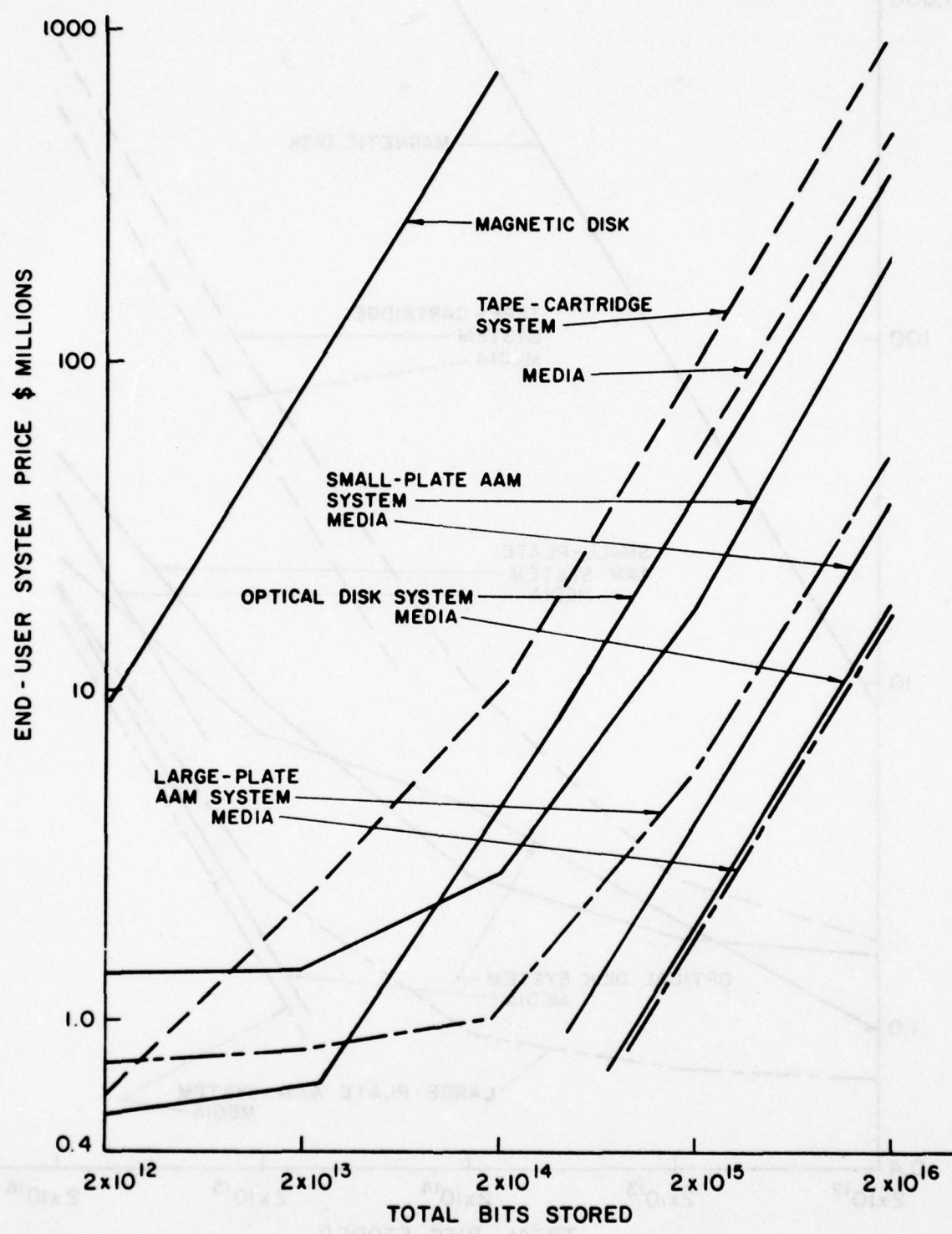


Figure 120. Library Application - Economy of Scale

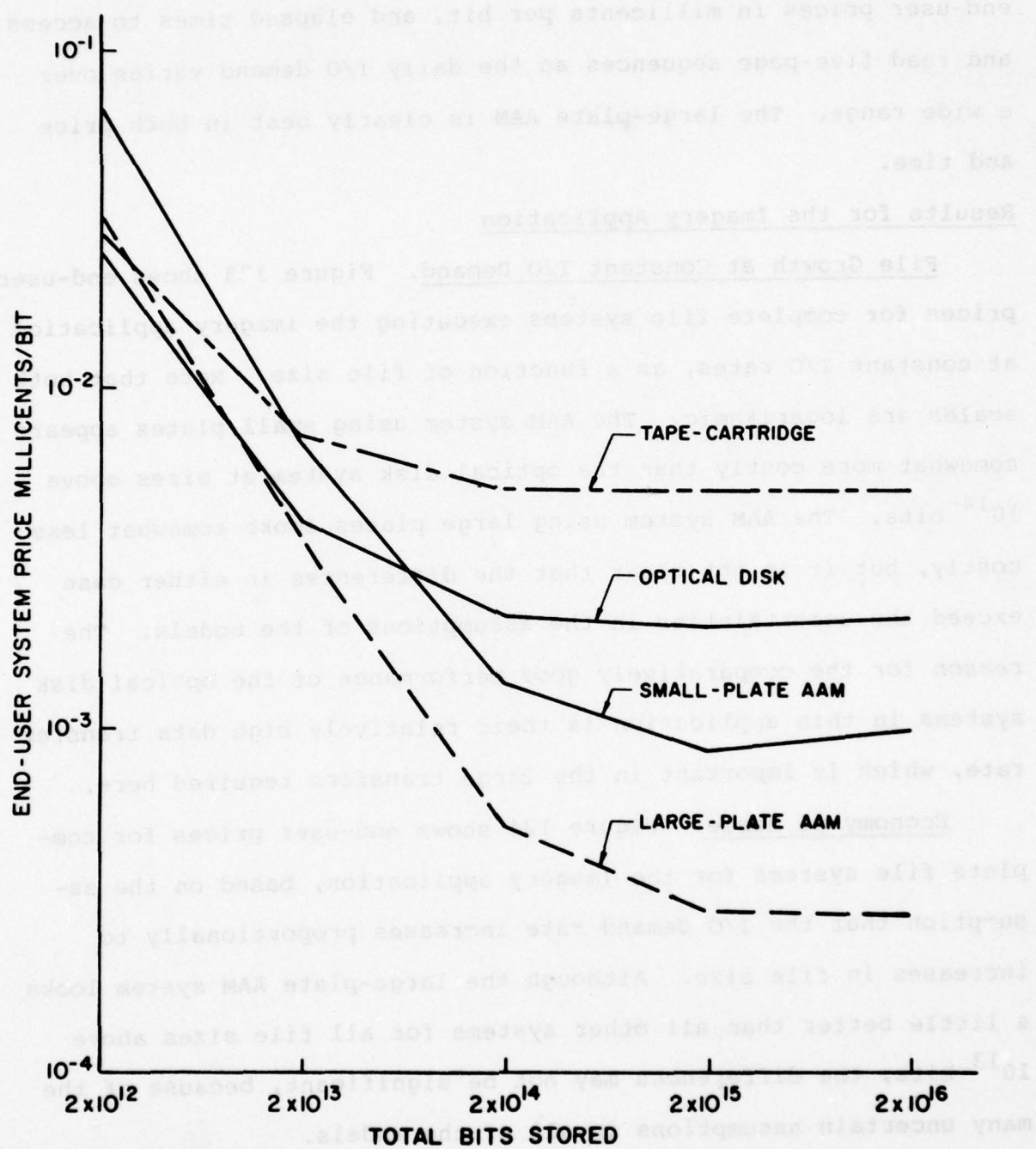


Figure 121. Library Application - Economy of Scale

Constant File Size with Varying I/O Demand. Figure 122 shows end-user prices in millicents per bit, and elapsed times to access and read five-page sequences as the daily I/O demand varies over a wide range. The large-plate AAM is clearly best in both price and time.

Results for the Imagery Application

File Growth at Constant I/O Demand. Figure 123 shows end-user prices for complete file systems executing the imagery application at constant I/O rates, as a function of file size. Note that both scales are logarithmic. The AAM system using small plates appears somewhat more costly than the optical disk system at sizes above 10^{14} bits. The AAM system using large plates looks somewhat less costly, but it is not clear that the differences in either case exceed the uncertainties in the assumptions of the models. The reason for the comparatively good performance of the optical disk systems in this application is their relatively high data transfer rate, which is important in the large transfers required here.

Economy of Scale. Figure 124 shows end-user prices for complete file systems for the Imagery application, based on the assumption that the I/O demand rate increases proportionally to increases in file size. Although the large-plate AAM system looks a little better than all other systems for all file sizes above 10^{13} bits, the differences may not be significant, because of the many uncertain assumptions in all of the models.

Figure 125 shows the same results plotted in terms of end-user price per bit stored. Scale economy extends out to about 10^{15} bits, but appears to reverse at large file sizes, except for the optical disk system.

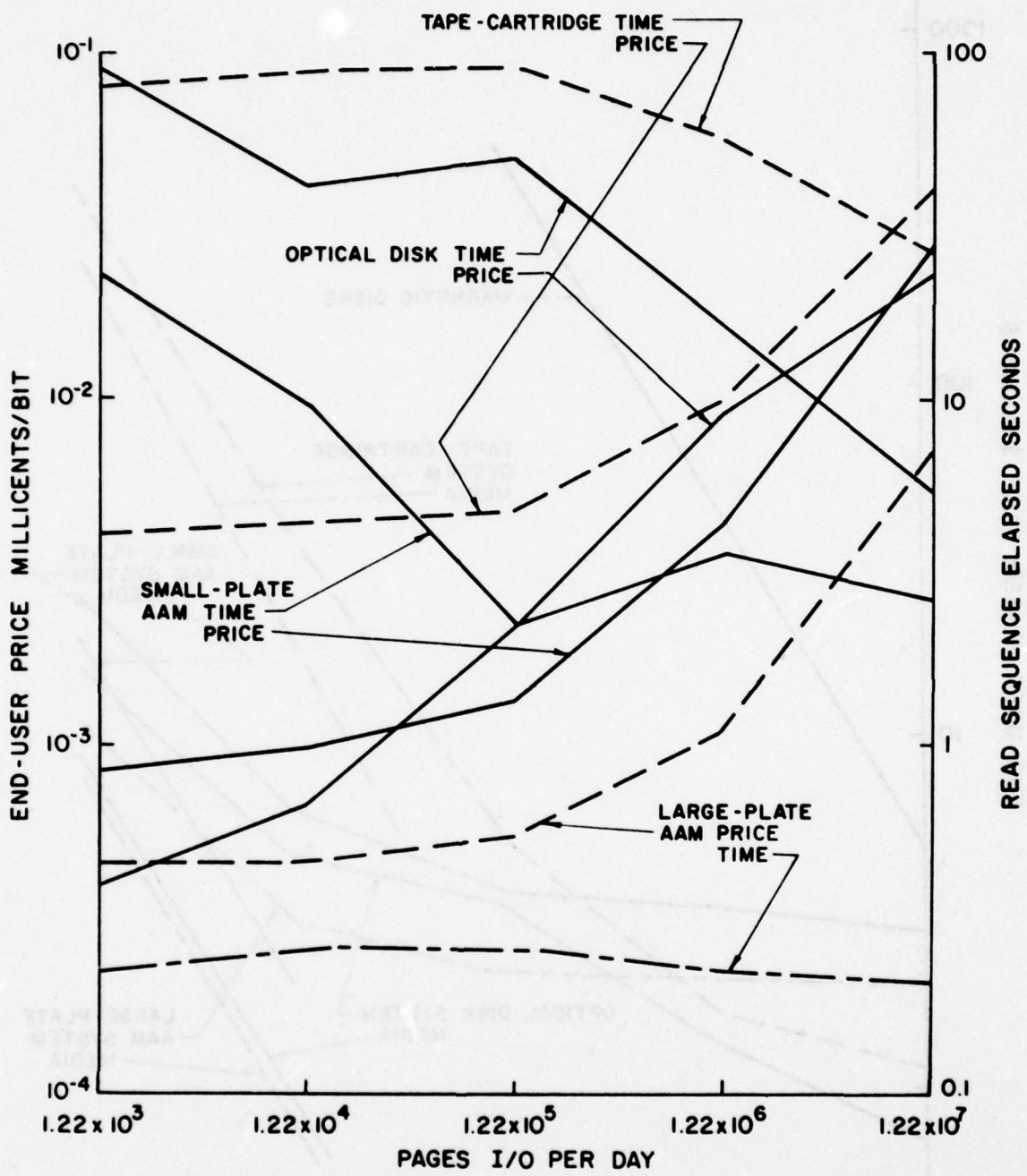


Figure 122. Library Application - Total File Size
 2.002×10^{14} bits

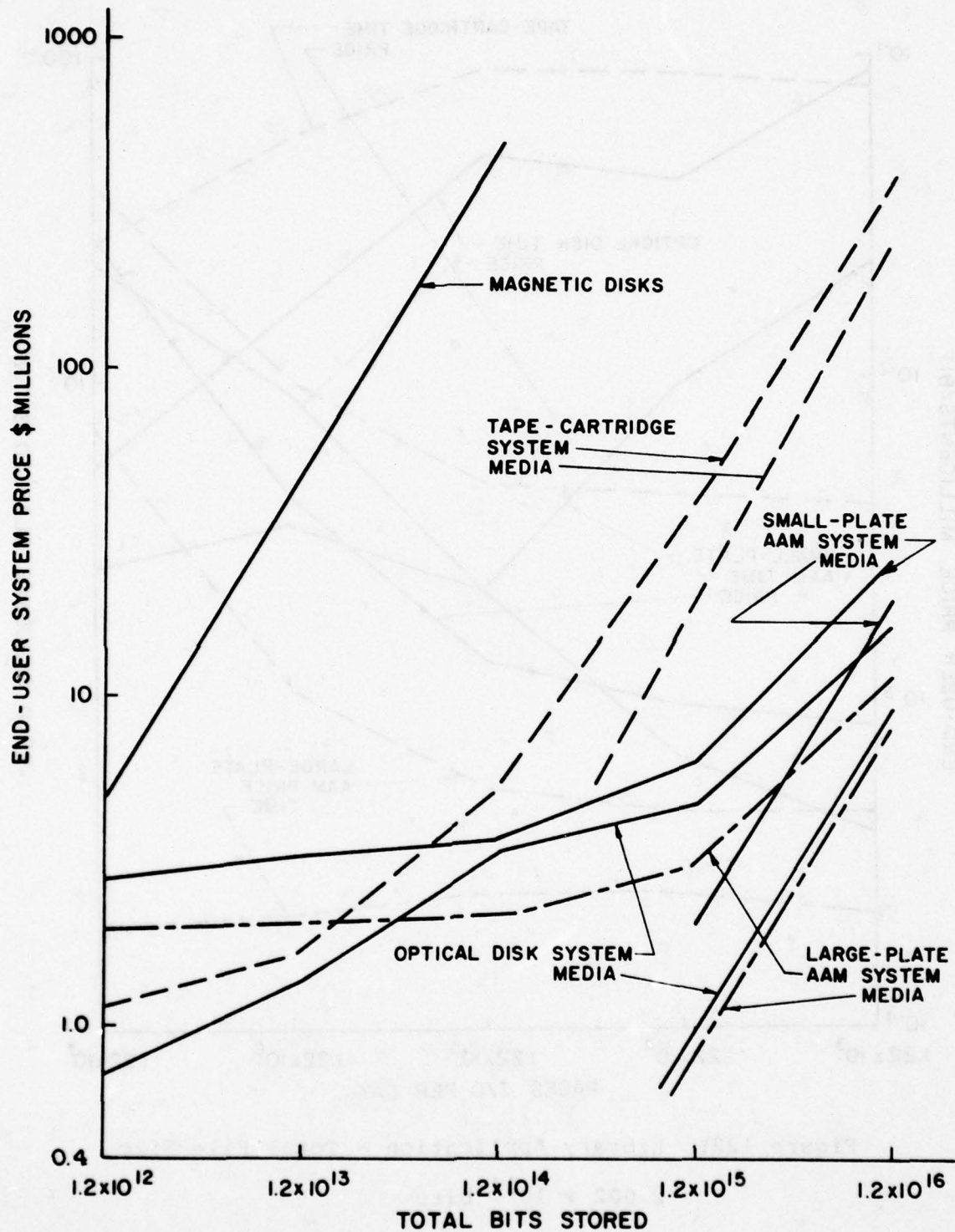


Figure 123. Imagery Application - Constant I/O Rates

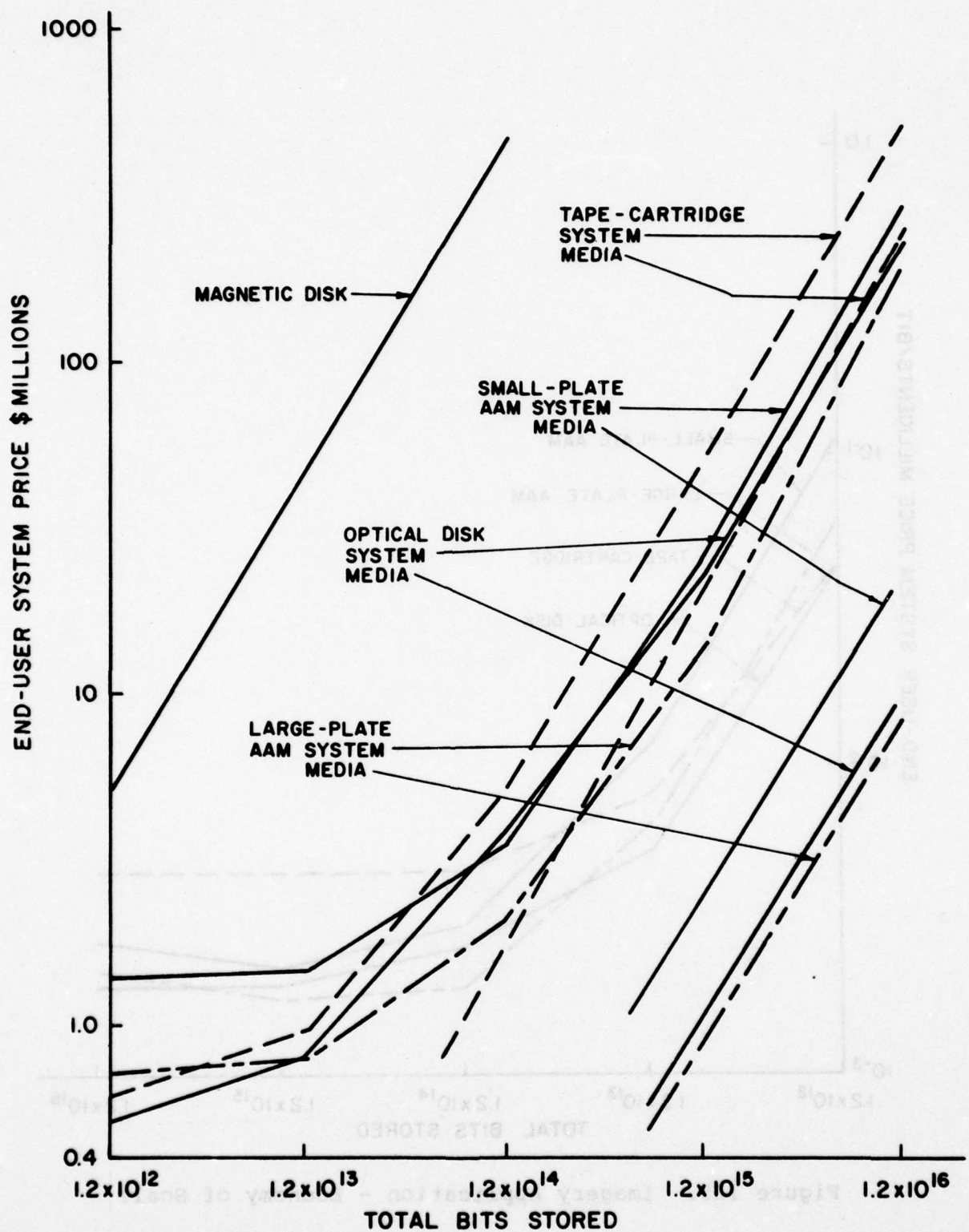


Figure 124. Imagery Application - Economy of Scale

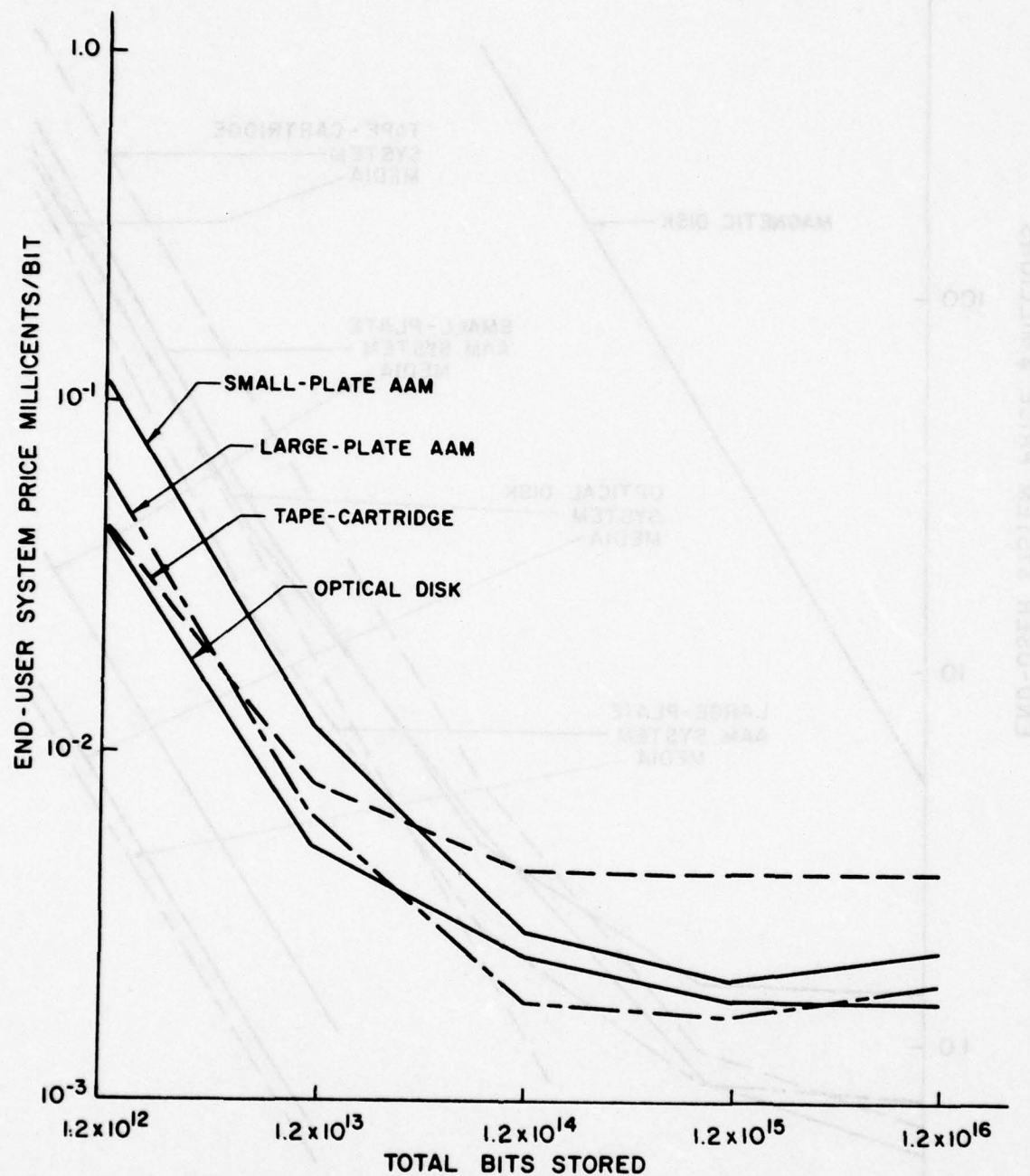


Figure 125. Imagery Application - Economy of Scale

Variable I/O Demand at Constant File Size. Figure 126 shows end-user prices in millicents per bit, and elapsed times to access and transfer five-page sequences. The large-plate AAM system shows elapsed times which are clearly better up to about 100 times the "normal" demand rate. The optical disk competes well.

Results for the Time-Sharing Application

File Growth at Constant I/O Demand. Figure 127 shows end-user prices for complete file systems as a function of file size at constant I/O demand rate. The small-plate AAM system looks better than the tape cartridge and optical disk systems for sizes of about 10^{14} bits and up. The large-plate AAM system appears clearly better at all file sizes, but simple magnetic disk systems compete very well at sizes up to about 5×10^{11} bits.

Economy of Scale. Figure 128 gives end-user system prices as functions of file size, on the assumption that the I/O demand rate is proportional to file size. The large-plate AAM system appears to be better than all other systems in this application for files of 10^{12} bits and up.

Figure 129 plots the same results in terms of price per bit of storage. The large-plate AAM system shows economy of scale for all file sizes examined. The small-plate AAM and the other kinds of systems lose scale economy for sizes above about 2×10^{13} bits.

Variable I/O Demand at Constant File Size. Figure 130 shows end-user system prices in millicents per bit and expected elapsed times to access and read sequences of five pages from the file. The large-plate AAM is somewhat better in price and clearly superior in elapsed time for all demand rates.

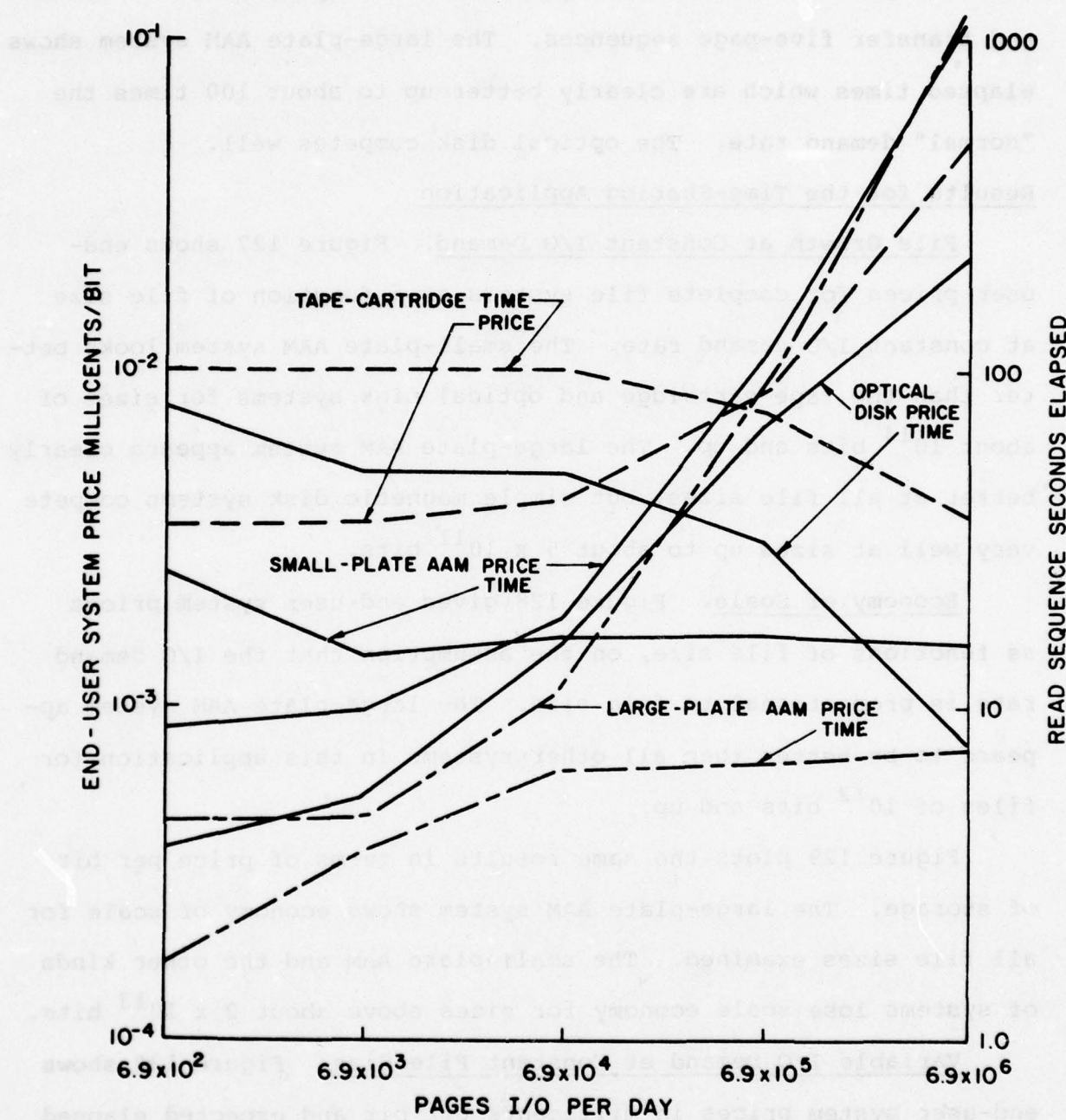


Figure 126. Imagery Application - Total File Size

$$1.922 \times 10^{14} \text{ Bits}$$

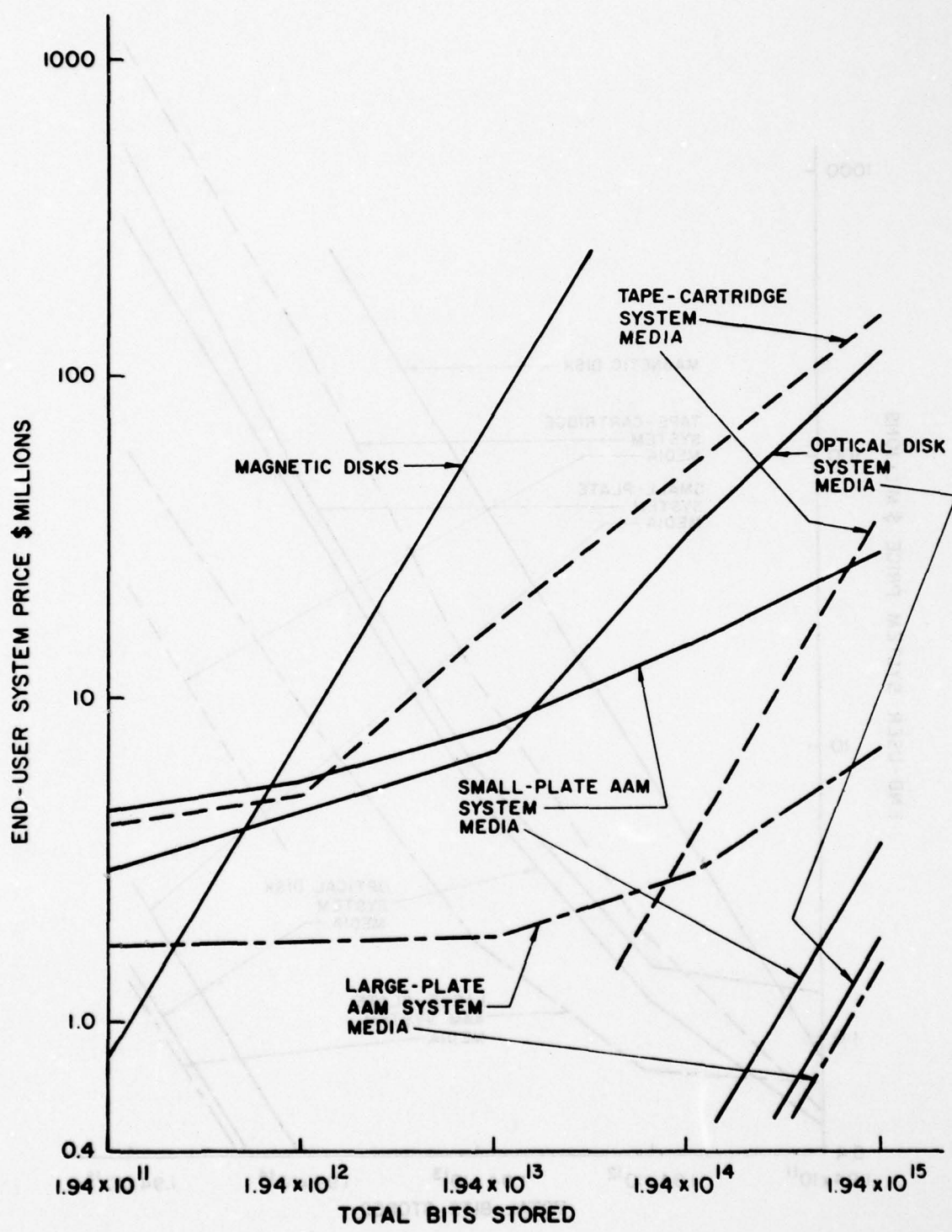


Figure 127. Time-sharing Application - Constant I/O Rates

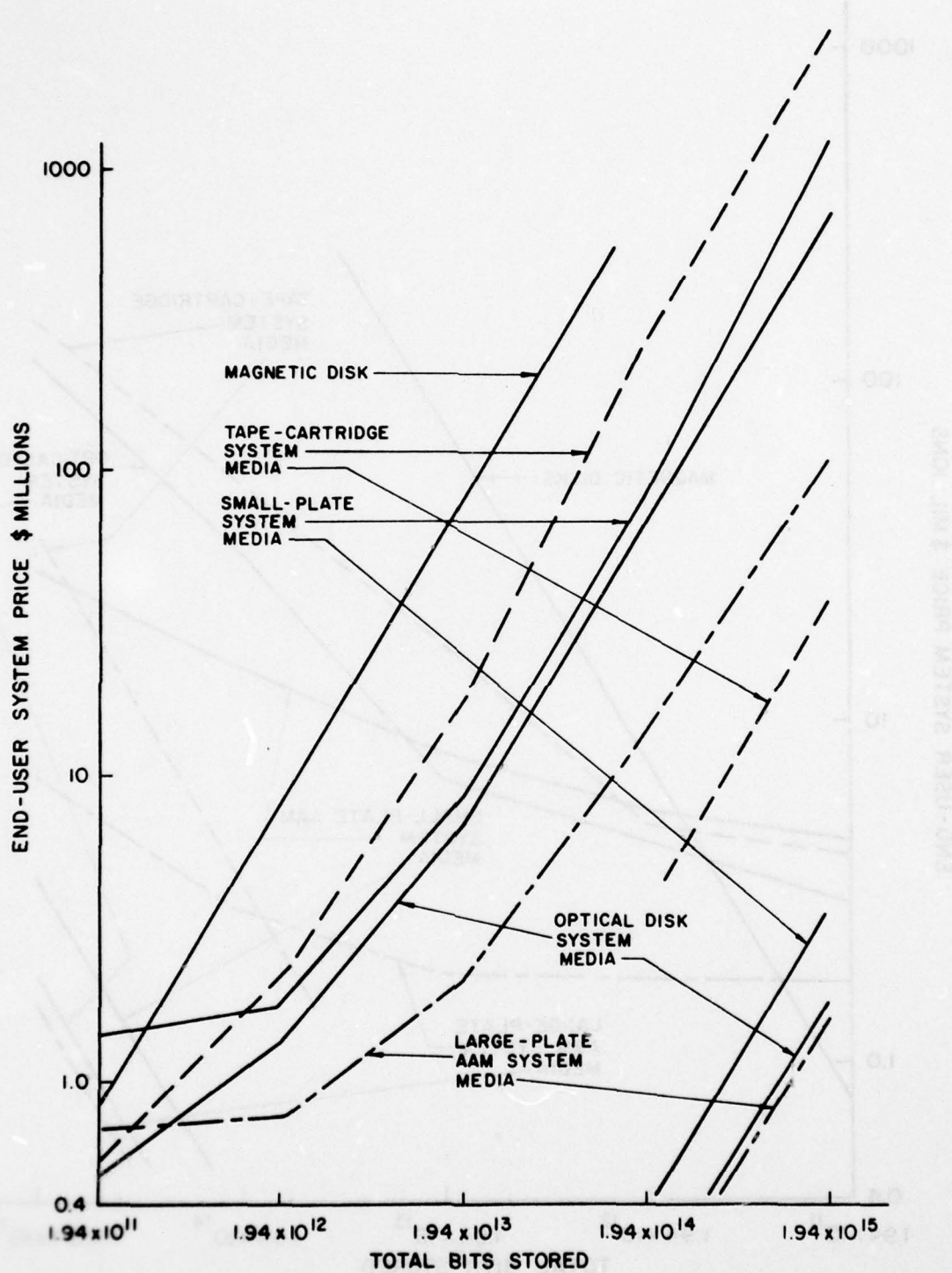


Figure 128. Time-sharing Application - Economy of Scale

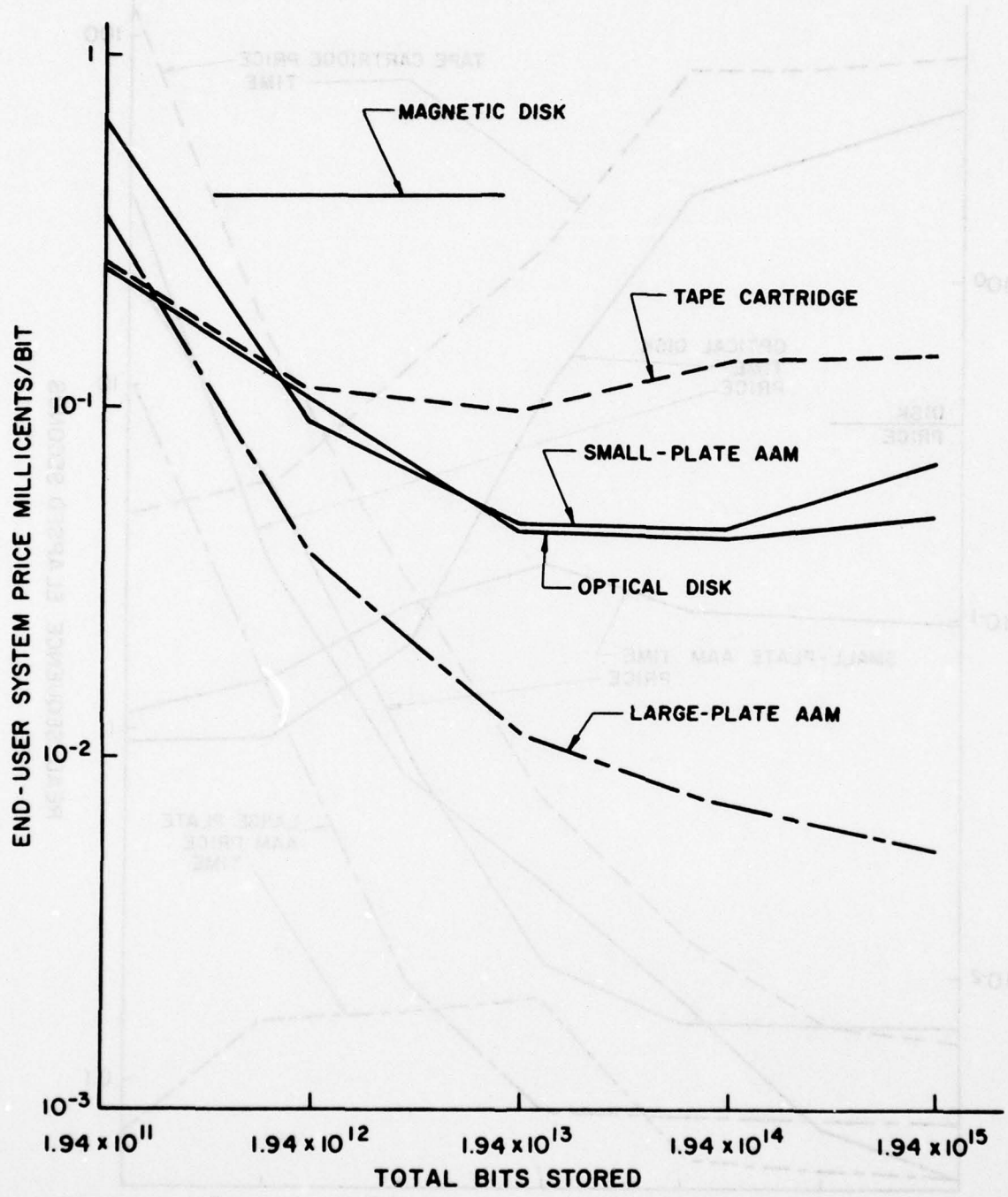


Figure 129. Time-sharing Application - Economy of Scale

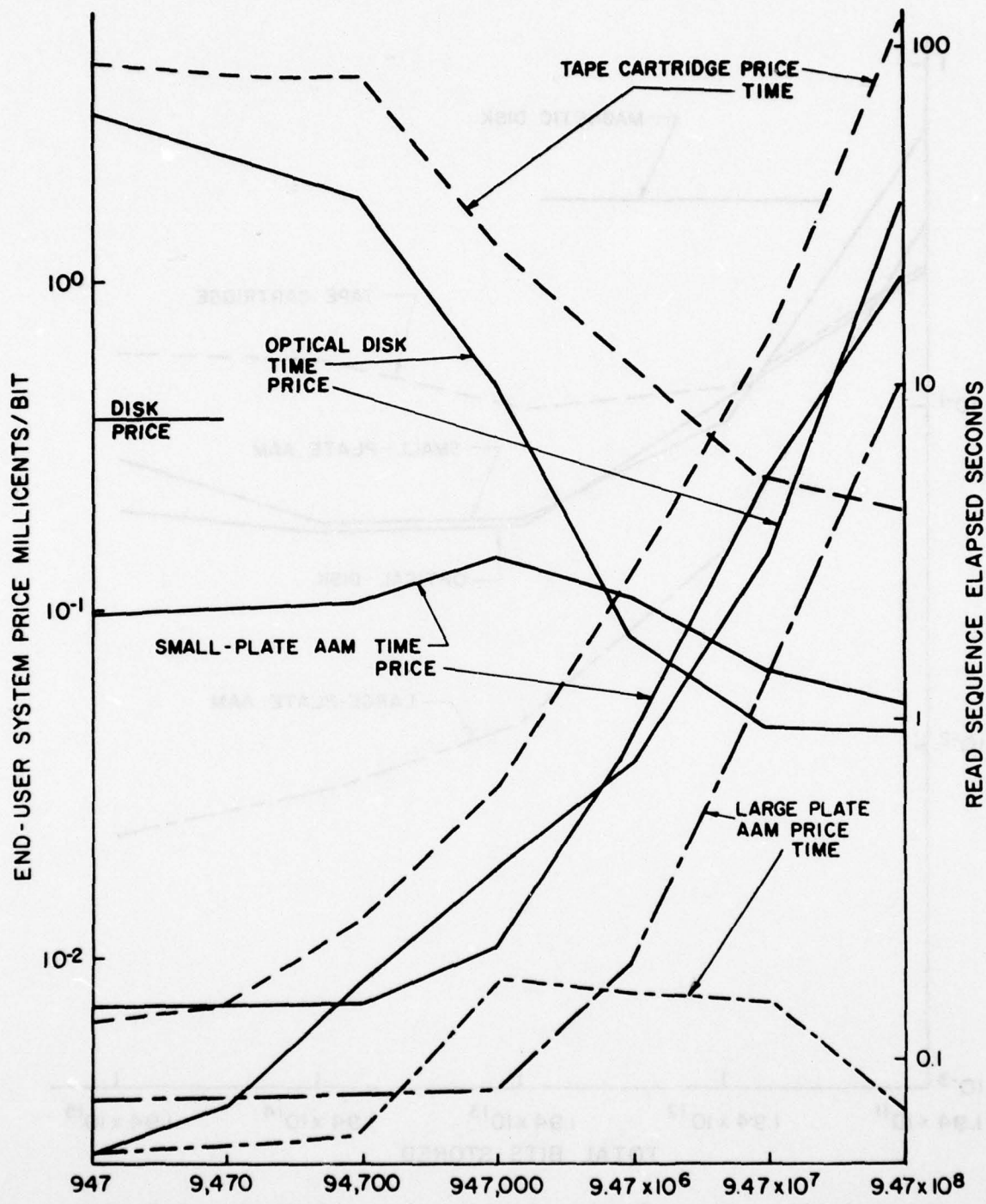


Figure 130. Time-sharing Application - Total File Size
 1.939×10^{13} Bits

APPENDIX A

Listing of ion-writing experiments. (*) indicates
high resolution patterns were used as implant masks.

Target Number	Ion Species	Energy (kV)	Fluence (#/cm ²)
B10C	Ne	25	10^9
A79A	Ne	25	10^9
B19A	Ne	25	10^9
A71D	Ne	25	10^9
B14C	Ne	25	10^{10}
A80A	Ne	25	10^{10}
A72D	Ne	25	10^{10}
B21A	Ne	25	10^{10}
B23A	Ne	25	5×10^{10}
A81A	Ne	25	5×10^{10}
A73B	Ne	25	5×10^{10}
B16C	Ne	25	5×10^{10}
A82A	Ne	25	10^{11}
B15C	Ne	25	10^{11}
A74B	Ne	25	10^{11}
B20A	Ne	25	10^{11}
A84C	Ar	60	10^9
B14B	Ar	60	10^9
A73D	Ar	60	10^9
B22C	Ar	60	10^9

APPENDIX A (Cont'd)

Target Number	Ion Species	Energy (kV)	Fluence (#/cm ²)
A74C	Ar	60	10^{10}
B23D	Ar	60	10^{10}
A85D	Ar	60	10^{10}
B15B	Ar	60	10^{10}
A84B	Ar	60	5×10^{10}
B13C	Ar	60	5×10^{10}
A72C	Ar	60	5×10^{10}
B22B	Ar	60	5×10^{10}
B23C	Ar	60	10^{11}
A85C	Ar	60	10^{11}
B11B	Ar	60	10^{11}
A70B	Ar	60	10^{11}
A70D	Kr	110	10^9
B22A	Kr	110	10^9
B10B	Kr	110	10^9
A83A	Kr	110	10^9
A72B	Kr	110	10^{10}
B17A	Kr	110	10^{10}
B13B	Kr	110	10^{10}
A89A	Kr	110	10^{10}

(b) (3)(A) X INFORMATION
APPENDIX A (Cont'd)

Target Number	Ion Species	Energy (kV)	Fluence (#/cm ²)
A73C	Kr	110	5×10^{10}
B18A	Kr	110	5×10^{10}
B14A	Kr	110	5×10^{10}
A85A	Kr	110	5×10^{10}
B23B	Kr	110	10^{11}
B12C	Kr	110	10^{11}
A85B	Kr	110	10^{11}
A75D	Kr	110	10^{11}
A84D	Xe	145	10^9
B22D	Xe	145	10^9
B15A	Xe	145	10^9
A75C	Xe	145	10^9
A83B	Xe	145	10^{10}
B21B	Xe	145	10^{10}
B11A	Xe	145	10^{10}
A75B	Xe	145	10^{10}
A82B	Xe	145	5×10^{10}
B19B	Xe	145	5×10^{10}
B11A	Xe	145	5×10^{10}
A71C	Xe	145	5×10^{10}
B20B	Xe	145	10^{11}
A81B	Xe	145	10^{11}
B12A	Xe	145	10^{11}
A70C	Xe	145	10^{11}

APPENDIX A (Cont'd)

Target Number	Ion Species	Energy (kV)	Fluence (#/cm ²)
A76E*	Si	40	10 ¹¹
A76C*	Si	40	10 ¹¹
A76D*	Si	40	3 x 10 ¹¹
A73A*	Si	40	3 x 10 ¹¹
B16A*	Xe	40	10 ¹²
B13A*	Xe	40	10 ¹¹
A76D*	Xe	40	10 ¹¹
A76B*	Xe	40	10 ¹¹
A51A*	Xe	40	10 ¹¹
A105A*	Xe	40	10 ¹¹
A101B*	Xe	40	10 ¹¹
A51A*	Xe	40	10 ¹¹
A105B*	Xe	40	10 ¹¹
A51B*	Xe	145	4 x 10 ¹¹
A101B*	Xe	145	4 x 10 ¹¹
A76B*	Xe	145	4 x 10 ¹¹
B13A*	Xe	145	10 ¹²
AR1-17(1)*	Ar	60	2 x 10 ¹²
AR1-17(2)*	Xe	145	10 ¹³
AR1-17(4)*	Xe	75	10 ¹³
B13D*	Xe	145	10 ¹³
A102C*	Xe	145	10 ¹³

APPENDIX A (Cont'd)

Target Number	Ion Species	Energy (kV)	Fluence (#/cm ²)
B13D*	Xe	145	10 ¹³
B15D*	Xe	145	10 ¹³
B16A*	Ar	50	10 ¹²
B109D*	Ar	50	10 ¹²
B13A*	Ar	50	10 ¹²
105-7(1)*	Ar	50	10 ¹²
B109A*	Ar	50	10 ¹²
B13D*	Ar	50	10 ¹²
105-10(1)	Ar	40	10 ¹⁰
105-10(2)	Ar	40	10 ¹¹
105-10(3)	Ar	40	10 ¹²
105-10(4)	Ar	40	3 x 10 ¹²
105-7(4)	Ar	60	10 ¹²
105-7(3)	Ar	60	10 ¹²
101-32(1)	Ar	40	10 ¹¹
101-32(2)	Ar	40	10 ¹²
101-32(3)	Ar	40	3 x 10 ¹²
101-32(4)	Ar	40	10 ¹³
101-30(4)	Ar	40	3 x 10 ¹³
105-7(4)	Ar	40	10 ¹¹
105-7(3)	Ar	40	5 x 10 ¹¹
B110A	Ar	40	10 ¹¹
B121C	Ar	40	10 ¹¹

APPENDIX A (Cont'd)

Target Number	Ion Species	Energy (kV)	Fluence (#/cm ²)
101-24(1)	Ar	40	10^{11}
101-19(1)	Ar	30	10^{11}
101-23(1)	Ar	20	10^{11}
101-9(1)	Ar	20	10^{12}
101-9(4)	Ar	30	10^{11}
101-30(2)	Ar	30	10^{12}
107-5(1)	Ar	30	10^{11}
107-15(2)	Ar	30	10^{12}
107-17(1)	Ar	30	10^{13}
107-15(4)	Ar	30	10^{14}
107-17(4)	Kr	50	10^{11}
107-5(4)	Kr	50	10^{12}
107-17(2)	Kr	50	10^{13}
107-5(3)	Kr	50	10^{14}
B121B*	Kr	50	10^{11}
105-7(2)*	Kr	50	10^{12}
105-10(3)*	Kr	50	10^{11}
110-14(1)	Kr	110	10^{11}
110-14(2)	Kr	110	3×10^{10}
110-14(3)	Kr	110	10^{12}
110-14(4)	Kr	110	10^{13}
110-17(1)	Xe	145	3×10^{10}
110-17(2)	Xe	145	10^{11}

APPENDIX A (Cont'd)

Target Number	Ion Species	Energy (kV)	Fluence (#/cm ²)
110-17(3)	Xe	60	10 ¹²
110-17(4)	Xe	145	10 ¹³
110-5(1)	Ar	60	3 x 10 ¹⁰
110-5(2)	Ar	60	10 ¹¹
110-5(3)	Ar	60	10 ¹²
110-5(4)	Ar	60	10 ¹³
109-8(1)	Xe	60	3 x 10 ¹⁰
109-8(2)	Xe	60	10 ¹¹
109-8(3)	Xe	60	10 ¹²
109-8(4)	Xe	60	10 ¹³
109-22(1)	Xe	60	3 x 10 ¹⁰
	Ar	30	10 ¹²
109-22(2)	Xe	60	3 x 10 ¹⁰
	Ar	30	10 ¹³
109-22(3)	Xe	60	3 x 10 ¹¹
	Ar	30	10 ¹²
109-22(4)	Xe	60	3 x 10 ¹¹
	Ar	30	10 ¹³
109-19(1)	Ar	60	10 ¹²
	Xe	60	3 x 10 ¹⁰
109-19(2)	Ar	60	10 ¹²
	Xe	60	3 x 10 ¹¹
109-19(3)	Ar	60	10 ¹³
	Xe	60	3 x 10 ¹⁰

APPENDIX A (Cont'd)

Target Number	Ion Species	Energy (kV)	Fluence (#/cm ²)
109-19(4)	Ar	60	10^{13}
	Xe	60	3×10^{11}
101-23(3)	Xe	60	10^{13}
101-30(1)	Xe	60	10^{12}
101-23(2)	Xe	60	10^{11}
108-20(1)	Ar	30	10^{11}
108-20(2)	Ar	30	3×10^{11}
108-20(3)	Ar	30	10^{12}
108-20(4)	Ar	30	10^{13}
108-3(1)	Ar	30	10^{11}
108-3(2)	Ar	30	3×10^{11}
108-3(3)	Ar	30	10^{12}
108-3(4)	Ar	30	10^{13}
A206A	Ar	30	10^{11}
A206B	Ar	30	3×10^{11}
A206C	Ar	30	10^{12}
A206D	Ar	30	10^{13}
A208A	Ar	30	10^{11}
A208B	Ar	30	3×10^{11}
A208C	Ar	30	10^{12}
A208D	Ar	30	10^{13}
B2-9A	Ar	30	10^{11}
B2-9B	Ar	30	3×10^{11}
B2-9C	Ar	30	10^{12}
B2-9D	Ar	30	10^{13}

APPENDIX A (Cont'd)

Target Number	Ion Species	Energy (kV)	Fluence (#/cm ²)
101-23(4)	Kr	50	10 ¹³
101-30(3)	Kr	50	10 ¹²
101-9(2)	Kr	50	10 ¹¹
101-9(3)	Kr	50	3 x 10 ¹⁰
109-20(1)	Xe	145	3 x 10 ¹⁰
109-20(2)	Xe	145	10 ¹¹
109-20(3)	Xe	145	3 x 10 ¹¹
109-20(4)	Xe	145	10 ¹²
109-21(2)	Xe	145	10 ¹³
109-8(1)	Xe	60	3 x 10 ¹¹
109-8(2)	Xe	60	10 ¹²
109-8(4)	Xe	60	5 x 10 ¹³
107-15(4)	Ar	30	10 ¹³
107-17(1)	Ar	30	10 ¹⁴
110-5(2)	Ar	60	10 ¹³
110-5(3)	Ar	60	10 ¹⁴
108-27(1)	Ar	30	10 ¹¹
108-27(2)	Ar	30	3 x 10 ¹¹
108-27(3)	Ar	30	10 ¹²
108-27(4)	Ar	30	10 ¹³
108-9(1)	Ar	30	10 ¹¹
108-9(2)	Ar	30	3 x 10 ¹¹
108-9(3)	Ar	30	10 ¹²
108-9(4)	Ar	30	10 ¹³

APPENDIX A (Cont'd)

Target Number	Ion Species	Energy (kV)	Fluence (#/cm ²)
B2-5A	Ar	30	10^{12}
B2-1C	Ar	30	10^{12}
109-23(1)	Ar	30	3×10^{10}
109-23(2)	Ar	30	10^{11}
109-23(3)	Ar	30	3×10^{11}
109-23(4)	Ar	30	10^{12}
109-27(1)	Ar	30	10^{13}
109-27(2)	Ar	30	10^{14}
109-27(3)	Xe	30	10^{11}
109-27(4)	Xe	30	10^{11}
109-16(1)	Ar	30	10^{11}
109-16(2)	Ar	30	3×10^{11}
109-16(3)	Ar	30	10^{12}
109-16(4)	Ar	30	10^{13}
109-26(1)	Ar	30	10^{11}
109-26(2)	Ar	30	3×10^{11}
109-26(3)	Ar	30	10^{12}
109-26(4)	Ar	30	10^{13}
109-23(3)*	Ar	30	3×10^{11}
B2-5D*	Ar	30	10^{13}
109-23(2)*	Ar	30	10^{13}
109-23(1)*	Ar	60	3×10^{12}
B2-1B*	As	50	2×10^{14}
B2-5A*	Ar	30	10^{12}
B2-1C*	Ar	30	10^{12}

APPENDIX B

Processed archival planar diode substrates. Unless otherwise specified, starting material was 10-30 ohm-cm Monex <111> Si. Ion species indicated was implanted at energy and fluence listed to form diode. Oxide thickness noted was present during diode implant and anneal. Anneals were done in argon ambient for 1 hr unless otherwise noted. Letters or numbers in parentheses in anneal column indicate anneal of a single target segment with that designation. The "sc" in the anneal column means the target was slow-cooled at the end of the annealing cycle.

Target Number	Ion Species	Energy (kV)	Fluence (#/cm ²)	SiO ₂ (Å)	Anneal (°C)	Back Contact
A40	As	100	10^{13}	200/half		
A41	As	100	10^{13}	200/half		
A42	As	100	10^{14}	200/half		
A43	As	100	10^{14}	200/half		
A44	As	100	10^{15}	200/half		
A45	As	100	10^{15}	200/half		
A46	As	100	10^{13}	800		
A47	As	100	10^{13}	800		
A48	As	100	10^{14}	800	(a) 800°	
					(b) 900°	
					(c) 900°	
					(d) 900°	
A49	As	100	10^{14}	800	900°	

APPENDIX B (Cont'd)

Target Number	Ion Species	Energy (kV)	Fluence (#/cm ²)	SiO ₂ (Å)	Anneal (°C)	Back Contact
A50	As	100	10 ¹⁵	800	900°	
A51	As	100	10 ¹⁵	800	900°	
A52	As	100	10 ¹³	1400		
A53	As	100	10 ¹³	1400		
A54	As	100	10 ¹⁴	1400	(a) 800° (b) 800° (d) 800°	
A55	As	100	10 ¹⁴	1400		
A56	As	100	10 ¹⁵	1400	900°	
A57	As	100	10 ¹⁵	1400		
A58	As	100	10 ¹⁴	800	(a) 750° (b) 850°	
A59	As	100	10 ¹⁴	800	(a) 800° (b) 800°, 10 min. @ 950°	
A60	As	100	10 ¹⁴	800	900°	
A61	As	100	10 ¹⁴	800	900°	
A62	As	100	10 ¹⁴	800	900°	
A63	As	100	10 ¹⁴	800	900°C	
A64	As	100	10 ¹⁴	800	900°	
A65	As	100	10 ¹⁴	800	900°	
A66	As	100	10 ¹⁴	800	900°	
A67	As	100	10 ¹⁴	800	900°	
A68	As	100	10 ¹⁴	800	900°	
A69	As	100	10 ¹⁴	800	900°	

APPENDIX B (Cont'd)

Target Number	Ion Species	Energy (kV)	Fluence (#/cm ²)	SiO ₂ (Å)	Anneal (°C)	Back Contact
A70	As	100	10 ¹⁴	800	(a) 900° (b) 900°	10 ¹⁵ B ⁺ /cm ²
A71	As	100	10 ¹⁴	800	(a) 900° (b) 900°	10 ¹⁵ B ⁺ /cm ²
A72	As	100	10 ¹⁴	800	(a) 900° (b) 900°	10 ¹⁵ B ⁺ /cm ²
A73	As	100	10 ¹⁴	800	(a) 900° (b) 900° (c) 900°	10 ¹⁵ B ⁺ /cm ²
A74	As	100	10 ¹⁴	800	(a) 900° (b) 900° (c) 900°	10 ¹⁵ B ⁺ /cm ²
A75	As	100	10 ¹⁴	800	(a) 900° (b) 900° (c) 900°	10 ¹⁵ B ⁺ /cm ²
A76	As	100	10 ¹⁴	800	(a) 900° (b) 900° (c) 900°	10 ¹⁵ B ⁺ /cm ²
A77	As	100	10 ¹⁴	800	(a) 950°	10 ¹⁵ B ⁺ /cm ²
A78	No Diode				900°	10 ¹⁵ B ⁺ /cm ²
A79	No Diode				(a) 950° (b) 950°, 20 min (c) 950°, 20 min (d) 950°, 20 min	10 ¹⁵ B ⁺ /cm ²

APPENDIX B (Cont'd)

Target Number	Ion Species	Energy (kV)	Fluence (#/cm ²)	SiO ₂ (A)	Anneal (°C)	Back Contact
A80	No Diode				(a) 950° (b) 950°, 20 min (c) 950°, 20 min (d) 950°, 20 min	10^{15} B ⁺ /cm ²
A81	No Diode				(a) 950° (b) 950°, 20 min (c) 950°, 20 min (d) 950°, 20 min	10^{15} B ⁺ /cm ²
A82	No Diode				(a) 950° (b) 950°, 20 min (c) 950°, 20 min (d) 950°, 20 min	10^{15} B ⁺ /cm ²
A83	No Diode				(a) 950° (b) 950°, 20 min (c) 950°, 20 min (d) 950°, 20 min	10^{15} B ⁺ /cm ²

APPENDIX B (Cont'd)

Target Number	Ion Species	Energy (kV)	Fluence (#/cm ²)	SiO ₂ (Å)	Anneal (°C)	Back Contact
A84	No Diode				(a) 950°	10^{15} B ⁺ /cm ²
					(b) 950°, 20 min	
					(c) 950°, 20 min	
					(d) 950°, 20 min	
A85	No Diode				(a) 950°	10^{15} B ⁺ /cm ²
					(b) 950°, 20 min	
					(c) 950°, 20 min	
					(d) 950°, 20 min	
A86	As	100	10^{15}	800	900°	10^{15} B ⁺ /cm ²
A87	As	100	10^{13}	800	(a) 900°	10^{15} B ⁺ /cm ²
A88	As	100	10^{13}	800		10^{15} B ⁺ /cm ²
A89	As	100	10^{12}	800	(a) 900°	10^{15} B ⁺ /cm ²
A90	As	100	10^{12}	800		10^{15} B ⁺ /cm ²
A91	As	100	10^{15}	800	900°	10^{15} B ⁺ /cm ²
A100	As	100	10^{14}	1000		5×10^{14} B ⁺ /cm ²
A101	As	100	10^{14}	1000	900°	5×10^{14} B ⁺ /cm ²
A102	As	100	10^{14}	1000	900°	5×10^{14} B ⁺ /cm ²
A103	As	100	10^{14}	1000	900°	5×10^{14} B ⁺ /cm ²

APPENDIX B (Cont'd)

Target Number	Ion Species	Energy (kV)	Fluence (#/cm ²)	SiO ₂ (Å)	Anneal (°C)	Back Contact
A104	As	100	10 ¹⁴	1000	900°	5 x 10 ¹⁴ B ⁺ /cm ²
A105	As	100	10 ¹⁴	1000	900°	5 x 10 ¹⁴ B ⁺ /cm ²
A106	As	100	10 ¹⁴	1000	900°	5 x 10 ¹⁴ B ⁺ /cm ²
A107	As	100	10 ¹⁴	1000	900°	5 x 10 ¹⁴ B ⁺ /cm ²
A108	As	100	10 ¹⁴	1000	900°	5 x 10 ¹⁴ B ⁺ /cm ²
A109	As	100	10 ¹⁴	1000	900°	5 x 10 ¹⁴ B ⁺ /cm ²
A78	Xe	30	10 ¹⁵	-		
	As	100	2x10 ¹⁴	800		
105-7	P	80	10 ¹²	1000	1100°, O ₂	POCl
	As	100	2x10 ¹⁴	800		
105-10	P	80	10 ¹²	1000	1100°, O ₂	POCl
	As	100	2x10 ¹⁴	800		
104-12	P	80	10 ¹²	1000	1100°, O ₂	POCl
	As	100	2x10 ¹⁴	800		
101-21	P	80	10 ¹²	1000	1100°, O ₂	POCl
	As	100	10 ¹³	800	900°	
101-24	P	80	10 ¹²	1000	1100°, O ₂	POCl
	As	100	10 ¹⁴	800	900°	
101-19	P	80	10 ¹²	1000	1100°, O ₂	POCl
	As	100	10 ¹⁴	800	900°	

APPENDIX B (Cont'd)

Target Number	Ion Species	Energy (kV)	Fluence (#/cm ²)	SiO ₂ (Å)	Anneal (°C)	Back Contact
Bar-1	P	80	10 ¹²	1000	1100°, O ₂	POCl
	As	100	10 ¹⁴	800	900°	
	P	80	10 ¹²	1000	1100°, O ₂	POCl
		100	5x10 ¹⁴	800	900°	
	P	80	10 ¹²	1000	1100°, O ₂	POCl
		100	5x10 ¹⁴	800	900°	
	P	80	10 ¹²	1000	1100°, O ₂	POCl
		100	5x10 ¹⁴	800	900°	
101-23	P	80	10 ¹²	1000	1100°, O ₂	POCl
	As	100	5x10 ¹⁴	800	900°	
	P	80	10 ¹²	1000	1100°, O ₂	POCl
	As	100	5x10 ¹⁴	80	900°	
101-30	P	80	10 ¹²	1000	1100°, O ₂	POCl
	As	100	5x10 ¹⁴	80	900°	
	P	80	10 ¹²	1000	1100°, O ₂	POCl
		100	5x10 ¹⁴	80	(1) 900° (3) 1000°	
101-15	P	80	10 ¹²	1000	1100°, O ₂	POCl
	As	100	5x10 ¹⁴	80	(1) 900° (3) 1000°	
B10	B	50	10 ¹⁴	2600	900°	10 ¹⁵ As ⁺ /cm ²
B11	B	50	10 ¹⁴	2600	900°	10 ¹⁵ As ⁺ /cm ²
B12	B	50	10 ¹⁴	2600	900°	10 ¹⁵ As ⁺ /cm ²
B13	B	50	10 ¹⁴	2600	900°	10 ¹⁵ As ⁺ /cm ²

APPENDIX B (Cont'd)

Target Number	Ion Species	Energy (kV)	Fluence (#/cm²)	SiO₂ (Å)	Anneal (°C)	Back Contact
B14	B	50	10 ¹⁴	2600	900°	10 ¹⁵ As ⁺ /cm ²
B15	B	50	10 ¹⁴	2600	900°	10 ¹⁵ As ⁺ /cm ²
B16	B	50	10 ¹⁴	2600	900°	10 ¹⁵ As ⁺ /cm ²
B17	No Diode			(a)	950°	10 ¹⁵ As ⁺ /cm ²
				(b)	950°, 20 min	
				(c)	950°, 20 min	
				(d)	950°, 20 min	
B18	No Diode			(a)	950°	10 ¹⁵ As ⁺ /cm ²
				(b)	950°, 20 min	
				(c)	950°, 20 min	
				(d)	950°, 20 min	
B19	No Diode			(a)	950°	10 ¹⁵ As ⁺ /cm ²

APPENDIX B (Cont'd)

Target Number	Ion Species	Energy (kV)	Fluence (#/cm²)	SiO₂ (A)	Anneal (°C)	Back Contact
B19	No Diode				(b) 950°, 20 min (c) 950°, 20 min (d) 950°, 20 min	
B20	No Diode				(a) 950° 10 ¹⁵ As ⁺ /cm ² (b) 950°, 20 min (c) 950°, 20 min (d) 950°, 20 min	
B21	No Diode				(a) 950° 10 ¹⁵ As ⁺ /cm ² (b) 950°, 20 min (c) 950°, 20 min (d) 950°, 20 min	
B22	No Diode				(a) 950° 10 ¹⁵ As ⁺ /cm ²	

APPENDIX B (Cont'd)

Target Number	Ion Species	Energy (kV)	Fluence (#/cm ²)	SiO ₂ (Å)	Anneal (°C)	Back Contact
B22	No Diode				(b) 950°, 20 min (c) 950°, 20 min (d) 950°, 20 min	
B23	No Diode				(a) 950° 10^{15} As^+/cm^2 (b) 950°, 20 min (c) 950°, 20 min (d) 950°, 20 min	
B33	B	50	10^{15}	2000	900°	10^{15} As^+/cm^2
B34	B	50	10^{15}	3000	900°	10^{15} As^+/cm^2
B35	B	50	10^{14}	2600	900°	10^{15} As^+/cm^2
B36	B	50	10^{13}	2600	900°	10^{15} As^+/cm^2
B100	B	50	10^{15}	2600		5×10^{14} As^+/cm^2
B101	B	50	10^{15}	2600		5×10^{14} As^+/cm^2

APPENDIX B (Cont'd)

Target Number	Ion Species	Energy (kV)	Fluence (#/cm ²)	SiO ₂ (Å)	Anneal (°C)	Back Contact
B102	B	50	10 ¹⁵	2600		5 x 10 ¹⁴ As ⁺ /cm ²
B103	B	50	10 ¹⁵	2600		5 x 10 ¹⁴ As ⁺ /cm ²
B104	B	50	10 ¹⁵	2600		5 x 10 ¹⁴ As ⁺ /cm ²
B105	B	50	10 ¹⁵	2600		5 x 10 ¹⁴ As ⁺ /cm ²
B106	B	50	10 ¹⁵	2600		5 x 10 ¹⁴ As ⁺ /cm ²
B107	B	50	10 ¹⁵	2600	900°	5 x 10 ¹⁴ As ⁺ /cm ²
B108	B	50	10 ¹⁵	2600		5 x 10 ¹⁴ As ⁺ /cm ²
B109	B	50	10 ¹⁵	2600	900°	5 x 10 ¹⁴ As ⁺ /cm ²
B110α	B	50	10 ¹⁵	1000		10 ¹⁵ As ⁺ /cm ²
B111α	B	50	10 ¹⁵	4000		10 ¹⁵ As ⁺ /cm ²
AR1-1	As	100	2x10 ¹⁴	1000		POCl
AR1-2	As	100	2x10 ¹⁴	1000		POCl
AR1-3	As	100	2x10 ¹⁴	1000		POCl
AR1-4	As	100	2x10 ¹⁴	1000		POCl
AR1-5	As	100	2x10 ¹⁴	1000		POCl
AR1-6	As	100	2x10 ¹⁴	1000		POCl
AR1-7	As	100	2x10 ¹⁴	1000	900°	POCl

APPENDIX B (Cont'd)

Target Number	Ion Species	Energy (kV)	Fluence (#/cm ²)	SiO ₂ (Å)	Anneal (°C)	Back Contact
ARl-8	As	100	2x10 ¹⁴	1000	900°	POCl
ARl-9	As	100	2x10 ¹⁴	1000	900°	POCl
ARl-10	As	100	2x10 ¹⁴	1000	900°	POCl
ARl-11	As	100	2x10 ¹⁴	1000		POCl
ARl-12	As	100	2x10 ¹⁴	1000	900°	POCl
ARl-13	As	100	2x10 ¹⁴	1000	900°	POCl
ARl-14	As	100	2x10 ¹⁴	1000	900°	POCl
ARl-15	As	100	2x10 ¹⁴	1000	900°	POCl
ARl-16	As	100	2x10 ¹⁴	1000	900°	POCl
ARl-17	As	100	2x10 ¹⁴	1000	900°	POCl
ARl-18	As	100	2x10 ¹⁴	1000		POCl
ARl-19	As	100	2x10 ¹⁴	1000		POCl
ARl-20	As	100	2x10 ¹⁴	1000	900°	POCl
ARl-21	As	100	2x10 ¹⁴	1000	900°	POCl
B110	B	50	10 ¹³	2600	900°	10 ¹⁵ As ⁺ /cm ²
B111	B	50	10 ¹⁴	2600	900°	10 ¹⁵ As ⁺ /cm ²
B112	B	50	10 ¹⁵	2600	900°	10 ¹⁵ As ⁺ /cm ²
B113	B	50	10 ¹⁵	2600	900°	10 ¹⁵ As ⁺ /cm ²
B114	B	50	10 ¹⁵	2600		10 ¹⁵ As ⁺ /cm ²
B115	B	50	10 ¹⁵	2600		10 ¹⁵ As ⁺ /cm ²

APPENDIX B (Cont'd)

Target Number	Ion Species	Energy (kV)	Fluence (#/cm ²)	SiO ₂ (Å)	Anneal (°C)	Back Contact
B116	B	50	10 ¹⁵	2600		10 ¹⁵ As ⁺ /cm ²
B117	B	50	10 ¹⁵	2600		10 ¹⁵ As ⁺ /cm ²
B118	B	50	10 ¹⁵	2600		10 ¹⁵ As ⁺ /cm ²
B119	B	50	10 ¹⁵	2600		10 ¹⁵ As ⁺ /cm ²
B120	B	50	10 ¹²	2600		10 ¹⁵ As ⁺ /cm ²
	B	50	10 ¹³	2600	900°	
B121	B	50	10 ¹²	2600		10 ¹⁵ As ⁺ /cm ²
	B	50	10 ¹⁴	2600	900°	
B122	B	50	10 ¹²	2600		10 ¹⁵ As ⁺ /cm ²
	B	50	10 ¹⁵	2600	900°	
B123	B	50	10 ¹²	2600		10 ¹⁵ As ⁺ /cm ²
	B	50	10 ¹⁵	2600	900°	
B124	B	50	10 ¹²	2600		10 ¹⁵ As ⁺ /cm ²
	B	50	10 ¹⁵	2600	900°	
B125	B	50	10 ¹²	2600		10 ¹⁵ As ⁺ /cm ²
	B	50	10 ¹⁵	2600		

APPENDIX B (Cont'd)

Target Number	Ion Species	Energy (kV)	Fluence (#/cm ²)	SiO ₂ (Å)	Anneal (°C)	Back Contact
B126	B	50	10 ¹²	2600		10 ¹⁵ As ⁺ /cm ²
	B	50	10 ¹⁵	2600		
B127	B	50	10 ¹²	2600		10 ¹⁵ As ⁺ /cm ²
	B	50	10 ¹⁵	2600		
B128	B	50	10 ¹²	2600		10 ¹⁵ As ⁺ /cm ²
	B	50	10 ¹⁵	2600		
B129	B	50	10 ¹²	2600		10 ¹⁵ As ⁺ /cm ²
	B	50	10 ¹⁵	2600		
AR2-1	B	50	10 ¹²	2600	900°	10 ¹⁵ As ⁺ /cm ²
	B	50	10 ¹⁵	2600		
AR2-2	B	50	10 ¹²	2600		10 ¹⁵ As ⁺ /cm ²
	B	50	10 ¹⁵	2600		
AR2-3	B	50	10 ¹²	2600		10 ¹⁵ As ⁺ /cm ²
	B	50	10 ¹⁵	2600		
AR2-4	B	50	10 ¹²	2600		10 ¹⁵ As ⁺ /cm ²
	B	50	10 ¹⁵	2600		
AR2-5	B	50	10 ¹²	2600		10 ¹⁵ As ⁺ /cm ²
	B	50	10 ¹⁵	2600		
AR2-6	B	50	10 ¹²	2600		10 ¹⁵ As ⁺ /cm ²
	B	50	10 ¹⁵	2600		

APPENDIX B (Cont'd)

Target Number	Ion Species	Energy (kV)	Fluence (#/cm ²)	SiO ₂ (Å)	Anneal (°C)	Back Contact
AR2-6	B	50	10 ¹⁵	2600		
AR2-7	B	50	10 ¹²	2600		10 ¹⁵ As ⁺ /cm ²
	B	50	10 ¹⁵	2600		
AR2-8	B	50	10 ¹²	2600		10 ¹⁵ As ⁺ /cm ²
	B	50	10 ¹⁵	2600		
AR2-9	B	50	10 ¹²	2600		10 ¹⁵ As ⁺ /cm ²
	B	50	10 ¹⁵	2600		
AR2-10	B	50	10 ¹²	2600		10 ¹⁵ As ⁺ /cm ²
	B	50	10 ¹²	2600		10 ¹⁵ As ⁺ /cm ²
AR2-11	B	50	10 ¹²	2600		10 ¹⁵ As ⁺ /cm ²
	B	50	10 ¹²	2600		10 ¹⁵ As ⁺ /cm ²
AR2-12	B	50	10 ¹²	2600		10 ¹⁵ As ⁺ /cm ²
	B	50	10 ¹⁵	2600		
AR2-13	B	50	10 ¹²	2600		10 ¹⁵ As ⁺ /cm ²
	B	50	10 ¹⁵	2600		
AR2-14	B	50	10 ¹²	2600		10 ¹⁵ As ⁺ /cm ²
	B	50	10 ¹⁵	2600		
AR2-15	B	50	10 ¹²	2600		10 ¹⁵ As ⁺ /cm ²
	B	50	10 ¹⁵	2600		

APPENDIX B (Cont'd)

Target Number	Ion Species	Energy (kV)	Fluence (#/cm ²)	SiO ₂ (Å)	Anneal (°C)	Back Contact
AR2-16	B	50	10 ¹²	2600		10 ¹⁵ As ⁺ /cm ²
	B	50	10 ¹⁵	2600		
AR2-17	B	50	10 ¹²	2600		10 ¹⁵ As ⁺ /cm ²
	B	50	10 ¹⁵	2600		
107-18	P	80	10 ¹²	1000	1100°, O ₂	POCl
	As	100	5x10 ¹⁴	800	900°, N ₂	
107-19	P	80	10 ¹²	1000	1100°, O ₂	POCl
	As	30	2x10 ¹⁴	800	900°, N ₂	
107-20	P	80	10 ¹²	1000	1100°, O ₂	POCl
	As	30	2x10 ¹⁴	800	900°, N ₂	
108-3	P	80	10 ¹²	1000	1100°, O ₂	POCl
	As	100	5x10 ¹⁴	800	900°, N ₂	
Bar-2	P	80	10 ¹²	1000	1100°, O ₂	POCl
	As	100	5x10 ¹⁴	800	900°, N ₂	
108-5	P	80	10 ¹²	1000	1100°, O ₂	POCl
	As	100	5x10 ¹⁴	800	900°, N ₂	
108-9	P	80	10 ¹²	1000	1100°, O ₂	POCl
	As	100	5x10 ¹⁴	800	900°, N ₂	
108-14	P	80	10 ¹²	1000	1100°, O ₂	POCl
	As	100	5x10 ¹⁴	800		
108-19	P	80	10 ¹²	1000	1100°, O ₂	POCl
	As	100	5x10 ¹⁴	800		
108-20	P	80	10 ¹²	1000	1100°, O ₂	POCl
	As	30	2x10 ¹⁴	800	900°, N ₂	

APPENDIX B (Cont'd)

Target Number	Ion Species	Energy (kV)	Fluence (#/cm ²)	SiO ₂ (Å)	Anneal (°C)	Back Contact
108-24	P	80	10 ¹²	1000	1100°, O ₂	POCl
	As	30	2x10 ¹⁴	800		
108-26	P	80	10 ¹²	1000	1000°, O ₂	POCl
	As	30	2x10 ¹⁴	800		
108-27	P	80	10 ¹²	1000	1000°, O ₂	POCl
	As	30	2x10 ¹⁴	800	1000°, N ₂	
A200	As	100	10 ¹⁴			
	As	40	10 ¹⁴		900°, sc	
A201	As	100	10 ¹⁵			
	As	40	10 ¹⁵		900°, sc	
A202	As	40	10 ¹⁴		900°, sc	
A203	As	40	10 ¹⁵		900°, sc	
A204	As	100	10 ¹⁴			
A205	As	100	10 ¹⁵			
A206*	As	100	10 ¹⁴			
	As	40	10 ¹⁴		900°, sc	
A207*	As	100	10 ¹⁴			
	As	40	10 ¹⁴			
A208*	As	100	10 ¹⁵			
	As	40	10 ¹⁵		900°, sc	
A209*	As	100	10 ¹⁵			
	As	40	10 ¹⁵			

*Starting material was 400 Ω-cm <111>
Monex Si

APPENDIX B (Cont'd)

Target Number	Ion Species	Energy (kv)	Fluence (#/cm ²)	SiO ₂ (A)	Anneal (°C)	Back Contact
A210*	As	40	10 ¹⁴		900°,sc	
A211*	As	40	10 ¹⁴			
A212*	As	40	10 ¹⁵		900°,sc	
A213*	As	40	10 ¹⁵			
A214*	As	100	10 ¹⁴			
A215*	As	100	10 ¹⁴			
A216*	As	100	10 ¹⁵			
A217*	As	100	10 ¹⁵			
109-23	P	80	10 ¹²	1000	1100°,O ₂	POCl
	As	100	10 ¹⁴			
	As	40	10 ¹⁴		900°,sc	
109-26	P	80	10 ¹²	1000	1100°,O ₂	POCl
	As	100	10 ¹⁴			
	As	40	10 ¹⁴		900°,sc	
109-29	P	80	10 ¹²	1000	1100°,O ₂	POCl
	As	40	10 ¹⁵		900°,sc	
109-27	P	80	10 ¹²	1000	1100°,O ₂	POCl
	As	100	10 ¹⁵			
	As	100	10 ¹⁵			
	As	40	10 ¹⁵		900°,sc	
109-16	P	80	10 ¹²	1000	1100°,O ₂	POCl
	As	40	10 ¹⁵		900°,sc	
109-33	P	80	10 ¹²	1000	1100°,O ₂	POCl
	P	100	10 ¹⁴		900°,sc	

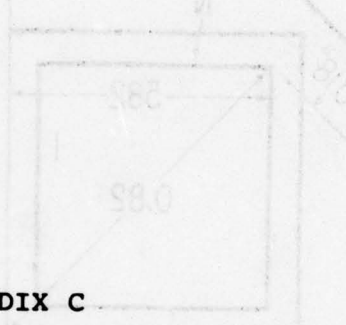
*Starting material was 400 Ω-cm <111>
Monex Si

APPENDIX B (Cont'd)

Target Number	Ion Species	Energy (kV)	Fluence (#/cm ²)	SiO ₂ (Å)	Anneal (°C)	Back Contact
109-13	P	80	10 ¹²	1000	1100°, O ₂	POCl
	P	100	10 ¹⁴		900°, sc	
109-25	P	80	10 ¹²	1000	1100°, O ₂	POCl
	P	100	10 ¹⁵		900°, sc	
109-30	P	80	10 ¹²	1000	1100°, O ₂	POCl
	P	100	10 ¹⁵		900°, sc	
112-25	P	80	10 ¹²	1000	1100°, O ₂	POCl
	P	100	10 ¹⁴			
112-9	P	80	10 ¹²	1000	1100°, O ₂	POCl
	P	100	10 ¹⁴			
112-7	P	80	10 ¹²	1000	1100°, O ₂	POCl
	P	100	10 ¹⁵			
112-22	P	80	10 ¹²	1000	1100°, O ₂	POCl
	P	100	10 ¹⁵			
B2-1	B	50	10 ¹⁵	2500	900°, sc	10 ¹⁵ P ⁺ /cm ²
B2-2	B	50	10 ¹⁵	2500	900°, sc	10 ¹⁵ P ⁺ /cm ²
B2-3	B	50	3x10 ¹⁵	2500		10 ¹⁵ P ⁺ /cm ²
B2-4	B	50	3x10 ¹⁵	2500	900°, sc	10 ¹⁵ P ⁺ /cm ²
B2-5	B	50	3x10 ¹⁵	2500		10 ¹⁵ P ⁺ /cm ²
	B	100	3x10 ¹⁴		900°, sc	
B2-6	B	50	3x10 ¹⁵	2500		10 ¹⁵ P ⁺ /cm ²
	B	100	3x10 ¹⁴		900°, sc	
B2-7	B	50	3x10 ¹⁵	2500		10 ¹⁵ P ⁺ /cm ²
	B	100	3x10 ¹⁴			

APPENDIX B (Cont'd)

TAJF



APPENDIX C

**(MASKS USED FOR TARGET FABRICATION
(SEE SECT. III))**

Below is shown a no enlarged sketch to show what appears
occurring just off axis of source if source is

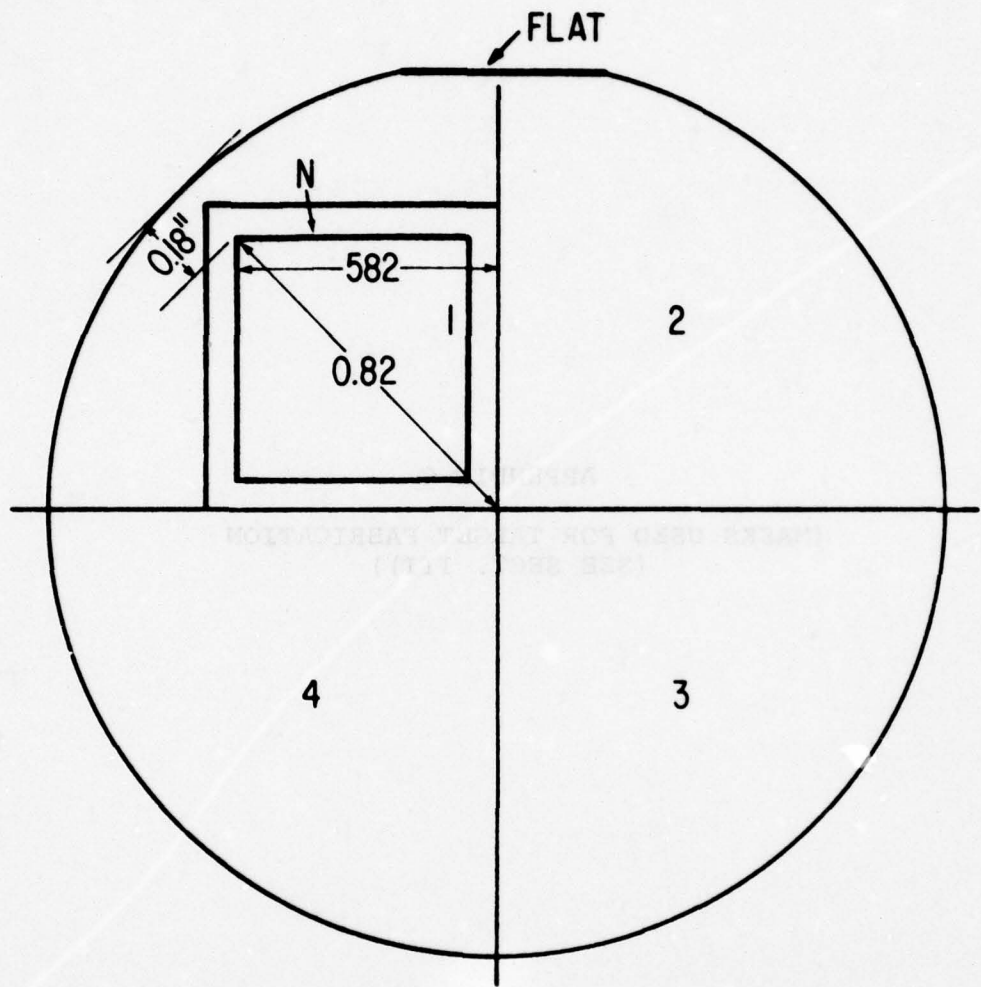


Figure 131. Layout of Target Segments on a Whole Si Wafer Is Shown. Segment 3 contains the test pattern.

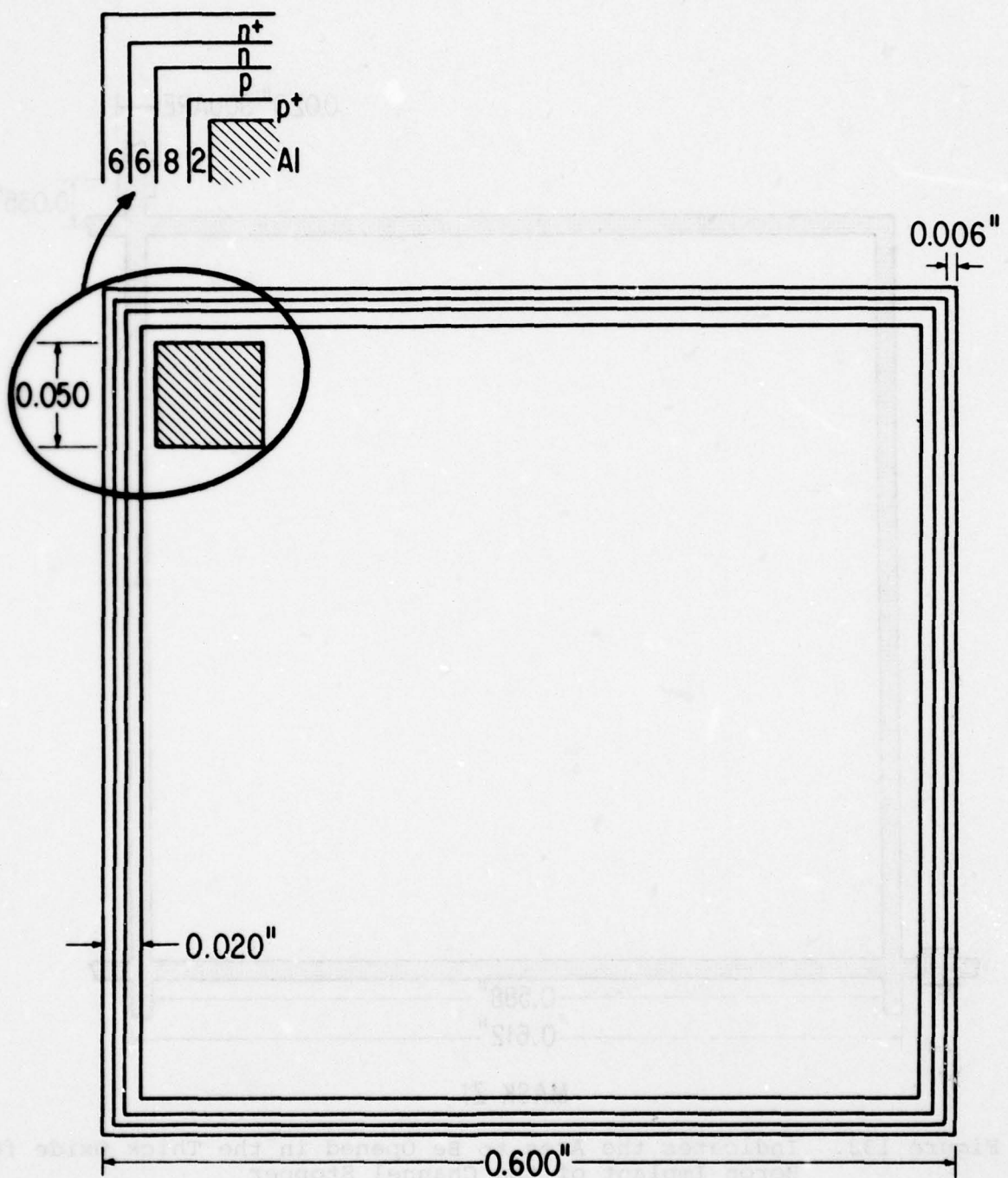


Figure 132. Diagram Indicates the Width of the Various Bands at the Target Edge

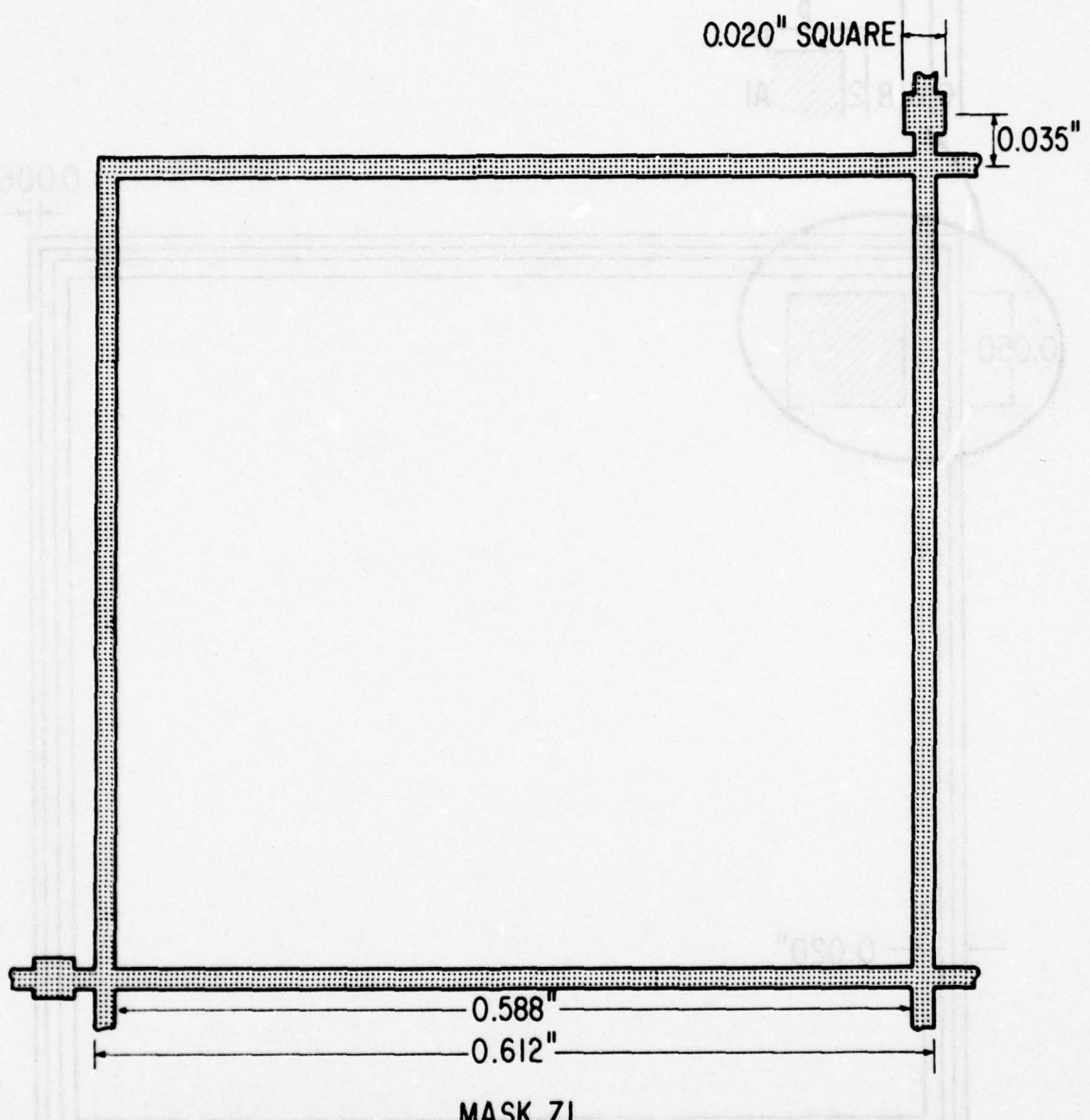
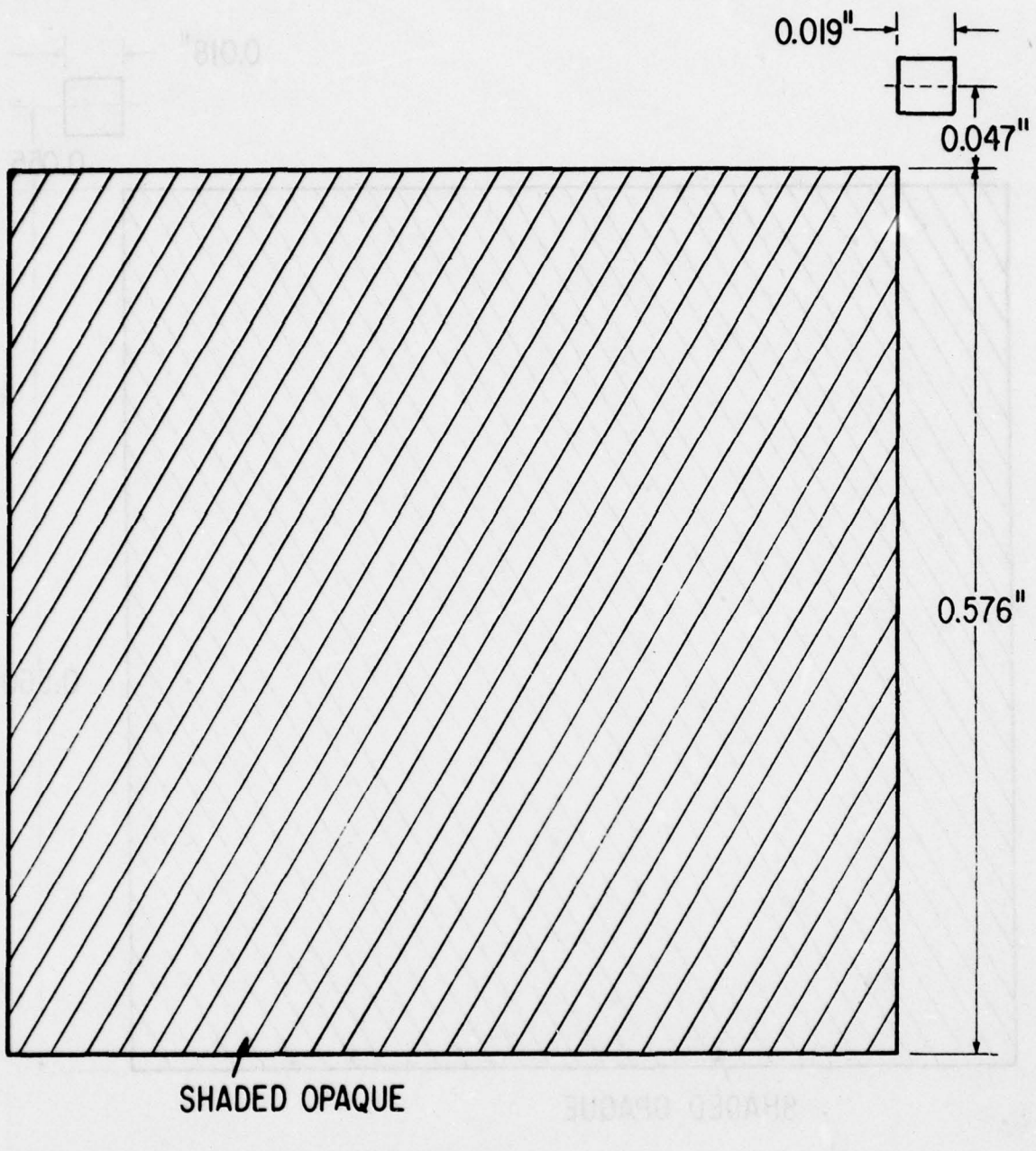
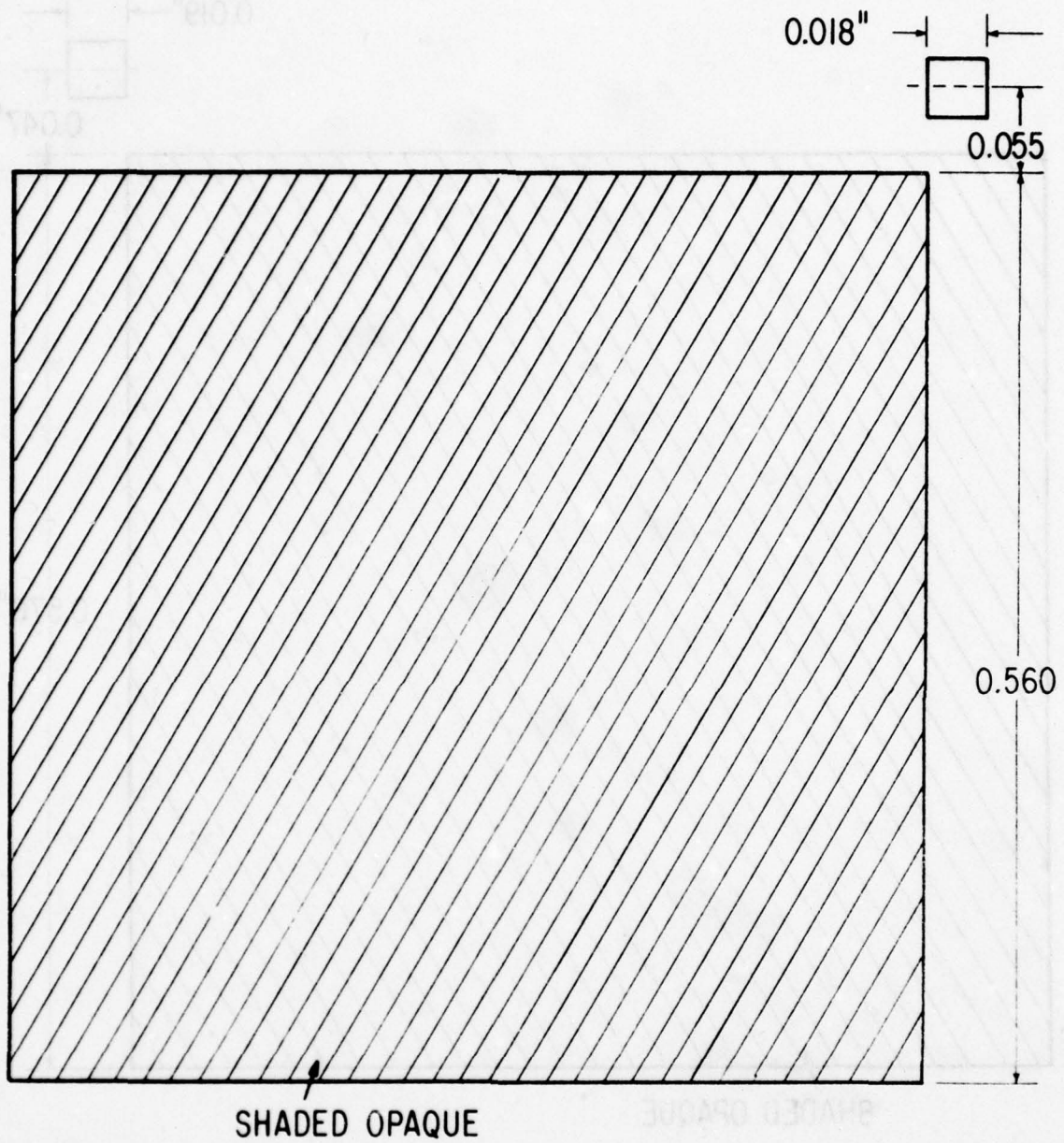


Figure 133. Indicates the Area to Be Opened in the Thick Oxide for Boron Implant of the Channel Stopper



MASK Z2

Figure 134. Indicates the Area to Be Opened in the Thick Oxide for the n-Field Implant



MASK Z3

Figure 135. Is Used to Clear the Oxide in the Field Through Which the Heavier Dose Field Implant Is Performed

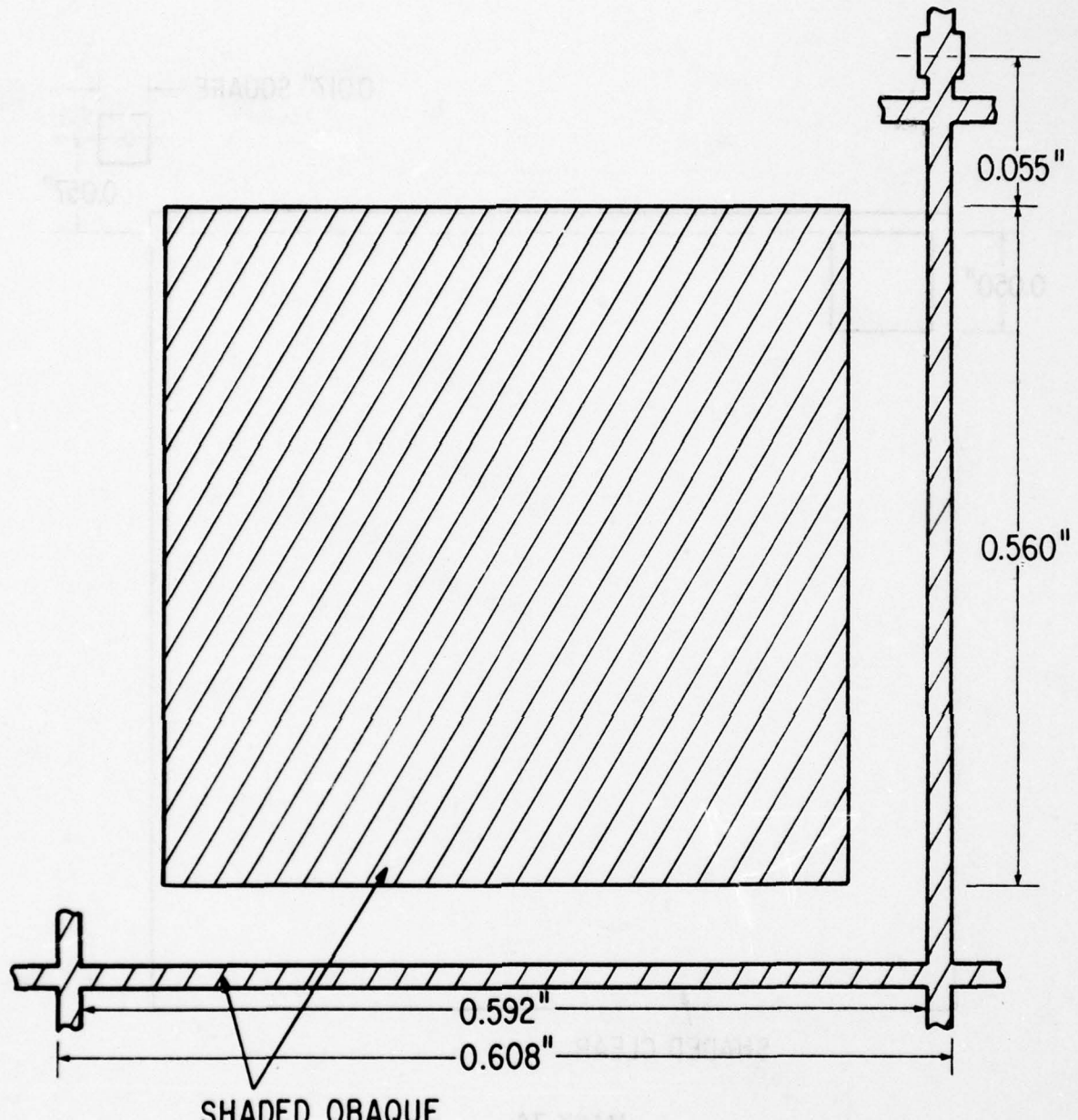
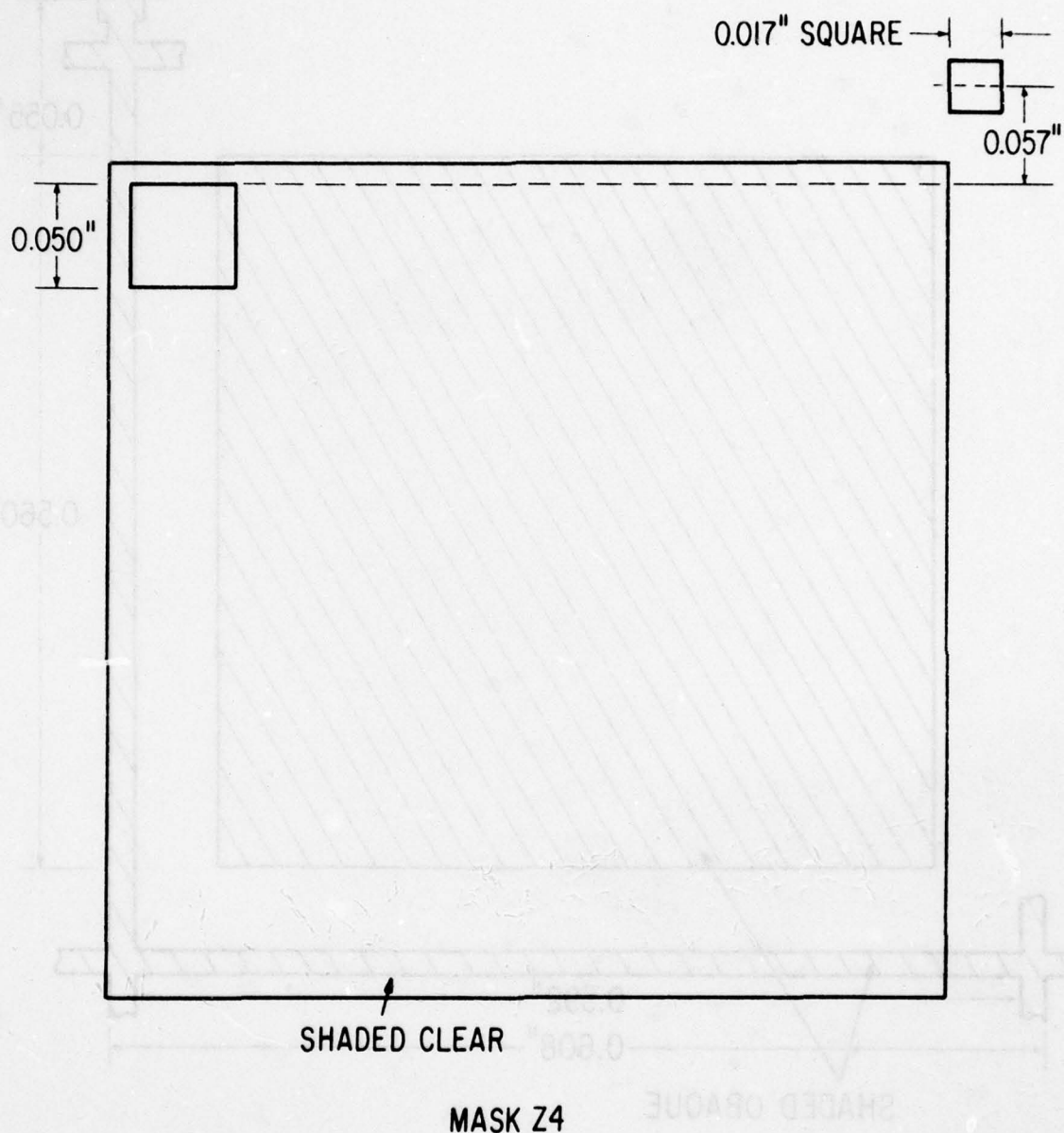
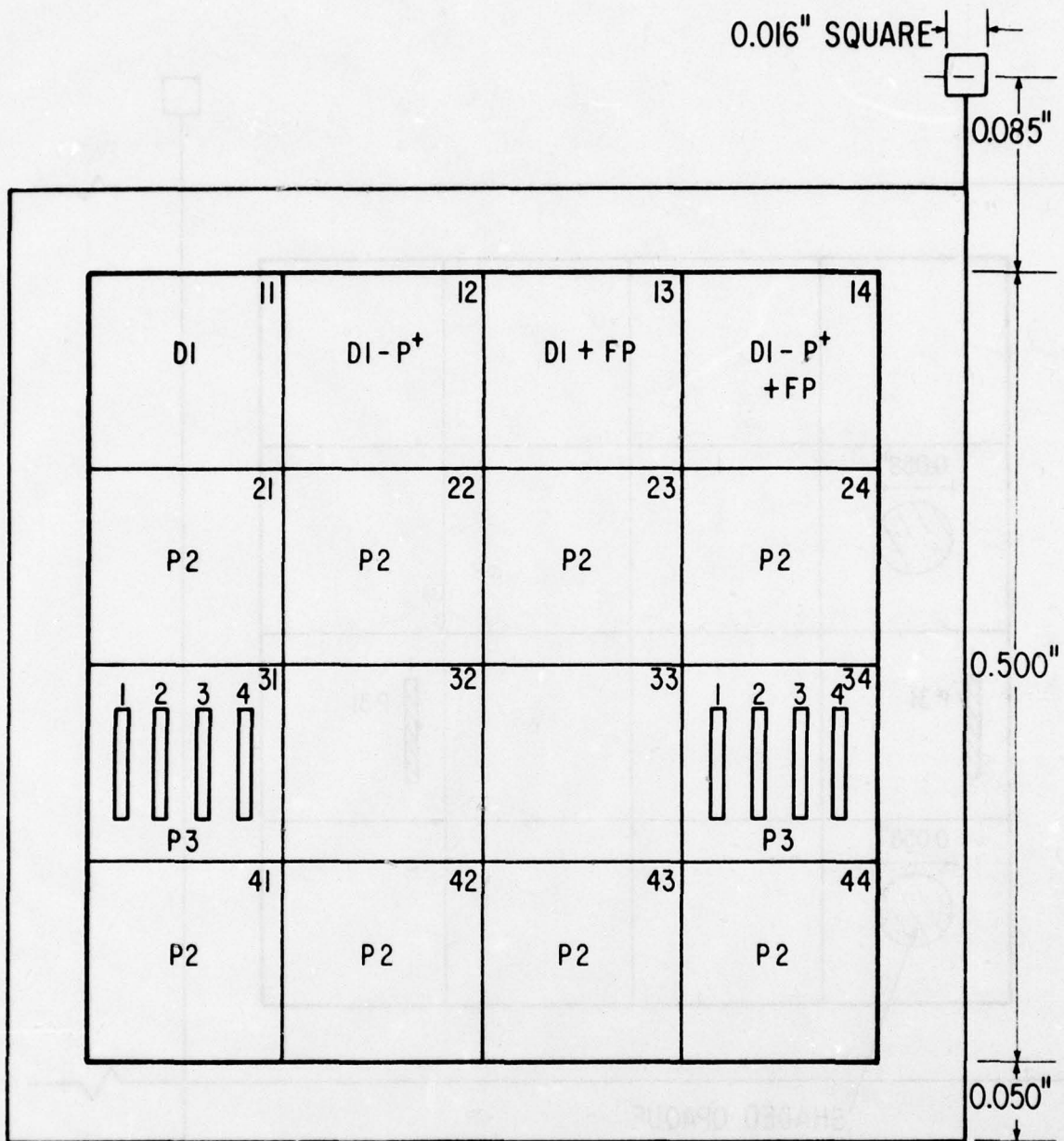


Figure 136. Is Used to Open Up the Field and Scribe Lanes



MASK Z4

Figure 137. Is Used to Pattern the Front Aluminum to Provide a Contact Pad



TEST STRUCTURE LAYOUT

Figure 138. Quadrant 3 Test Structure Layout Is Shown Indicating Bar Patterns for Writing Experiments

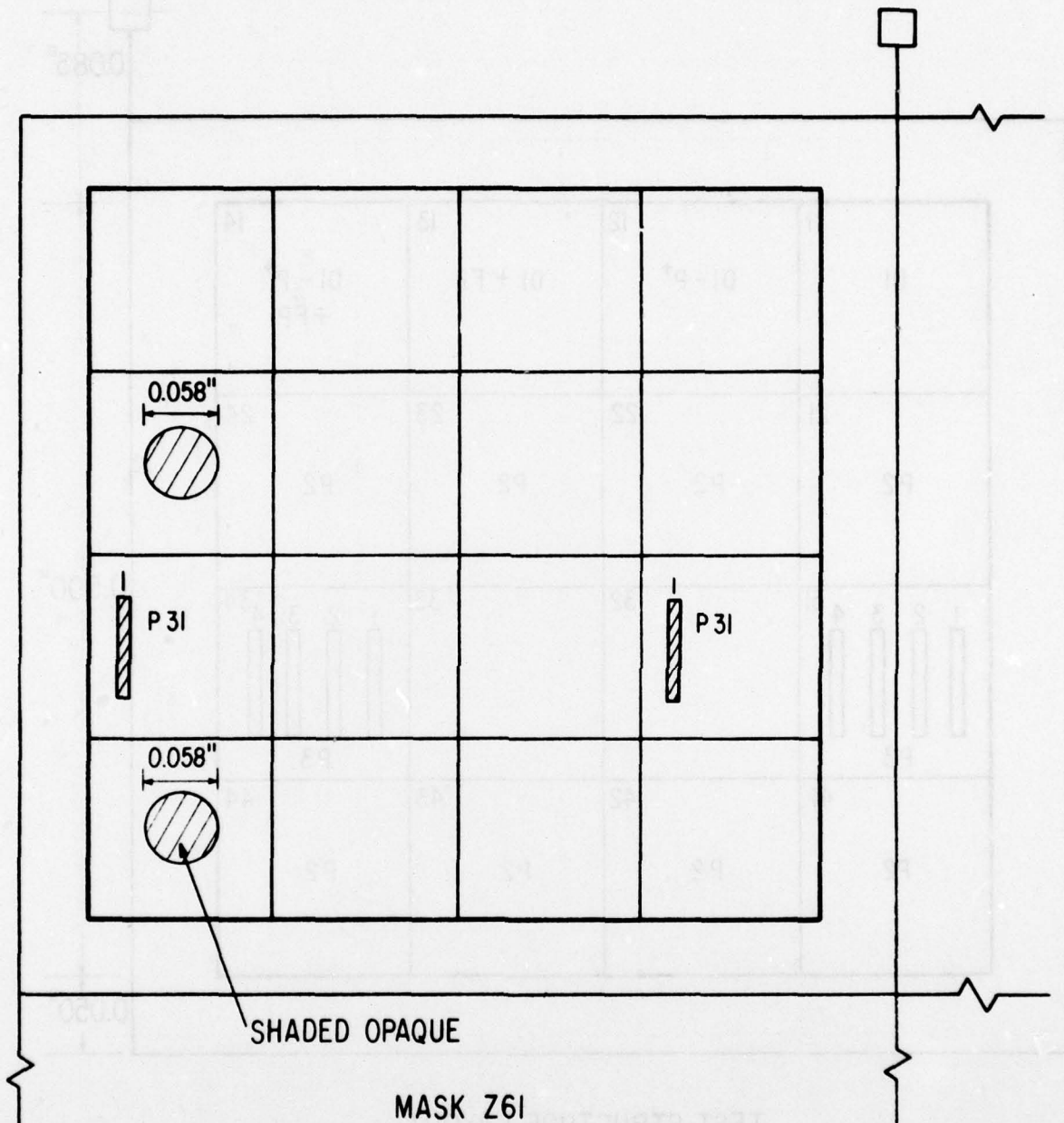
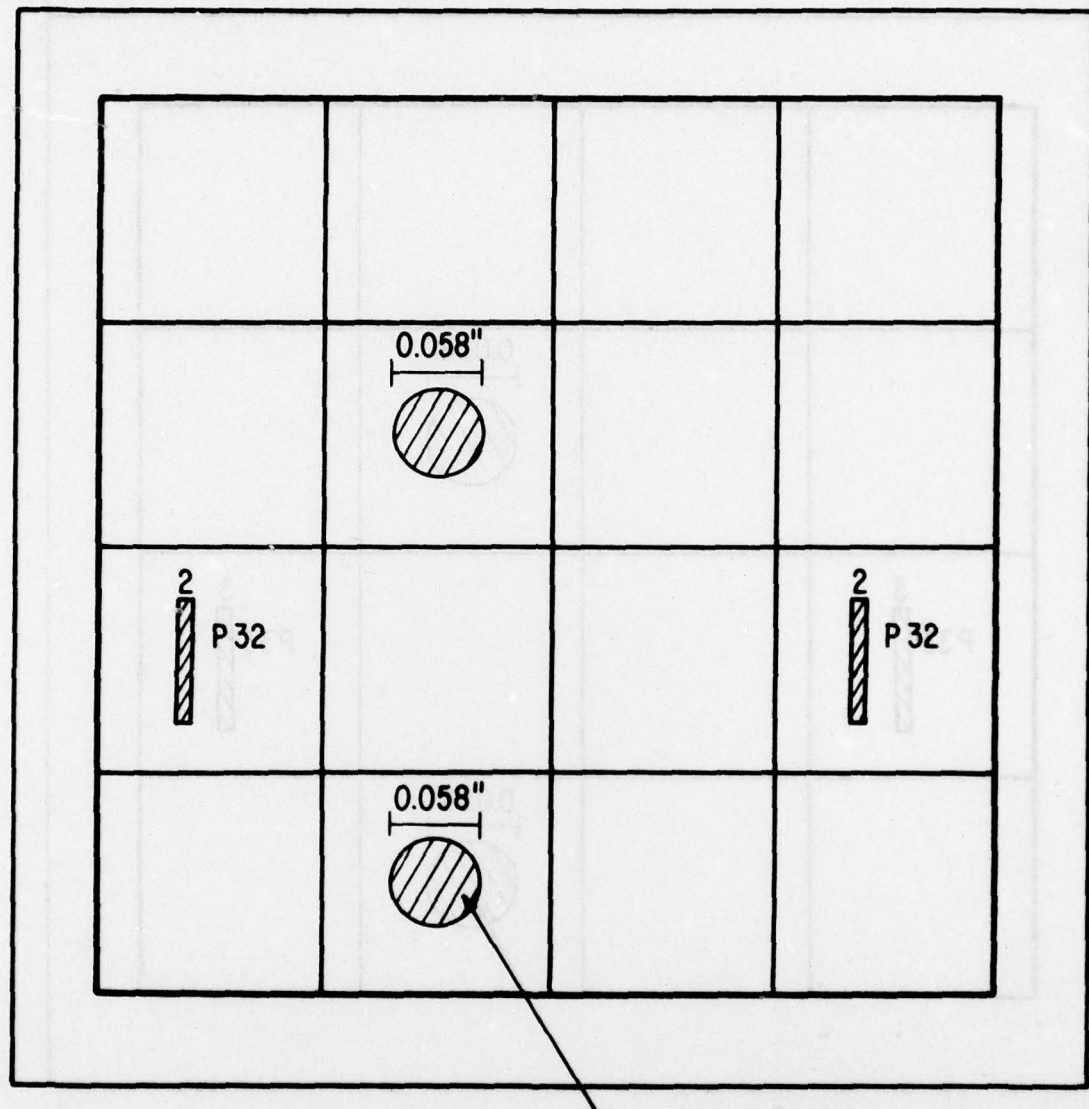
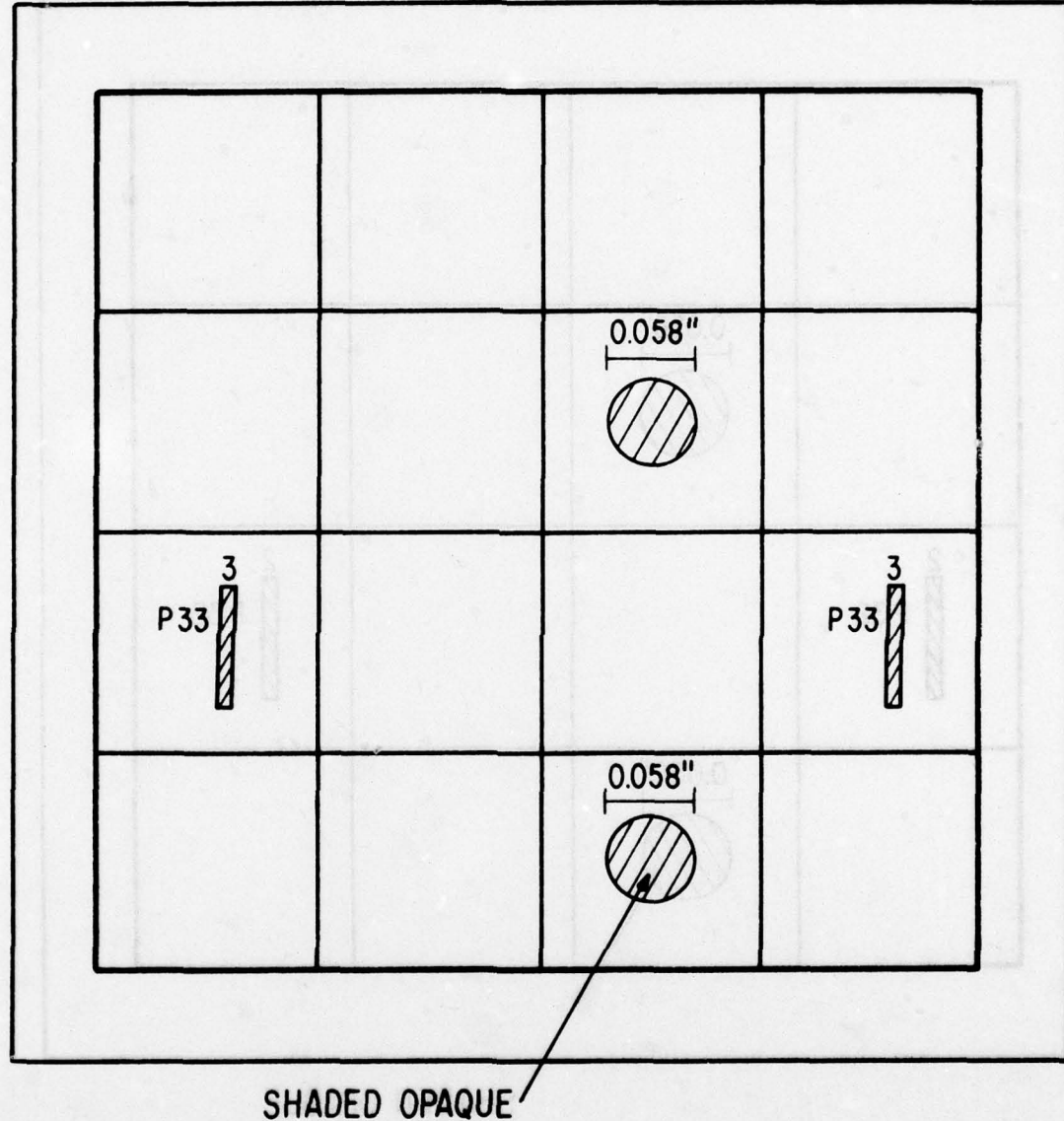


Figure 139. Is Used to Open Up Areas in the Resist for Ion Writing Experiments



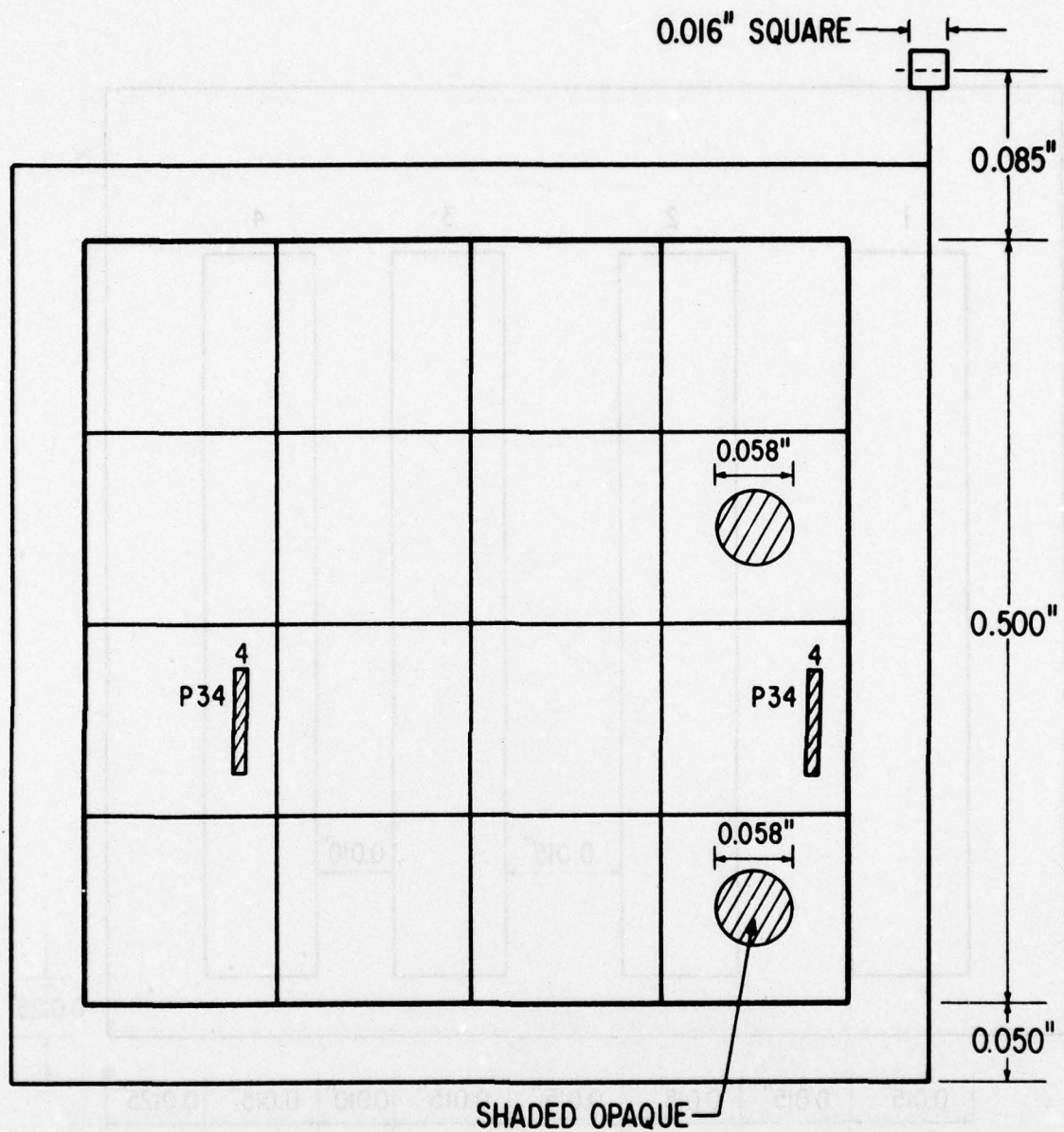
MASK Z62

Figure 140. Is Used to Open Up Areas in the Resist for Ion Writing Experiments



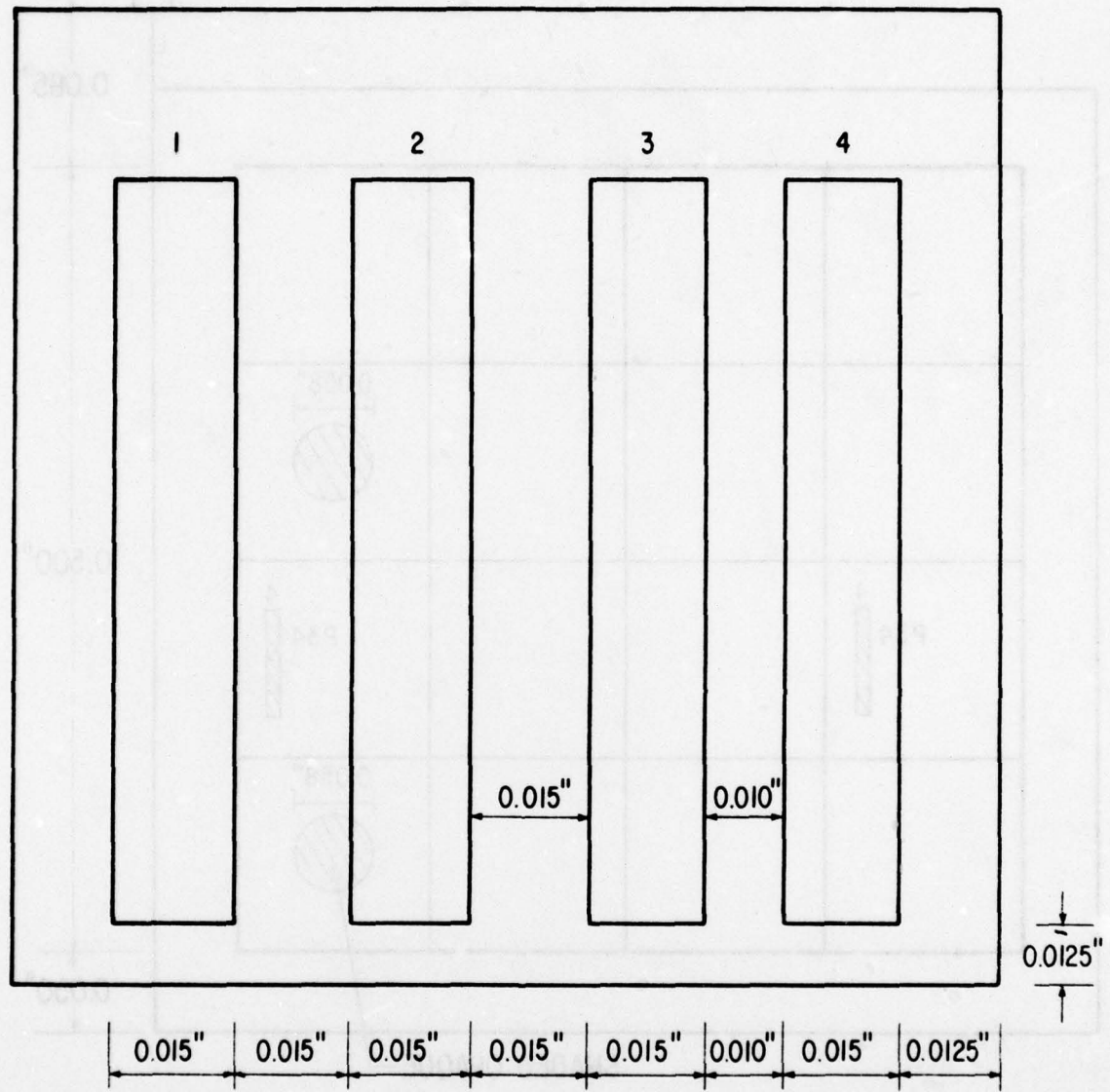
MASK Z63

Figure 141. Is Used to Open Up Areas in the Resist for Ion Writing Experiments



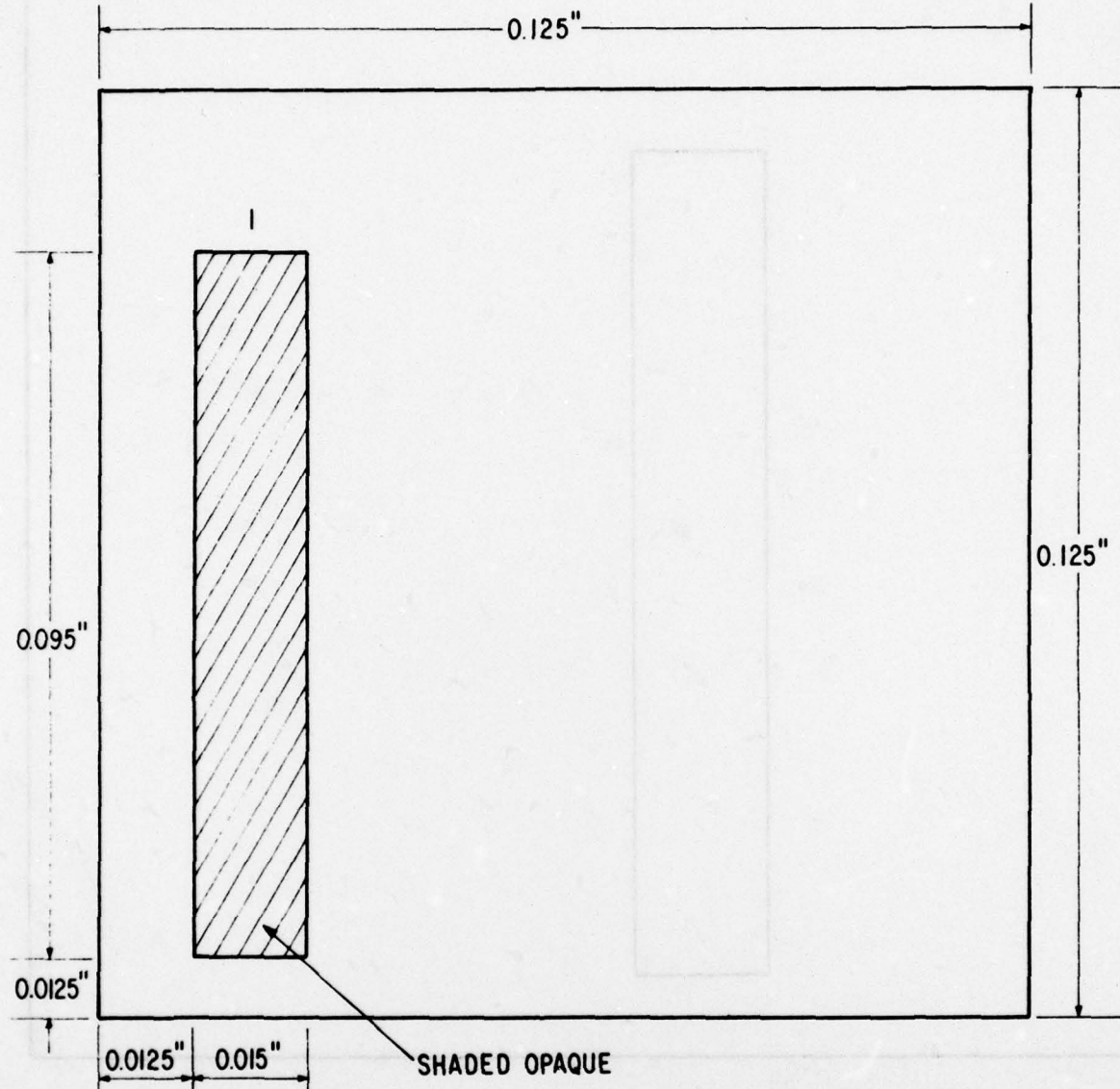
MASK Z64

Figure 142. Is Used to Open Up Areas in the Resist for Ion Writing Experiments



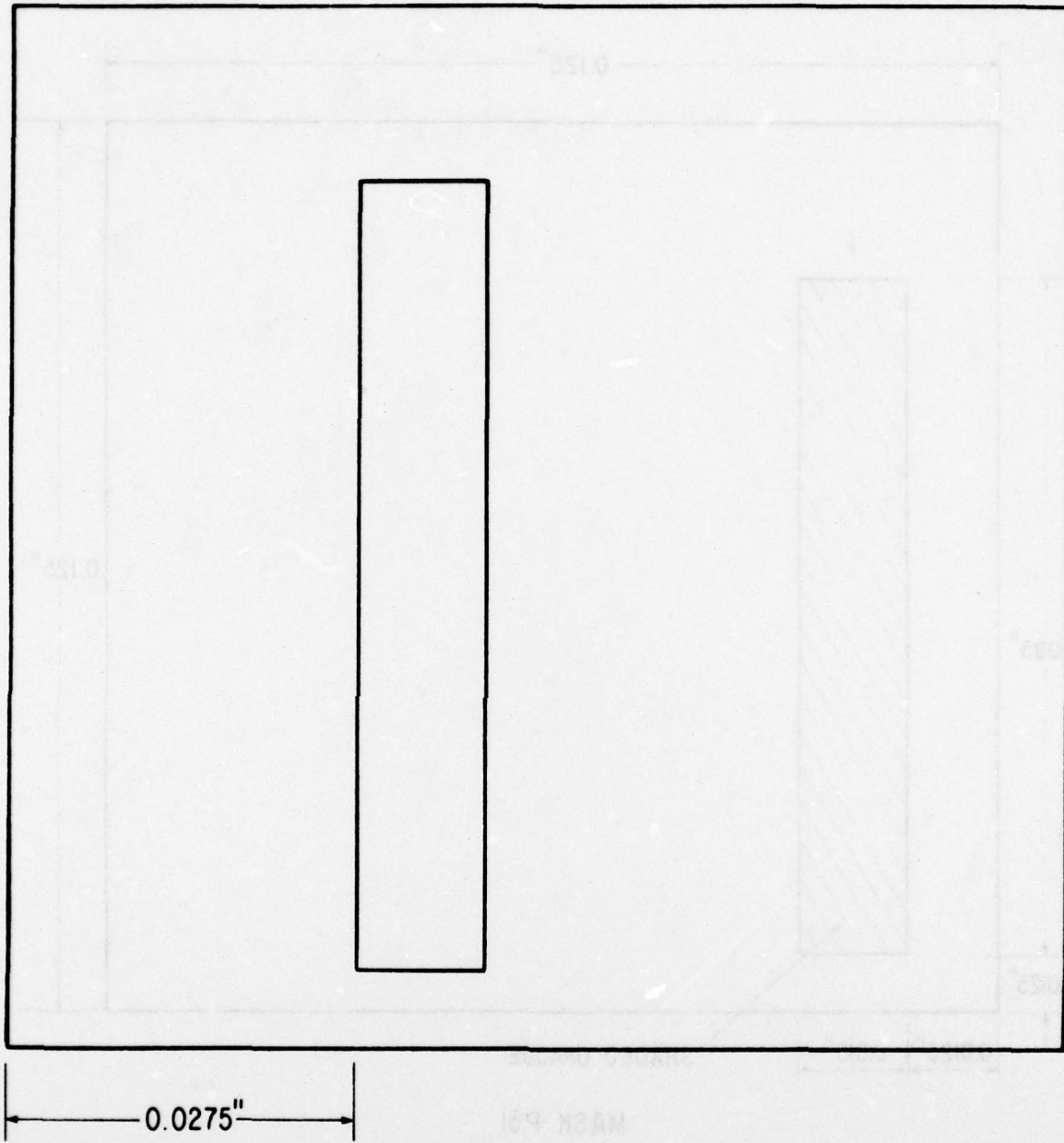
TEST PATTERN P3

Figure 143. Indicates Written Areas of a Completed Writing Experiment



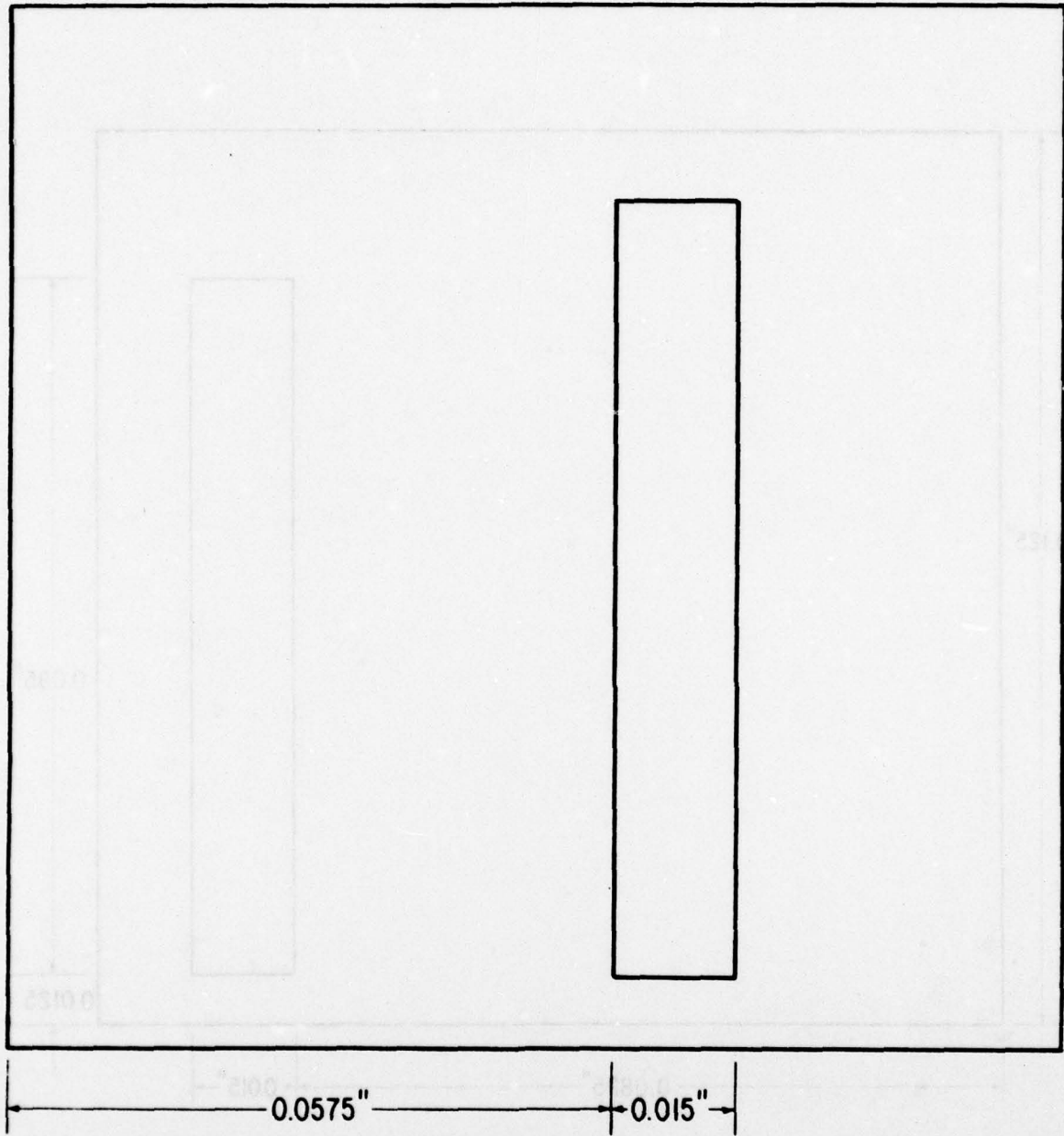
MASK P31

Figure 144. Is Used to Open Up a Resist Area for Ion Implant Writing Experiments



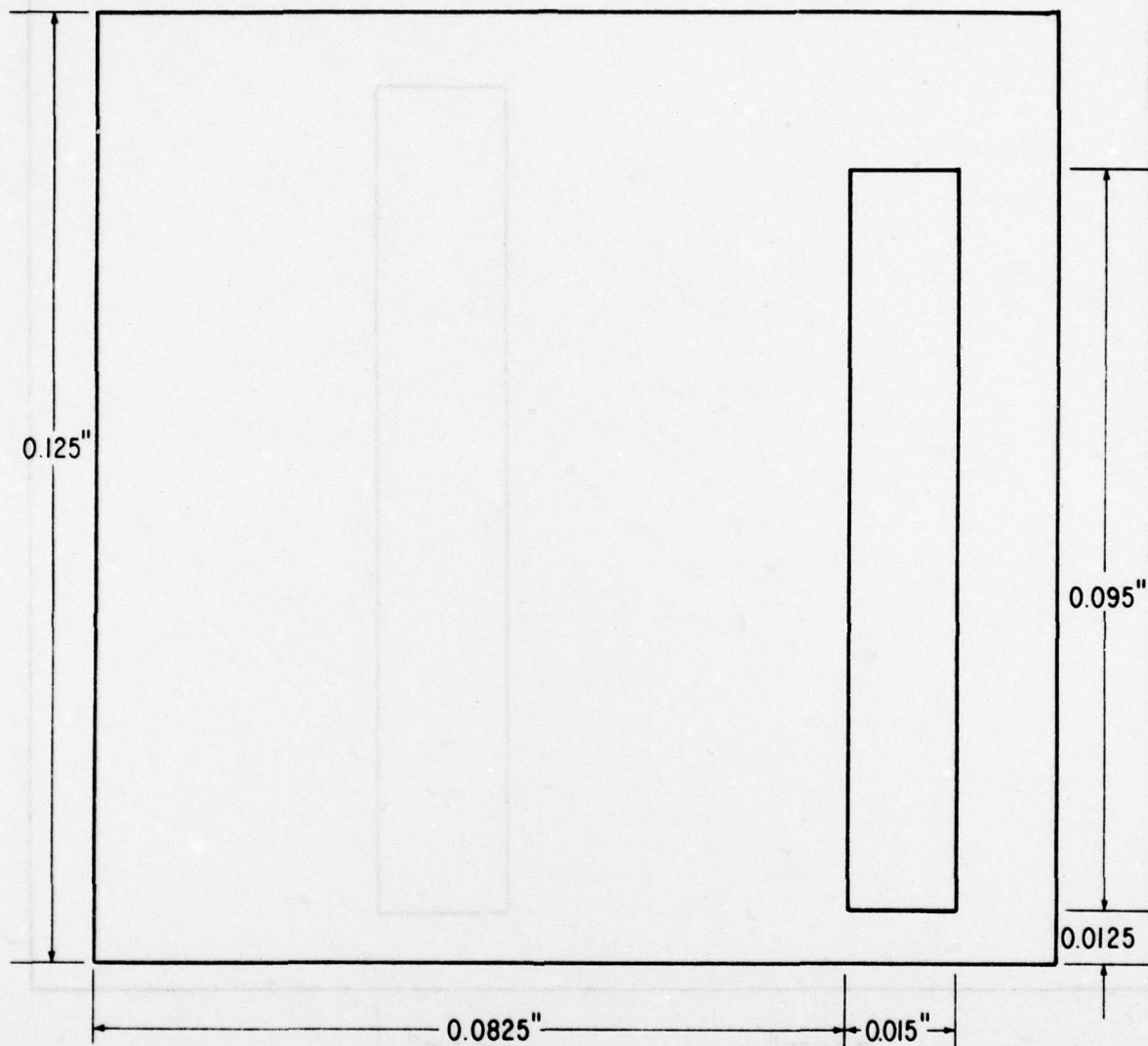
MASK P32

Figure 145. Is Used to Open Up a Resist Area for Ion Implant Writing Experiments



MASK P33

Figure 146. Is Used to Open Up a Resist Area for Ion Implant Writing Experiments



MASK P34

Figure 147. Is Used to Open Up a Resist Area for Ion Implant Writing Experiments

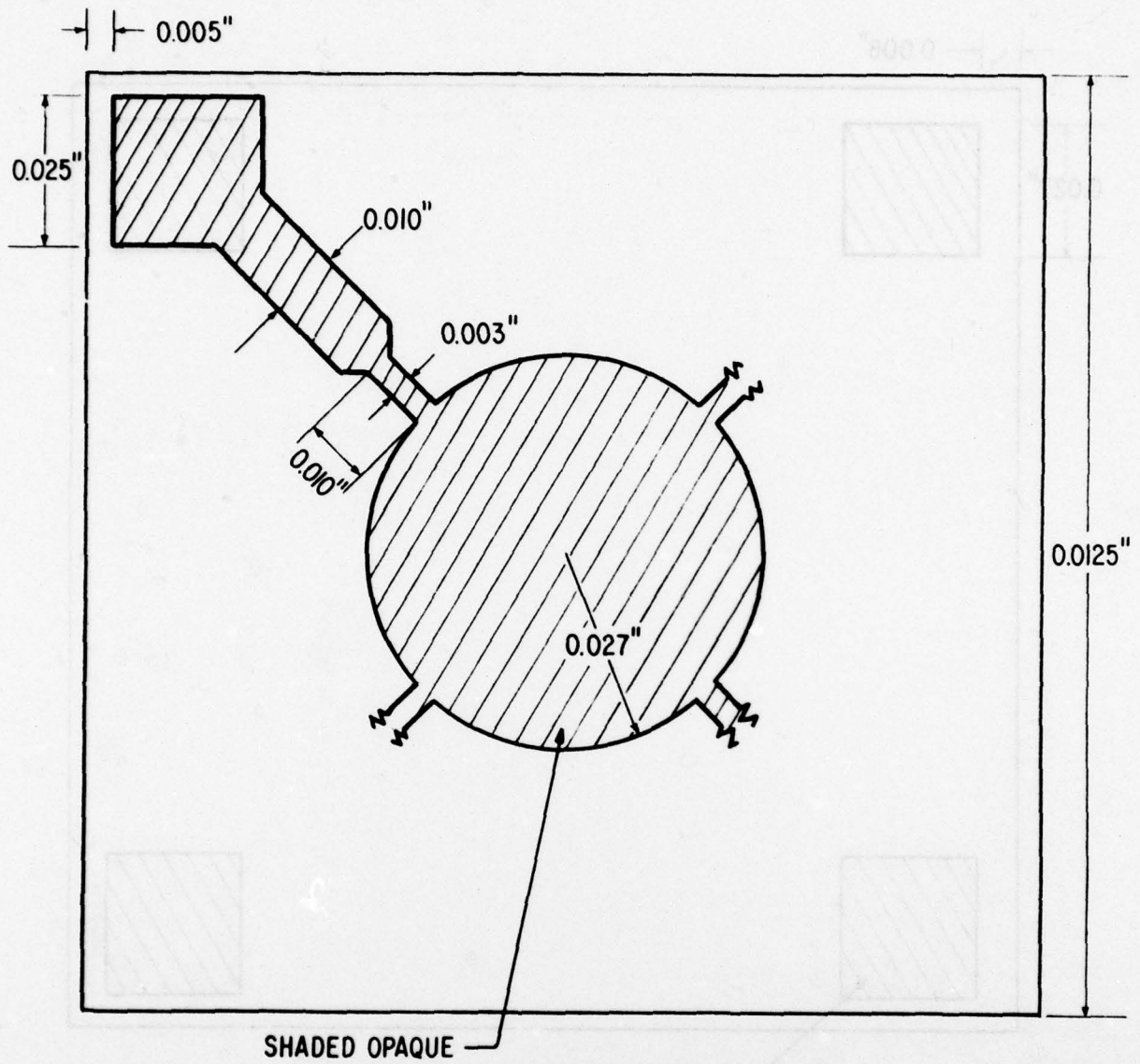


Figure 148. Test Pattern P2 Appears on Masks Z2 and Z3 to Open Up the Oxide for the Field Implants of Van der Pauw Patterns

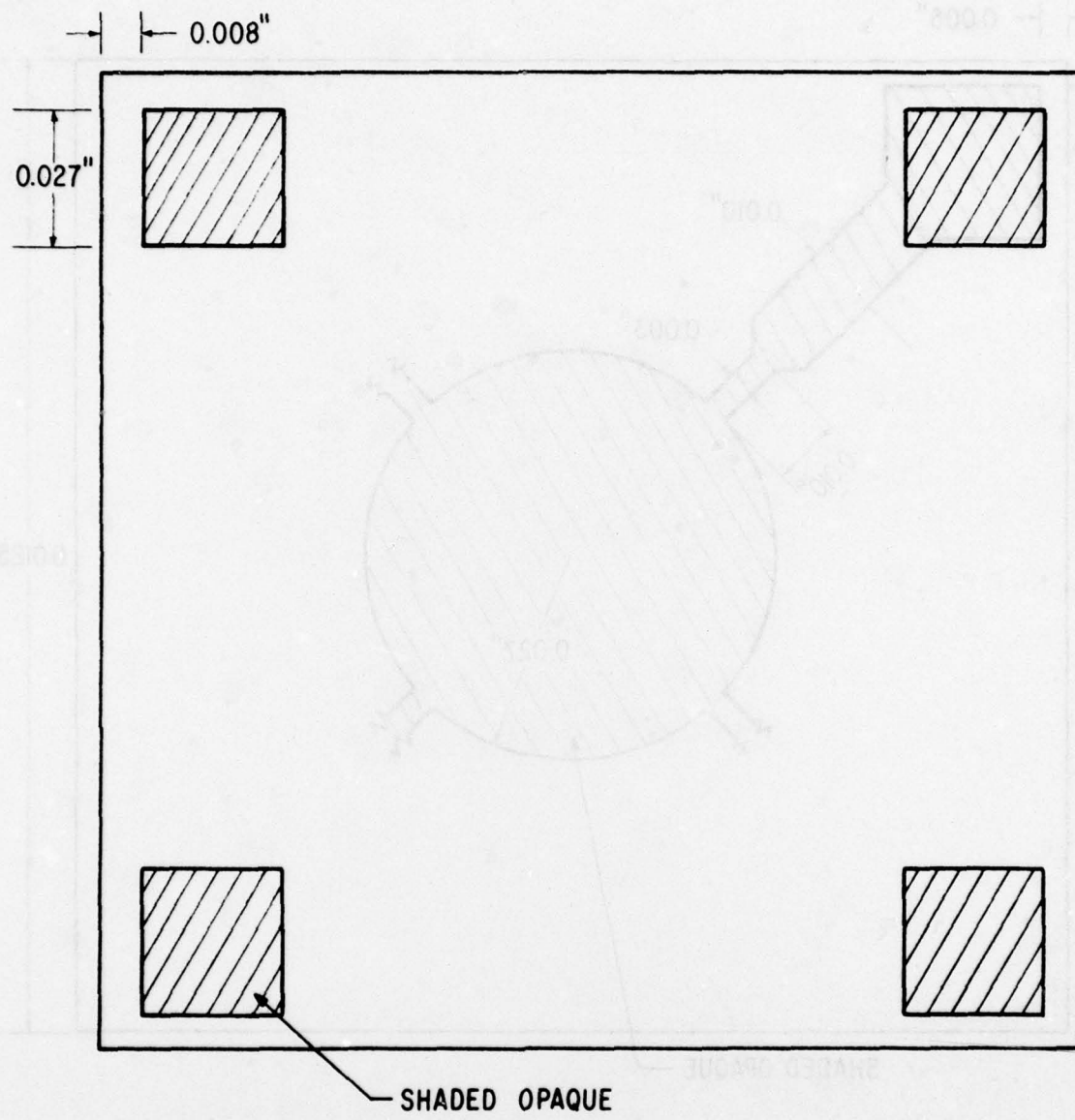


Figure 149. Test Pattern P2 on Mask Z4 Is Used to Pattern the Metallization for Contact Pads for Van der Pauw Patterns

REFERENCES

1. C.Q. Lemmond, et al, "Fourth Interim Report - Advanced Archival Memory" DARPA Contract Number F33615-76-C-1322, January 16 - April 15, 1977.
2. A.V. Crewe, et al, "Electron Gun Using a Field Emission Source" Review of Scientific Instruments, 39, 4 April 1965, p. 576.
3. G.H.N. Riddle, "Electrostatic Einzel Lenses with Reduced Spherical Aberration for Use in Field Emission Guns," Presented at the 14th Electron, Ion and Photon Beam Symposium, Palo Alto, Cal., May 1977.
4. D.L. Fraser, et al, "A Computer Analysis of the Spherical Aberration of Three Electrostatic Immersion Lenses," Record of the 11th Symposium on Electron, Ion, and Laser Beams, Boulder, Col., May 1971, p. 209, San Francisco Press Inc., 1971.
5. H.G. Parks, "Analytical Solution of the Axial Potential for a Three Element Electrostatic Lens." Record of the 11th Symposium on Electron, Ion, and Laser Beams, Boulder, Col., May 1971, p. 229, San Francisco Press Inc., 1971.
6. C. Liebmann, "An Improved Method of Numerical Ray Tracing Through Electron Lenses," Proceedings of the Physical Society, Vol. B62, No. 360, 50 1949.
7. S. Bertram, "Calculation of Axially Symmetric Fields," Journal of Applied Physics, Vol. 13, 496 1942.
8. A.B. El-Kareh, "Design and Analysis of Symmetrical and Asymmetrical Electrostatic Immersion Lenses Using a Digital Computer," Record of the 10th Symposium on Electron, Ion, and Laser Beam Technology, Gaithersburg, Md., 21-23, May 1969, p. 393, San Francisco Press, Inc., 1969.
9. H.G. Parks, MSEE Thesis, Syracuse University, Syracuse, N.Y., June 1969.
10. G.H. Shortley and R. Weller, "The Numerical Solution of Laplace's Equation," Journal of Applied Physics, Vol. 9, 334 1938.
11. G.A. Farrall, "Electric Field Enhancement and Field Optimization for Structures of Simple Geometry," General Electric Company TIS Report 74CRD128, Class 1, July 1974.
12. C.Q. Lemmond, et al, "Third Interim Report - Advanced Archival Memory," DARPA Contract Number F33615-76-C-1322, October 16, 1976 - January 15, 1977.
13. O'Klempner and M.E. Barnett, Electron Optics, 3rd Edition, Cambridge University Press, New York, N.Y., 1971.

14. R.G.E. Hutter, "Electron Beam Deflection, Part I: Small-Angle Deflection Theory," Journal of Applied Physics, Vol. 18, August 1947, pp. 740-758.